Low Temperature Fabrication of One-Dimensional Nanostructures and Their Potential Application in Gas Sensors and Biosensors

Nare Gabrielyan

A thesis submitted to De Montfort University
in partial fulfilment of the requirements for the
degree of Doctor of Philosophy

Emerging Technologies Research Centre
De Montfort University, Leicester

May 2013

Declaration

I declare that this thesis has not been submitted in part or whole for any other degree or qualification at De Montfort University, or any other academic institutions.

The work contained in this thesis is as a result of my own effort unless otherwise stated.

"I may not have gone where I intended to go
but I think I have ended up where I needed to be."
... Douglas Adams

Acknowledgements

I'd like to express my gratefulness to my first supervisor, Dr. Shashi Paul, Head of Emerging Technologies Research Centre (EMTERC), for his professional guidance and assistance, as well as for the offer of this PhD program without which this thesis would not have been produced.

My appreciation goes to Dr. David Armitage for their role of second supervisor.

I am thankful to Mr. Paul Taylor, principal research technician at EMTERC for ordering consumables and making sure the necessary equipment is working. My appreciation also goes to Dr. Iulia Salaoru, Dr. Richard Cross and Dr. Konstantin Vershinin for their training and help with equipment usage. Thanks also to all EMTERC students and my friends for their support, motivation and understanding throughout my PhD and especially during the writing of the thesis.

Thanks goes to Mr. Matthew Rosser and Mrs. Ecaterina Ware for scanning and transmission electron spectroscopy analyses.

My sincere professional and personal gratitude goes to Dr. Dominic Prime, my best friend who throughout my PhD became my second family, motivator and advisor, and for proofreading my thesis. Thanks also to Dr. Jonathan Nicholls for his advice and help with proofreading.

I would like to express my gratitude to my family for their support of my idea to study abroad and their understanding of our communication limitations throughout my writing up period.

Finally, I am thankful to De Montfort University for their financial support of my studentship.

Abstract

Nanomaterials are the heart of nanoscience and nanotechnology. Research into nanostructures has been vastly expanding worldwide and their application spreading into numerous branches of science and technology. The incorporation of these materials in commercial products is revolutionising the current technological market. Nanomaterials have gained such enormous universal attention due to their unusual properties, arising from their size in comparison to their bulk counterparts. These nanosized structures have found applications in major devices currently under development including fuel cells, computer chips, memory devices, solar cells and sensors. Due to their aforementioned importance nanostructures of various materials and structures are being actively produced and investigated by numerous research groups around the world. In order to meet the market needs the commercialisation of nanomaterials requires nanomaterial fabrication mechanisms that will employ cheap, easy and low temperature fabrication methods combined with environmentally friendly technologies.

This thesis investigates low temperature growth of various one-dimensional nanostructures for their potential application in chemical sensors. It proposes and demonstrates novel materials that can be applied as catalysts for nanomaterial growth.

In the present work, zinc oxide (ZnO) and silicon (Si) based nanostructures have been fabricated using low temperature growth methods including hydrothermal growth for ZnO nanowires and plasma-enhanced chemical vapour deposition (PECVD) technique for Si nanostructures. The structural, optical and electrical properties of these materials have been investigated using various characterisation techniques. After optimising the growth of these nanostructures, gas and biosensors have been fabricated based on Si and ZnO nanostructures respectively in order to demonstrate their potential in chemical sensors.

For the first time, in this thesis, a new group of materials have been investigated for the catalytic growth of Si nanostructures. Interesting growth observations have been made and theory of the growth mechanism proposed.

The lowest growth temperature in the published literature is also demonstrated for the fabrication of Si nanowires via the PECVD technique.

Systematic studies were carried out in order to optimise the growth conditions of ZnO and Si nanostructures for the production of uniformly shaped nanostructures with consistent distribution across the substrate.

The surface structure and distribution of the variously shaped nanostructures has been analysed via scanning electron microscopy. In addition, the crystallinity of these materials has been investigating using Raman and X-ray diffraction spectroscopies and transmission electron microscopy.

In addition to the fabrication of these one-dimensional nanomaterials, their potential application in the chemical sensors has been tested via production of a glucose biosensor and an isopropyl alcohol vapour gas sensor based on ZnO and Si nanostructures respectively. The operation of the devices as sensors has been demonstrated and the mechanisms explored.

Table of Contents

List of Figures

List of Tables

List of Acronyms

0D……... zero-dimensional
1D……..……..……. one-dimensional
1TO…….…….……. first order optical mode
2D…….…….…….. two-dimensional
3D…….……. three-dimensional
AC…….…… alternating current
AE…….…… auxiliary electrode
AFM…….……... atomic force microscopy
ASG…….…… aqueous solution growth
a-Si……..…….. amorphous Si
BE…….…….. backscattered electron
COB…….……... catalyst on the bottom
COT …….……..catalyst on the tip
c-Si…….……... crystalline Si
CV…….…….. cyclic voltammetry
CVD……..……..…… chemical vapour deposition
D.I. ……..……..…… de-ionised
DC…….…… direct current
DMA…….....…….…… dynamic mechanical analysis
DSC……...…….…… differential scanning calorimetry
DTA……..…….…… differential thermal analysis
EBL…….…….…… electron-beam lithography
EDS……...…….…… energy-dispersive X-ray spectroscopy
FAD……..…...…… flavin adenine dinucleotide
FTIR…….…… Fourier transform infrared
FWHM……..……..…… full width at half maximum
$Ga(acac)_3$……..…… gallium(III) acetylacetonate
GCE……..……..……..glassy carbon electrode
GOD…….…… glucose oxidase
HF……..…….hydrogen fluoride
HMT……..……..…… hexamine

IEP……. isoelectric point

IPA……. propan-2-ol

IR……. infrared

ITO……. indium tin oxide

LOD……. limit of detection

LPCVD……. low pressure chemical vapour deposition

LWHM……. left width at half maximum

MBE……. molecular beam epitaxy

MC-VLS……. metal-catalysed vapour-liquid-solid

MEMS……. microelectromechanical systems

MFC……. mass flow controller

MFP……. mean free path

MO……. metalorganic

MOC……. metalorganic compound

MW……. microwave

MWCNT……. multi-walled carbon nanotubes

NFD……. nickel(II) formate dihydrate

NFM……. nickel(II) formate

NiAc ·4H_2O……. nickel(II) acetate tetrahydrate

NL……. nucleation layer

NSL……. nanosphere lithography

NW……. nanowire

OA……. oriented attachment

OAG……. oxide–assisted growth

OR……. Ostwald ripening

PBS……. phosphate buffer saline

PdAc……. palladium(II) acetate

PECVD……. plasma-enhanced chemical vapour deposition

ppb……..parts per billion

RE……. reference electrode

RF……. radio-frequency

RIE……. reactive ion etching

RWHM……. right width at half maximum

SAED……. selected area electron diffraction

sccm……..…….…….standard cubic centimeter per minute
SE…….…… secondary electron
SEM……...…..…… scanning electron microscopy
SiNW…….……..…… silicon nanowire
SLS…….…… solid-liquid-solid
SPM……..……...……..…… scanning probe microscopy
TA……..…….……...…… thermal analyses
TEM……...……...…..……..…… transmission electron microscopy
TGA……..……..……...… thermogravimetric analyser
TMA……..……...…..…… thermomechanical analysis
UV-Vis……...……..…..……..… ultraviolet-visible
VLS…….…… vapour-liquid-solid
VS…….…….…… vapour-solid
VSS…….……..…… vapour-solid-solid
WE……...……. working electrode
XRD…….……...…… X-ray diffraction
ZNH…….…… zinc nitrate hexahydrate
ZnONW…….…… zinc oxide nanowire

Chapter 1

Overview of Thesis

Nanotechnology has a recognised and highly valued position in current scientific and technological world. The core of nanotechnology is nanomaterials, various structures and compositions of which have been produced and demonstrated. Due to their high potential for commercialisation, the current market demand has created an environment where the research focus in the field of nanotechnology is drawn towards expanding the methods for low temperature and low cost fabrication of nanostructured materials.

Silicon and zinc oxide nanostructures are of high importance in nanotechnology research due to the ease of their incorporation into already established microelectronics technologies, as well as their structural, electronic and optical properties [1-2]. Various structures of these nanomaterials have been fabricated via bottom-up and top-down approaches by researchers around the world for their application in a variety of devices such as memory units, solar cells, lithium batteries, field-effect transistors, diodes and sensors [3-6].

This thesis demonstrates a low-temperature growth of zinc oxide and silicon nanostructures and studies their potential application in gas and biosensors.

1.1. Organisation of thesis

This thesis is divided into 9 chapters describing the history, science, fabrication methodologies, characterisation technologies and results of this work. The arrangement of the chapters (except for this chapter which gives an overview) is as follows:

Chapter 2 gives an overview to the main topic of this research, namely nanostructures. The general idea and research trend in gas and biosensors are also discussed in this chapter, followed by nanostructure promise and application in those devices.

Chapter 3 introduces the fabrication and characterisation techniques used for the development of nanostructures, analyses of their structural and optical properties, and development and testing of gas and biosensors.

Chapter 4 starts with a literature review of one-dimensional zinc oxide nanostructures and their fabrication methods, followed by experimental results of this work for the production and testing of zinc oxide nanowires.

Chapter 5 is concerned with glucose biosensor fabrication based on zinc oxide nanowires. It starts with a literature overview of available zinc oxide nanowire based glucose biosensors and then demonstrates the biosensor (and its characteristics) fabricated in the framework of this thesis.

Chapter 6 starts with introducing to the work done in the field of silicon nanowire growth, with various growth methods used until now. The second part of the chapter provides the results of silicon nanowire growth and characteristics obtained in this work via low-temperature plasma-enhanced chemical vapour deposition technique.

In Chapter 7 metalorganic compounds are discussed and their application as catalyst materials for silicon nanostructure growth demonstrated.

Information on gas sensor fabrication based on silicon nanostructures grown in this work is demonstrated in Chapter 8, with an introduction to the available literature on silicon nanowire based gas sensors discussed at the beginning.

Conclusions of the work and suggestions for the future work are given in Chapter 9.

1.2. Important outcomes of the research

This section outlines the most important outcomes obtained in this thesis.

Even though there is much work done in the literature on understanding the effect of various parameters governing the growth of zinc oxide nanowires via hydrothermal method, optimisation experiments of growth parameters for the production of uniformly sized and evenly distributed nanowires arrays across the sample was performed in this thesis for the first time at De Montfort University (Section 4.3).

Electrochemical glucose biosensors were fabricated using zinc oxide nanowire based working electrodes with direct growth of the nanowires from the gold electrodes. When carrying out cyclic voltammetric experiments, increase in current was observed with addition of glucose pointing to the catalytic oxidation of glucose.

The lowest growth temperature (150 ºC) in the published literature was achieved for the fabrication of silicon nanowires from Ga catalyst layers via the plasma-enhanced chemical deposition technique.

It was demonstrated via Raman spectroscopy and transmission electron microscopy that the Si nanowires grown from Ga catalyst layers have crystalline core with amorphous Si shell surrounding the core.

A new group of compounds, namely metalorganic compounds, were for the first time in the published literature demonstrated to act as catalysts for the production of Si nanostructures.

A gas sensor based on silicon nanostructures grown from gallium(III) acetylacetonate was developed for the detection of propan-2-ol vapours.

1.3. Peer Reviewed Published Work and Conference Presentations

"Growth of low temperature silicon nano-structures for electronic and electrical energy generation applications" N. Gabrielyan, K. Saranti, K. Nama, S. Paul, *Nanoscale Research Letters*, 2013, 8:83 (Highly accessed)

"Zinc oxide nanowires for biosensor applications", N. Gabrielyan and S. Paul, *Proc. SPIE*, 2011, 8414, 841407

"Optimising the low temperature growth of uniform ZnO nanowires", N. Gabrielyan, R.B.M. Cross, S. Paul, *Materials Research Society Symposium Proceedings*, 2010, 1201, pp. 295-300

"Zinc oxide nanowires for biosensor applications", oral presentation at "Photonics & Micro- and Nano- structured Materials" Workshop, June 2011

"Zinc Oxide Nanowire Growth Optimisation" poster presentation at "ICPAM-9" Conference, September 2012

"Electrochemical Biosensors Based on Zinc Oxide Nanowires" poster presentation at "Biosensors" Conference, May 2010

"Optimisation of the Uniform Growth of Zinc Oxide Nanowires" poster presentation at "Materials Research Society" Conference, November 2009

1.3.1. Papers (submitted)

"Optimisation of Uniform Zinc Oxide Nanowire Growth Conditions", N. Gabrielyan and S. Paul, *Nanoscience and Nanotechnology Letters*, submitted

1.3.2. Papers (in preparation)

"Growth of Si Nanostructures From Metalorganic Compounds" N. Gabrielyan and S. Paul, to be submitted to Nature Nanotechnology

"Optimisation of the Growth Parameters for Low Temperature Si Nanowire Growth via the VLS method" N. Gabrielyan and S. Paul, to be submitted to Small

"Growth of Si Nanowires from Ga catalyst layer at 150 ºC in a PECVD reactor" N. Gabrielyan and S. Paul, to be submitted to Nano Letters

"Resistor Gas Sensors Based on Si Nanowires Fabricated using Metalorganic Compounds as Catalysts" N. Gabrielyan and S. Paul, to be submitted to Sensors and Actuators B: Chemical

"Electrochemical Glucose Biosensor Based on ZnO Nanowires Grown Directly From the Electrode", N. Gabrielyan and S. Paul, to be submitted to Biosensors and Bioelectronics

Chapter 2

Nanostructures and their application in chemical sensors

This chapter gives a brief overview of various nanostructures that are at the centre of attention of many research groups. In the last few decades, a significant amount of research has been done on the growth of nanostructures with various compositions, dimensionality, structure and properties. The adopted fabrication methods, various properties and applications of these structures will be discussed in the first part of this chapter.

The second section of this chapter introduces sensor technology with more in depth discussion of gas sensors and biosensors. The advantages of the application of nanomaterials in these devices are also discussed.

2.1. Nanomaterials and nanotechnology

Currently, there is tremendous amount of interest in nanomaterials and nanotechnologies [7]. The word "nanotechnology" was first coined by Tokyo Science University Professor Norio Taniguchi in a paper in 1974 describing it as a study of manipulating the matter at the atomic or molecular scale [8]. However, the beginning of nanotechnology is accepted to be the speech on "There's plenty of room at the bottom" given by Richard Feynman on December 29th, 1959 at an American Physical Society meeting at Caltech [9]. In his lecture Feynman said "*What I want to talk about is the problem of manipulating and controlling things on a small scale… what I have demonstrated is that there is room – that you can decrease the size of things in a practical way. I now want to show that there is plenty of room. I will not now discuss how we are going to do it, but only what is possible in principle… we are not doing it simply because we haven't yet gotten around it… arrange the atoms one by one the way we want*". Feynman has realised that at the atomic level new forces arise and hence new possibilities and effects [10].

Nanotechnology originates from the term "nano", which is derived from Greek word for dwarf, while the modern scientific meaning of nano means the billionth part in an SI unit. Materials that have at least one dimension smaller than 100 nm can be considered nanomaterials. Nanotechnology deals with the progress of technology and research into the nanoscale. The United States National Nanotechnology Initiative website [11] defines

nanotechnology as: “The understanding and control of matter at dimensions of roughly 1 to 100 nm, where unique phenomena enable novel applications” [10].

It is well known that at the nanoscale physical, chemical and biological properties of the material differ from these of individual atoms, molecules and bulk materials. This is due to two major influences; (i) high surface to volume ratio and (ii) quantum effects. High surface to volume ratio means that a significant fraction of atoms are at the surface of the materials [12], this property affects the reactive, as well as mechanical and electrical properties, whereas the quantum effect is the confinement of charge carrier motion in a small volume of the material [12] and this property affects the optical, electrical, thermo-electric and magnetic properties of the material. The main objective of the research in nanotechnology is to discover these properties and use them for making devices with better characteristics and performance [13-14]. Currently nanomaterials are applied in a wide range of commercial fields including technology, environment, cosmetics, medicine, food, energy and agriculture [8].

2.1.1. Nanomaterials classification

There are a large number of nanomaterial varieties and the most common way to classify those is by their dimensions describing how many dimensions of the material size has not been reduced to <100 nm. The size of nanoscale materials can be reduced in (i) one direction, resulting in two-dimensional (2D) nanostructures, (ii) two directions creating one-dimensional (1D) nanostructures, and (iii) three directions, resulting in zero-dimensional (0D) nanostructures [14]. There are also three-dimensional (3D) nanostructures, also called bulk nanomaterials [7]. All these materials can be amorphous, single or poly-crystalline, have various forms and be made of single or multiple elements of metals, ceramics or polymers [7].

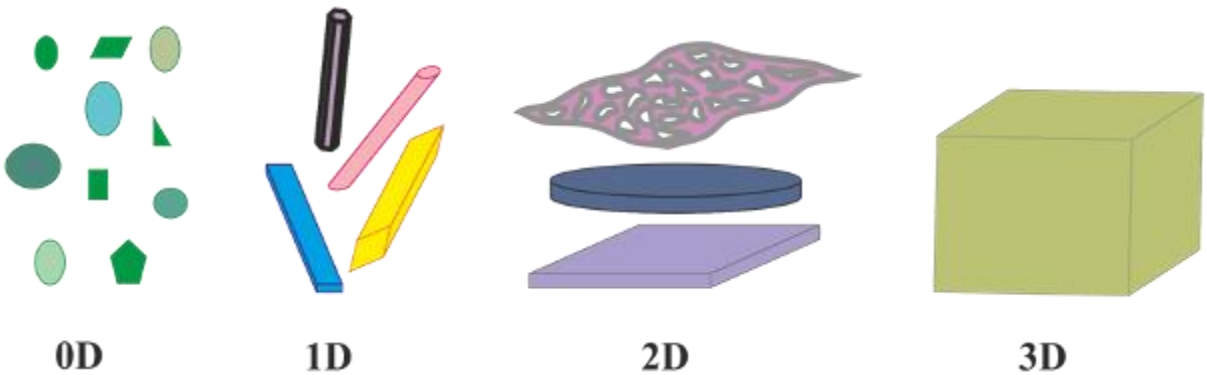

Figure 2-1. Classification of nanomaterials according to dimensions.

Zero-dimensional nanostructures are of high importance as their investigation is very informative as a means of understanding the size-dependent physical and chemical properties. In addition, many active components have been fabricated using these structures, such as single-electron transistors, memory units, optical detectors, lasers, light-emitting diodes and sensors [14]. Various 0D structures have been reported such as uniform particle arrays, also known as quantum dots, heterogeneous particles arrays, core-shell quantum dots and hollow spheres [15].

One-dimensional nanostructures, such as wires, rods, tubes, ribbons and belts, have been fabricated and used in many fields of science and technology [2, 15-16]. These structures are ideal candidates for studying electrical and thermal transport-processes in one-dimensionally confined objects [14]. There have been many fabrication methods devoted to the investigation of 1D nanostructure growth, such as chemical vapour deposition (CVD), laser ablation, electrochemical deposition, sol-gel and template assisted growth [17]. These nanostructures have found their application in nanoelectronics, nanodevices, and national security [15].

Two-dimensional structures are usually deposited on a substrate or a support. In this case the 2D nanomaterials are considered nanocoatings. These can be monolayers (layers with a thickness of one molecule) and multilayers (if the substrate thickness is in nanoscale or in case of few layers being deposited sequentially) [7]. Various shapes have been reported such as branched structures, nanocoatings, nanoprisms, nanoplates, nanodisks and nanosheets [15]. These structures have a wide range of applications in components for medical devices, flat-panel displays, chemical sensors, solar cells, and the food industry [18].

Three-dimensional materials are not confined to 100 nm in any dimension. The reason that these structures are called nanostructures is because they possess nanocrystalline structures or have features at the nanoscale. These materials can be composed of many nanocrystals of different orientations called nanocrystalline materials (Figure 2-2(a)), incorporate nanoparticles, nanowires or nanotubes in a matrix called matrix-reinforced nanocomposites (Figure 2-2(b and c)) or be layered nanocomposites incorporating multinanolayers (Figure 2-2(d)) or sandwiches of nanolayers bonded to a matrix [7]. Various types of these structures have been reported such as nanocomposites [19-21], porous materials [22-23] and nanocrystal arrays [24-25]. Their demand is increasing in optoelectronics and bio-MEMS (microelectromechanical systems) devices. Nano imprint lithography is the most common method for 3D nanoscale pattern fabrication due to its simplicity, short processing time and high manufacturing precision [26].

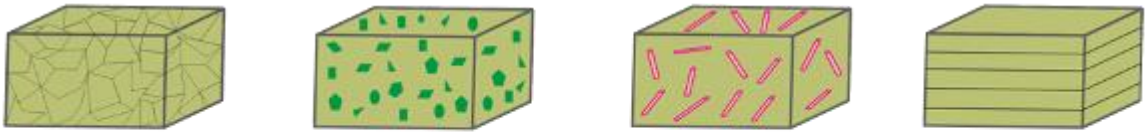

(a) (b) (c) (d)

3D nanostructures

Figure 2-2. 3D nanostructures with (a) nanocrystalline materials, (b) embedded nanoparticles, (c) embedded 1D nanostructures and (d) multinanolayers.

2.1.2. Nanomaterials size and quantum effects

As it was discussed earlier, with size reduction of materials two effects take place: (i) increase of surface to volume ratio and (ii) quantum effects.

Due to the surface to volume effect of the nanomaterials, the size and shape of nanomaterials are very important in dictating the properties of the nanomaterials. The surface to volume ratios are easily calculated from the formulas presented in Table 2-1 [7].

Table 2-1. Calculations for surface to volume ratios of various dimensional nanomaterials.

$\frac{A}{V} = \frac{3}{r}$	For a sphere of radius *r*
$\frac{A}{V} = \frac{2}{r}$	For cylinder (nanowire) of radius *r*
$\frac{A}{V} = \frac{6}{L}$	For a cube of size *L*

where *A* is the nanomaterial surface area and *V* is the volume.

Therefore, if we take a big particle and reduce it to many small particles keeping the overall volume of the material the same, the surface area will increase drastically. It has been calculated that when reducing 10 μm diameter sized particle into particles with 10 nm diameters, the total amount of particles becomes 1 billion and increase in overall surface area is by a factor of 1,000. Decrease in particle size also means increase of surface atoms at the expense of bulk atoms. It has also been calculated and shown that reducing size of nanoparticles leads to their easy coalescence even at room temperature and reduction of lattice parameter, and another interesting structural property of nanoparticles is their self healing characteristics of planar defects [7].

When discussing quantum effects of nanomaterials, it is important to firstly understand the energy levels. In bulk materials the atomic energy levels are broadened into energy bands (Figure 2-3).

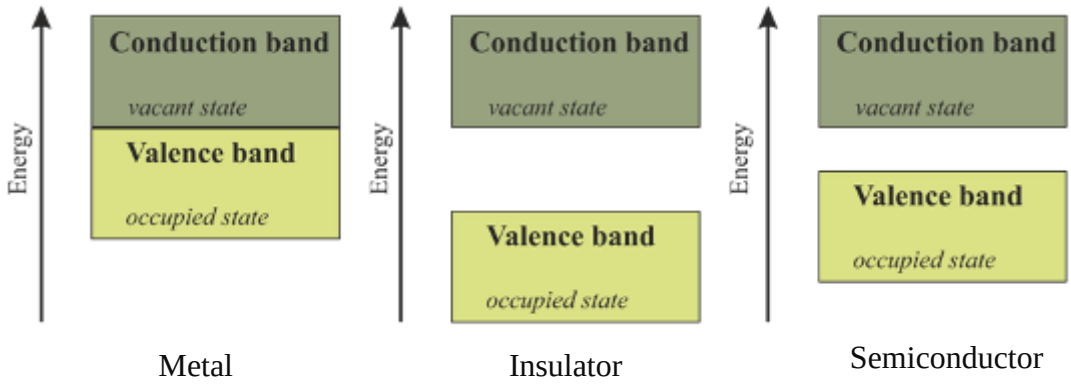

Figure 2-3. Energy bands in metals, insulators and semiconductors.

In metals and conductors the valence band is not separated from the conduction band with a bandgap, whereas for insulators and semiconductor materials there are wide and not so wide energy gaps correspondingly. Therefore, in metals electrons are free to flow and very little energy is required to move electrons from valence to conduction band, whereas for insulators it is difficult. For semiconductors it is possible to excite electrons from valence to conduction band with certain amounts of energy. When the bulk material is reduced in size in 3 dimensions (0D nanomaterials) the electron is confined in all 3 directions, therefore electrons are not free to move (are not delocalised). In 1D and 2D nanomaterials electron confinement takes place in 2 and 1 directions correspondingly (electrons are free to move along the nanowire/nanotube axis for 1D and the plane of the nanolayers for 2D structures) and delocalisation takes place in 1 and 2 directions respectively. In 3D structures electrons are completely delocalised. In order to calculate the effect of this confinement on the energy states, the "particle in the box" problem is calculated in quantum mechanics where the electron is considered to be confined in the nanostructure in an infinitely deep potential well from where it cannot escape. The calculations show that with a decrease of the nanostructure dimensions the energy level separation gets wider. This leads to a discrete energy spectrum. Therefore, by spatially confining electrons the bandgap of the semiconductor materials can be increased and well-defined energy levels at the band edges developed [7, 12].

The conduction electrons are dependent on the energy state, therefore when this value is changing due to dimensionality of the material, the number of conduction electrons of that state is also altering. The density of states which represents the number of electrons within an

energy range (D(E) = dN/dE) highly depends on the dimensionality and will be different for 0D, 1D, 2D nanomaterials and bulk material (see Figure 2-4) [7].

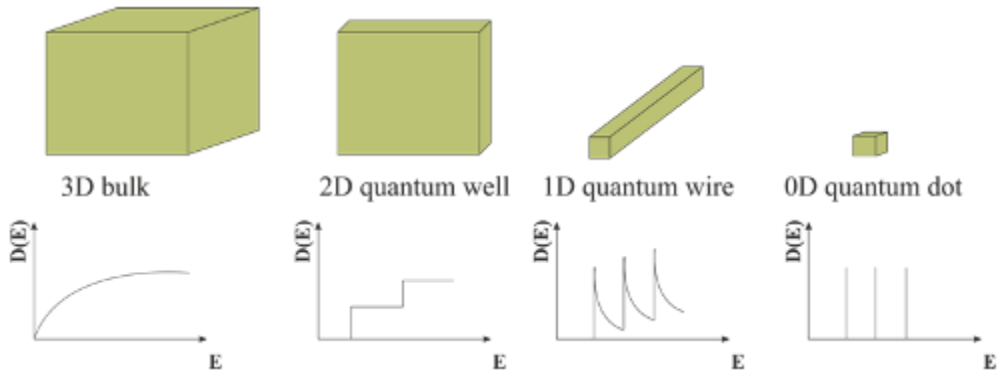

Figure 2-4. Density of states in a bulk material, 2D, 1D and 0D nanomaterials.

The density of states is a very important characteristic of the material that determines material properties including the excitons in semiconductors, superconducting energy gap, and thermo-power effect and therefore requires proper tuning which is done by using nanomaterials [7].

2.1.3. Nanomaterial properties

There are several interesting properties that arise in materials when decreasing their size to the nanoscale. One of them is the possibility of increasing the strength of steel, aluminium, magnesium and titanium alloys by reducing the scale of individual grains to the nanoscale. It is also possible to alter the melting temperature both upwards and downwards in respect to their bulk materials. The other thermal benefit they bring is the thermal transport; 1D nanostructures behave like phonon waveguides for transferring heat (as heat gets transferred via free electrons or lattice vibration waves (phonons)). For 2D nanomaterials the thermal conduction is low and is still under investigation. When looking at the electrical properties of nanomaterials, the important effects are the quantum effect and the classical effect. In the quantum effect due to discreet energy levels, conducting materials can behave like semiconductors or insulator. For the classical effect the mean-free path for inelastic scattering is comparable with the size of the system and therefore the scattering events get reduced. In 3D nanostructures the incorporated nanograins are inclined to reduce the electrical conductivity. The same effect can take place for 2D nanostructures (reduction of grain size results in reduction of the electrical conductivity). In 1D nanostructures the conductivity can

be extremely high due to the confinement. The electrons get reflected back from the surface not allowing them to get out of the nanomaterial, and electrons travel without noteworthy loss of kinetic energy. In 0D nanomaterials no electron delocalisation occurs therefore metallic systems can behave as insulators [7]. When looking at optical property changes when moving from bulk to nanomaterials, the exciton binding energy increases resulting in high excitonic state appearance in the absorption spectra of nanomaterials at room temperature. By tuning the nanomaterial dimensions the emission of visible light (photons released due to recombination of an electron and a hole) can be altered. Typically there is blue shift (shorter wavelengths) with size reduction [7, 12].

2.1.4. Nanomaterial fabrication methods

Two main approaches are used in nanomaterials fabrication: bottom-up approach where the materials and devices are assembled chemically from molecular components by carefully monitoring and controlling the formation on atomic, molecular and supramolecular levels. Nanostructures fabricated by bottom-up method have less defects compared to the other approach of nanomaterials fabrication and more cost effective, but it is hard to obtain large-scale fabrication. The top-down approach starts with a bulk of material and through etching, elimination and layering of the material reduces it to a desired size and shape. Lithography is one of the most common top-down fabrication techniques and can achieve good control over the structure dimension, location and organisation. Still, when the device size is reduced below 100 nanometers, the precision starts to fail or becomes very costly [17]. In addition, this method can contribute to imperfections in the surface structure and defects within the nanomaterials. These can affect the chemical and physical properties of the structures. Nevertheless, this is an important fabrication technique and continues to be used widely [13].

From bottom-up fabrication techniques for making 0D, 1D and 2D nanostructures, there are many techniques that are commonly used. Inert gas condensation method uses a vacuum chamber where the material of interest is vaporised under constant admission of an inert gas. This method can use laser ablation, sputtering or evaporation to heat the material. Vapour phase expansion uses an inert gas to move the evaporated material into a vacuum chamber, where the material undergoes rapid expansion, thus cooling and agglomeration forming clusters. Sono-chemical processing uses ultrasound to nucleate a chemical reaction leading to nanoparticles formation. In sol-gel deposition method a solution of precursors is subjected to a polymerisation reaction forming a colloidal suspension (‘sol’) of particles kept in

suspension by adding a surfactant. Afterwards the solution is converted into a gel to stop the particles forming networks. Thereafter the solvent is evaporated leaving the nanomaterials behind. Molecular self-assembly uses the self-organisation of the molecules such as crystallisation meaning no external pressure is applied. It is about creating favourable conditions for the atoms/molecules to self-assemble into desired shapes. Langmuir-Blodgett method uses self-assembly to create 2D nanofilms. The substrate is dipped into a solvent (usually water) that is covered by fatty acids (these have both hydrophobic and hydrophilic chemical groups), when the substrate is withdrawn from water, the fatty acids stick to the sample leaving the solvent behind [7, 27]. Various numbers of layers can be made by repeatedly dipping the substrate. Electrodeposition is used to deposit metal nanomaterials on a conducting substrate [28-30]. In this method the ions from the solution are deposited onto the negative cathode. Physical vapour deposition includes plating where vapour condensates onto the cool substrate, ion plating which uses electrical field to accelerate the ionised vapour, and sputtering which uses argon gas to eject the ions of interest from the target [7]. In the case of the CVD method the precursor gas is brought into contact with the substrate where it decomposes leaving a layer of the compound to be deposited. The deposit can be formed either (i) via chemical reactions taking place in the vapour or (ii) by reaction of the vapour with the substrate surface. Varieties of this technique include metal organic CVD, where metal organic precursors are used, plasma-enhanced CVD (this will be discussed in more details in Chapter 6) and laser CVD where laser light is used for activating the chemical reactions in the vapour [31].

2.1.4.1. Nanomaterials applications

Nanomaterials and nanotechnologies have a high potential for being applied in a wide range of technologies. Nanomaterials are not only used for making the devices smaller, even though this is one of the benefits that is mostly stated for nanotechnology. Another benefit is also the performance alterations of the devices when nanomaterials are employed [7].

Nanomaterials are used to manipulate material strength and thermal properties which is possible to achieve by introducing impurities in the form of dispersed particles. By the introduction of various shapes of nanoparticles it is possible to reduce or increase the thermal conductivity. Increase of thermal conductivity is often achieved using various nanostructures (carbon nanotubes, nanofibrils). Moreover, it is also possible to increase the conductivity

more in one direction than another. In addition, nanofoams and nanocoatings/nanoparticle mixtures are made as thermal insulators [32] and barriers correspondingly [7, 33].

Nanomaterials are thought to make a huge difference in electronic applications. In addition, they are used to increase the multifunctionality in the devices such as computer chips that also serve as biodetectors [7]. Nanotechnologies are rapidly becoming the centre of semiconductors, memory units, interconnects, energy generation, solar cells and storage devices (fuel cells, batteries and supercapacitors), light emitting diodes, display devices, devices for sound insulation, and sensor technology (including thermal, electrical, magnetic, chemical and mechanical). With nanomaterial application the detection types and sensitivities of sensors are expected to improve. These sensors are part of interactive, smart and intelligent systems and incorporation of nanomaterials into these systems increases the performance and multifunctionality while decreasing the size and the cost [7].

2.2. Chemical sensors

The modern sensor era is thought to have started in the 1970s with commercialisation of sensors for non-professional uses, such as semiconductor combustible gas sensors, solid electrolyte oxygen sensors and humidity sensors [34]. Sensors can be categorised into two main groups; physical and chemical. Physical sensors are sensitive to environmental variables such as temperature, pressure, magnetic field and force. Chemical sensors have chemical interface and rely on particular chemical reactions for their response; they respond selectively to the analyte of interest via a chemical reaction and can respond either (i) qualitatively or (ii) quantitatively. Both gas and biosensors are chemical sensors [35].

Chemical sensing includes three steps: a recognition step (selective chemistry), a transducing step and a signal processing step.

A simple diagram of the chemical sensor can be seen in Figure 2-5.

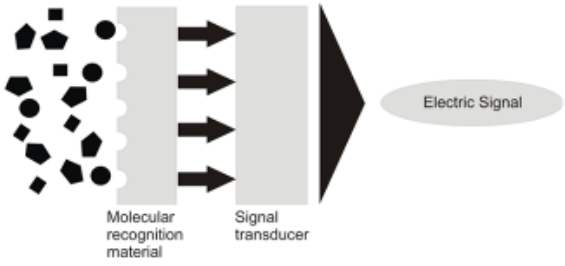

Figure 2-5. General diagram and working principle of a chemical sensor.

In the recognition step the analyte to be sensed undergoes a specific reaction with the molecular recognition material. This recognition generates a signal which is then recognised by the transducer and transformed into a measurable signal. The molecular recognition molecule should be specific only to the analyte of interest and should in ideal case not react with any other molecule in the environment. It may convert the analyte into another chemical species. This is accompanied with a change in electrical, optical, mechanical or other properties of the system thus indicating the presence of the material of interest in the environment. The output signal depends on the transducer of choice [36].

Chemical sensors can be classified based on various specifications, such as the biorecognition molecule in case for biosensor, their attachment method, analyte of interest and sensitivity but the most common classification is by the transducer type [36].

There are a wide variety of transducers that can be used in chemical sensors, including electrical (surface conductivity, conductivity and capacitance), magnetic (paramagnetism and bead-based devices), optical (absorption, fluorescence, luminescence, internal reflection, surface plasmon resonance, light scattering, and evanescent waves), mass sensitive/piezoelectric (surface acoustic wave, and quartz crystal microbalance), heat sensitive/thermometric (calorimetry, and enzyme thermistor), and the most commonly used electrochemical (potentiometric, conductometric and voltammetric/amperometric) transducers that were used in the first biosensor[36-38]. Electrochemical biosensors are widely used in research as they have an important factor which is a non-destruction of the host system during functioning.

2.2.1. Biosensors

Biosensors have promising applications in interdisciplinary fields: they are being used in the areas of drug discovery, biodefence, environmental monitoring, narcotic detection security, military, environmental monitoring, and the process industry.

A biosensor is a special type of a chemical sensor incorporating a biological element (an enzyme, antibody, nucleic acid, microorganism or cell). In this work Turner's definition of the biosensor will be adopted [39-40] which is "*compact analytical device incorporating a biological or biologically-derived sensing element either integrated within or intimately associated with a physicochemical transducer. The usual aim of a biosensor is to produce either discrete or continuous digital electronic signals which are proportional to a single analyte or a related group of analytes*".

Biosensors are one of the most investigated chemical sensors and have gained much research interest during the last few decades, with the rate of publications on biosensors dramatically rising over the last two decades. The number of publications per year starting from the 1970s can be seen in Figure 2-6.

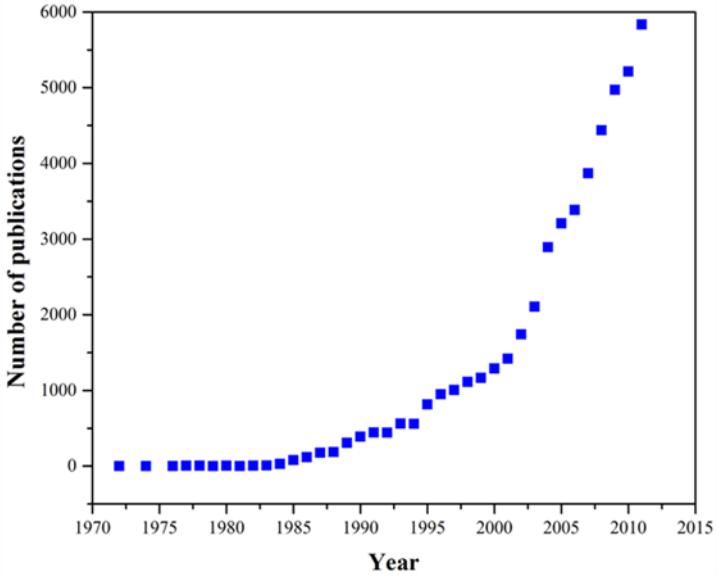

Figure 2-6. Approximate number of publications on biosensors compared for each year. Source: Scopus; search date March 24, 2013.

The biosensors used in this work use electrochemical transducers, particularly amperometric, therefore this sensing method and working principle is discussed and provided in detail.

2.2.1.1. Amperometric biosensors

Amperometry works on the principle of measuring the current at a constant potential. The current is measured as a function of the fraction of converted material. When using the biosensor, the current is measured for various analyte concentrations and compared to one with no analyte.

Amperometric biosensors are divided into first, second and third generation devices.

The first generation biosensors worked by detecting enzymatically produced electroactive species [41]. For example, first generation glucose sensors detected the hydrogen peroxide that was produced during the oxidation of glucose, catalysed by the enzyme glucose oxidase (GOD) (Equation 2-1). The disadvantage of this method includes the strong dependence of the electrical signal on the oxygen concentration [42].

$$\boldsymbol{Glucose + O_2 \xrightarrow{GOD} gluconolactone + H_2O_2}$$ **Equation 2-1**

The second generation sensors replaced the oxygen with an artificial electron acceptor capable of transporting the electrons involved in the redox reaction from the electrode to the enzyme and vice versa [43]. These carriers are called mediators. The reactions taking place in these systems can be seen in Equation 2-2.

$$\begin{aligned} Glucose + GOD_{ox} &\longrightarrow gluconolactone + GOD_{red} \\ GOD_{red} + 2M_{ox} &\longrightarrow GOD_{ox} + 2M_{red} + 2H^+ \\ M_{red} &\longrightarrow M_{ox} + ne^- \end{aligned}$$ **Equation 2-2**

The limiting step in this type of biosensor response is the transfer of the electrons between the enzyme active centres and the electrode. In the ideal case, there would be a direct contact between the electrode and the redox enzyme. In this case no mediator would be required and the electrons involved in the redox reaction would be measured directly at the electrode. The devices using this principle belong to the third generation biosensors.

When fabricating and testing third-generation amperometric biosensors there are a few processes determining the quality and speed of the device. These are; (i) transport of the analyte to the surface of the sensor, (ii) binding of the analyte to the biorecognition molecule, and (iii) conversion of the analyte by the biorecognition molecule and transfer of the resulting electrons to the electrode [42]. When enzyme electrodes are used (the enzyme is attached to the electrode) the enzyme catalysed reaction takes place in a finite region in close proximity to the electrode surface. For this reason, the transport of the analyte to the electrode surface is an important consideration for the biosensor speed. This process can take place via three different routes: migration, diffusion, and convection [44].

Migration is the movement of charged species due to the electrical potential gradient present in the system (this does not occur for neutral molecules, such as glucose). However, most of the biosensors work in a solution where the inert electrolyte suppresses this potential gradient. Therefore, migration does not play a massive role in biosensor response limitations.

Diffusion occurs when there is a concentration gradient and is always present wherever there is concentration difference from one part of the medium to another, but this is a relatively slow process as it involves random movement of molecules.

Convection is the movement of the bulk solution which should be important for biosensors. Unfortunately, when using magnetic stirrers for example, the system does not

hold a reproducible and calculable mass transport conditions. However, there are some methods adopted for well defined and calculable transport, such as rotating disc, wall jet or chemical flow geometries [44]. If done properly, convection can increase the sensitivity, stability and reproducibility of the biosensor. It makes sure that the concentration of the analyte and various species is maintained the same near the electrode surface.

It is noticed that under forced convection conditions convection dominates in the bulk solution but near the close proximity of the surface diffusion is still dominant. This layer is called a diffusion layer (δ). In this layer there is an equilibrium between the analyte mass transport and surface reaction [42] (Figure 2-7).

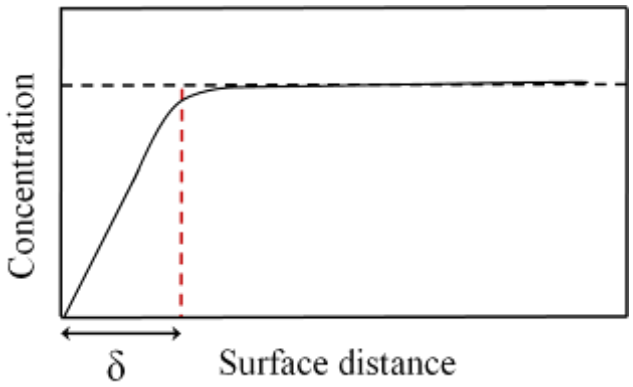

Figure 2-7. Concentration profile under convection control.

The second important step in the biosensor functioning is the recognition of the analyte by the biorecognition molecule. The formation of a complex with the analyte/substrate (S) and biorecognition molecule/enzyme (E) is usually very fast and the rate is limited by the diffusion. If the biorecognition molecule is a redox enzyme then there is a redox reaction after the complex formation. In cases where the analyte is glucose and the biorecognition molecule is GOD, the redox reaction is glucose oxidation.

In the third step, the enzyme converts the analyte into a product (P) and at the same time gets reduced itself into its reduced form. The enzyme gets reoxidised by the electron conductor which transfers the electrons to the electrode.

The schematic representation of the third generation amperometric biosensor can be seen in Figure 2-8.

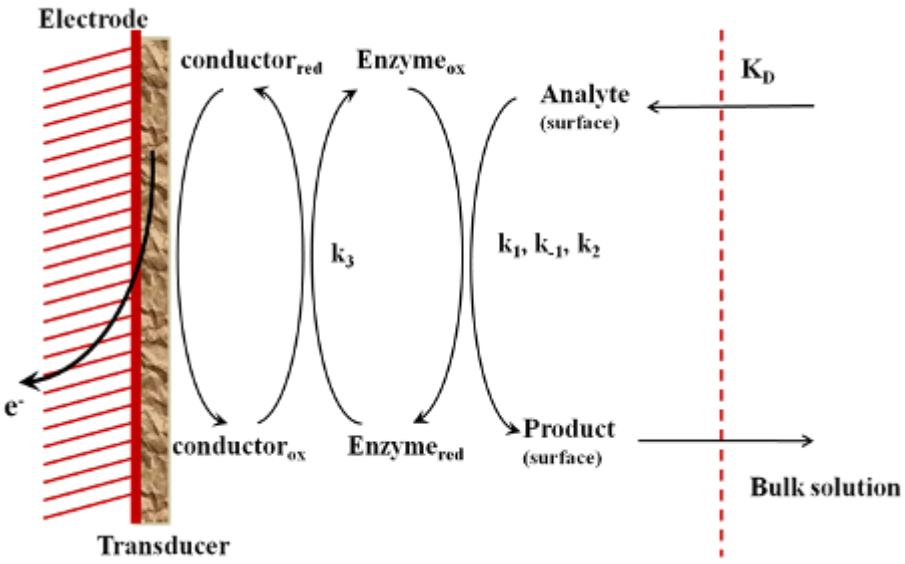

Figure 2-8. Schematic representation of the third generation biosensor working principle.

The kinetics of the biosensor work shown in Figure 2-8 is given by Equation 2-3.

$$S + E_{ox} \underset{k_{-1}}{\overset{k_1}{\rightleftarrows}} E_{ox}S$$

$$E_{ox}S \xrightarrow{k_2} P + E_{red}$$

$$E_{red} + conductor_{ox} \xrightarrow{k_3} E_{ox} + conductor_{red}$$

$$conductor_{red} \longrightarrow conductor_{ox} + e^-$$

Equation 2-3

In Figure 2-8 and Equation 2-3 the rate constants k_1, k_{-1} and k_2 are those for Michaelis-Menten kinetics which describes a system where the [S] binds reversibly to the [E] to form an [ES] complex which then reacts irreversibly to produce [P] and to regenerate free [E], k_3 is the rate constant for heterogeneous electron transfer and k_D is the rate constant for the analyte transport to the electrode surface.

The theory of enzyme electrode processes will be described in more details in Section 3.2.10.

2.2.2. Gas sensors

As the name suggests, gas sensors are devices for detection of various gases in the environment, especially toxic and harmful ones. Their importance has recently been drawn towards monitoring environmental pollutions [45]. Gas sensors can be designed to work

either in air or in liquid [35, 46]. The dramatic rise of the number of publications on gas sensors since the 1960s can be seen in Figure 2-9.

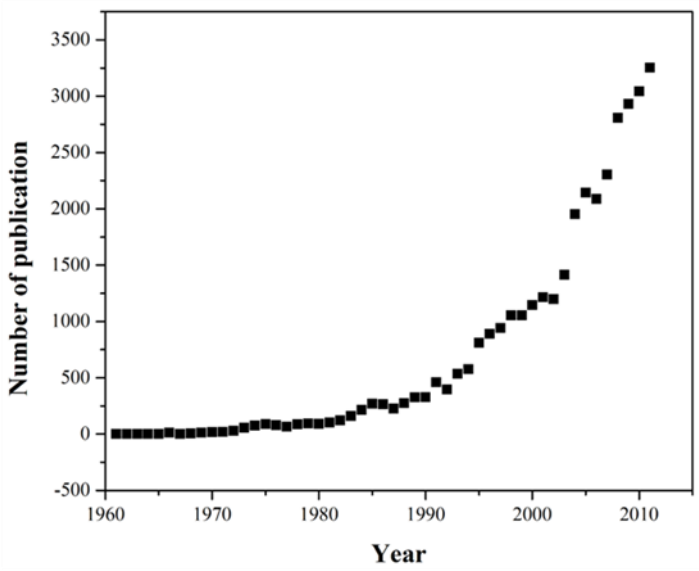

Figure 2-9. Approximate number of publications on gas sensors compared for each year. Source: Scopus; search date March 24, 2013.

Many types of materials have been tested for gas sensor applications including monocrystalline elementary semiconductors (with covalent bonding), polycrystalline compounds (ionic bonding) and oxides [47]. Out of these, metal oxide gas sensors have been widely used due to their small size, low cost and compatibility with microelectronic processing. The detection principle of the gas sensors can be due to one of the following interactions between the analyte gas molecules and the semiconductor surface; (i) the reduction/oxidation of the semiconductor in the gaseous ambient, (ii) ion exchange or (iii) adsorption [48]. The most important type of gas sensors is based on absorption of gas molecules on the surface of the sensors causing change in the electrical conductivity of metal oxides. Due to lattice defects of semiconductor metal oxides (excess or deficiency of metal or oxygen in the lattice) after chemisorption there is a change in conductivity associated with electron interaction with these defects. When using small surface to volume thin films or polycrystalline ceramics, only small amounts of species absorbed on the surface are able to modify the electrical transport properties resulting in high sensitivity of the sensor. In addition, these devices work at high temperatures (200 – 600 ºC) for enhancing chemical reactivity of the gas with the sensor material [49]. The gas sensor research has been focused on CO_2, CO, SO_2, O_2, O_3, H_2, Ar, N_2, NH_3 and H_2O gases, as well as the organic vapours such as methanol, ethanol, propan-2-ol, benzene and some amines [50].

The performance factors of the gas sensor such as sensitivity, selectivity, time response, stability, durability, reproducibility, and reversibility are highly affected by the sensing materials properties (such as polymers, semiconductors, organic/inorganic composites that have been used as sensing materials). The sensitivity of gas sensors is increased with increase of the surface to volume ratio of sensing materials. This makes nanostructures very attractive materials for increasing the sensitivity of chemical gas sensors [45].

2.2.3. Nanomaterials application in gas sensors and biosensors

Considering the nanoscale functionality and interaction of biological and chemical systems the obvious effect of nanotechnology in sensors is undeniable [51].

Nano sensors and nano-enabled sensors have vast range of applications including in communication, transportation, buildings and facilities, robotics, safety, defence, military operations and medicine [52]. They are anticipated to be used in the areas stated in Figure 2-10.

Figure 2-10. Anticipated nanosensor applications [52].

These devices can be inserted into the body and also targeted to destroy tumors [51]. The interest of this integration is coming from their special optical and electrical properties, stability and possibility of reducing the size of the sensing systems, high surface to volume ratio, chemically modifiable physical properties coming from their small size, ability to be

functionalised, unusual target binding properties and structural robustness [53]. In general nanotechnology offers design of miniature, less power hungry and more sensitive sensors compared to macro- and microsensors. In sensor technology nanomaterials are thought to mainly influence gas and biosensors [51].

Various types of nanomaterials have been used in gas sensors for detecting gases such as NO_x [54-55], NH_3 [56], CO [57-58], CO_2 [59], CH_4 [60-61] and alcohol vapours [62-64]. Some gas sensors have the potential to be sensitive enough to detect a single chemical and biological molecule [51, 65].

Functionalisation, namely bio-functionalisation of nanomaterials is a significant step for fabrication of nanomaterials based biosensors. Over the past decade, various nanomaterials have been functionalised by biomaterials by physical adsorption, electrostatic binding, specific recognition or covalent coupling. These functionalised nanomaterials can already be used as catalysts by inducing the target to produce a detectable signal; electronic conductors by accelerating electron transfer between target and electrode (thus enhancing amperometric response or producing reagentless sensing); optical emitters due to being labelled onto recognition probes to produce detectable optical signal for target detection [53].

Nanoscience can bring huge advantages for sensor technology, including high sensitivity which can be achieved due to making changes in the conductivity of the material, selectivity, lower level of detection limit, reduced production cost and power consumption, ability to sense extremely small amounts of analyte, and higher stability. In addition, the analytes can be sensed directly, without the use of a label. The use of nanotechnology in sensor technology has shown rapid growth during the last 6-7 years. This was due to a report for low-potential detection of nicotinamide adenine dinucleotide enzyme using carbon nanotube-modified electrode and the first use of gold nanoparticles as labels for electrochemical immunosensors [66]. It is thought that this technique will make the sensing of even just one atom/molecule possible. The whole nanomaterials structure makes contact with analyte compared to just the surface contact when using conventional sensor technology [10]. New bioanalytical systems are using less sample material for performing sophisticated tests within minutes at the point of care, allowing multiple variable analyses through one device. Moreover, nanomaterials allow the continuous monitoring of live cells, as well as in vivo testing of organisms.

The selectivity does not immediately connect with the size of the transducer, but by using nanomaterials it is possible to implement surface modifications and functionalisation of the nanostructures which will directly affect the selectivity.

The speed of the detection is immediately affected by the sensor size, so using nanoscale technologies will have a great influence on the speed of the biosensor.

Various structures of nanomaterials are being fabricated for use in sensors. These include nanoparticles, one-dimensional nanostructures and nanomembranes. From various nanomaterials, one-dimensional nanostructures, particularly nanowires, have gained considerable attention for chemical sensor fabrication [67].

Introducing 1D nanostructures into biosensors instead of the technologies used previously adds the advantages of higher sensitivity, higher signal-to-noise ratio, robustness, and shorter response time [68]. Nanomaterials can serve as electrodes or interconnect micro- and nanoelectronic systems and at the same time work as electric wirings/connectors of enzymes due to their dimension being comparable to those of biological molecules. On the other hand, the length of nanowires can be up to few micrometers which makes their use in micrometre-scale circuitry easily feasible. Electron transport properties of nanowires are very important for electrical and electronic/sensor application of these materials. These are directly connected to the wire diameter, wire surface condition, crystal structure and its quality, chemical composition and crystallographic orientation along the wire axis [67]. However, until now a few limitations remain for biosensors based on nanowires to be readily used and marketed. Those are the selectivity, response time, multiplexed detection, and long-term stability [68].

2.3. Conclusions

Nanomaterials possess highly important and interesting properties coming from their size that make them one of the promising topics of current research. These materials are being integrated in many fields of science and technology with sensor research being one of them.

Among many types of sensors, gas and biosensors are one of the highly investigated devices due to their importance in healthcare. Nanomaterials applications in these devices promise to improve most of their properties, such as sensitivity, selectivity, size and production cost.

This work is devoted to low-temperature fabrication of various types of nanostructures, particularly 1D nanomaterials, and their application/testing in gas and biosensors.

Chapter 3

Fabrication and characterisation techniques

The first part of this chapter gives an overview of various deposition techniques used in this work for the growth of nanostructures and fabrication of gas and biosensors. The second part of the chapter presents the characterisation techniques for both the nanostructures and gas and biosensors. The working principle of these techniques will also be explained.

3.1. Fabrication techniques

Most of the deposition technologies used in this work operate in vacuum systems, such as sputterer, evaporator and plasma-enhanced chemical vapour deposition (PECVD) system. Therefore, prior to describing each of the deposition equipment separately, it is appropriate to discuss the vacuum systems in general.

There are many reasons for using vacuum deposition techniques, such as reduction of contamination by removing air and dust particles from the chamber; this will also reduce possible oxidation of the material. In addition, the film quality can be improved as the mean free path (MFP) of the molecule can be increased up to 5 cm for vacuum of the order 10^{-4} Pa. It is found that 10 collisions of the molecule can make a noticeable deviation from its original path, therefore if the distance between the deposition material and substrate is kept under 10 MFP, the film should maintain its good quality [69].

Most of the deposition equipment used for semiconductor fabrication operates in rough ($13 – 10^5$ Pa) or medium (0.013 – 13.3 Pa) vacuum regime. Rough vacuum pumps are usually working by mechanical movement of a piston, vane, plunger, or diaphragm. In most microelectronic processing equipment rotary vane system is used. All mechanical pumps work in the basis of capturing the gas, compressing the volume, followed by gas expulsion [70]. These are used to bring the pressure down to appropriate pressure for high vacuum pumps to operate; which is usually around 1 Pa. The equipment used in this work used three types of high vacuum pumps: diffusion pumps used by thermal evaporators, a cryopump used by radio-frequency (RF) magnetron sputterer and a mechanical booster pump for the PECVD system.

The diffusion pump working mechanism is quite simple. It uses vapour of a boiling fluid (oil) to capture air molecules. Afterwards the fluid condenses on the cold walls of the pump

(due to water pumped around the outside of the pump). As the oil starts heating up again at the bottom of the pump, gas molecules get released and removed via a roughing pump. The downside of this type of pump is the possible contamination of the chamber via "backstreaming" of the oil, which can be improved by placing a liquid nitrogen "cold trap" at the top of the pump which will trap the oil vapours that might escape into the chamber [70-71].

Cryopumps capture the gas (except from He) by freezing the gas particles onto a cold head of the refrigerator, at a temperature of around 20 K. This is done by liquid helium cooling. The gas remains in the pump in a frozen form. For this reason it is important to periodically allow the pump to warm up to release the trapped gases [70-71].

The typical arrangements of the diffusion pump and cryopump operated vacuum systems can be seen in Figure 3-1.

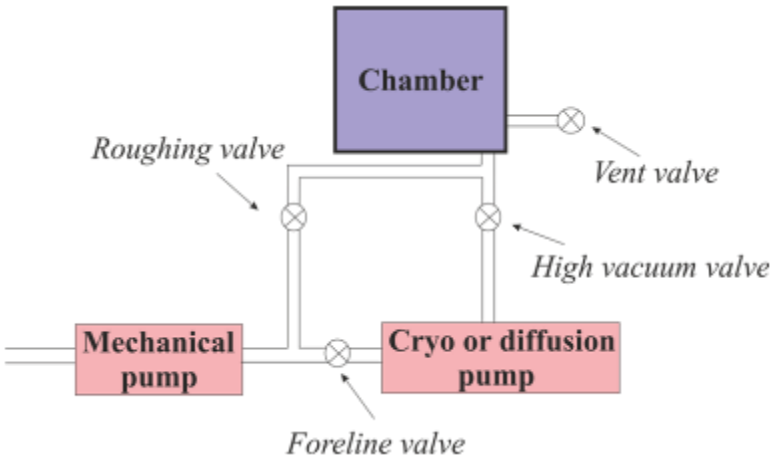

Figure 3-1. Schematic interpretation of a vacuum system.

A mechanical booster pump consists of a positive displacement vacuum pump. The operating principle is as follows: during rotation, a small clearance is maintained between the rotors and between each rotor and a stator wall. The air from the chamber passes into the pump inlet and is drawn into this space between the rotor and the stator wall. There it gets trapped and on further rotation it gets discharged from the booster pump to the backing system [72].

3.1.1. Thermal evaporator

As the name suggests, thermal evaporation is a process that deposits thin films by evaporating the required target material onto the sample substrates. The target material is loaded into a container which can be of different shapes, such as a boat, a coil, a basket or a

spiral depending on the material that needs to be deposited. These containers are made of a material with high melting point to withstand high temperatures, such as tungsten, molybdenum or tantalum. A high current is passed through the filament, heating it and triggering vapourisation of the evaporation material. Considering the low pressure of the chamber, this vapour travels across the chamber to the substrate where it accumulates in the form of a film. In order to start and stop the evaporation process abruptly, a mechanical shutter is placed above the container. It is possible to deposit a wide variety of materials by means of evaporation, such as metals, metal oxides and some organic materials [70]. The model of the evaporator used in this work was Edwards Auto 306, the photograph of which can be seen in Figure 3-2.

Figure 3-2. Photograph of Edwards evaporator used in this work.

3.1.2. Sputterer

Sputtering is an important alternative to evaporation. It was developed as a thin film deposition technique in 1920s by Langmuir. It has several advantages over evaporation, including better step coverage and is excellent for fabrication of alloys and compound materials [70].

Schematics of the sputtering process can be seen in Figure 3-3.

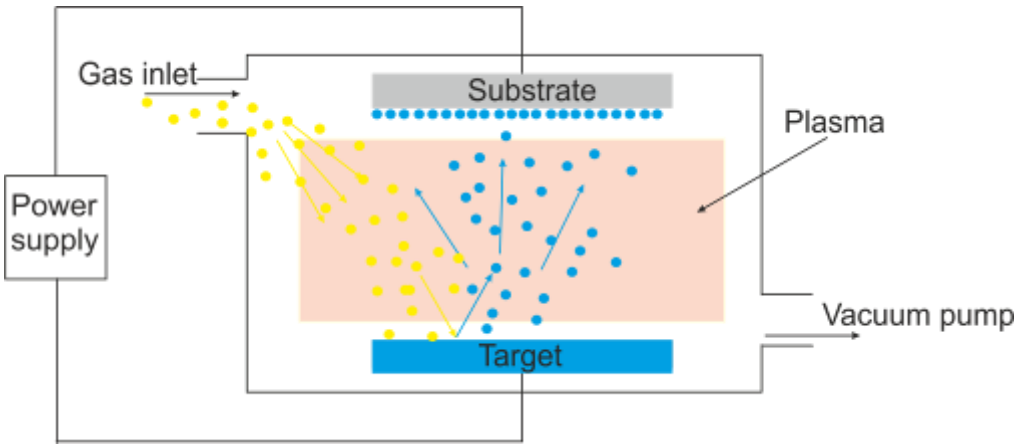

Figure 3-3 Schematic illustration of the sputtering process.

In this picture a parallel-plate plasma reactor is used. During this process a vacuum is created and an inert gas (Ar used in this work) is introduced to the chamber. Gas pressure in the chamber is normally 13 – 1.3 Pa [73] for the purposes of keeping the MFP in the order of hundreds of micrometers. The substrate is placed on the anode (positive potential), whereas target (deposition material) is at the cathode side. When a potential is applied between these plates, plasma discharge gets ignited. The electrons in the chamber will accelerate away from the target, hitting outer shells of neutral gas molecules on their way causing these to lose outer electrons and become positively charged ions. Thereafter, these positive ions accelerate towards the negatively charged target and "bombard" it releasing/sputtering material from the target. In addition, secondary electrons get generated at the surface. The atoms ejected from the target arrive at the substrate (which is placed in close proximity to the target; usually under 10 cm) mostly in the form of neutral atoms [70, 73-74].

In order to enhance the rate of the deposition and avoid overheating and damage of the substrate by electron bombardment magnets are placed under the target. This results in entrapment of the electrons above the target, so those cannot easily reach the substrate and also increases the chances of collision with the neutral gas molecules [75], thus the name of "magnetron sputtering".

The sputtering process can be used for the deposition of a wide variety of materials; for metals or materials with some electrical conductivity direct current (DC) sputtering is usually applied. However, DC sputtering cannot be used for insulators, as surface charges will build up due to striking ions. For semiconductor and insulator materials RF sputtering is used [70, 73].

In the case of RF sputtering, when the alternating power supply is used, in the first phase of a sputtering process the substrate is at a higher potential compared to the target, thus

causing the electrons to accelerate away from the target (as is the case for DC sputtering). But when the ions start to accumulate above the target, (causing self-bias and hindering the acceleration of ions towards the target) a quick potential reversal takes place (second phase). This results in pushing the ions away from the target. There is no deposition during this phase but it minimises the self-bias in the system [76].

The sputterer used in this work is a Nordiko Ltd model 1500 RF sputterer (see Figure 3-4) that incorporates three 20.3 cm targets some of which can be replaced. It incorporates both DC and RF systems. The RF power operates at 13.56 MHz. In this system the reflected power should ideally be kept below 5 % of the forward power.

Figure 3-4. The sputtering system used in this work.

3.1.3. Furnace

The furnace used in this work is a Carbolite elevator hearth furnace (Figure 3-5), capable of temperatures up to 1500 °C. The samples are placed on the ceramic holder and then mechanically lifted into the furnace chamber. This furnace is not air tight, thus in order to avoid oxide formation of the materials, nitrogen environment should be created in the chamber before the heating process. Prior to annealing of the samples nitrogen is introduced into the chamber at a high flow rate for half an hour, after which the rate is reduced and the furnace temperature is brought up to the required value. After the annealing process is

finished, the furnace is left to cool down to room temperature in a nitrogen environment before sample removal.

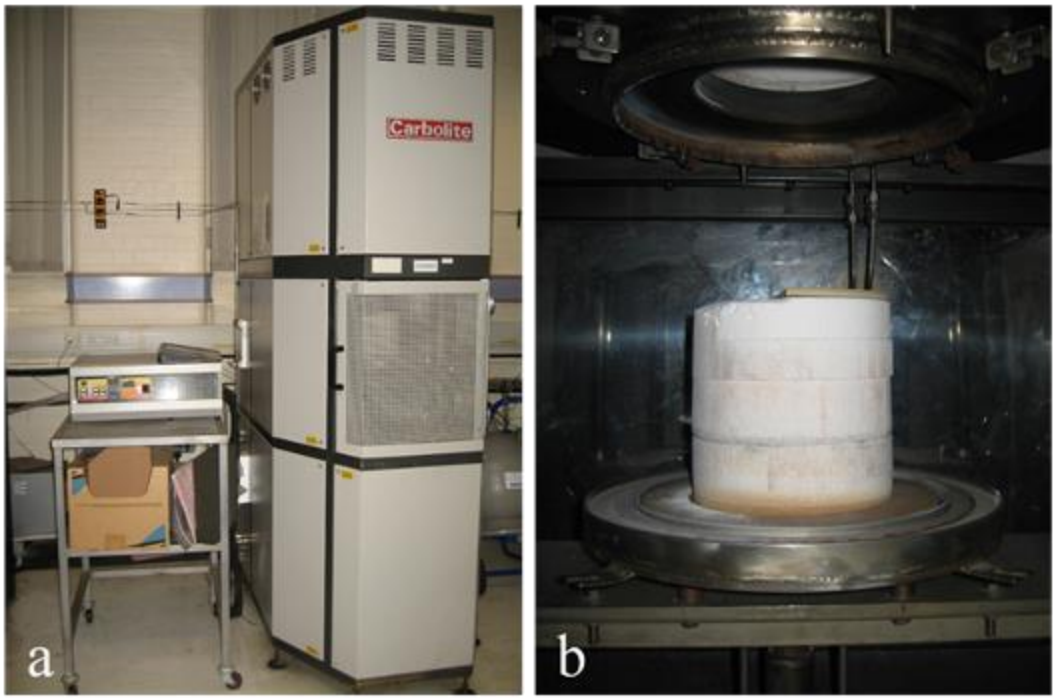

Figure 3-5. Photograph of Carbolite furnace used in this work: (a) the whole system, (b) the ceramic sample holder and the chamber entrance.

3.1.4. Plasma-enhanced chemical vapour deposition reactor

Plasma-enhanced chemical vapour deposition is a very important technique for deposition of materials when low growth temperatures are required. Plasma in the PECVD reactor can be excited electrically by DC, RF and microwave (MW) power applied to the gaseous mixture confined between two electrodes. When using DC powered system conducting electrodes are required, but still there are limitations on the material possibilities that can be deposited. Dielectric materials cannot be deposited via DC plasma technique as the electrodes get covered with the dielectric material. This causes the DC charges to get extinguished due to negative charge accumulation on the surface of the insulating material covering the anode, which then recombines with the available ions, whereas the cathode gets covered with positively charged ions.

This problem is overcome by using alternating current (AC) plasma; the alternating electric field is applied between the two electrodes making them swap between anode and cathode. Above a certain critical frequency a temporary DC discharge is created. This critical

frequency is the reciprocal of the time for the positive ion to move from one electrode to the second one, thus if the frequency is higher than the critical value, the ions in close proximity to the anode cannot reach the cathode before the field is reversed. Due to this effect some positive space charge is retained between two electrodes which helps the re-initiation of the discharge. This mechanism creates a potential difference across the plasma layer similar to DC operated field [77]. The bias generated via this method is called self-bias. Below the critical frequency it is not possible to sustain a self-bias. A common value for the frequency used in PECVD systems is 13.56 MHz.

The temperatures used in PECVD reactors are usually below 400 °C as the energy for the chemical reaction is provided not only by the heated cathode but also from the AC discharge.

The schematic diagram of the PECVD system used in this work is shown in Figure 3-6.

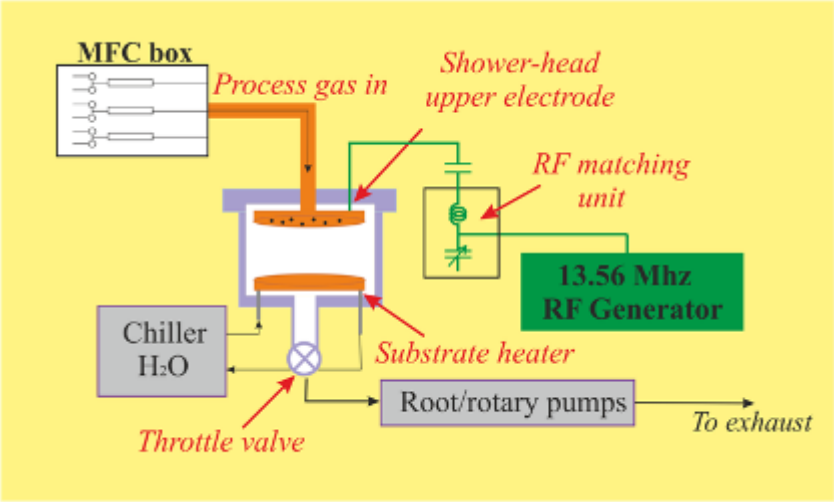

Figure 3-6. Schematic diagram of the PECVD unit used in this work [78].

The system consists of a chamber with two electrodes, the vacuum of which is sustained via root and rotary pumps that are able to pump the system down to 3 Pa. The electrodes are separated by a 40 mm gap. The lower electrode serves as a substrate holder which can also get heated from beneath and it is electrically grounded (see Figure 3-7(a)). The upper electrode serves as a shower head for uniform injection of process gases across the entire diameter. The RF-matching unit manually matches the impedance of the glow discharge system with the output from the RF generator. The flow of the deposition gases, which were silane (SiH_4) and hydrogen (H_2) for Si nanowire growth, is regulated by a system of separate mass flow controllers (MFCs). The maximum temperature the system can go up to is 400 °C, and the maximum RF power is 300 W. The photograph of the PECVD reactor used in this work is shown in Figure 3-7(b).

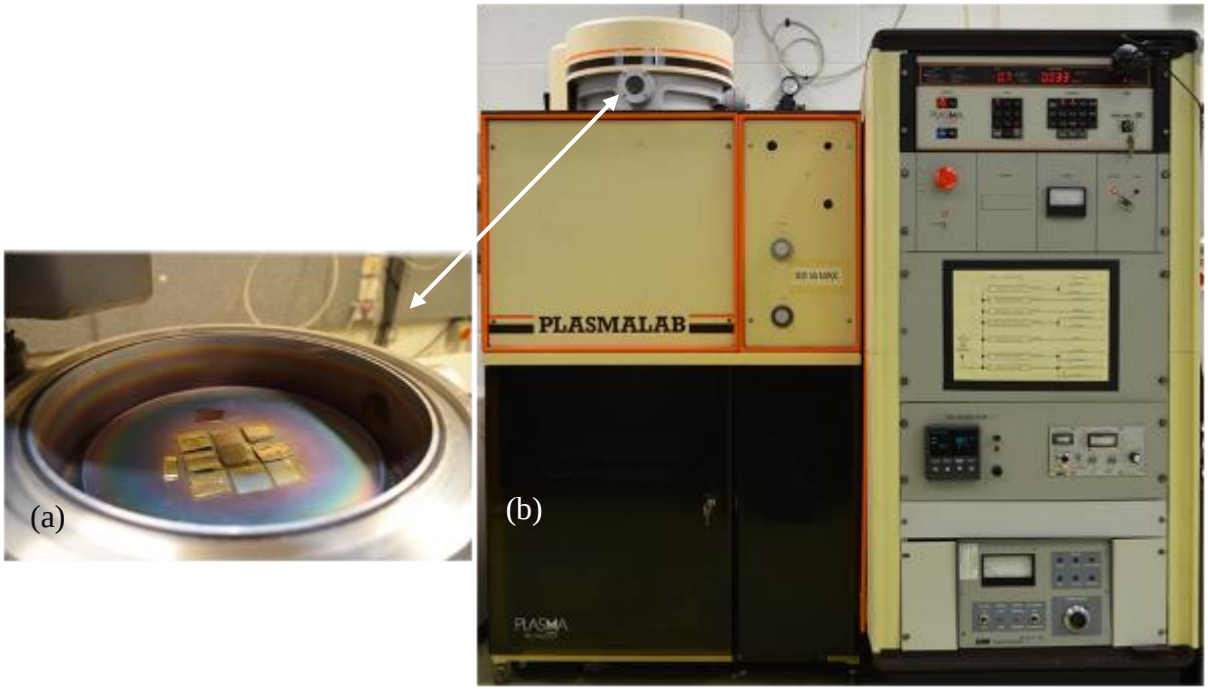

Figure 3-7. Photograph of the PECVD (a) chamber and (b) reactor system used in this work.

3.1.5. Hydrothermal growth

Hydrothermal growth of zinc oxide nanowires has been carried out in a temperature controlled vessel, the top of which was covered with a glass plate (not an airtight lid). The temperature was controlled via constant flow of water (from a temperature controlling unit) surrounding the vessel. Firstly, the solutions of zinc nitrate hexahydrate and hexamine were prepared in separate beakers, transferred into the temperature controlled vessel and left for 30 minutes to get to the nanowire growth temperature and mix properly. Only after this were the samples submerged into the bath, being held in a horizontal position facing downwards.

3.1.6. Glucose oxidase immobilisation

Glucose oxidase solution with a concentration of 5 mg per 1 mL of 0.01 phosphate buffered saline (PBS) was ultrasonicated for half an hour and then drop-cast onto the sample. The sample was left in the laminate bench allowing the buffer to evaporate. After this, Nafion solution (0.5 wt % in ethanol) was drop cast onto the sample to form a membrane for GOD immobilisation. The samples were left for the ethanol to evaporate and refrigerated at 4 °C until usage.

3.2. Characterisation techniques

3.2.1. Scanning electron microscopy

Scanning electron microscopy (SEM) is a very important technique when working with micro- and nanomaterials. The SEM uses electrons instead of light to image the samples and is generally used for imaging the surface of materials. All material types can be analysed via SEM, but if the material is non-conductive, a thin conductive layer of gold or carbon is applied to avoid electron charging and image degradation. The diagram of the SEM working principle can be seen in Figure 3-8.

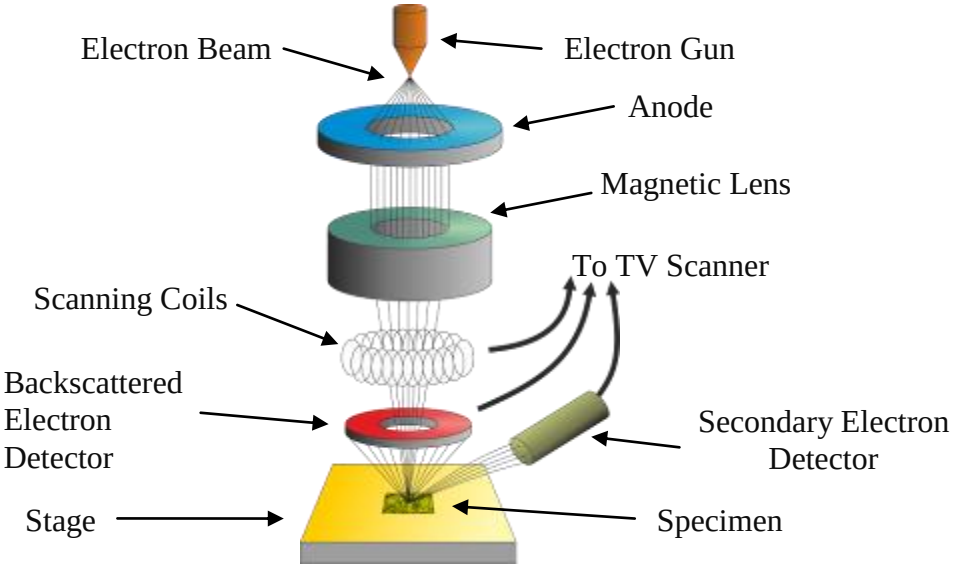

Figure 3-8. Schematic diagram of the SEM operation.

The SEM operates in vacuum. A beam of electrons is generated at the top of the microscope by an electron gun. After release, electrons follow a vertical path through electromagnetic fields and lenses and get focused on the sample. When the beam hits the sample, the electrons interact with the specimen and get scattered. Two types of scatterings are possible; (1) electron trajectory changes but the kinetic energy and the velocity stay essentially constant (due to difference in mass of electron and atomic nuclei) known as elastic scattering, and (2) inelastic scattering, where the trajectory changes only slightly, but the energy is lost due to interactions with the electrons of the specimen atoms. The inelastic interactions can produce X-ray radiation, secondary electrons and backscattered electrons which are possible to detect with the corresponding detector usage [74, 79].

The production and detection of X-rays in the SEM system by bombarding the sample with electrons is called energy-dispersive x-ray spectrometry (EDS) which measures the

intensity of X-ray emission as a function of the energy of the x-ray photons. The measured intensity of X-ray emission is related to the concentration of the elements present in the sample [80].

Two different SEM models were used in this work; Carl-Zeiss EvoHD 15 and Leica S430. The stage (where specimens were held) could be tilted to angles up to 90º for cross sectional analysis of the samples. The specimens were investigated in secondary and backscattered electron modes, as well as EDS analyses were performed for qualitative chemical analysis of the samples. In secondary electron mode the shape and the topography of the sample is mainly identified via low energy electrons (around 50 eV) emitted from the surface (down to 30 nm) due to interaction with the incident beam. In backscattered mode atomic formation of the specimen can be analysed as the backscattered energy strongly depends on interactions in the nuclei. The signal is collected by high energy electrons reflected or backscattered from the sample that are emitted from a depth down to one μm with practically no change in their kinetic energy. But the disadvantage of backscattered mode compared to secondary mode is the resolution, which is lower due to larger penetration depth from which electrons are emitted [7].

3.2.2. Transmission electron microscopy

The design of the transmission electron microscope (TEM) is similar to that of the optical microscope. The difference is the usage of an electron beam instead of light. Due to the small monochromatic wavelength of the electron beam (five orders of magnitude smaller than the wavelength of the visible light) smaller structural details can be observed via a TEM in comparison to the optical microscope [81]. The TEM can be operated in both image and diffraction modes. For the diffraction image the selected area electron diffraction (SAED) aperture is used, the size of which determines the area of the sample from which the diffraction pattern is going to be produced [7]. When the electron beam interacts with the matter, elastic (no energy change) or inelastic (energy change) scattering may occur. In the case of elastic scattering the diffraction pattern will be determined by the arrangement of atoms in the material. In the case of well-ordered arrangement of atoms (single crystal) the produced diffraction pattern will be spots, whereas the polycrystalline material will form rings [7, 27]. From these patterns it is possible to calculate the d-spacing of the lattice planes. After the diffraction pattern is obtained, the image can be produced via bright field (using an

aperture that blocks the diffracted electrons) or dark field (blocks the transmitted electrons) modes.

When the diffraction aperture is removed, the TEM operation is changed from diffraction to image mode. When working with crystalline materials diffraction contrast is often used (including in this work). Depending on the sample being investigated and its orientation some of the beam will get transmitted and some diffracted. The variations in the crystalline regularity of the sample will cause different fraction of the beam intensity to be diffracted out leading to a variation in the image darkness on the viewing screen at the base of the microscope [81].The working principle of the TEM can be seen in Figure 3-9.

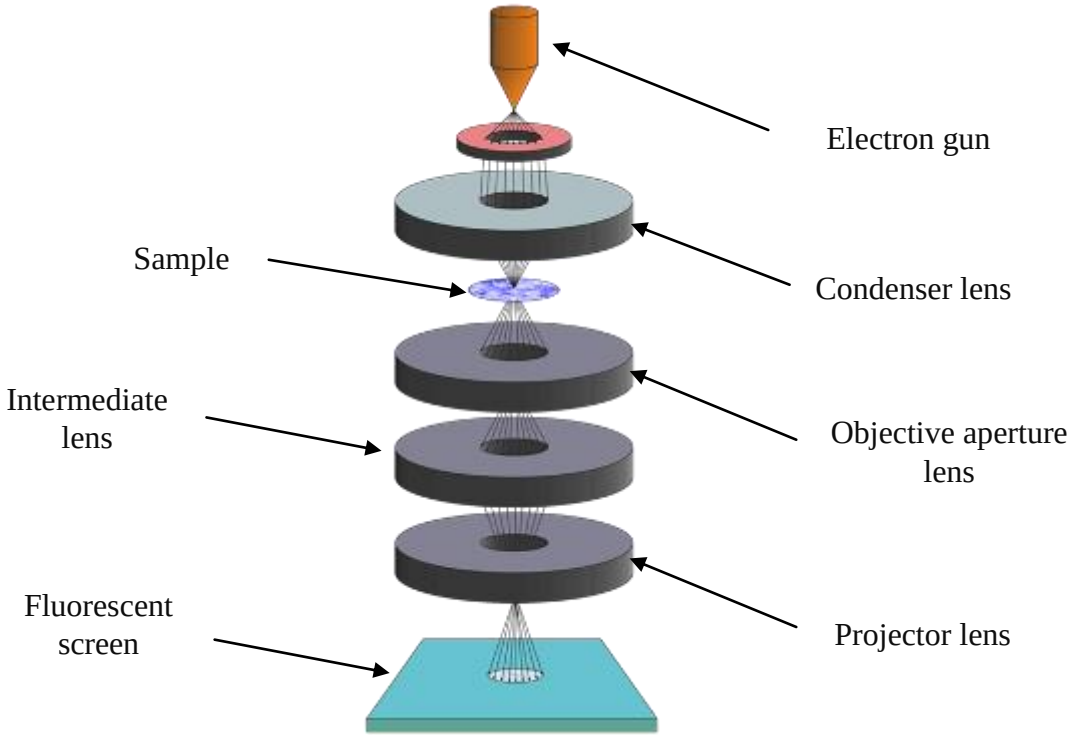

Figure 3-9. Schematic diagram of the TEM operation.

The model of the TEM used in this work is JEOL TEM FX 2000 operated at 200 kV in Imperial College London. The SAED analyses were performed in the bright field mode.

3.2.3. Atomic force microscopy

Atomic force microscopy (AFM) was invented in 1982 to investigate the surface of insulating samples. It belongs to the family of scanning probe microscopy (SPM), the operation of which is based on bringing a probe into close proximity with a sample surface and measuring the interactions between the probe and the surface. The small size of the probe tip (usually tens of nanometers radius of curvature) enhances the SPM technique with the

possibility of atomic scale imaging of the sample surface. This is the only technique apart from the TEM that can image at atomic resolution [82].

All the AFM measurements during this research were carried out on Park Systems XE-100 SPM.

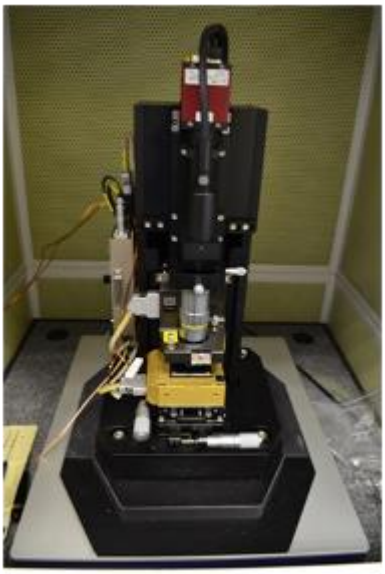

Figure 3-10. Photograph of Park Systems XE-100 SPM used in this work.

The AFM consists of a flexible cantilever with a sharp tip mounted on its end (see Figure 3-11(a)).

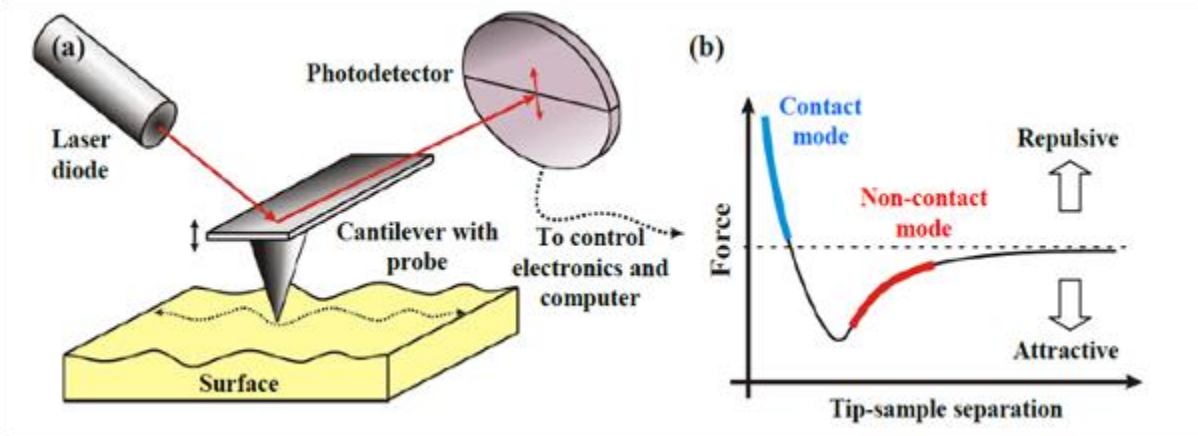

Figure 3-11. (a) Schematic of an AFM operating in contact mode and (b) dependence of interatomic forces on distance showing the regions where various AFM modes operate. Reprinted with permission of Dr. D. Prime [83].

The raster scanning of the surface is done by moving the sample, and the technique to detect the movement of the cantilever is to sense the light reflected from the cantilever into the photodetector.

The forces between the probe and the sample are the basis of building the surface topography image. Two modes of AFM are usually used; contact mode and non-contact mode (Figure 3-11(b)). In contact mode the probe is in actual physical contact with the sample, while the probe is being scanned across the surface. The sample topography is formed by means of the probe tip being repelled from the surface by interatomic forces. This mode has its drawbacks such as damage to both the sample surface and the tip causing image artifacts in the data. In non-contact mode the tip distance from the surface is increased so that Van der Waals attractive forces dominate. But as these forces are very weak compared to contact mode forces, a small alternating current is applied to the tip making it oscillate, the amplitude and phase of which are affected by the sample and tip interactions. These changes are used to construct the surface topography [83].

3.2.4. Ultraviolet-visible spectroscopy

Ultraviolet-visible (UV-Vis) spectroscopy was used to investigate the absorption and transmission properties of the deposited films and nanomaterials, as well as estimate their optical bandgap from the spectra using Tauc plots. UV-Vis spectroscopy works by measuring the attenuation of light either when the light is transmitted through a transparent material or reflected from a surface [84]. These measurements can be done at a single wavelength of light or over a spectrum of frequencies. The spectral range of UV-Vis spectrometers usually is between 190 – 900 nm. The limit on the short wavelength (< 180 nm) is the absorption of these wavelengths by atmospheric gases. The higher limit of the range is set by the response of the detector and depends on the spectrometer. This technique is very useful also for quantitative analysis as there is a linear dependence between absorbance and the concentration of absorbent. UV-Vis spectroscopy is used in two types of research. The first type uses it for quantitative analysis to monitor the concentration of reactants and precursors, this usually requires single wavelength for the analysis. The second type of measurements is done for qualitative analysis of optical and electronic properties of materials which is usually done within a spectral range [84].

UV-Vis spectrum can also be used to calculate the bandgap of a semiconductor, the value of which can vary from UV to near infrared depending on the material. The method will be described in Section 3.2.4.1.

Percentage transmittance (T) of light is the quantity usually measured via UV-Vis spectroscopy and is expressed via the following formula:

$$T = \left(\frac{I}{I_0}\right) x100\ \% \qquad \textbf{Equation 3-1}$$

Where I_0 and I are initial and final intensities respectively.

Absorption is related to transmission via Equation 3-2

$$A = -log_{10}T \qquad \textbf{Equation 3-2}$$

Both A and T are unitless and T is expressed as a percentage.

The instrument available for use in EMTERC is the Thermo Scientific Evolution 300 UV-Vis spectrometer (see Figure 3-12).

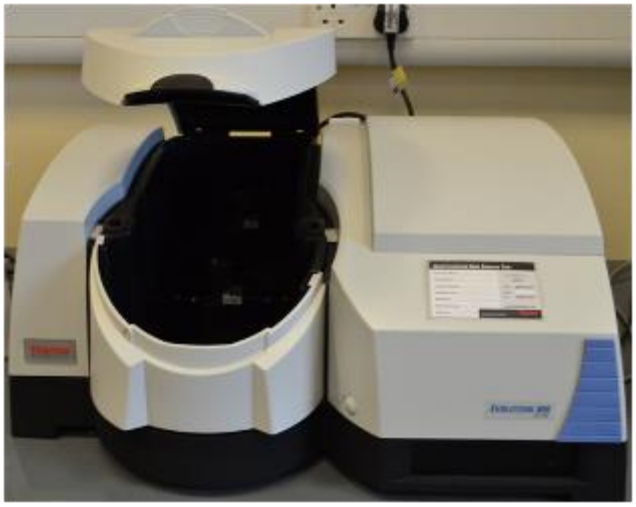

Figure 3-12. Thermo Scientific Evolution 300 UV-Vis spectrometer used in this work.

It is a dual beam spectrometer that splits the beam prior to entering the measurement chamber. A reference substrate is placed in the second compartment to constantly be compared with the sample of interest in order to reject the effect of the substrate and get spectra of the film and not the substrate. Prior to measuring the sample a reference sample is placed in the sample compartment for scanning and eliminating the background. The spectral range is chosen between 300 nm to 1000 nm, as glass substrates have high absorption below these values.

3.2.4.1. Estimation of optical bandgap from Tauc Plot

As mentioned earlier UV-Vis spectroscopy is a useful tool for the estimation of the optical bandgap of the sample. This technique was first demonstrated by Tauc [85] and adopted by the scientific community.

The absorption coefficient data as a function of wavelength has been proposed by Tauc, and is given by the following equation:

$$(\alpha h\nu)^n = Constant \times (h\nu - E_g) \quad \textbf{Equation 3-3}$$

where $h\nu$ is the photon energy and can be represented via Equation 3-4:

$$h\nu = \frac{hc}{\lambda} \quad \textbf{Equation 3-4}$$

and α is the absorption coefficient and can be calculated with the rearrangement of Lambert-Bouguer law:

$$I = I_0 \exp(-\alpha d) \quad \textbf{Equation 3-5}$$

$$\alpha = -\frac{1}{d}\ln\left(\frac{I}{I_0}\right) = \frac{1}{d}\ln\left(\frac{\%T}{100}\right) \quad \textbf{Equation 3-6}$$

where d is the material thickness, I_0 is the intensity of the incident light and I is the intensity of the transmitted light.

In the Tauc formula (Equation 3-3) n = 2 and 1/2 in the case of allowed direct and indirect optical transitions respectively.

In order to plot Tauc's plot the transmission plot/data is required. The graph is plotted by using the y axis for $(\alpha h\nu)^n$ and the x axis for $h\nu$. Thereafter, the optical bandgap is determined by extrapolating the linear part of the following function $[\alpha(E) \times E]^n$ *vs.* the photon energy E to α(E) = 0.

3.2.5. Fourier Transform Infrared Spectroscopy

Fourier transform infrared (FTIR) spectroscopy is based on emitting thermal radiation across a range of wavelengths, rather than a monochromatic light at each wavelength.

The frequency of vibrations of atoms in a material depends on the type of atom and type of bond. When the infrared (IR) light interacts with the material, groups of atoms absorb the light of specific vibrational frequencies, thus wavelengths. The remaining light gets transmitted through the sample into a detector. After analysis of the transmitted light, the absorbed frequencies can be determined and referred to specific atomic and chemical structure of the material. IR spectroscopy can be used for liquids, solids and gases [7].

The working mechanism of the FTIR is based on Michelson interferometer [82] and can be seen in Figure 3-13. When the beam is released out of the source in the FTIR spectrometer it is split into two beams via passing through a beam splitter. One of the beams reaches the fixed mirror and gets reflected. Part of the reflection gets back to the source via passing the splitter again, whereas the second part reaches the detector. The second beam gets reflected from a moving mirror which can move only parallel to itself. Even though the beam from the source is incoherent, they become coherent after passing the splitter and can create interference phenomena when combined at the detector. The light intensity at the detector will be the combination of the two reflected beams. When the path length between two beams is equal, they will constructively interfere with each other at the detector, but when the path is out of phase by 180° they will cause destructive interference.

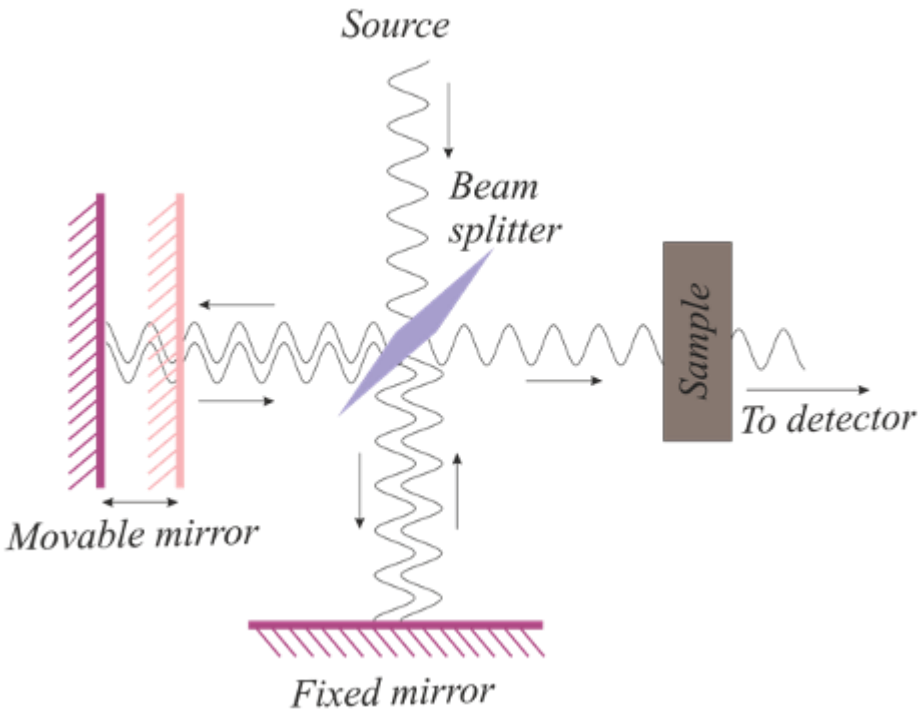

Figure 3-13. Schematics of the FTIR spectroscopy operation [82].

It is evident that by varying the movable mirror position, an interference pattern can be obtained which consists of maxima and minima. This effect for just one frequency of light emitted can be described by the following equation:

$$I(x) = B(f)[1 + \cos(2\pi x f)] \qquad \textbf{Equation 3-7}$$

where $I(x)$ is the intensity of light depending on the value of x (the distance travelled by the mirror), f is the frequency of light, $B(f)$ is the intensity modified by the sample.

When the source emits a range of frequencies, the interference pattern will be the integral sum over all the frequencies used and Equation 3-7 will be modified to the following one:

$$I(x) = \int_0^f B(f)[1 + \cos(2\pi x f)]df \qquad \textbf{Equation 3-8}$$

But the interference pattern is not of interest to the user, thus Fourier Transform is carried out by the computer resulting in spectral response. This is done via Equation 3-9.

$$B(f) = \int_{-\omega}^{\omega} I(x)cos(2\pi x f)dx \qquad \textbf{Equation 3-9}$$

This transformation results in spectrum of transmittance (or absorption) *vs.* wavenumber measured in cm^{-1}.

The FTIR data was obtained using a Bruker Alpha compact spectrometer (see Figure 3-14).

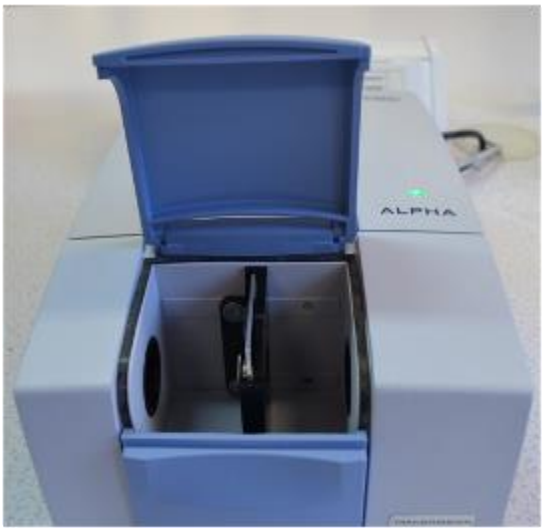

Figure 3-14. Bruker Alpha FTIR spectrometer used in this work.

3.2.6. Profilometry

A Profilometer is a device that can measure the thickness of a film, roughness of the surface and depth of the etched material. In this work, it has been used to measure thickness of various films as mentioned in the thesis. It scans the surface of the sample with a sharp tip at a specified position while measuring the vertical depth. The Profilometer used in EMTERC is Alpha-Step 200 from Tencor (see Figure 3-15).

Figure 3-15. Photograph of the Step Profilometer used in this work.

The tip of this model can travel horizontal distance of up to 800 μm and vertically up to ± 0.16 μm. The limitation of this equipment is the need for a sharp edge of the layer to be measured as the maximum height of the film should be reached within the scanning distance of the tip. For this reason, a line was made with a permanent marker on the middle of the substrates to be deposited on. After deposition the marker was removed with acetone and the newly available edge in the middle of the sample scanned.

3.2.7. Raman spectroscopy

Raman spectroscopy is a vibrational spectroscopic technique. Its operation is based on inelastic scattering of light by the sample. It can be used to analyse amorphous and crystalline solids, liquids and gases. The beam can also be focused on small areas to analyse very small

amounts of material, as well as particles embedded in other phases, as long as the other phases are optically transparent [82, 84].

When light is scattered from the surface of a material, it mainly contains incident light wavelength, which is called Raleigh scattering (this can be eliminated with use of appropriate filters). Very low intensity light is scattered at different wavelength which stores information about the interaction of the incident light with the material called Raman scattering. This effect was first described by Sir Chandrasekhara Raman in 1928 [86]. As the Raman scattering intensity is very low, the source of the incident light should be very intense monochromatic light, such as laser. Laser power in Raman spectroscopy is usually kept under 5 mW to reduce sample heating and material degradation/decomposition.

The effect that Raman has described is the following: when the incident photon interacts with the matter, it parts with some of its energy in the form of a phonon and gets into a lower energy state (red shift), known as Stokes-shifted scattering, whereas if via the interaction it absorbs a phonon and increases its energy (blue shift), the scattering is called anti-Stokes-shifted, which is very weak compared to the Stokes-shifted mode and it is the latter that usually gets monitored [82]. The energies of Rayleigh, Stokes and anti-Stokes scatterings are presented in Figure 3-16.

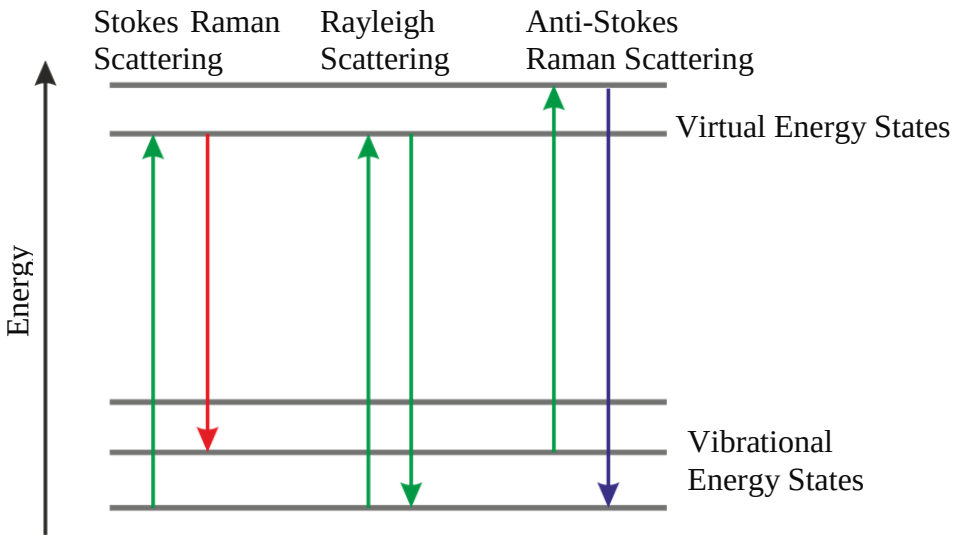

Figure 3-16. Representation of Rayleigh and Raman types of scattering.

Micro Raman Spectroscopy is often used for samples of microscopic dimensions.

In this work, two micro Raman spectroscopes with 514.5 nm Ar^+ laser have been used; (i) Horiba Jobin Yvon Lab Ram HR in the University of Leicester and (ii) Renishaw inVia in Warwick University.

3.2.8. X-Ray diffraction spectrometry

X-ray diffraction (XRD) method is widely used to investigate the structural properties of crystals and amorphous samples. It is a non-destructive technique with wide range of information that can be extracted from the data.

The X-ray diffraction working principle can be explained on a simplified perfect crystal example. If monochromatic light is diffracted from the parallel planes separated by an interplanar spacing d (see Figure 3-17) at an angle of "θ" in respect to the planes, then the reflected beam intensity will be at its maxima if reflected beams 1´and 2´ are in phase. That means that the path length difference between 1 to 1' and 2 to 2' should be integral number of wavelength.

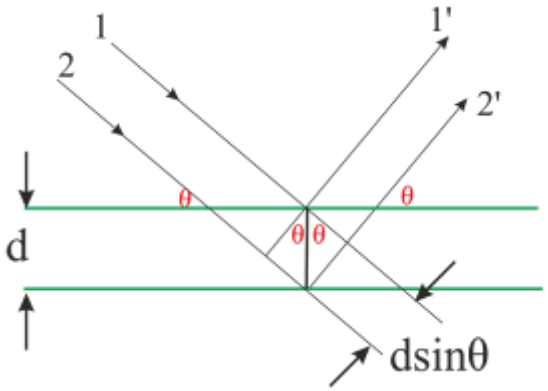

Figure 3-17. Schematic representation of the X-ray diffraction principle.

This relationship is explained by Bragg's law (Equation 3-10):

$$2dsin\theta = n\lambda$$ **Equation 3-10**

where d is the spacing between two planes in the atomic lattice, θ is the angle between the incident ray and the scattering planes, n is an integer and λ is the wavelength of the incident wave.

The diffracted rays are collected by a photographic plate which should be placed perpendicular to the secondary X-rays for the best resolution.

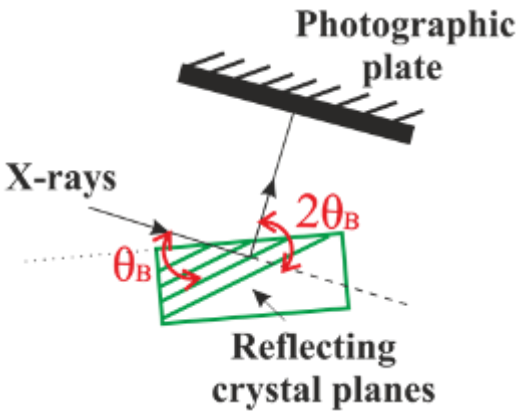

Figure 3-18. Schematic representation of the XRD working principle [82].

Bragg's law of diffraction only works for atoms situated at the corners of the cell unit, thus the atoms that are located in non-corner positions create extra scattering affecting the interference. This means that only certain crystallographic planes will appear in the XRD spectrum for each crystal structure. In addition, the peak intensity of the XRD spectra is affected by the size of the crystal and for finite sized crystals the peak is becoming shorter and broader despite the fact that the area under the peak remains the same. This phenomenon makes it possible to calculate the size of the crystals from the peak shape [7].

The crystal size has been calculated in this work from the XRD spectra using Scherrer formula [7] which can only be used for crystal sizes smaller than 100 nm (Equation 3-11):

$$L = \frac{0.9\lambda}{\beta cos\theta}$$ **Equation 3-11**

where λ is the wavelength of the incident X-ray radiation, β is the broadening of the peak at full width at half maximum and θ is the Bragg angle.

The XRD spectrometer used in this work was Philips 1730 generator with a diffractometer in θ-2θ geometry in the University of Leicester.

3.2.9. Thermal analysis

Thermal analyses (TA) are analytical experimental techniques used to describe the sample behaviour as a function of temperature. There are several types of TA techniques currently used, including differential scanning calorimetry (DSC), differential thermal analysis (DTA), thermogravimetric analysis (TGA), thermomechanical analysis (TMA) and

dynamic mechanical analysis (DMA) [87]. The analyser types used in this work are TGA and DSC.

3.2.9.1. Thermogravimetric analyser

The TGA measures the weight loss in the material as a function of temperature or time in a controlled atmosphere (e.g. air, nitrogen or oxygen). These analyses can give information about humidity content of the sample, its stability and decomposition. TGA data is highly affected by the physical characteristics of the sample, sample holder and atmosphere of the chamber. TGA data is obtained using a thermobalance, which includes an electronic microbalance, a furnace, a temperature programmer and an instrument for recording the results [87].

The TGA used in this work was Perkin Elmer Pyris 1 TGA (see Figure 3-19). The experiments were conducted in the constant nitrogen flow environment.

Figure 3-19. Perkin Elmer Pyris 1 TGA analyser used in this work.

3.2.9.2. Differential Scanning Calorimetry

The DSC used in this work was Perkin Elmer Jade DSC (see Figure 3-20).

Figure 3-20. Perkin Elmer Jade DSC analyser used in this work.

This is a heat flux (energy input per unit time) DSC which uses a single furnace for both the sample of interest and the reference sample (which was an empty sample pan and a lid). It measures and records the temperature difference between the sample and the reference and calculates the resultant heat flow (which is proportional to the temperature difference) out of and into the sample from the calibration data. The construction of the DSC cell can be seen in Figure 3-21.

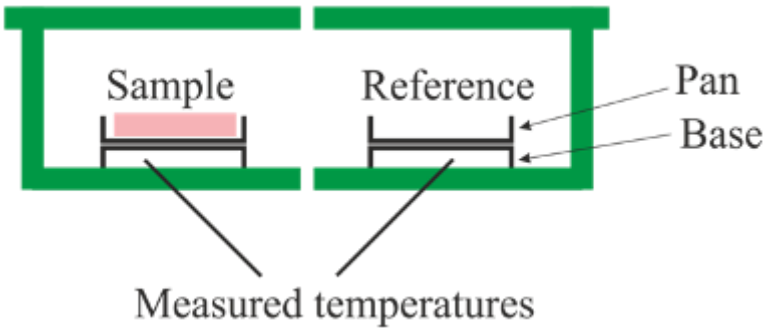

Figure 3-21. Single furnace Heat Flux DSC cell structure.

The thermocouples are attached to the base of the sample and the reference. During a phase change or decomposition of the sample, heat is absorbed or emitted by the sample changing the heat flux through the base. In the DSC analyser the difference in energy required to keep both the sample and the reference at the same temperature is the measure of the energy change in the sample in relation to the reference. The temperature difference between the sample and the reference causes heat flow between these two. To find out the

small difference, both the sample and the reference should be kept in the same temperature program [87].

3.2.10. Electrochemical sensing of the biosensor

Biosensors (enzyme electrodes) fabricated in this work were tested via electrochemical methods. Cyclic voltammetry and chronoamperometry were implemented for testing and characterisation of the biosensors. The model of equipment used in this work for both analyses was the VersaSTAT 3 Potentiostat.

All the voltammetric methods are based on the fundamental theories of thermodynamics, hence prior to discussing each method separately, the theory governing the processes in electrochemical cells will be explained. The theory section to follow is written using the books of C.H. Hamann and A.J. Bard [88-89] (unless otherwise specified) and will not be referenced throughout the section.

3.2.10.1. Theory of electrode processes

In this chapter, when referring to an electrode, the working electrode at which the reactions take place will be understood as that is the electrode of interest.

In voltammetry the applied potential controls the concentration of redox species at the electrode surface via the Nernst equation. When the mass transport of the materials is controlled via diffusion, Fick's law is applied [90]. These equations will be discussed in more details further in this chapter.

Two types of processes occur at the electrode: faradaic and nonfaradaic. In the faradaic process the amount of chemical reaction caused by the flow of current is proportional to the amount of electricity passed. Nonfaradaic processes occur when at certain range of potential no charge transfer reactions occur (not kinetically or thermodynamically favourable) but adsorption and desorption can still occur. Faradaic and nonfaradaic reactions occur when electrode processes take place, but faradaic ones are the ones of interest.

The anode is the electrode at which oxidations occur. The cathode is the one at which reductions occur. Cathodic current is when electrons cross the interface from the electrode to the species in solution, whereas when electrons flow from species in the solution to the electrode, it is known as anodic current. The electrode reaction is a heterogeneous reaction which occurs only at the electrode-electrolyte interface.

The rate of heterogeneous reaction is represented by the following equation:

$$Rate = i/nFA \qquad \textbf{Equation 3-12}$$

where i is the current flowing, n is the number of electrons consumed in the electrode reaction, F is the Faraday constant, and A is the electrode area.

If the electrode process involves only fast heterogeneous electron transfer reaction and homogeneous reaction, then the net rate of the electrode reaction is governed by the rate at which the electroactive species are brought to the surface of electrode (mass transfer):

$$Rate = \nu_{mt} = \frac{i}{nFA} \qquad \textbf{Equation 3-13}$$

where ν_{mt} is the rate of mass transfer.

The current of the electrochemical cell is governed by the following processes:

- Mass transfer
- Electron transfer at the electrode surface
- Chemical reactions such as catalytic decomposition
- Surface reactions, such as absorption, desorption and crystallisation

The simplest case involves the mass transfer of the species to the electrode, the electron transfer, and mass transfer of the product back to the solution. The steady state current is obtained when the rates of all the reaction steps are the same. The magnitude of this current is often determined by one of the steps (referred to as rate determining step) if it is taking place slower than the rest of the steps.

In the electrochemical cell the simplest electrode reactions are the ones where the rates of associated chemical reactions are very fast compared to those of mass transfer processes. The three modes of mass transfer as discussed in Chapter 2 are:

- Migration; the movement of charged species under the influence of an electric field.
- Diffusion; the movement of species under the concentration gradient.
- Convection; through stirring or hydrodynamic transport.

In order to simplify the process the electrochemical cells are designed in a way to be able to neglect some of these types of transport. For example, to neglect the migration, it is possible to use an inert electrolyte, the concentration of which is much higher than the concentration of the electroactive species. Convection also can be neglected by using a non-stirred solution and preventing vibrations in the system.

The movement of the material via diffusion is expressed via Fick's equations:

Fick's first law (Equation 3-14) describes the relationship between the flux due to the molecule diffusion and the concentration gradient, and the second law (Equation 3-15) gives a mathematical representation of the rate of the concentration change with time (the equations are written for one dimension):

$$J = -D\frac{dc}{dx} \qquad \textbf{Equation 3-14}$$

$$\frac{dc(x,t)}{dt} = D\frac{d^2c(x,t)}{dx^2} \qquad \textbf{Equation 3-15}$$

where *J* (Equation 3-14) is the rate of movement of the material via diffusion, *dc/dx* is the concentration gradient, *dc/dt* is the rate of concentration change, and *D* is the diffusion coefficient. The negative sign means that the movement is down the concentration gradient (from high concentration region to low concentration region).

These equations are responsible for the molecule movement in one dimension therefore not enough for describing the movement of the analyte to the biosensor surface. In order to know the concentration of the analyte at the certain point of the biosensor surface, it is important to know the rate at which the analyte gets transported towards the electrode which is described by Fick's first law (Equation 3-14) and the consumption of the analyte at the surface (described by Fick's second low given by Equation 3-15). In order to solve these equations the boundary conditions need to be defined. For the initial boundary condition the initial bulk concentration will be taken; $c(x,0) = c_b$. The final boundary condition considers the enzymatic reaction to be fast enough to reduce the build-up of the analyte at the surface to zero; $c(0,t) = c_0 = 0$. If there are no other types of mass transport present in the environment then the transport of the analyte to the electrode surface would be defined by the $c_b - c_0$ concentration gradient. In this case, the reaction rate is diffusion controlled. Equation 3-15 can be resolved to give the following equation:

$$c = c_\infty erf\left(\frac{x}{2D^{1/2}t^{1/2}}\right) \qquad \textbf{Equation 3-16}$$

where c_∞ is the analyte concentration at an infinite distance from the electrode and *erf* is the error function which describes approach to unit limit when *x* (distance) reaches infinity. Equation 3-16 shows the increase of the analyte concentration with increase of the distance from the electrode surface. In addition, it shows that increase in the reaction time (t) causes decrease of the analyte concentration [42] (Figure 3-22).

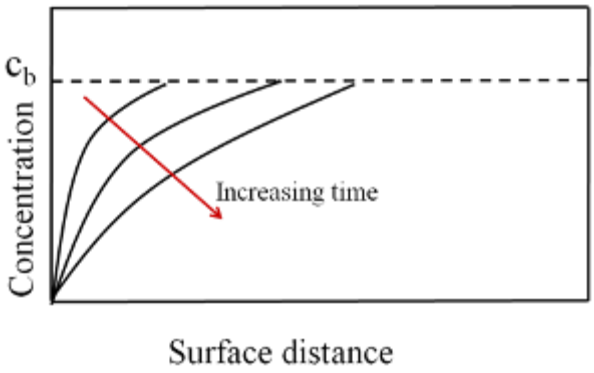

Figure 3-22. Analyte concentration dependence on the distance from the electrode surface and reaction time.

The simplest model to describe the steady state enzyme kinetics when there is constant supply of analyte at the electrode surface is Michaelis-Menten model [42, 44]. In this model it is assumed that firstly the substrate (S) and enzyme (E) form a complex in a reversible step and there is equilibrium maintained between the enzyme, substrate, and the complex. After this, due to an irreversible breakdown, the complex yields a product.

$$E + S \underset{k_{-1}}{\overset{k_1}{\rightleftarrows}} ES \overset{k_2}{\rightarrow} E + Product \qquad \textbf{Equation 3-17}$$

$$v = \frac{k_2[E]_0[S]}{K_M + [S]} \qquad \textbf{Equation 3-18}$$

Equation 3-17 is a more generalised model of the enzyme kinetics, where the rate constants for the reversible reaction are given separately as k_1 and k_{-1}; this model was proposed by Briggs and Haldane [44].

In Equation 3-18 v is the reaction rate, $K_M = (k_{-1} + k_2)/k_1$ is the Michaelis-Menten constant and the equation is called Michaelis-Menten equation, $[E]_0$ is the total concentration of enzyme, $[S]$ is the concentration of analyte and $k_2[E]_0$ (V_{max}) is the maximum velocity of the reaction.

Michaelis-Menten constant (K_M) approximates the affinity of the enzyme to its substrate and is the substrate concentration at which the enzyme velocity is half its maximum ($k_2[E]_0$) [91]. Michaelis-Menten equation (Equation 3-18) can be rewritten in different ways to give straight-line plots. These are useful when calculating K_M and $k_2[E]_0$. Lineweaver-Burk plot (given by Equation 3-19) is one of those straight lines and the plot is $1/v$ *vs.* 1/[S]:

$$\frac{1}{v} = \frac{K_M}{k_2[E]_0[S]} + \frac{1}{k_2[E]_0} \qquad \textbf{Equation 3-19}$$

This model is only valid if the concentration of S is sufficiently higher than the concentration of ES complex. In amperometric biosensors this usually is true and the model is therefore valid and widely used [44].

The redox reaction (taking place in electrochemical cells) can be represented by the following way:

$$O + ne^- \leftrightarrows R$$

where *O* is the oxidised species, and *R* is the reduced form of the species.

When the electrolysis of O takes place (electrolysis in this work is defined to include chemical changes accompanying faradaic reactions at electrodes in contact with electrolytes), its concentration at the electrode surface becomes less than in the bulk:

$$C_O\ (x = 0) <\ C_O^*$$

Here we assume that a stagnant layer (Nernst diffusion layer) exists at the electrode surface (δ_O) and the stirring (if applied) keeps the concentration at C_O^* at distances beyond $x =\ \delta_O$.

In the case of excess of electrolyte (no migration), the rate of mass transfer is determined by diffusion (Fick's first law) and is proportional to the concentration gradient at the electrode surface:

$$\nu_{mt} = \mathrm{D}(dC_O/dx)_{x=0} \qquad \textbf{Equation 3-20}$$

Where ν_{mt} is the rate of mass transfer, *D* is the diffusion coefficient (cm^2/s) and (dC_O/dx) is the concentration gradient at distance x.

In the assumption of linear concentration gradient the Equation 3-20 simplifies into the following:

$$\nu_{mt} =\ \mathrm{D}[C_O^* -\ C_O(x = 0)]/\delta_O \qquad \textbf{Equation 3-21}$$

Since δ_O is often unknown, it is convenient to combine it with the diffusion coefficient under one constant, $m_O = D/\delta_O$, called mass transfer constant (cm/s). With this new definition Equation 3-21 now becomes:

$$\nu_{mt} =\ m_O[C_O^* -\ C_O(x = 0)] \qquad \textbf{Equation 3-22}$$

Considering the reduction current as positive, from Equation 3-13 and Equation 3-22 we have:

$$\frac{i}{nFA} = m_O[C_O^* - C_O(x=0)] \quad \textbf{Equation 3-23}$$

$$\frac{i}{nFA} = m_R[C_R(x=0) - C_R^*] \quad \textbf{Equation 3-24}$$

$$\frac{i}{nFA} = m_R C_R(x=0) \quad \textbf{Equation 3-25}$$

(When no R is in the bulk solution)

As is evident from Equation 3-23, the largest rate of mass transfer of O occurs when $C_O(x=0) \ll C_O^*$ so that

$$C_O^* - C_O(x=0) \approx C_O^*$$

The value of current under such conditions is called limiting current:

$$i_l = nFAm_O C_O^* \quad \textbf{Equation 3-26}$$

At the limiting current the electrode process is occurring at its maximum rate, meaning as soon as the reducing species is brought to the surface it gets reduced.

From Equation 3-26 and Equation 3-23

$$C_O(x=0) = \frac{i_l - i}{nFAm_O} \quad \textbf{Equation 3-27}$$

Thus the concentration of O species at the electrode surface linearly depends on the current and varies from C_O^* (when $i = 0$) to a negligible value when $i = i_l$.

If the kinetics of the electron transfer is rapid the concentration of O and R species at the electrode surface will obey Nernst equation (Equation 3-28 or Equation 3-29 at 25 ºC):

$$E = E^{o\prime} + \frac{RT}{nF} ln \frac{C_O(x=0)}{C_R(x=0)} \quad \textbf{Equation 3-28}$$

$$E = E^{o\prime} + (0.0591/n) log \frac{C_O(x=0)}{C_R(x=0)} \quad \textbf{Equation 3-29}$$

Or

$$\frac{C_O(x=0)}{C_R(x=0)} = \exp\left[\frac{nF}{RT}(E - E^{0\prime})\right] \quad \textbf{Equation 3-30}$$

Where E is the potential of the cell at non standard condition, $E^{O\prime}$ is the formal potential (it incorporates the standard potential and some activity coefficients which are almost always unknown, and depends on the nature of electrolytes in the solution), R is the universal gas constant, F is the Faraday constant, T is the absolute temperature in Kelvin, n is the number of electrons involved in the reaction.

3.2.10.2. Cyclic voltammetry

Cyclic voltammetry (CV) is one of the main techniques used in electrochemical biosensors. The working principal of it is based on studying redox reactions taking place between the species in the system. In third generation electrochemical glucose biosensors, the redox reactions at the enzyme electrode are studied.

In a typical CV experiment a cell with three electrodes is used; a working electrode (WE) at which the reactions take place (the electrode of interest), a reference electrode (RE) (Ag/AgCl electrode has been used in this work) with known potential in respect to which the potential is measured, and the auxiliary (or counter) electrode (AE), between which and the WE current is measured (Figure 3-23). The AE can be any convenient electrode as the behaviour of the WE is not affected by its properties. It is chosen not to produce species that can reach the WE causing interfering reactions. The RE tip is placed near to the WE. The potential difference measuring device between the WE and RE has very high input impedance so that only small current is drawn from RE. This way the RE potential will remain equal to its open-circuit value throughout the experiment [88].

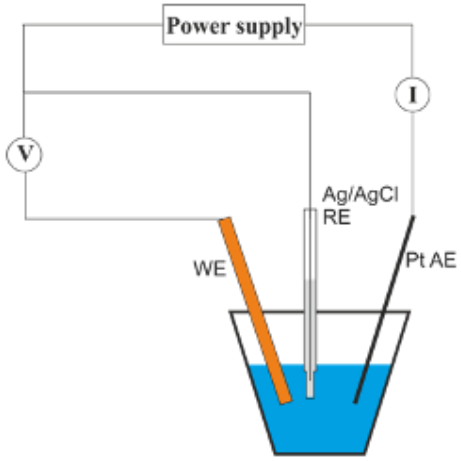

Figure 3-23. Schematics of a three electrode cell.

Cyclic voltammetry works on the principle of imposing triangular waveform as the potential on the WE (see Figure 3-24). The current is measured simultaneously and its

response is plotted as a function of the applied potential (known as voltammogram). The scans can consist of one or more cycles. Quite often the successive scans are the same as the first one, but other times the picture can change depending on various mechanisms of the reactions [92].

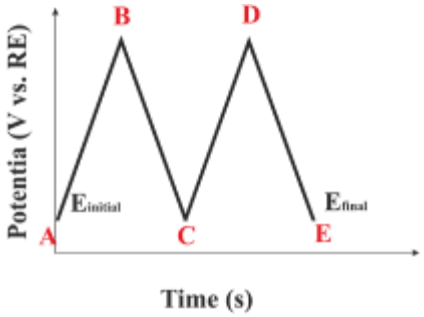

Figure 3-24. Potential behaviour at the working electrode triggered during a CV cycle.

When the voltage scans back and forth, the following reactions take place, assuming there are oxidative and reductive species in the solution [93]:

Anodic scan $R \rightarrow O + ne^-$

Cathodic scan $O + ne^- \rightarrow R$

The potential at any moment of forward scan (forward scan is quite often referred to scanning towards more negative potentials) is represented via the following equation:

$$E(t) = E_i - \nu t \qquad \textbf{Equation 3-31}$$

Where E_i is the initial potential and ν is the scan rate (rate at which the potential is changing: $\nu = dE/dt$).

Therefore, Nernst equation (Equation 3-30) will be rewritten:

$$\frac{C_O\,(0,t)}{C_R\,(0,t)} = \exp\left[\frac{nF}{RT}(E_i - \nu t - E^{0\prime})\right] \qquad \textbf{Equation 3-32}$$

The turn-round potentials (at B, C and D in Figure 3-24) are chosen to lie between the hydrogen and oxygen evolution (formation of the molecular hydrogen and oxygen respectively) potentials which would otherwise influence the analytical signal of interest [89]. When this condition is met, it is possible to gain highly reproducible current-voltage behaviour with metals such as gold and platinum. The reproducibility also depends on the purity of the electrolyte, electrode material, turn-round potentials and scan rate (rate at which

the potential is changed). The scan rate is thought best to be kept above 10 mVs^{-1}, otherwise the electrode surface often gets deactivated (increased diffusion layer) [89].

An example of a typical CV voltammogram can be seen in Figure 3-25. This voltammogram does not represent any particular redox reaction, it is drawn to make the explanations more vivid. This particular voltammogram describes a reversible electron transfer process.

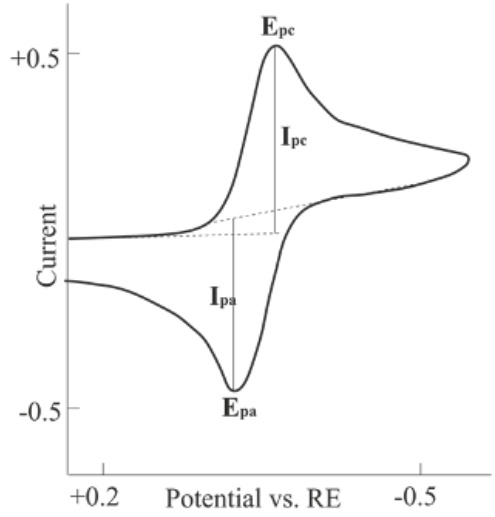

Figure 3-25. Typical cyclic voltammogram.

The current during CV scan can depend on the movement of the electroactive material to the electrode surface and on the electron transfer reaction. As the experiment is performed at a stationary electrode (linearly varying potential) in an unstirred solution, the reactant moves to the surface via diffusion which is not fast enough to maintain steady state concentration profile (where the rates of all the reactions are the same) at the electrode surface. Thus the depletion zone, which is the distance that the reacting species should travel to reach the electrode, increases. This causes the current to stop increasing exponentially reaching its maximum and the mass transport of the reactants becomes the rate determining step of the reaction. Beyond the peak, where the current was at its maximum, it stops depending on the potential and becomes time dependent. In this region current is proportional to $t^{-1/2}$ [92].

When the scan is reversed, the reduced species start re-oxidising causing a reversed reaction current to be measured.

The scan rate has a major effect on the voltammogram. With increasing of the scan rate the peak current is increasing. This can be explained with the diffusion layer that is formed above the electrode and the time that it takes to record the voltammogram. At slower scan rates, there is more time for the diffusion layer to grow further from the electrode, thus reducing the flux of material. Considering that the current is proportional to the flux, it will

also decrease. One important piece of information to obtain from varying the scan rate is to check whether the peak current appears at the same voltage. In case of this condition being met, rapid electron transfer kinetics takes place, thus a reversible reaction. In case the electron transfer reactions (between redox species and the WE) were slower than the scan rate, the reactions are called quasi-reversible or irreversible [94-95].

Important parameters in CV are the cathodic and anodic peak potentials (E_{pc} and E_{pa}), peak currents (i_{pc} and i_{pa}), cathodic half-peak potential ($E_{p/2}$) and half-wave potential ($E_{1/2}$) [96].

The half wave potential (Equation 3-33) is the potential where the current equals half of the diffusion current density represented by Cottrell equation (Equation 3-34) [88]. It is the midpoint of anodic and cathodic potentials in the CV, where the concentrations of reduced and oxidised species at the electrode/electrolyte interface are equal [84].

$$E_{1/2} = E^{o\prime} + \frac{RT}{nF} ln \left(\frac{C_O}{C_R}\right)^{1/2}$$ **Equation 3-33 [96]**

$$i_d = \frac{nFAD^{1/2}C_O}{\pi^{1/2}t^{1/2}}$$ **Equation 3-34**

Peak potential is given by the following formula:

$$E_p = E_{1/2} - 1.109\frac{RT}{nF}$$ **Equation 3-35**

Half-peak potential is the potential at $i_p/2$ and is related to half-wave potential with the following equation:

$$E_{p/2} = E_{1/2} + 1.09\frac{RT}{nF}$$ **Equation 3-36**

The approximate positions of the half-peak and half-wave potentials can be seen in Figure 3-26.

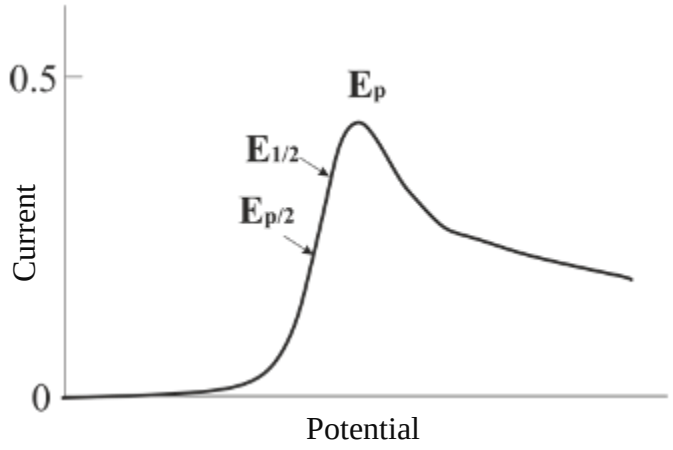

Figure 3-26. Linear potential sweep voltammogram with approximate positions of $E_{1/2}$ and $E_{p/2}$ in respect to E_p [88].

From Equation 3-35 and Equation 3-36 we get:

$$\left|E_p - E_{p/2}\right| = 2.20\frac{RT}{nF} = \frac{56.5}{n} mV \ at\ 25°C \qquad \textbf{Equation 3-37}$$

If the electron transfer is faster compared to other processed, then the reaction is electrochemically reversible and the peak separation should be [90, 96]:

$$\Delta E_p = \left|E_{pa} - E_{pc}\right| = 2.303\frac{RT}{nF} \qquad \textbf{Equation 3-38}$$

$$\Delta E_p = \frac{57}{n} mV \qquad \text{At 25 °C}$$

The value at 25 °C is a theoretical value as in practice there are factors affecting it, such as cell resistance. In addition, the position of the return peak in a reversible system is dependent on the switching potential [97].

The maximum current (peak current) for reversible processes is given by the Randles-Sevcik equation (which is derived from the solution of Equation 3-32) [88, 90]:

$$i_p = 2.686\ X\ 10^5 n^{3/2} A C_O^* \mathrm{D}^{1/2} \nu^{1/2} \qquad \textbf{Equation 3-39}$$

where *n* is the number of moles of electrons transferred, *A* is the area of the electrode in cm^2, D is the diffusion coefficient in cm^2/s, C_O^* is the concentration of the species in bulk and is measured in mol/cm^3, *v* is the scan rate in V/s and i_p is the peak current in Ampere.

It can be seen from Equation 3-39 that peak current is directly proportional to the concentration and square root of scan rate. The linear relationship between the peak current and concentration has been widely used to detect the amount of an analyte in the solution.

The proportionality of the peak current to the square root of scan rate is a very valuable relationship as it helps to distinguish between diffusion controlled processes and other processes, such as adsorption controlled process, where there is a linear relationship between the current and scan rate. The adsorption peaks can occur in the voltammogram simultaneously with the diffusion peak, thus the primary method to distinguish those is via the current-scan rate relationship [93].

3.2.10.3. Chronoamperometry

Chronoamperometry is another powerful tool in electrochemistry which can show diffusion controlled reactions. In this method a square wave potential is applied to the working electrode, it is fixed at a value just past the peak potential (in the CV) and current is measured as a function of time. The current will drop in this case with the formation of the diffusion layer. The decrease is illustrated by Cottrell equation (Equation 3-34) and so the current decay is reciprocal to $t^{1/2}$ [98].

3.3. Conclusions

This chapter described all the equipment used in this work for the fabrication and characterisation of zinc oxide and silicon nanostructures, as well as gas and biosensors based on these materials. For the fabrication of ZnO nanowires the sputterer and hydrothermal growth method was utilised. For the ZnO nanowire based biosensor characterisation cyclic voltammetry and chronoamperometry were used. Silicon nanostructures were fabricated using the evaporator and the PECVD technique. The conditions used for the device fabrication and characterisation will be given in the experimental sections of the corresponding chapters.

Chapter 4

Zinc oxide nanowire growth via aqueous solution method

The first part of this chapter gives an overview on zinc oxide nanostructures, their fabrication methods and detailed discussion on the previous research done in the field of ZnO nanowire (ZnONW) growth via a hydrothermal growth method.

The second part of the chapter investigates the growth of ZnONWs fabricated in this work. The fabrication of those nanostructures was performed via a two-step hydrothermal growth method. Various growth conditions were optimised for the production of uniformly sized nanowires with consistent distribution across the sample. The main instrument used for analysis of the produced nanowires was SEM. Structural and optical properties of the nanowires were also investigated using an XRD and UV-Vis spectroscopy respectively.

4.1. Introduction to zinc oxide nanostructures

Interest in nanoscience and nanotechnology is rising due to the realisation of the possibilities to explore new phenomena and overcome the limitations of current technologies. Currently electronic devices are being improved by the introduction of nanometer scale components and materials. Due to their versatile physical and chemical properties coming from their dimensionality, size and surface area nanomaterials have become a research focus and building blocks for electronic, photonic, and sensing devices[99].

Particular attention has been drawn to ZnO nanostructures (such as quantum dots, nanowires, and complex shapes with dimensions from 0 to 3) [100-104]. Zinc oxide is a piezoelectric, transparent wide bandgap (bandgaps between 3.2 and 3.4 eV have been reported [4, 105-107]) II-IV compound semiconductor with a large exciton binding energy (60 meV) and the use of ZnO nanostructures has been demonstrated in many high-performance electronic devices, including transparent electronics, UV light emitters, chemical sensors and spin electronics [4].

Zinc oxide has a hexagonal wurtzite crystal structure with lattice parameters of a = 0.3296 and c = 0.52065 nm [108] as illustrated in Figure 4-1.

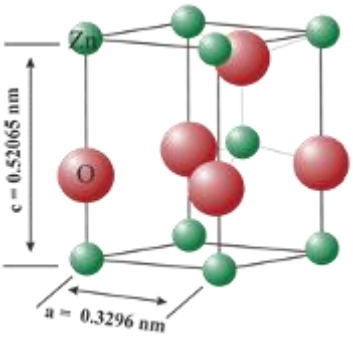

Figure 4-1. Model of the hexagonal wurtzite structure of ZnO.

Concerning the shape of the nanowire formation, it is reported that ZnO is formed of polar {0001} and non-polar {01T0} faces [109]. The polar surfaces have higher surface energy compared to non-polar surfaces. As the crystal tends to minimise the total surface energy, it will grow along the [0001] direction.

In ZnO crystals (001) plane is the basal plane, the ends of planes being terminated by partially positive Zn lattice points on one side and partially negative oxygen lattice points on the other side [110] (see Figure 4-2).

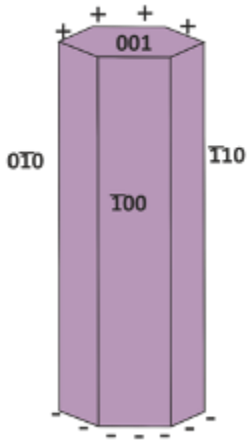

Figure 4-2. Crystal structure of ZnO nanowire with planes marked [110].

Electrical transport properties of ZnONWs have been investigated in order to see the potential use of these materials in nanoscale electronics. It was found that ZnO is an n-type semiconductor resulting from native defects including oxygen vacancies and zinc interstitials. These defects are concentrated at the surface, and considering high surface to volume ratio of these materials, they vastly influence optical and electrical properties of these nanowires [2].

Zinc oxide nanowires have also gained much attention in biosensors due to their important characteristics, such as non-toxicity, biosafety, biocompatibility and high specific surface area. There is a good optical and electrical interaction between ZnO and

biorecognition molecules which makes it a promising material for biodevices. In addition, ZnO has a high isoelectric point (IEP) of 9.5, which makes it a good candidate for adsorption of low IEP proteins and enzymes [111]. The nanowires not only provide a favourable matrix for immobilisation of negatively charged biomaterials, but also promote the electron transfer between the immobilized bio-molecules and the electrode [112]. A few of the key parameters of glucose biosensors fabricated via attachment of glucose oxidase (GOD) to various nanomaterials are shown in Table 4-1. The K_M^{app} stands for apparent Michaelis-Menten constant which evaluates the biological activity of the immobilised enzyme and smaller values represent higher affinity of the enzyme to the analyte. This constant will be discussed in more details in Chapter 5.

Table 4-1. Summary of various GOD modified nanomaterials as working electrodes reported for glucose detection [113].

Electrode material	K_M^{app} (mM)	Sensitivity ($\mu A\ cm^{-2} mM^{-1}$)	Detection limit (μM)
Titania sol-gel membrane	6.43	7.2	70
Carbon nanotubes	...	30.14	0.5
Au nanoparticles	4.3	8.8	8.2
TiO_2nanoporous film	6.08	4.58	...
ZrO_2/chitosan film	3.14	0.028	10
ZnO nanocombs	2.19	15.33	20
ZnO nanowires	2.9	23.1	10

It can be seen from Table 4-1 that ZnO nanowires show comparable or even better characteristics, such as higher sensitivity, lower detection limit and smaller Michaelis-Menten constant compared to other nanostructures in exception of carbon nanotubes. Therefore, ZnO nanostructures are promising materials to be further investigated and optimised for their application in biological sensors.

4.1.1. Zinc oxide nanowire fabrication and orientation

There have been various methods proposed and developed for synthesizing aligned one-dimensional ZnO nanomaterials. These include: chemical vapour deposition [114-117], hydrothermal methods [110, 118-122], electrochemical deposition [123-124], thermal

decomposition [125] or physical evaporation [100, 126-130], pulsed laser deposition [131-132], and reduction or oxidation of ZnS [133-134].

Despite a multitude of possible methods, there are only a few growth mechanisms for 1D ZnO nanostructures. These mechanisms are vapour-liquid-solid (VLS), vapour-solid (VS) or solution growth processes [135-136].

4.1.1.1. One-dimensional ZnO nanostructure synthesis mechanisms

4.1.1.1.1. Vapour-liquid-solid

As the name suggests, three phases (vapour, liquid, and solid) are involved in this process. The schematic illustration of the steps taking place in this process is demonstrated in Figure 4-3. This is a catalyst-assisted process that uses metal nanoparticles as nucleation sites for nanostructure growth (Figure 4-3(a)). In this process the gaseous reactants impinge on the metal catalyst which is in its liquid form, dissolving in the latter, forming an alloy (Figure 4-3(b)). The final stage of the process is the supersaturation of the droplet leading to the precipitation of the grown material from the liquid alloy (Figure 4-3(c) or Figure 4-3(d)).

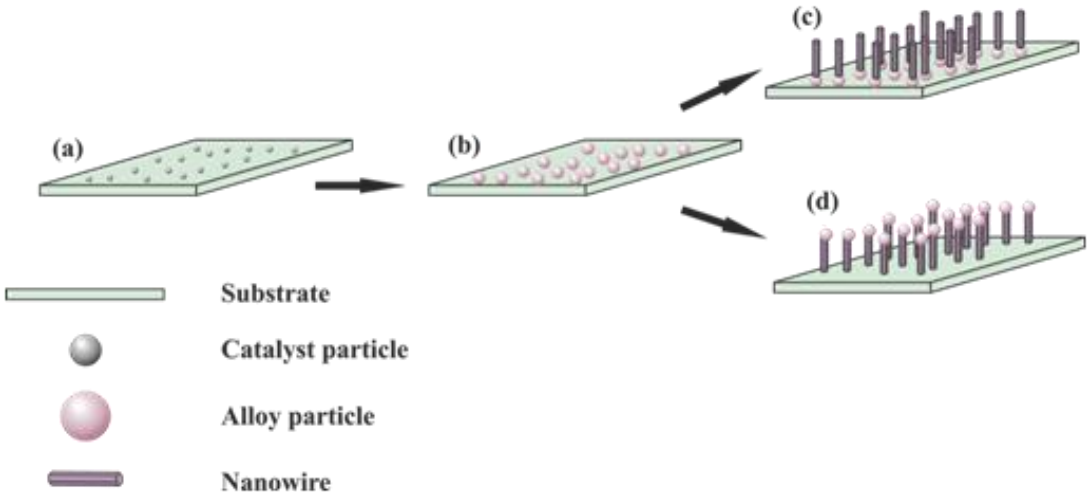

Figure 4-3. Schematic illustration of the VLS growth mechanism: (a) catalyst particles on the substrate, (b) alloy formation of the reactant gas with catalyst particle, (c) catalyst on the bottom nanowire growth and (d) catalyst on top nanowire growth.

The size and the shape of the grown material are directly related to the alloy droplet. Gold, tin, copper, and cobalt are the most common metal catalysts used for this process. The VLS process is more of a generic term, as in some observations, vapour-solid-solid (VSS) process has been observed. Kodambaka *et al.* demonstrated that 1D nanomaterials can grow either from liquid or from solid state alloy particles [137].

4.1.1.1.2. Vapour -solid

This mechanism is based on a catalyst free process. During this process the material grows without the help of the catalyst particle, instead it uses defects, such as screw dislocations, stacking faults, steps and kinks [135]. The temperature of the source material is increased to its vaporisation temperature which gets directly condensed on the low-temperature substrate from vapour phase. Owing to the processes taking place, this mechanism is also called evaporation-condensation mechanism. After the initial vaporisation, the condensed material forms the seed layer for nucleation of the further nanostructure growth. The growth rate of this mechanism is much slower compared to that of the VLS process. In addition, there is less control on the geometry, alignment and location of the nanostructures [4].

4.1.1.1.3. Solution phase synthesis

This synthesis method mainly uses aqueous solutions and in such conditions the process is referred to as hydrothermal growth process [108].

The possible growth mechanism of ZnONWs via aqueous solution growth (ASG) was suggested by Ahsanulhaq *et al.* [138] and the simplified version of it is illustrated in Figure 4-4.

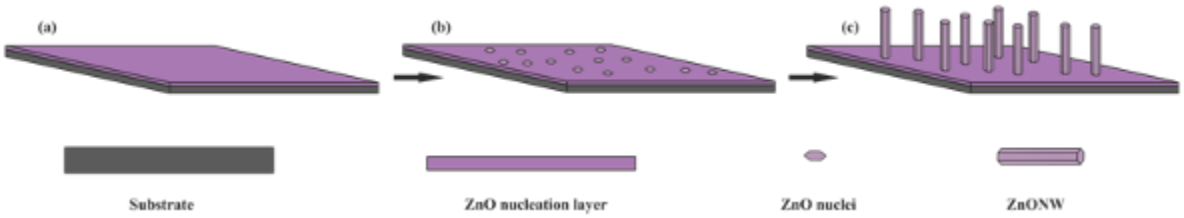

Figure 4-4. Schematic illustration of ZnO nanowire hydrothermal growth: (a) substrate covered with ZnO nucleation layer, (b) hexagonal ZnO nuclei formation in the solution upon heating and (c) hexagonal ZnONW growth.

In the hydrothermal growth process a substrate with a ZnO nucleation layer is required to initiate the growth of the nanowires [139]. Often a solution of zinc nitrate (source of Zn^{2+} ions) and hexamine is used for ZnONW growth [110].

In the ASG method more experimental parameters should be considered compared to vapour phase growth. These include growth temperature, growth time, solution concentration and precursor types, ionic strength, pH value and surfactant additives [135]. The ASG

process can be classified into three main growth types: (i) ion-by-ion addition growth, (ii) Ostwald ripening (OR) and (iii) oriented attachment (OA) [135]. The OR and OA processed are not as commonly observed compared to the ion-to-ion addition process, but they were observed at very specific growth conditions. In the OR mechanism the nanowire growth takes place in the expense of smaller particles. This is based on the phenomenon of higher dissolution of smaller particles compared to larger ones. In the OA mechanism the adjoining nanoparticles align in a manner where they share a common crystallographic axis. This may occur via collision of aligned nanoparticles or rotation of the nanoparticles in contact (that are misaligned) towards a low-energy interface configuration resulting in a single nanoparticle by eliminating the interface [135, 140].

An extensive family of ZnO nanomaterials have been synthesized using the aforementioned growth methods, such as nanowires, nanorods, nanobelts, nanoplatelets, nanotubes, nanocombs, nanorings, nanosprings, nanotetrapods, nanohelixes, nanocastles and hollow ZnO nano-spheres [4, 136].

The zinc oxide nanostructure fabrication via the VLS method utilises a metal catalyst for the growth process which might introduce unwanted and unintentional doping impurities to the nanowires affecting its physical properties, in addition the VLS and the VS methods often use high temperature, which will limit the choice of substrate material. Moreover, these growth methods might not be simple to use and/or employ expensive technology with high energy consumption, which are unwanted attributes for commercial use [141].

Among the aforementioned fabrication methods ASG method has many advantages that allow the growth of ZnO nanowires at low cost and low temperatures (< 90°C). This allows the usage of glass and other flexible materials as substrates for the nanowire growth [142].

4.1.1.2. Patterned growth and alignment of 1D ZnO nanostructures

Control of the nanowire growth parameters is one of the tasks for semiconductor nanomaterial fabrication as the spatial distribution (site, orientation, packing density, size) of these materials is of high importance in device fabrication. Both horizontal and vertical growth of 1D nanostructures have been achieved [2]. Several techniques have been applied to manipulate the orientation and alignment of the nanowires via either direct controlled growth route or alignment of as-grown nanostructures.

A simple method includes direct control of the site, size and growth direction of the nanostructure during the growth process. As most of the methods utilise catalyst seed

particles to initiate the growth, it is possible to fix the growth site by controlling the location of the seed particle [2, 143]. Alternatively, by choosing the appropriate substrate, epitaxial growth of 1D nanostructures is possible due to lattice matching between the crystal and substrate. Nanospheres and polymers have been used as patterning methods [144-145] and are known to be cost effective, simple and applicable to large scale lithographic techniques. These materials form some patterned structures on the substrate, afterwards the catalyst material is deposited in the void of these structures. The spheres are removed from the substrate by chemical or plasma etching. So the catalyst, therefore, has the shape of the open areas between spheres. This is called nanosphere lithography (NSL) [146]. The size of the catalyst particles depend on the sphere size.

Another method of nanowire spatial distribution includes manipulation of as grown nanostructures by various techniques including electric and magnetic fields assisted alignment [2] and microfluidic alignment [147].

4.1.1.3. Two-step hydrothermal method for ZnO nanowire fabrication

Hydrothermal growth of ZnO nanowires achieved in this work used a two-step combination method proposed by R.B.M. Cross *et al.* [118]. In this combination method, the first step included sputtering of zinc oxide nucleation layer on the substrate (silicon or glass) followed by a hydrothermal growth step in the equimolar solution of zinc nitrate hexahydrate (ZNH) and hexamine (HMT). Many parameters including those of the nucleation layer and hydrothermal growth step can influence the nanowire growth.

Aqueous solution growth of ZnO nanostructures results in both homogeneous and heterogeneous crystallizations. These occur simultaneously and competitively. Yang *et al*. [148] have reported crystal growth governed by Ostwald ripening mechanism, stating that the growth process is limited by the reactants transportation, which they state to be a very simplified model for such a complicated system. After the growth was performed, they found white powder-like material present both on the substrates and on the bottom of the beaker. Investigation of the powder revealed these to be microrods formed in the solution. When the substrate was immersed facing down or held vertically, these microrods were absent on the substrate surface, while still appearing on the bottom of the beaker. But the seed layer is superior for the initiation of the nanowire nucleation compared to the mother solution where the contaminants play the role of the nucleation initiation sites. The ZnO nucleation layer on the substrate already has negatively or positively charged ZnO surface which will initiate the

nanorod growth from the substrate. The simplified Ostwald ripening mechanism could explain the homogeneous growth of microrods in the solution but it is invalid for the interpretation of the heterogeneous growth of ZnONWs from the substrate. In case of heterogeneous growth not only the transportation to the surface, but also the reaction at the surface should be encountered. Thus, this means that the following parameters play an important role for the nanorod growth from the substrate: substrate material choice, nucleation layer thickness and structure, solution temperature, concentration of the source material, duration of the growth and pH value.

4.1.1.3.1. Nucleation layer

Nucleation layers of various thicknesses deposited via different methods have been used for nanowire growth and even nanowire growth on substrates with no ZnO layer has been attempted [142, 149-150]. It has been shown that the seed layer plays an important role in the growth, determining the nanowire orientation and diameter.

In the paper published by Ji *et al.* [142] the XRD analysis of ZnO nucleation layers of various thicknesses have been performed. An increase in the crystallinity of the nucleation layer was observed as a result of increasing its thickness. The nanowires grown from thicker seed layers (500 and 1000 nm in particular) were vertically aligned, whereas the ones grown from thinner layers (20 and 240 nm) were of poor vertical alignment. This is explained by poor crystallinity of the seed layers causing poor vertical growth of nanowires. The crystallinity of ZnO nanowires was also increased via annealing the films at 450 °C due to reduction of defects such as oxygen vacancy and interstitial oxygen ions.

In addition, increase in the diameter of the nanowires, thus decrease in the density (number of nanowires in unit area) of the latter has been observed with the increase of the seed layer thickness. Therefore, the surface area for the thinner seed layers with thinner nanowires was higher compared to thicker seed layers with large diameter nanowires [149]. The XRD data of the seed layers of various thicknesses has shown direct dependence of the crystal size of the seed layer with the seed layer thickness. Decrease of crystal size for thinner layers suggests that smaller nanowires at thinner seed layers are due to small crystal structures of the seed layer. Song *et al.* have reported a linear increase of the crystal size of the seed layer with its thickness [149]. Growth of nanowires with larger diameters as a result of bigger grain size formation in thicker nucleation layers was also observed by Yin *et al.* [141].

Zinc oxide rod growth was also attempted without ZnO nucleation layer on Si [150] and ITO (indium tin oxide) [141] substrates. While no nanowire growth was observed from the ITO substrate, ZnO rods were reported on the bare silicon substrate but these had diameters above 900 nm, were limited in density [150] or were randomly distributed on the substrate [138]. Whereas when the nucleation layer was introduced the diameter of these was reduced, the density increased and alignment controlled.

The as-prepared zinc oxide films have been annealed in air [151] and in vacuum [151-152] and in both cases (002) plane diffraction peaks were observed. This indicates wurtzite (hexagonal) structure consisting of zinc and oxygen atoms occupying tetrahedral sites which arises from basal ZnO planes in grains that are oriented with c-axes, perpendicular to the substrate. An increase in the peak intensity, but decrease in the FWHM (full width at half maximum) was reported with annealing, which is associated with the enlargement of the crystal. During various deposition procedures atoms are often deposited at inappropriate positions. When annealed, these atoms receive thermal energy, thus migrating to relative equilibrium positions. This also results in partial intrinsic stress relief, thus suggesting that the annealing process is beneficial for improvement of the crystalline structure. No changes of the nucleation layer after annealing was observed with AFM [152].

4.1.1.3.2. Growth duration

Theoretically, if feed material is not continuously added to the solution, the growth rate of the nanowires should slow down as the source material at the growth site becomes depleted. Eventually the growth will come to a stop when the source material is exhausted.

Ji *et al.* [135] have observed that the length of the nanowire reaches the maximum value within 10 hours and stops even with extension of the growth time. It was also demonstrated [141] that nanowire length is mostly influenced during the first hour of hydrothermal growth, whereas the diameter seems to be less affected (compared to the length) by the growth duration within the first hour. However, the lateral growth (diameter) was not completely independent of the duration as Yin *et al.* [141] observed that after half an hour the nanowires were starting to get thicker than the grain size (whereas at the start of the growth the diameter of the nanowires was almost the same as that of the crystal grain) indicating lateral growth. Eventually, after one hour growth duration, the nanowires were starting to coalesce creating larger structures with less surface area.

In contrary, in the study of *Wang et al.* [153] the length and diameter of the nanowires were both observed to increase almost linearly with the reaction time up to 240 min. Wang *et al.* explain this difference with ZNH/HMT concentration ratio (5:1) used in their work (compared to equimolar concentrations used in [135] and [141]) which could supply sufficient Zn^{2+} ions and due to alteration in the reactions taking place prohibit its consumption in the vicinity of nanorods.

4.1.1.3.3. Solution temperature

The aqueous growth solution temperature has shown to have direct influence on the nanowire fabrication. No growth has been observed at 40 °C and temperatures below [141]. In addition, they found out that the lateral growth is less sensitive to temperature than the (002) plane growth velocity in the temperature range of 40 – 95 °C.

Ji *et al.* [135] have reported that higher growth temperatures cause faster growth rate of nanowires with larger diameters. However, the length of the nanowires was observed to be the same or even shorter compared to lower temperature solution growth due to depletion of source material. In addition, with increase of the solution temperature the homogeneous nucleation in the solution is also enhanced and can even compete with the nanowire growth on the substrate, thus further reducing the source material availability for heterogeneous nanowire growth on the substrate.

Similar results were obtained by Sugunan *et al.* [110] when investigating the influence of the solution temperature on the nanowire growth. They discovered that 7 hour growth of nanowires at 65 °C and 95 °C resulted in the same nanowire length.

4.1.1.3.4. Solution concentration

Quantitative information for the dependence of the nanowire diameter on the precursor concentration has been reported by L. Vayssieres [154]. In their work it is shown that a decrease in the precursor concentration in the ZNH/HMT equimolar solution by one order of magnitude results in decrease of nanowire diameter by about an order of magnitude. Microrods of 1-2 μm diameter were obtained at a concentration of 0.1 M, nanorods of 100-200 nm width at 0.01 M and 10-20 nm diameter nanowires at 1 mM concentration of ZNH/HMT equimolar solution.

When investigating the dependence of the nanowire length on the solution concentration, Sunuganan *et al.* observed the nanowires grown in 1 mM equimolar solution of ZNH/HMT to be 2-3 times longer compared to 0.5 mM solution, taken that the rest of the conditions remained the same [110].

In contradiction to the observation of Sunuganan *et al.* [110], it was suggested that while the diameter of the nanowire is getting smaller at lower concentrations, longer nanowires are able to be obtained as the homonucleation in the solution is suppressed thus allowing more source material for heterogeneous growth on the substrate [135].

In the work published by *Yin et al.* [141] no nanowires were observed when the zinc precursor concentration was reduced to 0.02 M, whereas nanowires coalesced to a structure resembling a film when the concentration was increased to 0.06 M.

In the work by Wang *et al.* [153] the dependence of the diameter and length of the nanowire was observed to increase with increase of the precursor concentration in the ZNH/HMT ratio of 5. The dependence of the lateral growth rate was linear for precursor concentrations between 0.008 M and 0.04 M, whereas at higher concentrations an initial high growth rate of the nanowire length was observed, but the growth stopped in a shorter period of time.

The influence of ratio between ZNH and HMT was also investigated [153] and observed to strongly affect the growth of ZnONWs. It was observed that the maximum length of the nanowires and highest aspect ratio was achieved when the ZNH/HMT ratio was one, whereas it decreased with the shift of the ratio from the unity. In addition, it was found that the uniformity, crystallinity and alignment of nanowires were also better for ZNH/HMT concentrations in the vicinity of one.

4.1.1.3.5. Precursor types

Zinc acetate, chloride, perchlorate, sulfate and nitrate hexahydrate have been used as precursor materials in the literature [141, 155]. It was shown that the precursor type has a noticeable effect on the morphology of the grown films. Nanostructures obtained from nitrate and perchlorate were acicular whereas the structures obtained from the rest of the precursors were rod-like.

4.1.1.3.6. Role of hexamine

Hexamine ($C_6H_{12}N_4$), also known as methenamine and hexamethylenetetramine (HMT), is a non-ionic tetradentate cyclic tertiary amine with high solubility in water [108, 154]. It is reported that the primary role of hexamine in aqueous solution is to act as a buffer to regulate the pH value of the solution [155]. The decomposition of hexamine is pH dependent; it slowly thermally decomposes into formaldehyde and ammonia slowly supplying OH^- ions. However, Sugunan *et al.* [110] state that hexamine does not decompose in aqueous conditions even upon boiling. They propose that HMT is a molecule that will rather attach to the non-polar facets of the wires (Figure 4-5), thus stopping the access of Zn^{2+} ions to these surfaces leaving only the polar (002) plane for epitaxial growth.

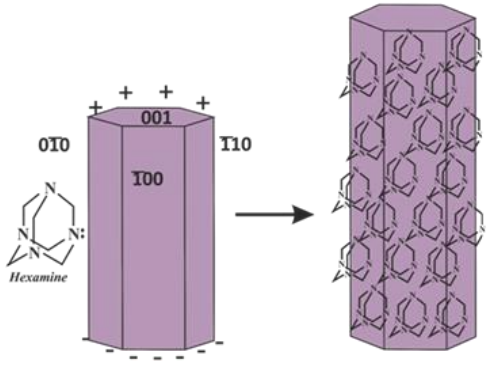

Figure 4-5. Illustration of possible attachment of hexamine onto the non-planar facets of a ZnO crystal.

In this case HMT acts as a shape-inducing agent rather than a buffer [108].

The following reactions have been reported to be involved in ZnONW growth in the solution of HMT and ZNH [138, 156]:

$$(CH_2)_6N_4 + 6H_2O \rightarrow 6HCHO + 4NH_3 \qquad \textbf{Equation 4-1}$$

$$NH_3 + H_2O \leftrightarrow NH_4^+ + OH^- \qquad \textbf{Equation 4-2}$$

$$Zn^{2+} + 2OH^- \rightarrow Zn(OH)_2(s) \quad (a)$$

$$Zn^{2+} + 2OH^- \rightarrow ZnO(s) + H_2O \quad (b) \qquad \textbf{Equation 4-3}$$

$$Zn(OH)_2 \rightarrow ZnO(s) + H_2O \qquad \textbf{Equation 4-4}$$

where (*s*) stands for solid nuclei. It can be seen from Equation 4-1 and Equation 4-2 that HMT decomposes to formaldehyde and ammonia in the chemical solution. The latter acts as a pH buffer and supplies OH^- ions slowly. It can be estimated from the abovementioned equations that for generation of 1 mol of ZnO product, 1 mol of ZNH and 0.5 mol of HMT is

required (equivalent to ZNH/HMT ratio of 2:1). But the highest growth rate was achieved in the excess of ammonia or OH^-ions (with the ZNH/HMT ratio of one) [153]. This is because the actual concentration of ammonia is less in the solution than the estimated value because of its low solubility in water at high temperatures and its evaporation level.

When the concentration of Zn^{2+} and OH^- exceeds the critical value, zinc oxide nuclei can precipitate from aqueous solution either directly (Equation 4-3(b)) or via the hydroxide (Equation 4-3(a) and Equation 4-4) [156].

Ahsanulhaq *et al.* have noted that ZnO precipitates are less soluble in the chemical bath compared to $Zn(OH)_2$ precipitates, thus the latter dissolves forming more Zn^{2+} and OH^- ions which eventually form ZnO nuclei. These nuclei have hexagonal shape due to ZnO crystal characteristics and play a role of building blocks for ZnO nanowire growth [138].

According to Ashfold *et al.* [156], at the initial stage nanostructure formation will occur via $Zn(OH)_2$. But then as a result of increase in the pH of the solution and decrease in zinc ion concentration $Zn(OH)_2$ becomes less thermodynamically stable, thus it will dissolve and the further growth will take place with direct deposition of ZnO.

The net reaction from the HMT decomposition after all the hydroxide ions have reacted with the Zn^{2+} ions is given with the Equation 4-5 [157]:

$$(CH_2)_6N_4 + 8H_2O + 2Zn^{2+} \longrightarrow 6HCHO + 4NH_4^+ + 2ZnO \qquad \textbf{Equation 4-5}$$

It was measured that the pH of the solution stays constant after the precipitation has started even though the concentration of Zn^{2+} ions continues to fall. Thus, it was believed for the role of HMT to be as buffer. This statement was investigated by Ashfold *et al.* [156]. The concentration of zinc ions and HMT was measured in regular intervals by removal of small aliquots of solution from the chemical bath. It was shown that HMT decomposition rate is independent of the ZnO fabrication reaction, thus HMT behaves as a kinetic buffer for the solution pH.

In this study hydrothermal growth of ZnONWs is attempted for further incorporation of these nanostructures in biosensors. The optimisation of various growth parameters including the nucleation layer thickness and growth temperature is performed.

4.2. Experimental procedure

Prior to the growth of nanowires the substrates were pre-cleaned and pre-cut into 1 cm^2 and 2.5 cm^2 pieces for Si and glass respectively. The cleaning procedure is described in details in Appendix A.

4.2.1. Sputtering

The deposition of the nucleation layer was performed via RF magnetron sputtering system with a base pressure of $<10^{-5}$ Pa. The sputtering was carried out at room temperature using a 20.3 cm ZnO (99.99% purity) target in an argon (Ar) (99.999% purity) gas atmosphere, with an RF power of 160 W at a frequency of 13.56 MHz. The Ar flow rate was such that the sputtering pressure was 1.3 Pa and the distance between the target and the substrate was approximately 7 cm. The duration of the sputtering was varied in order to obtain various thicknesses of the nucleation layers for analysis.

4.2.2. Hydrothermal growth

Hydrothermal growth of the nanowires was conducted in a temperature controlled vessel covered by a non airtight lid and samples were held in the solution by a Teflon holder. The equimolar aqueous solutions (0.025 M) of ZNH and HMT were combined in the bath at the growth temperature and left for 30 minutes to mix well and for the temperature to establish evenly throughout the solution.

After the period of temperature stabilization, the samples were suspended upside down in the growth solution for the desired duration. The samples were then removed from the growth vessel, rinsed with D.I. water, blow dried with nitrogen and then left to dry in air. The image of the experimental setup for the hydrothermal growth of ZnONWs can be seen in Figure 4-6.

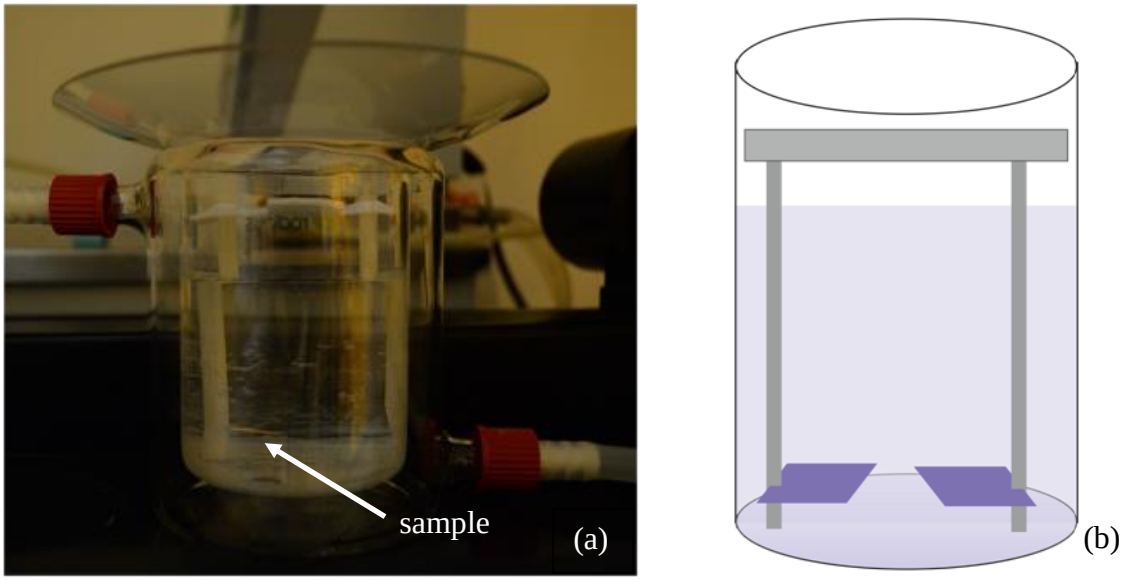

Figure 4-6. The experimental (a) and (b) schematic representation of the set-up used in this work for ZnONW growth.

4.3. Results and discussions

As it was demonstrated in Section 4.1.1.3 many papers have been devoted to the optimisation of ZnO nanowires fabricated by hydrothermal method. Still, there are some inconsistencies within published reports, where the dependence of the nanowire growth on various parameters is slightly different. In order to apply the nanowires fabricated in this work as transducers in biosensors, the ZnO nanowire growth conditions needed to be optimised first.

Firstly, SEM images revealed interesting and unexpected circular formations on most of the samples after the hydrothermal growth of the nanowires (Figure 4-7).

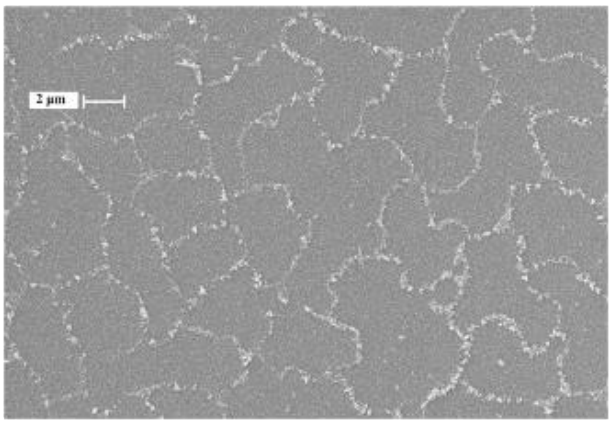

Figure 4-7. SEM image of ZnONW growth attempt from 75 nm nucleation layer at 85 °C.

These formations were discovered to consist of smaller and larger nanowires inside and on the circles respectively. This phenomenon will be addressed in more details further in this chapter.

4.3.1. Nucleation layer variation

The SEM images of ZnONWs grown in a 75 °C solution bath from 5 nm, 25 nm, 50 nm and 75 nm nucleation layers are shown in Figure 4-8.

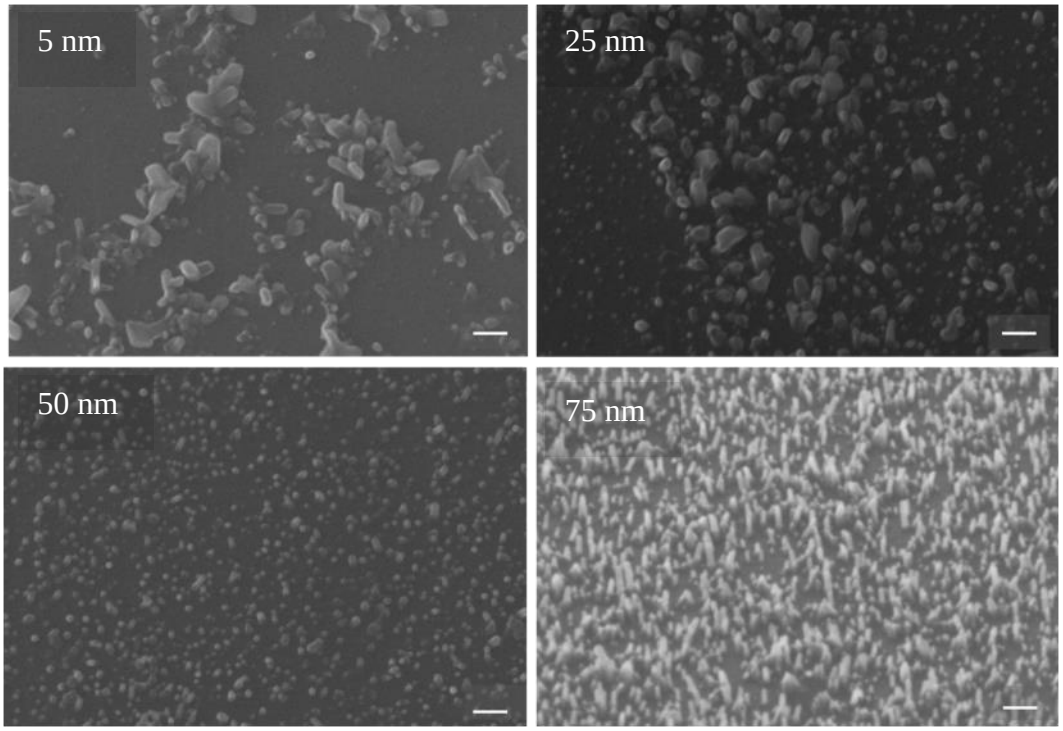

Figure 4-8. SEM images (at a 25° tilt) of ZnONW arrays grown from various thicknesses of nucleation layers (the scale bar is the same for each image and equals 200 nm).

It is important to note that the images of nanowires from 50 nm and 75 nm nucleation layers are taken inside the circles whereas the images from 5 nm and 25 nm nucleation layers are directly from the circles. It is evident from the images of 5 nm and 25 nm nucleation layers that there is either no growth or only small particle formation inside the circles. Therefore, Figure 4-8 reveals the fact that the nanowire size is highly influenced by the thickness of the nucleation layer.

The SEM images of ZnONWs grown from 150 nm and 200 nm nucleation layers are given in Figure 4-9. Reduction in density of the nanowires and increase in their diameter was observed for these nucleation layers.

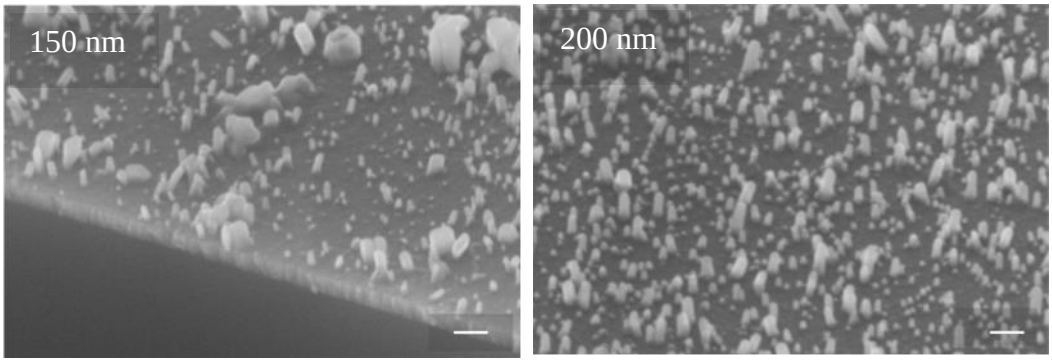

Figure 4-9. SEM images (at a 25° tilt) of ZnONW arrays grown from 150 nm and 200 nm thick nucleation layers (the scale bar is 200 nm for both images).

A possible explanation for this phenomenon could be the following: thicker sputtered layers result in larger grain size formation within the nucleation layer initiating larger diameter nanowire growth. In addition, the length and distribution of the nanowires became less uniform for thicker layers compared to those of 75 nm sample (Figure 4-8).

Sputtered thin films are known to have rough surfaces. It has been suggested that surface roughness improves the initiation and the process of hydrothermal growth of the nanowires [152]. To check the validity of this statement for the current growth mechanism, the surface roughness measurements of ZnO nucleation layers with thicknesses of 5 nm, 25 nm, 50 nm, 75 nm, 100 nm, 150 nm and 200 nm have been carried out by contact-mode AFM (Figure 4-10).

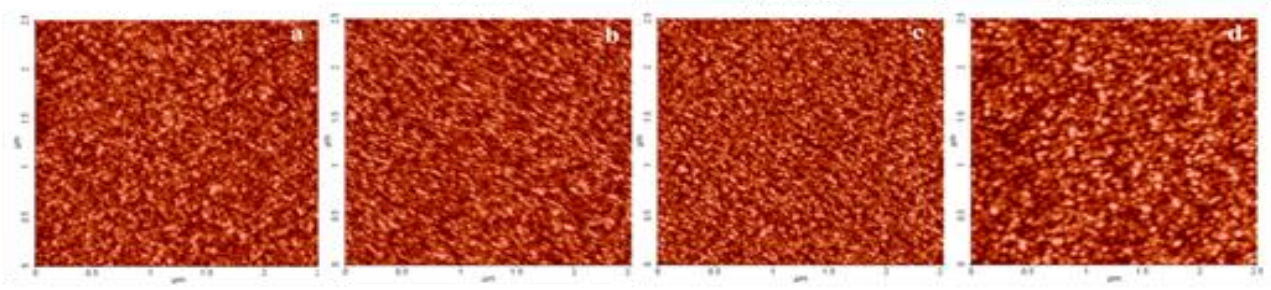

Figure 4-10. AFM images of a) 25 nm, b) 50 nm, c)100 nm and d) 200 nm ZnO nucleation layers.

Figure 4-11 represents the root mean square (RMS) roughness of the nucleation layer as a function of its thickness.

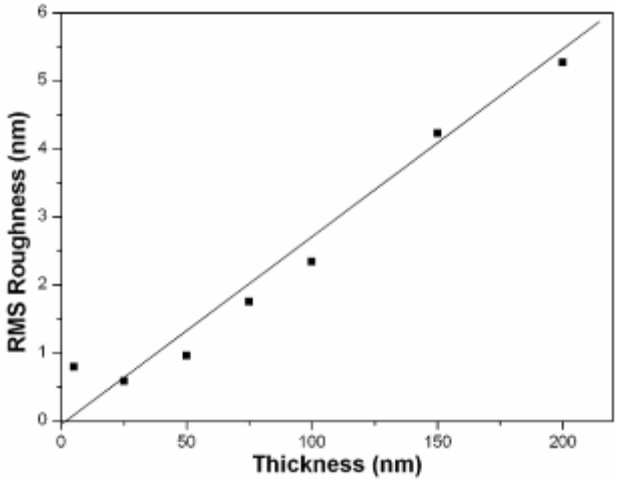

Figure 4-11. RMS Roughness dependence of the nucleation layer on its thickness.

It is noticeable from the graph that the RMS roughness increases with the thickness of the layer. However, the roughness of the 5 nm nucleation layer does not fit with the general trend of the results. This could possibly be explained by an initial island formation of the sputtered layer at thinner layers not covering the whole surface therefore creating a very rough layer.

X-ray diffraction spectroscopy is a powerful tool for investigating the crystal structure, lattice parameters and crystal size of the material [158]. In that respect, in order to investigate the crystallinity of the grown nanowires and the effect of the nucleation layer on the ZnONW growth and orientation, XRD analyses of a range of samples were performed. The samples were prepared on Si substrates, the XRD peaks of which can be seen in Figure 4-12.

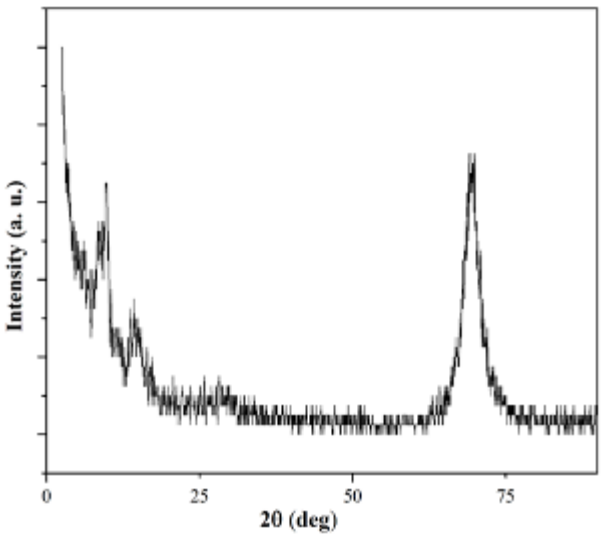

Figure 4-12. The XRD peaks of the Si substrate.

It can be seen from Figure 4-12 that Si substrate itself has a few sharp XRD peaks that were also evident in the spectra of the samples with ZnO nanostructures. However, no

additional peaks appeared under 20º and above 65º for ZnO nanostructured samples. For this reason for more clear representation and in order to avoid the interference of Si peaks in the interpretation of the results, the XRD analysis of ZnO samples are demonstrated between 20º and 65º. Samples with 5 nm, 25 nm, 100 nm and 200 nm thick nucleation layers (NL) and their corresponding nanowire (NW) arrays were subjected to XRD analysis (Figure 4-13).

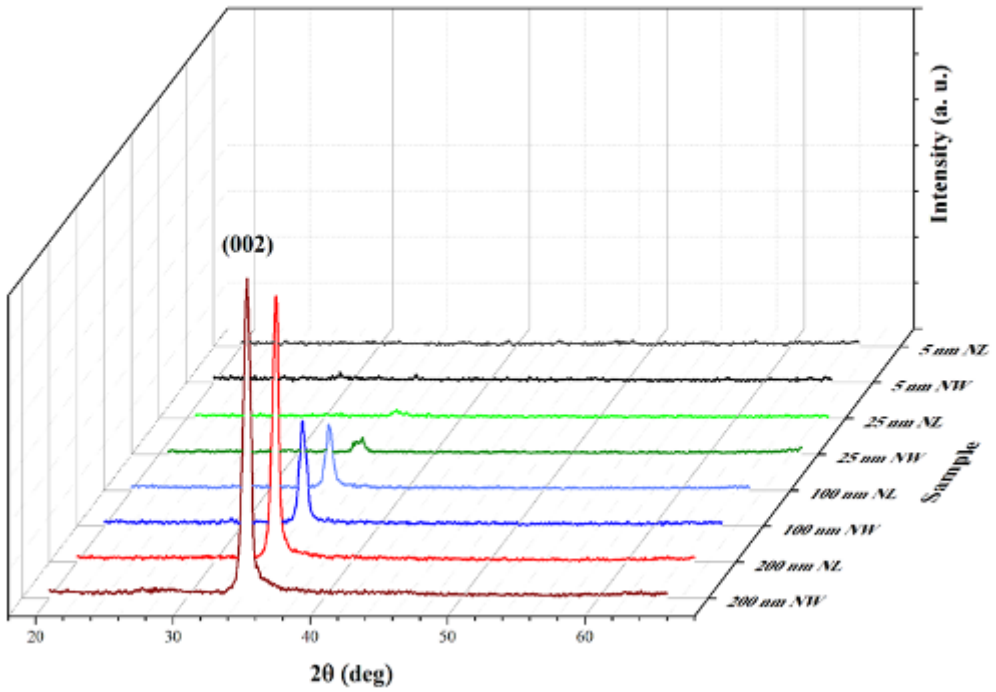

Figure 4-13. The XRD patterns of the 5 nm, 25 nm, 100 nm, 200 nm nucleation layers and corresponding as-grown nanowire arrays grown on Si substrate at 70 °C.

From the XRD patterns in Figure 4-13 for all the samples with 25 nm NL and above (the samples with 25 nm, 100 nm and 200 nm nucleation layers and the corresponding samples with ZnONW growth) a peak at 34.4º is observed. This peak is assigned as ZnO (002) crystal plane which corresponds to the [0001] growth direction of the nanowires. The sharpness of the peak indicates that the nanowires are highly c-axis oriented [138, 159-160]. It can be seen from the data, that the 5 nm nucleation layer does not show any significant crystallinity and with increasing the layer thickness, the crystallinity of the nucleation layer increases (Figure 4-13). In addition, it is evident from the thinner NL spectra and corresponding NW spectra in Figure 4-13 that in the case of low crystallinity layer (5 nm thick layer), the crystallinity of the nanowires grown on the corresponding nucleation layer is also negligible. It can be explained with only island formations for 5 nm ZnO layers which result in sparse nanowire growth as was observed via the SEM (Figure 4-8). As the thickness of the NLs is

increased the crystallinity of the as-grown nanowire arrays also increases gradually. The same dependence of the NL crystallinity on its thickness was observed by Ji *et al.* [142]. As a summary, we suggest that thicker nucleation layers (and the higher the crystallinity) result in highly crystalline nanowire growth.

These XRD results were also used to calculate the crystal sizes of the nucleation layers (Table 4-2) by the Scherrer equation [149, 161]:

$$L = \frac{0.9\lambda}{B(2\theta)cos\theta} \qquad \textbf{Equation 4-6}$$

where L is the average crystal size, λ is the X-ray wavelength and is 0.154 nm, $B(2\theta)$ is the FWHM of the diffraction peak calculated in radians where θ is the angle corresponding to the peak.

Table 4-2. Effect of thickness of the ZnO nucleation layer on crystal size.

Film Thickness (nm)	25	100	200
FWHM (002)(radians)	0.0136	0.0104	0.0091
Crystal size (nm)	12.5	16.3	18.7

It can be seen from Table 4-2 that the crystal size of the nucleation layer increases with its thickness resulting in growth of ZnONWs with wider diameters (as was observed from the SEM images presented in Figure 4-8 and Figure 4-9). Similar observation was made by Song and Lim [149].

Due to the bandgap of the materials being related to their size and dimensionality, the small size of the crystals (as demonstrated in Table 4-2) suggests that the bandgap of the ZnO nucleation layers might be affected by the confinement effect [162]. If the crystal size becomes comparable to the exciton diameter, which is < 10 nm, quantum confinement effect takes place. In this situation the optical bandgap of semiconductor quantum dots and wires increases with the decrease of the nanocrystal size, for groups IV, III-V and II-VI semiconductors [106, 162-163]. It can be seen (Table 4-2) that the crystal size of the nucleation layers is slightly above the reported size for the quantum confinement inducing crystal. Nonetheless, the optical bandgap of the nucleation layers was estimated using Tauc relation [164]. For this study the optical transmission spectra of these layers with various thicknesses were recorded as a function of wavelength in the wavelength range of 300 – 1000 nm. Several of these spectra can be seen in Figure 4-14.

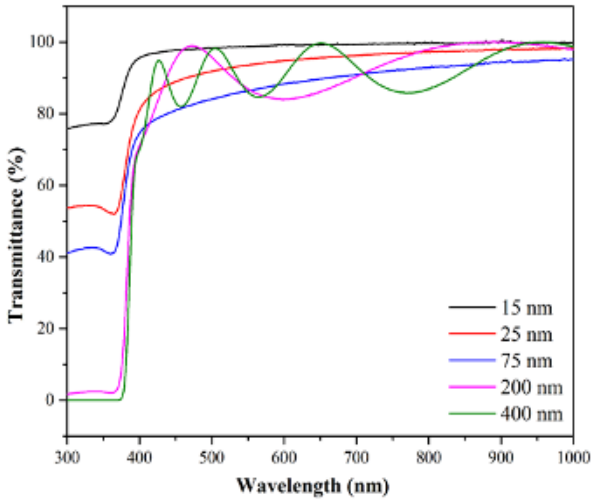

Figure 4-14. Optical transmittance spectra of ZnO nucleation layers of different thicknesses.

Using optical transmittance data it is possible to estimate the optical bandgap using Tauc relation [164]:

$$(\alpha h\nu)^2 = A(h\nu - E_g) \qquad \textbf{Equation 4-7}$$

where A is a constant that is different for different transitions, α is the absorption coefficient, $h\nu$ is the photon energy, and E_g is the optical bandgap.

The curve of $(\alpha h\nu)^2$ versus photon energy hν is shown in Figure 4-15(a). The energy at which a straight line extrapolated from the linear portion of the curve intersects the energy axis is defined as the optical bandgap of the sample [165]. The optical bandgap of the layers is measured and the dependence on the thickness of the layer given in Figure 4-15(b).

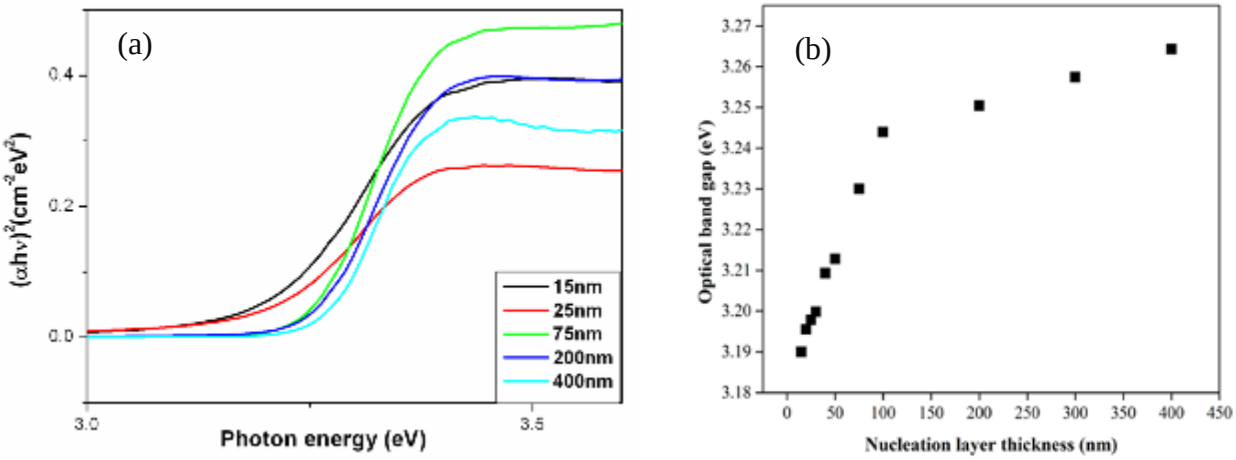

Figure 4-15. (a) The curves of $(\alpha h\nu)^2$ versus photon energy for 15 nm, 25 nm, 75 nm, 200 nm and 400 nm thick ZnO nucleation layers, (b) the bandgap dependence of ZnO layer on its thickness.

It can be seen from Figure 4-15(b) that most of the values (above 3.2 eV) of the optical bandgap of the nanostructured nucleation layers are between those reported in literature for bulk ZnO. However, the optical bandgaps of the samples under 50 nm thick nucleation layer are between 3.19 eV and 3.2 eV. The 3.19 eV band gap value was reported to correspond to nanocrystalline ZnO reported by Aydin *et al.* [166].

4.3.2. Temperature variation

The second set of experiments were concerned with the variation of the growth solution temperature between 40 ºC to 90 ºC. The results from these experiments can be seen in Figure 4-16.

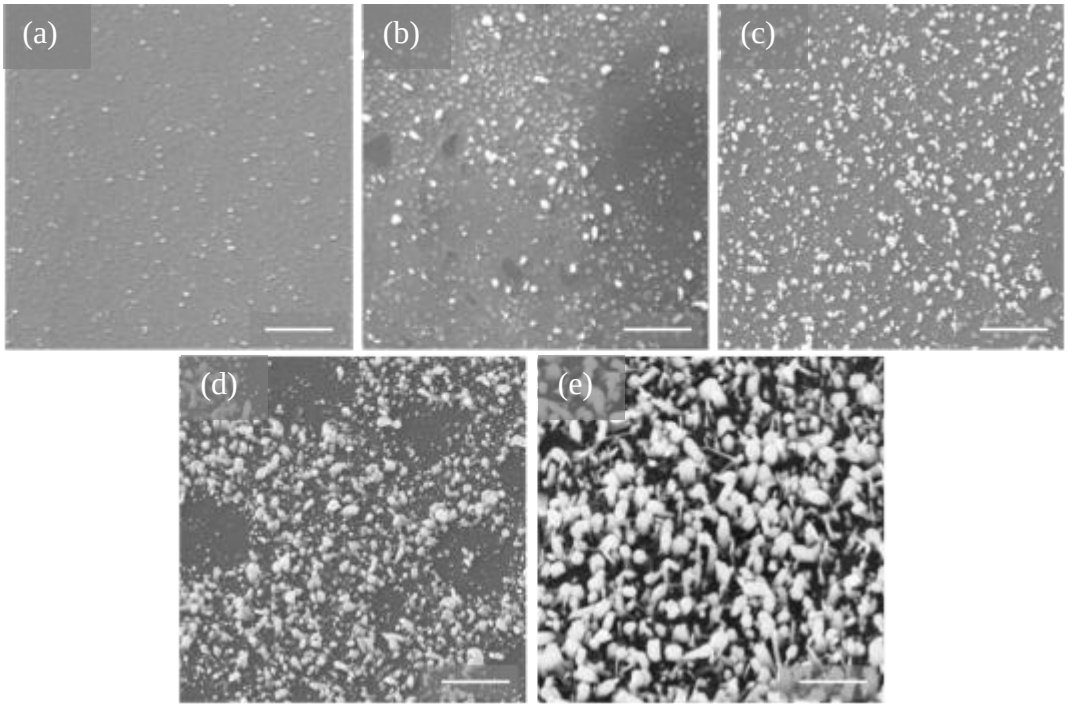

Figure 4-16. SEM images of ZnO nanowire arrays grown from 75 nm ZnO sputtered layer at various growth solution temperatures; (a) 50 ºC, (b) 60 ºC, (c) 70 ºC, (d) 80 ºC and (e) 90 ºC (the scale bars are all 1 µm).

From Figure 4-16 it is obvious that there is a temperature threshold (as was also observed by Yin *et al.* [141]) for aqueous solution growth of ZnONWs. No nanowire growth was observed at temperatures up to 50 °C. Higher magnification images of ZnONWs grown at temperatures of 60 °C and above can be seen in Figure 4-17.

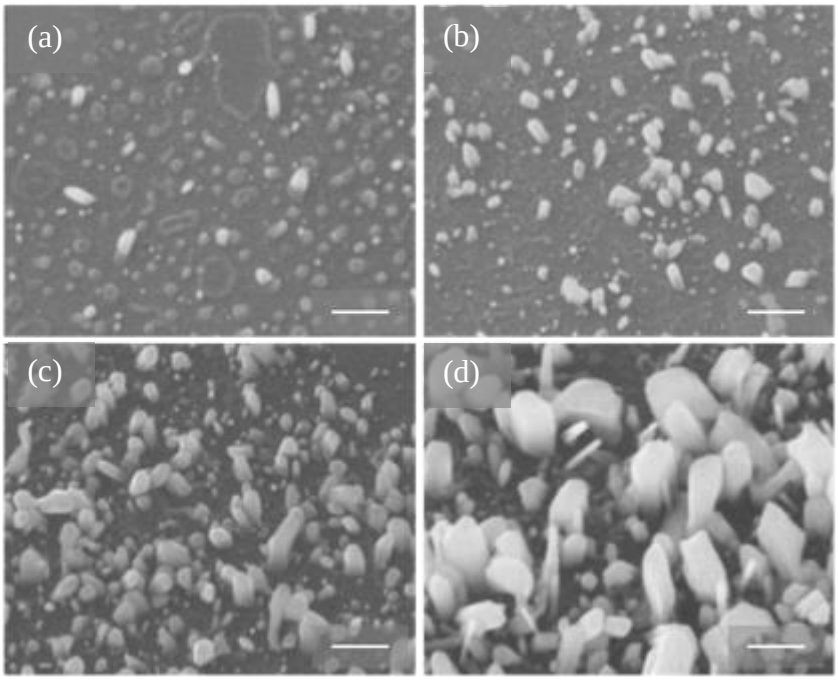

Figure 4-17. ZnO nanowires grown from 75 nm ZnO nucleation layer at various growth solution temperatures; (a) 60 ºC, (b) 70 ºC, (c) 80 ºC, and (d) 90 ºC at higher magnification (the scale bars are all 300 nm in size).

SEM images presented in Figure 4-17 make the temperature dependence of the nanowire growth very vivid. It can be seen that nanowires grow denser and larger in size with increase of temperature, which agrees with the observations of Ji *et al.* [135]. However, when the growth temperature reaches 90 ºC the growth of large diameter wires takes place in addition to the nanowires growth. At such elevated temperature the growth might be influenced by (i) Ostwald ripening, (ii) oriented attachment mechanisms or simply (iii) coalescence of neighbouring nanowires forming larger polycrystalline structures. The higher growth temperature (90 ºC) results in samples with smaller growth density (number of nanowires per unit area). The most uniform samples, in terms of the diameters of the nanowires and the uniform distribution (spatial) of nanowires across the sample, were observed for growth temperatures between 70 °C and 80 °C.

4.3.3. Investigation of circle formation

It was observed that on the majority of the samples there were circular formations of nanowire growth on the surface. Figure 4-18(b) shows the edge of one of the circle formations in high magnification. As can be seen, the circles consist of large nanowires on the perimeter with smaller nanowires inside the circle.

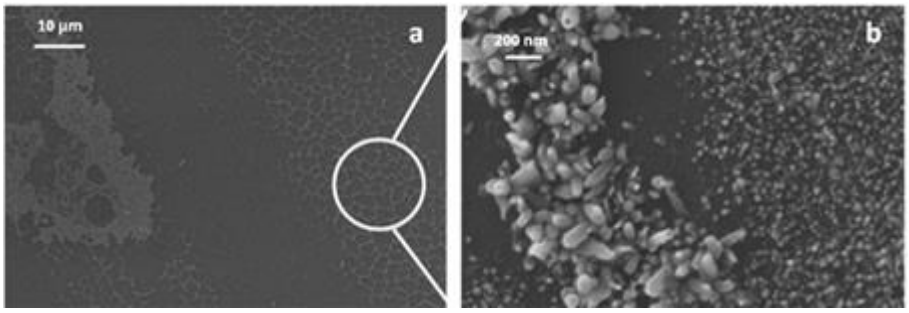

Figure 4-18. Planar view SEM images of ZnO nanowire arrays grown from 75 nm ZnO sputtered layer in 90 °C temperature solution at the magnifications of (a) 650 and (b) 46,000.

There could be various factors playing role in the circle formation. One of the possible reasons could be the structure of the sputtered layer; in case the sputtering is not uniform and the nucleation layer already consists of larger and smaller grains. Another possibility is that air bubbles form in the solution and sit on the substrate surface prohibiting the growth from these areas (see Figure 4-19), while submerged in the solution at the growth temperatures.

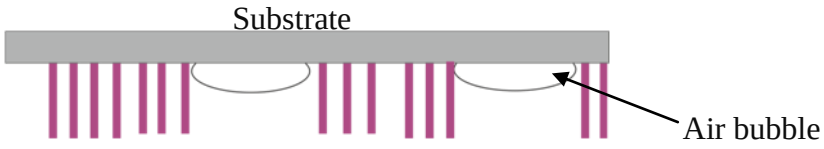

Figure 4-19. Schematics of air bubble formation on the substrate.

In order to find out whether the bubbles in the solution are playing the role of the circle creation, samples grown at different solution temperatures were investigated. The results can be seen in Figure 4-20. A noticeable difference can be seen between the samples grown at different temperatures from the same thickness of the nucleation layer. The circles are more intense at higher temperatures suggesting that the temperature does play a role in this phenomenon.

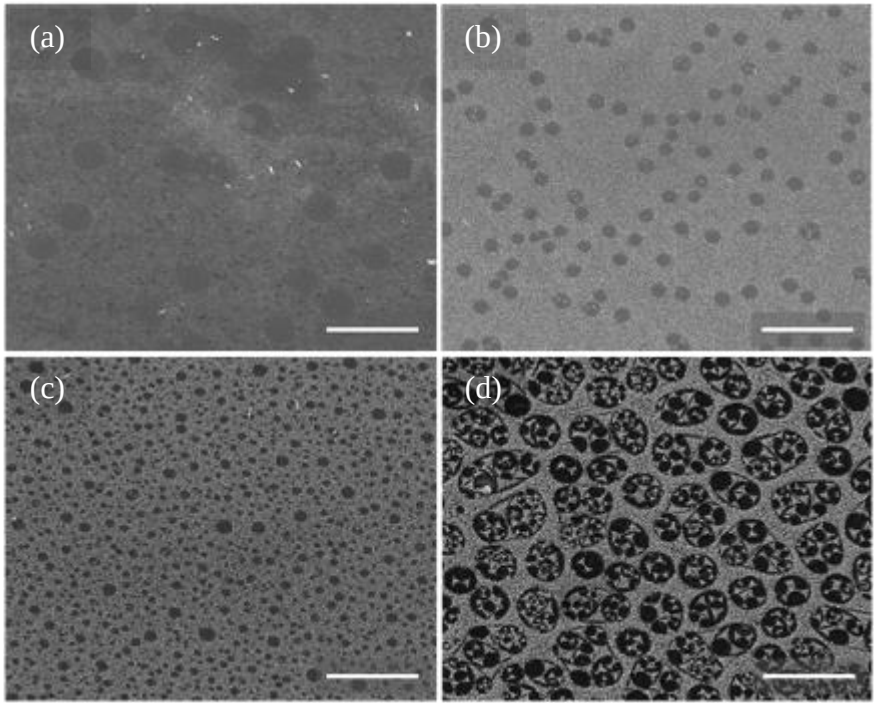

Figure 4-20. ZnO nanowires grown from 75 nm ZnO nucleation layer in various growth solution temperatures; (a) 60 ºC, (b) 70 ºC, (c) 80 ºC and (d) 90 ºC (the scale bars are all 20 µm in size).

In addition, it was discovered that the circle formation was more pronounced at the edges of the samples which could be due to higher likelihood of bubble formation at the rough edges of the samples (Figure 4-21).

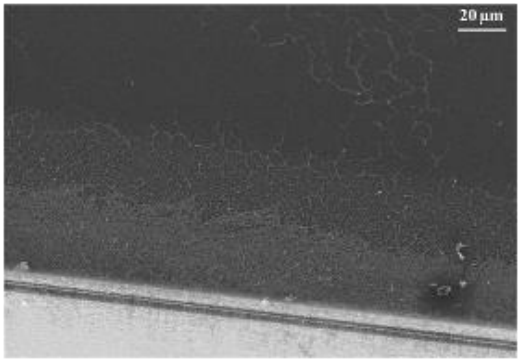

Figure 4-21. SEM image of ZnO nanowires grown from 50 nm nucleation layer at 75 °C solution.

The SEM image of the as-sputtered 75 nm ZnO nucleation layer was also examined to see whether the circular forms are observable on as-sputtered samples (Figure 4-22).

Figure 4-22. SEM image of the as-sputtered 75 nm ZnO nucleation layer.

Figure 4-22 suggests that the nucleation layer has some structure itself that could influence the circle formation if not determine it.

Overall, it was observed that either or both the nucleation layer and the temperature of the solution could play a role in the circle formation.

4.3.4. Hydrothermal growth duration variation

In order to investigate the influence of the growth duration on the nanowire size an experiment has been conducted where two samples with the same nucleation layer thickness (75 nm) were simultaneously immersed in the growth solution at 75 ºC. One of the samples was removed after two hours (Figure 4-23(a)) whereas the second one was left in the solution for four hours (Figure 4-23(b)).

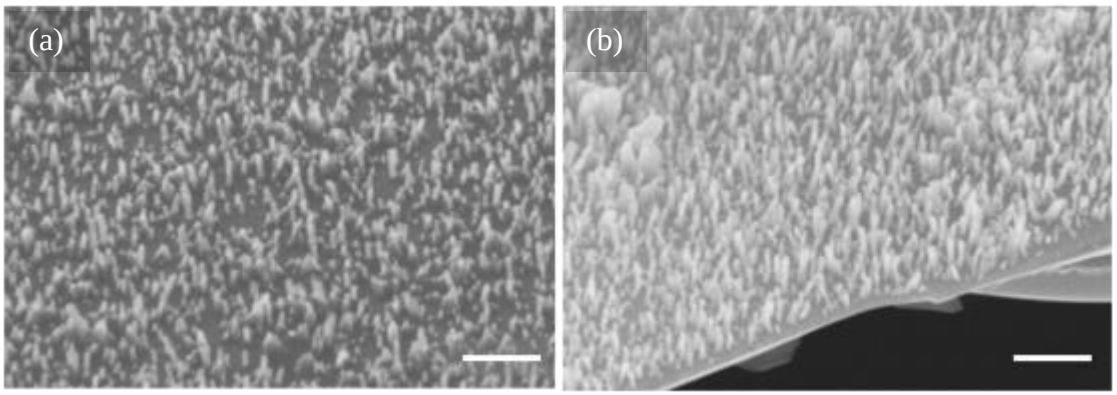

Figure 4-23. SEM images of nanowires grown from 75 nm nucleation layer for (a) 2 hours and (b) 4 hours respectively (the scale bars are 500 nm).

It can be seen from the images that when increasing the duration of the hydrothermal growth step, the length of the nanowires gets more uniform; the shorter nanowires present on the two hour growth sample (Figure 4-23(a)) are missing from the sample of four hour

growth (Figure 4-23(b)). But the side effect of the longer immersion time is that the nanowires get agglomerated into wider structures (Figure 4-23 (b)).

4.3.5. Homogeneous microwire growth investigation

After the hydrothermal growth step, the back side of the samples and the bottom of the vessel were always covered with white powder, some of which was also apparent on the sample surface itself. The SEM images of this powder revealed those to be microwires (Figure 4-24).

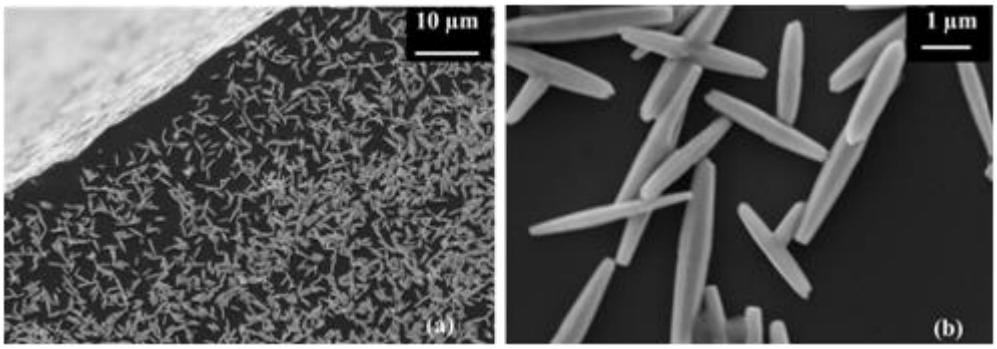

Figure 4-24. Low (a) and high (b) magnification SEM images of microwires formed in the solution (90 °C).

These microwires correspond to the homogeneous crystal growth in the solution as reported by Yang *et al.* [148]. These microwires grow simultaneously with heterogeneous nanowires (from the nucleation layer) therefore there is a competition growth between micro- and nanowires.

4.4. Conclusions

In conclusion, an aqueous solution deposition combined with sputtering technique was used to grow ZnONWs. Well aligned ZnONWs were heterogeneously grown vertically from ZnO nucleation layers. The crystallographic analysis showed that the nanowires are single crystalline and grow along the c-axis. It was discovered that the thickness and the structure of the nucleation layer is a very important factor determining the size of the nanowires. The hydrothermal growth step was shown to have a critical temperature of 60 °C, below which no nanowire growth was observed. A longer duration of the solution step (four hours) resulted in nanowire growth of uniform lengths, but the downside of this was agglomeration of the

nanowires into wider structures. In addition to heterogeneous ZnONW growth, homogeneous ZnO microwires were produced competing with the fabrication of nanowires.

An interesting effect of circle formation was observed on the samples. The investigation of these circles revealed these to consist of larger nanowires on the perimeter compared to those inside the circles. There are a few possible explanations for this phenomenon such as the non-uniformity of the sputtered layer and the air bubble formation in the solution.

Nanowires grown in the temperature range between 70 ºC and 80 ºC from a 75 nm nucleation layer were found to be the most uniform in structure and evenly distributed on the surface, therefore these were chosen to be the conditions for glucose biosensor fabrication based on ZnONWs.

Chapter 5

Zinc oxide nanowire application in electrochemical glucose biosensors

This chapter will give a summary of electrochemical glucose biosensors available in the literature and advantages of using nanomaterials in those. Detailed background information will be presented on ZnO nanostructures applied to glucose biosensor development.

The second part of the chapter looks into incorporating zinc oxide nanowires fabricated via the mechanism presented in Chapter 4 into an electrochemical biosensor and discusses the device performance characteristics. The study is carried out for a glucose biosensor. Glucose oxidase (GOD) enzyme was used as a biorecognition molecule. Cyclic voltammetry and chronoamperometry techniques were applied for testing of the biosensors.

5.1. Introduction

Many sensors that are in use today contain electrochemical transducers due to their advantages, such as low cost, simplicity of construction, portability, ease of use and miniaturisation, compared to optical, calorimetric or piezoelectric sensors [66]. Electrochemical techniques can operate with very low sample quantities and no preparation step. Electrochemical measurements are not affected by the sample components that might otherwise interfere with spectrophotometric detection techniques such as chromophores and fluorophores [167].

When constructing the glucose biosensor a GOD enzyme electrode was fabricated. Enzyme electrodes are defined as having an enzyme layer (selectivity provider) immobilised to the working electrode (WE) surface. The disadvantage of these is the loss of activity of the enzyme with time and the limited number of available enzymes for numerous analytes to be detected [167]. Enzyme electrodes can be divided into three generations. The first generation was oxygen-based, the second was electron-transfer mediator-based, whereas in the third generation enzyme biosensor the enzyme is directly coupled with the electrode. Glucose oxidase immobilised glucose biosensors have been studied since the 1950s. The enzyme is taken from *Aspergillis Niger.* It is inexpensive, stable and very specific to glucose. The active centre of GOD is flavin adenine dinucleotide (FAD), which undergoes reduction to $FADH_2$

while oxidising glucose to gluconolactone (Figure 5-1). Eventually the $FADH_2$ gets oxidised back to its FAD state with its two electrons getting transferred to the electrode either via oxygen (1st generation biosensors), mediator (2nd generation biosensors) or via a direct "wiring" (3rd generation biosensors).

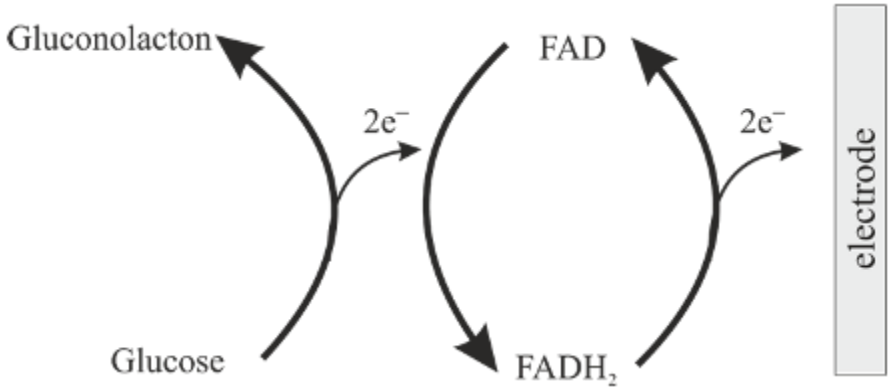

Figure 5-1. The cycle of the FAD during glucose oxidation.

First generation biosensors use natural oxygen as co-substrate. They work on detection of hydrogen peroxide generated from glucose oxidation by the GOD in the presence of oxygen. These are prone to errors due to their reliability on oxygen as the physiological electron acceptor, which is not completely soluble in aqueous solutions, can undergo tension fluctuations and stochiometric limitations [43].

In mediator-based (second generation) biosensors metalorganic mediators are usually used, which are small components that enable the reversible heterogeneous exchange (shuttle) of electrons with the electrode. The mediator can be chosen to have certain oxidation potential, thus suiting the potential range to minimise the interference of the oxidation and reduction from other components in the system [66, 167]. These mediators reduce but do not stop the oxidation of other endogenous electroactive species. The usage of mediators is also avoided for in-vivo applications due to their possible leakage and toxicity. In addition, they show low stability in continuous operations [43]. Even in the second generation biosensor the mediator catalysed oxidation of the enzyme is competing with the oxidation of the reduced GOD by oxygen [43].

As mentioned earlier, the third generation biosensors have the enzyme coupled with the electrode, which can be done by co-immobilisation of the enzyme and the mediator at the electrode surface, immobilisation of the enzyme and mediator in a conductive polymer or wiring of the enzyme to the electrode by immobilising it in a conductive redox polymer [167]. The direct electron transfer between the enzyme and the electrode is time dependent as the redox centre of the enzyme (FAD) is buried deep inside a protein shell, thus slowing

down the produced electron exchange with the electrode. Many reports of the biosensors with direct electron transfer are available in the literature, but there is still the concern whether these reports have enough proof of working on the basis of a direct electron transfer [43].

Nanomaterials have been used to offer an effective electrical wiring of enzymes to the electrode surface [66] due to their size being comparable to that of the redox centres. They act as nano-connectors between the redox centre and the electrode surface. It was shown that the electron transport mechanism in the nanowires depends on its diameter, surface conditions, crystal structure and quality, chemical composition and crystallographic orientation [67]. One of the important factors to consider when immobilising the enzyme to the transducer is to ensure high V_{max} (maximum velocity of the reaction at saturated enzyme conditions) and low K_m (Michaelis-Menten constant is the substrate concentration at which the reaction velocity is half V_{max}) [91]. When V_{max} is high the transducer which is responding to the enzyme catalysed reaction has a broader range where the signal is proportional to the concentration of the analyte. This allows reliable quantitation of the analyte.

Michaelis-Menten constant is calculated from the electrochemical version of Lineweaver-Burk equation [168]:

$$\frac{1}{i} = \left(\frac{K_m^{app}}{i_{max}}\right)\left(\frac{1}{C}\right) + 1/i_{max} \qquad \textbf{Equation 5-1}$$

where i is the steady state current after the addition of the analyte (glucose), i_{max} is the maximum current measured under saturated analyte conditions, C is the analyte concentration in the bulk solution. K_m^{app} value is determined from the slope and the intercepts for the plot of $\frac{1}{i}$ vs. $\frac{1}{C}$. The measured K_m^{app} stands for the system as a whole, not only for GOD. Smaller values of K_m^{app} ensures maximal catalytic efficiency at low analyte concentrations and high affinity of the biosensor towards the analyte. By designing the correct environment around the enzyme, its activity can be enhanced and the biosensor performance improved [167].

In the last two decades, research into detecting glucose with the use of metal oxide nanomaterials has been very active. The benefit of using oxide semiconductors compared to non-oxide semiconductor materials is that due to innate oxygen atoms inbuilt into their surface sites, the formers do not undergo surface passivation caused by insulating native oxide formation [169]. Many nanostructures have been investigated for incorporation into biosensors including multi-walled carbon nanotubes (MWCNT) [170], and nanofibers [171], as well as metal oxides such as TiO_2 nanofilm [172], CuO nanospheres [173], nanostructured

CeO_2 [174], SnO_2 film [175], a range of 1D ZnO nanostructures [113, 176-180], composites of two nanostructured materials such as graphene/Au nanoparticles/chitosan nanocomposites film [181], ZnO nanorods/Au hybrid nanocomposites [182], ZnO nanorods/MWCNT nanocomposites [183-184] and ZnO:Co nanoclusters [185].

Out of these, ZnO nanomaterials are very attractive for biosensor applications due to their biocompatibility, chemical stability, non-toxicity, electrochemical activity and fast electron transfer rate [186]. In addition, ZnO is relatively stable at biological pH-values and has high isoelectric point (IEP) of 9.5. The IEP is the pH at which the material carries no net charge. High IEP of ZnO makes it a good absorbent for low IEP enzymes or proteins at the physiological pH of 7.4, as protein immobilisation is primarily driven by electrostatic interaction. As GOD with IEP of approximately 4.2 [187] is used for the detection of glucose, ZnO nanowires are appropriate immobilisation materials for the biosensor fabricated in this work. In addition, low K_m^{app} values have been obtained for glucose biosensors with GOD immobilised on ZnO nanostructures, whereas higher values of this constant have been observed for native enzyme GOD, Au nanoparticles, nanopore-TiO_2 film electrodes, thus the small value for ZnO nanostructures makes them promising materials for retaining GOD activity when immobilised onto these structures [180].

Determination of glucose via GOD modified electrode can take place via two ways: direct and indirect detection. During the direct detection of glucose, the electrons get directly transferred from the $FADH_2$ of GOD to the electrode via the "wires", this usually takes place in anaerobic solutions (deaerated with nitrogen), where there is no oxygen present. The reaction can be seen in Equation 5-2 [170]:

$$\mathrm{GOD(FAD)} + \text{ glucose} \rightarrow GOD(FADH_2) + \ gluconolactone$$
$$GOD(FADH_2) \rightarrow \mathrm{GOD(FAD)} + \ 2e^- + 2H^+ \qquad \textbf{Equation 5-2}$$

The indirect sensing of glucose is the actual detection of hydrogen peroxide (H_2O_2) which is generated from oxidation of glucose catalysed by GOD. The reaction takes place via the route presented by Equation 5-3 and Figure 5-2 [188]:

$$\mathrm{GOD(FAD)} + \text{ glucose} \rightarrow GOD(FADH_2) + \ gluconolactone$$
$$GOD(FADH_2) + \ \mathrm{O_2} \rightarrow \mathrm{GOD(FAD)} + \ H_2O_2$$
$$H_2O_2 \rightarrow O_2 + \ 2e^- + 2H^+$$

Equation 5-3

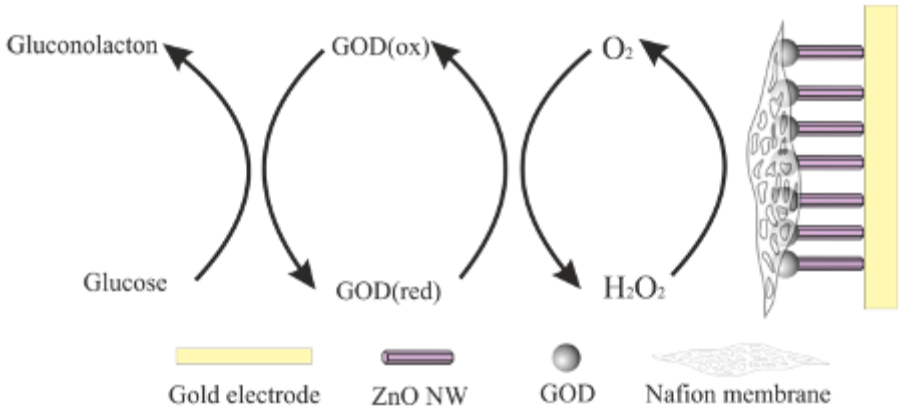

Figure 5-2. The mechanism of glucose sensing via indirect route on ZnO modified electrode [189].

Biosensors with indirect detection operate either by measuring O_2 consumption (reduction at cathode) [177] or monitoring H_2O_2 oxidation at anode at +0.6 V vs Ag/AgCl [190-191]. In case of indirect detection the nanostructures used in the biosensor (see Figure 5-2) play the role of immobilisation platform for GOD, ensure GOD bioactivity and stability [189].

It is difficult to be sure about the detection method. To find out whether it was a direct or indirect detection, hydrogen peroxide is often tested separately at the same voltage range. If the biosensor does not respond to hydrogen peroxide then it could confidently be assumed that the detection method was via the direct route [170].

At potentials used for amperometric measurements of the hydrogen peroxide (0.6 – 0.8 V) some other species that are present in biological fluids are also electroactive, such as ascorbic and uric acids [192]. The contribution of these interactions will lead to non-specific signals affecting the accuracy and selectivity of the biosensor. A useful method to eliminate this effect is to use a permselective coating/membrane that will minimise or prohibit the access of these species to the electrode surface. These coatings, including different polymers and multilayers, also exclude surface-active macromolecules, thus protecting the electrode and confining GOD onto the surface. One of the commonly used materials for this purpose is Nafion [43].

5.1.1. Work done in the field

One-dimensional ZnO nanostructures have been used in electrochemical glucose biosensors for more than 5 years.

Various ZnO nanostructures were fabricated and applied to glucose biosensors by many research groups. The various sensing parameters of those, such as sensitivity, the range of the linear response upon the analyte concentration, limit of detection (LOD) and Michaelis-Menten constant are presented in Table 5-1.

Table 5-1. Various parameters of electrochemical glucose biosensors with various GOD-modified ZnO nanostructures as the working electrode.

Type and Growth Method of the ZnO Nanostructure	Sensitivity ($\mu A/cm^2 \cdot mM$)	Linear range (mM)	K_m^{app} (mM)	LOD (µM)	Ref.
Nanorods grown on standard Au electrode (hydrothermal decomposition)	23.1	0.01-3.45	2.9	10	[113]
Nano-flowers transferred to GCE (glassy carbon electrode) (aqueous solution)	41.13	0.01-5.2	-	3	[189]
Tetragonal pyramid-shaped porous nanostructures transferred to GCE (wet chemical method)	-	0.05-8.2	-	10	[193]
Nanowires grown on Si (vapour-liquid-solid)	-	0.1-10	-	-	[194]
Nanotubes grown on ITO (electrochemical deposition)	30.85	0.01 – 4.2	2.59	10	[178]
Hollow nanospheres transferred to GCE (aqueous solution)	65.82	0.005-13.15	-	1	[189]
Nanonails transferred to Au electrode (thermal evaporation)	24.613	0.1 – 7.1	14.7	5	[195]
Nanocombs transferred to Au electrode (vapour-phase transport)	15.33	0.02 – 4.5	2.19	20	[180]
Porous ZnO grown on Au electrode (electrochemical method)	0.89	18	-	-	[196]

Hierarchical nanodisks transferred to Au electrode (aqueous thermal decomposition)	16.9		2.61	10	[197]
Nanorods transferred to Au electrode (hydrothermal decomposition)	15.46	0.05-5.45	3.097	50	[187]
Nanorods grown on Au electrode (hydrothermal decomposition)	23.43	0.01-5.9	2.749	10	[187]
Nanorods grown on ITO glass (two-step solution approach)	-	0.005-0.3	-	3	[177]

5.2. Experimental procedure

Zinc oxide nanowire based biosensor fabrication consisted of the following steps:

- Glass substrate preparation/cleaning (explained in Appendix A).
- DC sputterer deposition of thin titanium layer for adhesion of gold onto glass.
- Thermal evaporation of conducting gold layer with thickness of approximately 50 nm.
- Annealing of Au/Ti/glass substrate in nitrogen for adhesion of gold to the glass substrate.
- Deposition of zinc oxide nucleation layer via the RF-sputterer.
- Hydrothermal growth of zinc oxide nanowires.
- Adsorption of GOD enzyme onto the electrode surface.
- Immobilisation of the GOD onto electrode surface by Nafion membrane.

The aforementioned steps can be seen in Figure 5-3.

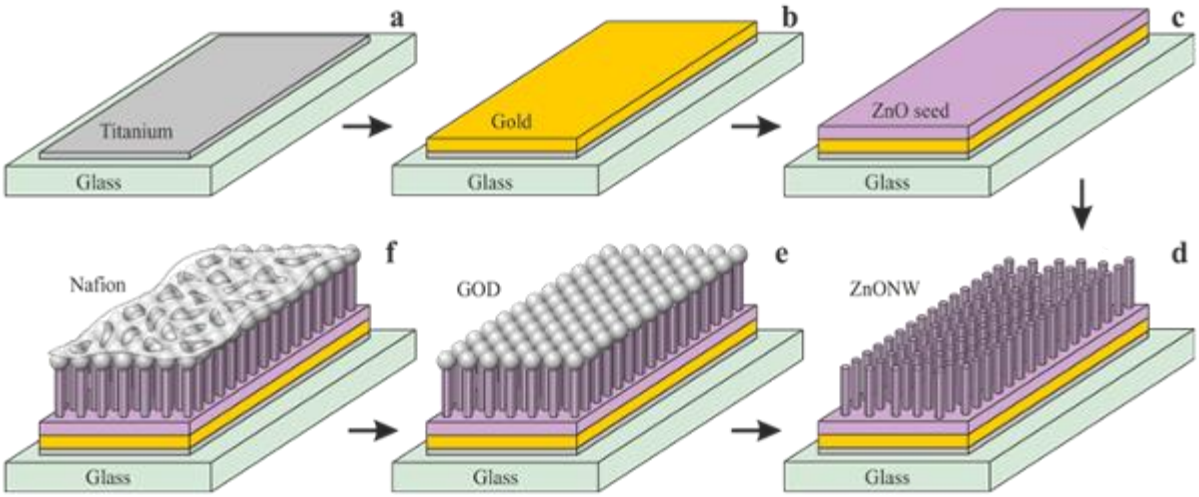

Figure 5-3. Fabrication steps of ZnO nanowire based biosensors. (a) Ti adhesive layer deposition, (b) Au conductive layer deposition, (c) ZnO nucleation layer deposition, (d) growth of ZnONWs, (e) adsorption of GOD, and (f) immobilisation of GOD by Nafion membrane.

The testing of the biosensor was performed in the electrochemical cell, the image of which can be seen in Figure 5-4.

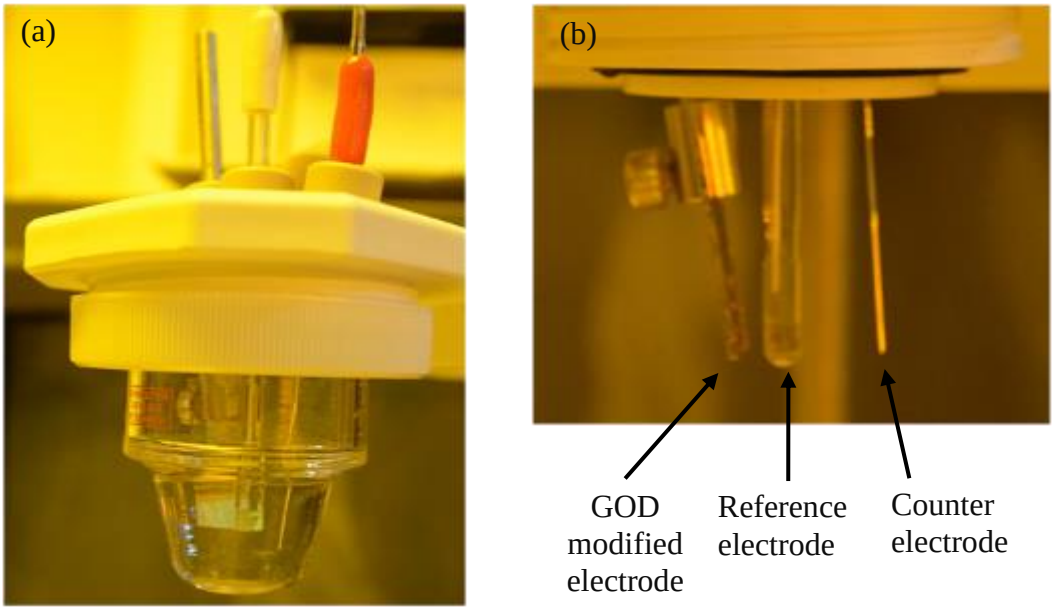

Figure 5-4. (a) The electrochemical cell used for the biosensor experimentation and (b) the arrangement of the electrodes in the cell.

The main technique used for testing the glucose biosensors was cyclic voltammetry and the second technique was chronoamperometry as will be discussed further in the chapter.

5.2.1. Titanium thickness optimisation

Glucose biosensors fabricated in this study were initially fabricated without a titanium adhesion layer; gold was being evaporated directly onto glass. It was discovered that when immersed in a buffer solution and especially when the working potential was applied, the gold along with the subsequent biosensor layers was delaminating of the substrate.

To avoid this problem, titanium is used both in industry and academia as an adhesive between gold and glass [198-201], it has also been used in ZnO nanostructure-based biosensors [196], thus a thin Ti layer was deposited prior to gold evaporation.

Experiments were conducted to find the optimum conditions for Ti layer deposition. Different thicknesses of Ti layers were sputtered by varying the duration and the RF power. The results of the parameter variation can be seen in Figure 5-5.

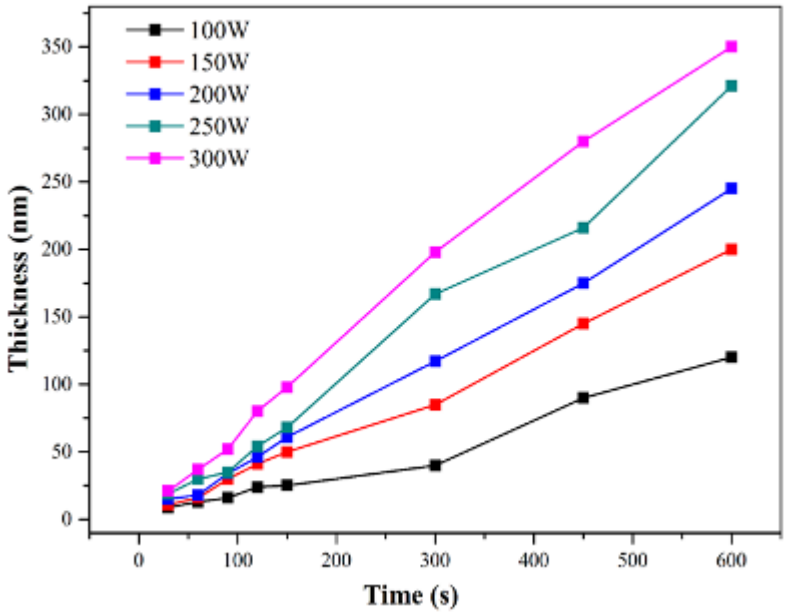

Figure 5-5. Titanium thickness dependence on the deposition duration and RF power.

It was also discovered that the roughness of the layers increased with its thickness, reaching up to 40 nm difference between the higher and lower points for layers above 200 nm. Therefore, these thicknesses would not be of use with gold layers of 50 nm. Adhesive layers of 10-15 nm thick Ti were employed in this work for the biosensor fabrication.

After these measurements, the samples were tested in PBS with evaporated Au layer of approximately 50 nm on top of Ti. In contrast with the previous experiments with no adhesion layer, where gold delaminated within ten minutes of submersion, the samples with titanium adhesion layer between the glass substrate and gold did not delaminate during investigations lasting up to five hours. The next set of experiments was designed to

investigate the stability of the bi-layer during cyclic voltammetry measurements. While the gold without titanium layer had been delaminating from the substrate after the first cycle from -1 to 1 V, samples with titanium layers remained stable until the 8^{th} or 9^{th} cycle. However, if the voltage was alternated between -2 to 2V, then the delamination was occurring at considerably earlier cycles, such as 3^{rd} or 4^{th}. To overcome this problem, the Au/Ti/glass samples were annealed at various temperatures as will be explained further in the section.

Taking these results into consideration, fabrication of biosensors was therefore conducted with a titanium adhesion layer between gold and glass.

In addition, different thicknesses of titanium layers showed the same adhesive characteristic and 10 nm thick Ti layers were chosen to be used throughout this project as the only role this layer is playing is of an adhesive. The sputtered Ti layer width on the glass substrate was 8 mm.

5.2.2. Gold layer evaporation

A gold (99.99 % pure) conductive layer was deposited on the Ti adhesion layer via thermal evaporation. There is no quartz microbalance crystal in the gold evaporator for measuring the thickness of the layer, therefore the thickness of the layer was measured in advance for few test samples via Profilometry. The length of the evaporating gold wire was therefore determined and fixed to 40 mm for deposition of approximately 50 nm thick layers. This value therefore is an approximation, but should not affect the performance of the biosensor as the role of the gold is to create a conductive surface for electron transfer. The width of the gold layer on glass was kept at 10 mm to fully cover the Ti layer. It was discovered that the edges of the gold layer, where there was no Ti beneath, were still delaminating during the experiments.

5.2.3. Annealing of Au/Ti/glass samples

The Au/Ti/glass samples were annealed for 40 minutes using both an oven in atmospheric conditions at 270 °C and a furnace under a nitrogen atmosphere at 350 °C and 450 °C. Cyclic voltammetry experiments were then performed on these samples. The two samples from (a) the oven and (b) furnace at 350 °C showed no change in the peeling characteristics, while the 450 °C annealed samples of Au/Ti double-layer did not delaminate even when the CV

potential range was varied between -5 and 5V and being cycled through the whole day (though the parts of the samples with no Ti layer under Au still peeled off). Therefore, the annealing of the Au/Ti bi-layer was performed for all the biosensors at 450 °C for 40 minutes.

5.2.4. Zinc oxide nanowire growth

Zinc oxide nanowire growth conditions were chosen to be 75 nm nucleation layer deposition with the consecutive two hour growth of ZnONWs at 75 °C as described in Chapter 4.

5.2.5. Adsorption of glucose oxidase

Enzyme loading is shown to influence the performance of the biosensor, thus studies have been done to choose the best GOD concentration to be used for glucose biosensors [202]. The amount of GOD used in this work is adopted from the work of Sun *et al.* [197].

Glucose oxidase was used as a biorecognition molecule for glucose detection. The GOD solution was prepared by mixing 5 mg GOD in 1mL 0.01M PBS (pH 7.4). The solution was ultrasonicated for 15 minutes to ensure that the enzyme is fully dissolved and then was drop-cast onto the surface of ZnONWs by a pipette, left for PBS to evaporate and then kept in the refrigerator in dry conditions at 4 ºC until usage.

5.2.6. Nafion membrane deposition

A Nafion membrane was not being used in the preliminary experiments, but GOD leakage from the electrode surface and accumulation at the bottom of the electrochemical cell in a form of a yellow residue was noticed. Thus, a Nafion membrane was introduced as an additional layer for GOD immobilisation.

Nafion solution was prepared by mixing 1 mL Nafion solution (5 wt. % in mixture of lower aliphatic alcohols and water) purchased from Sigma Aldrich with 9 mL ethanol. A small amount of this material was drop- cast on top of the GOD layer making sure it covered the whole GOD- modified surface.

The radius of the Nafion/GOD/ZnONW/Au electrode surface was approximately 0.4 cm, therefore the surface area was approximately 0.5 cm^2.

5.3. Results and discussions

Cyclic voltammograms of Nafion/GOD/ZnONW/Ti/Au biosensors constructed by the structure described in the experimental section (Figure 5-3) can be seen in Figure 5-6. The experiments were conducted in 0.01 M PBS (pH 7.4) without glucose (black curve), with 1 mM glucose (green curve) and with 3 mM glucose (red curve) correspondingly. Compared to the background curve of the electrode with no analyte, a dramatic change in the voltammogram is evident with the addition of glucose. The increase in anodic (oxidation) current demonstrates that ZnONWs are good wires for glucose biosensor fabrication [202].

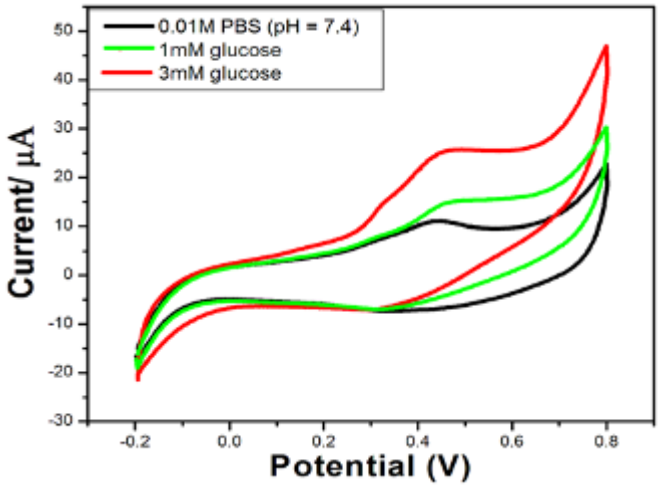

Figure 5-6. Cyclic voltammograms of Nafion/GOD/ZnONW/Ti/Au electrode in PBS without glucose (black), with 1 mM glucose (green) and 3 mM glucose (red), at a scan rate of 20 mV/s.

The obvious increase in current observed starting from 0.3V is caused by glucose oxidation under GOD electrocatalysis.

The GOD- modified electrodes were tested for catalytic current response to different concentrations of glucose. From cyclic voltammograms of successive addition of 2 mM glucose illustrated in Figure 5-7 it is noticeable that the oxidation current increases linearly with glucose concentration and reaches saturation at higher concentrations of above 10 mM. This suggests that the active sites of GOD get saturated by the analyte at these concentrations [195].

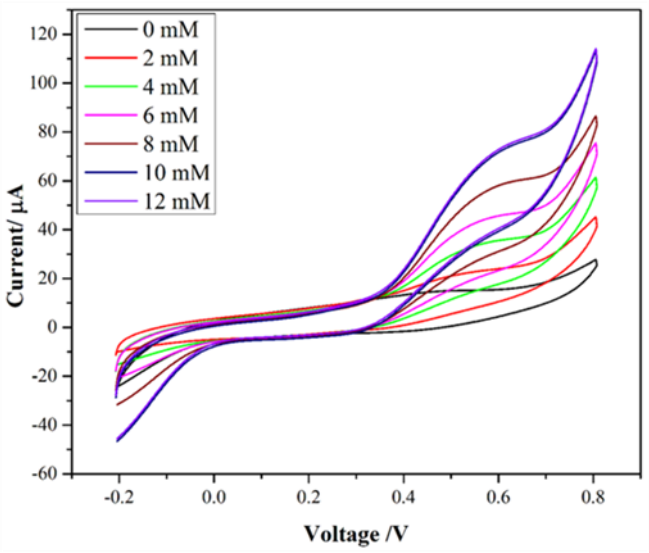

Figure 5-7. Cyclic voltammograms of Nafion/GOD/ZnONW/Ti/Au electrode at a scan rate of 50 mV/s in the presence of various concentrations of glucose.

The plot of peak current dependence on glucose concentration is represented in Figure 5-8. The linear part of the biosensor is observed to be between 2 mM and 10 mM.

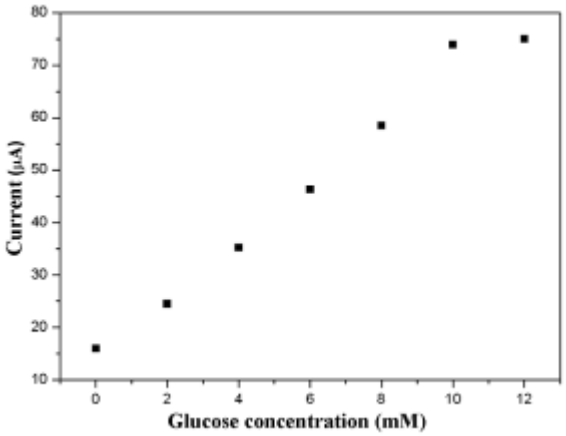

Figure 5-8. Catalytic current response to successive addition of glucose.

In order to evaluate the biological activity (enzymatic affinity) of the immobilised GOD, Michaelis-Menten constant is estimated using Lineweaver-Burk equation. The apparent Michaelis-Menten constant (K_m^{app}) is determined from the *x*-intercept of the Lineweaver-Burk plot of the reciprocals of steady-state current ($1/i$) vs. glucose concentration ($1/C$) and was found to be 6.8 mM (Figure 5-9).

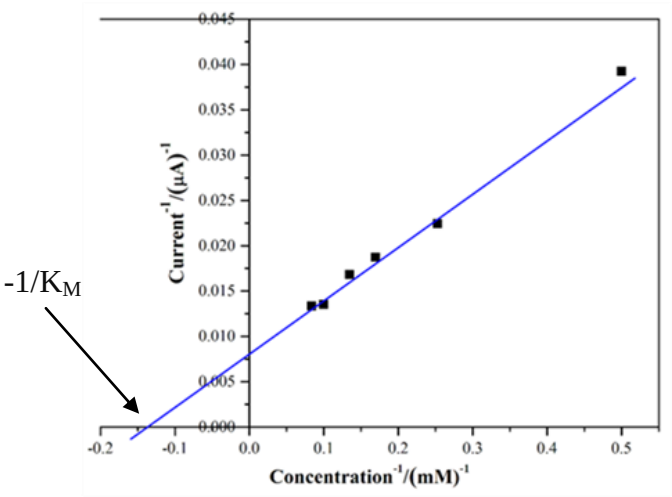

Figure 5-9. Lineweaver-Burk plot for Nafion/GOD/ZnONW/Ti/Au electrode.

The small value for K_m^{app} obtained in this study means that the immobilised GOD possesses high enzymatic activity and high affinity for glucose [180, 203].

This is a smaller value compared to some values available in the literature, such as 27 mM for native GOD in solution and 14.7 mM calculated for ZnO nanonails based biosensors by Umar *et al.*[195]. But at the same time it is higher than other ZnO nanostructure-based glucose biosensors available in the literature (See Table 5-1). Possible explanation of this could be attributed to high GOD loading and electrocatalytic activity for H_2O_2 as explained by Umar *et al.* [195].

The sensitivity (slope in Figure 5-10) of the biosensor is calculated to be 12.2 μA/cm^2·mM with the correlation coefficient of the line R^2 = 0.99. This sensitivity is close to but not as high as the sensitivity of other ZnO nanostructure based biosensors reported (see Table 5-1). A few factors could be responsible for the aforementioned sensitivity and its increase. It might be possible to increase the sensitivity of the biosensor with increase of the active surface area for GOD immobilisation, as this way there will be more GOD involved for simultaneous oxidation of glucose, therefore higher current associated with increase of glucose concentration. Alternatively, the sensitivity might be associated with the amount of oxygen available in the solution for hydrogen peroxide formation (if the reaction takes place via the indirect route). In case of low oxygen concentrations it could be a limiting step in the sensor performance. Stirring of the solution would also play a major role for increasing the sensitivity (due to the increased mass transfer). It is also possible that Nafion membrane thickness was too high slowing down the diffusion of glucose to GOD.

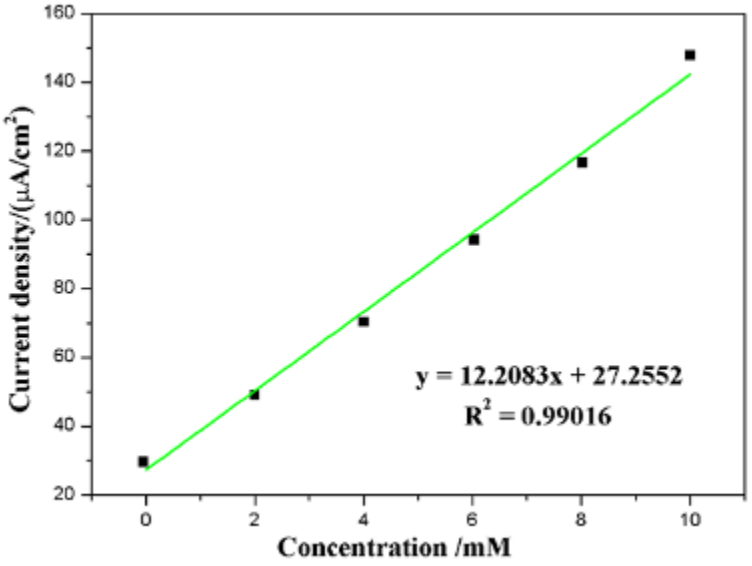

Figure 5-10. Biosensor current density response dependence on the glucose concentration. The formula represents the linear best fit line.

In order to check whether the glucose biosensor sensitivity is due to ZnONWs, Nafion/GOD/Ti/Au electrode has been tested for glucose detection. In Figure 5-11 the black curve represents the electrode in 0.01 M PBS without glucose and the red curve represents the electrode in presence of 3 mM glucose. The glucose oxidation is catalysed by GOD immobilised directly on Au without intermediate ZnONW structures.

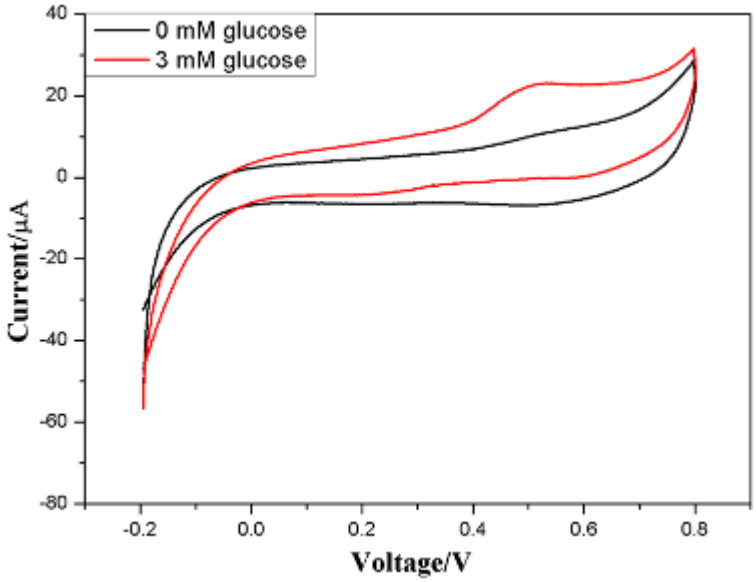

Figure 5-11. Cyclic voltammogram of Nafion/GOD/Ti/Au electrode in 0.01 M PBS (black curve) and in presence of 3 mM glucose (red curve) at 50 mV/s scan rate.

It can be seen from Figure 5-11 that the simple Nafion/GOD/Ti/Au electrode also can be used as glucose biosensor, but the catalytic current (I_p(with glucose) - I_p(without glucose)) is only 12 μA for 3 mM glucose, which is less than the 15 μA catalytic current that was measured for Nafion/GOD/ZnONW/Au electrode with only 2 mM glucose. This shows that the nanowires play a major role in increasing the sensitivity of the device, most probably due to the provision of an increased surface area and improved catalytic activity of GOD when attached to ZnONWs (see the values of K_M in Table 5-1). Considering the surface area increase with incorporation of nanowires into biosensors, the anodic current of the nanowire based electrode is expected to be larger than measured in this study if we consider that all the surface of the electrode is active for glucose oxidation. The lower peak current is explained by the diffusion layer: at the start of the cycle the diffusion layer surrounding the nanowires is very thin allowing the whole surface of the electrode to be active (Figure 5-12(a)), but with time this individual nanowire diffusion layer thickness increases and eventually starts to overlap creating a surface area similar to that of a planar electrode (Figure 5-12(b)) [204].

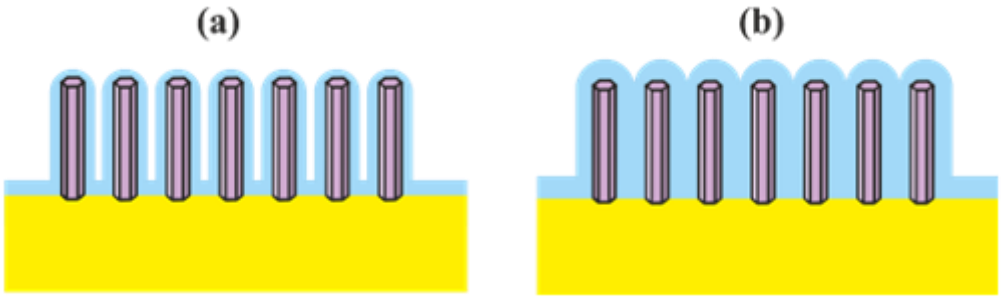

Figure 5-12. Schematic representation of diffusion layer formation on nanowire based biosensors: (a) thin diffusion layer enveloping individual nanowire and the substrate, (b) overlapping diffusion layer [204].

Glucose is an electrochemically inactive organic compound at the potential range chosen, therefore the oxidation does not take place by its oxidation at the Pt electrode surface [188] hence GOD enzyme is used to catalyse the oxidation.

As described earlier, glucose detection by most enzyme electrodes takes place via an indirect route by detecting the generated hydrogen peroxide. For that reason H_2O_2 was tested by the nanowire-based biosensor. The cyclic voltammograms of the electrode in the absence and presence of 0.2 mL H_2O_2 are shown in Figure 5-13. It can be seen that the biosensor is highly sensitive to hydrogen peroxide in the potential range chosen for glucose detection. Considering that observation and that the solution was not deoxygenated prior and/or during

the glucose sensing process, glucose detection current is expected to correspond mainly, if not only, to hydrogen peroxide oxidation that has been produced from the enzymatic reaction.

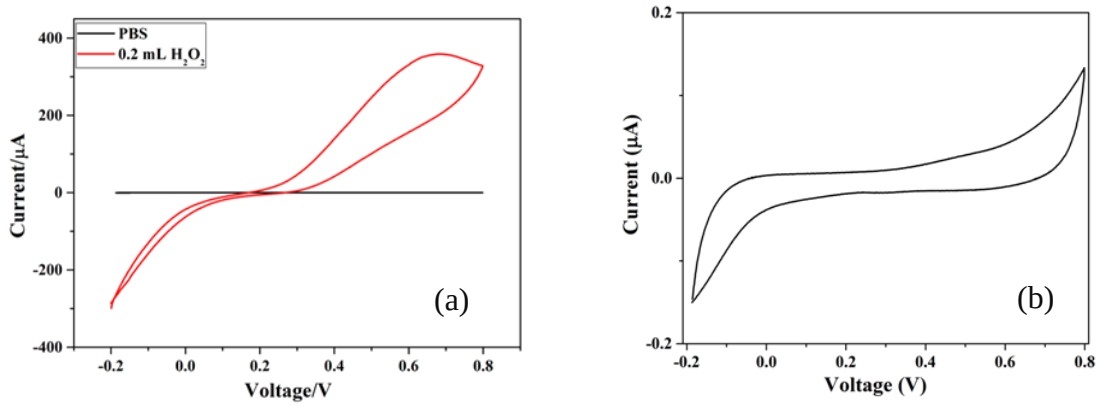

Figure 5-13. (a) Cyclic voltammograms of Nafion/GOD/ZnONW/Ti/Au electrode in 0.01 M PBS (black curve) and in presence of approximately 0.2 mL H_2O_2. (b) Magnified version of the electrode response in the absence of H_2O_2 .

In order to investigate which factors are playing the role of limiting steps, cyclic voltammogram of the Nafion/GOD/ZnONW/Ti/Au with 3 mM glucose was recorded at various scan rates (Figure 5-14(a)). It can be seen that peak currents of the redox reactions are increasing with the increase of scan rate whereas the corresponding redox potentials are not shifting (Figure 5-14(a)). It addition, it can be seen in Figure 5-14(b) that the dependence of cathodic (reduction) (red dots) and anodic (black squares) peak currents increases linearly with the square root of scan rate (ranging from 20 mV/s to 100 mV/s). These indicate that the redox reaction is diffusion controlled.

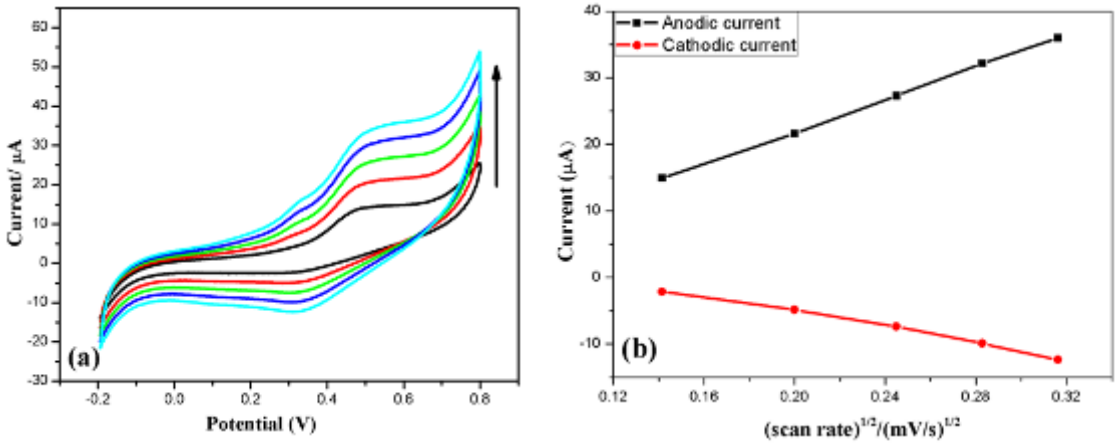

Figure 5-14. Cyclic voltammograms of Nafion/GOD/ZnONW/Ti/Au electrode with 3 mM glucose at scan rates of 20, 40, 60, 80 and 100 mV/s (a), anodic and cathodic currents versus square root of scan rate (b).

Figure 5-15 shows a typical amperometric response of Nafion/GOD/ZnONW/Ti/Au enzyme electrode on successive additions of 0.5 mM of glucose at + 0.65V under unstirred conditions.

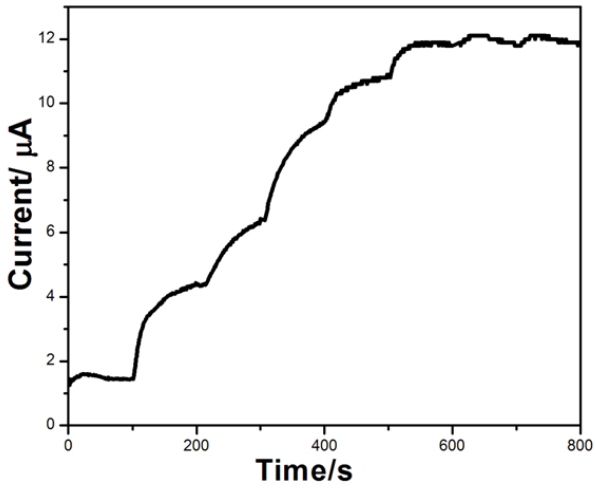

Figure 5-15. The amperometric response for the Nafion/GOD/ZnONW/Ti/Au electrode to successive additions of 0.5 mM glucose at +0.65V (under unstirred conditions).

Typical catalytic current response to successive additions of glucose is obvious from the graph. It can be seen that the amperometric response of the catalytic current is non-linear with increase of analyte concentration under the chosen experimental conditions. The reason could be explained by two factors: (i) lack of stirring and (ii) low voltage choice. The first factor will influence the diffusion layer build-up. As in the case of chronoamperometric measurement there is no reverse scan to change the direction of the gradient and reduce the diffusion layer thickness, thus, in the absence of a stirrer, the product (gluconolactone) stays at the electrode surface, inhibiting the penetration of the substrate (glucose) to the electrode. Therefore, lack of stirring affects both the response time and the saturation level. Unfortunately, the addition of a magnetic stirrer in the cell was tested but increased the noise level so that the response of the biosensor to the glucose concentrations became distorted. The second factor (low voltage choice) could have resulted in longer time requirement for reaching the steady state current, therefore giving a smoothed staircase behaviour (long response time) rather than showing a sharp response to each addition of glucose.

5.4. Conclusions

Zinc oxide nanowire based electrochemical glucose biosensors were fabricated. The Nafion/GOD/ZnONW/Ti/Au biosensor performance was tested via cyclic voltammetry and

chronoamperometry. The experimental results showed that the cathodic and anodic peak currents are proportional to the square root of scan rate indicating a diffusion controlled process. In addition, reference samples with the same structure but without ZnONWs were tested and it was discovered that ZnONWs enhance the sensitivity of the biosensor. The biosensors showed high sensitivity towards hydrogen peroxide in the same potential range as for glucose oxidation indicating that the glucose sensing takes place partly, if not completely via an indirect route of detecting hydrogen peroxide (produced via GOD catalysed oxidation of glucose). The linear range of the biosensor was found to be 2 – 10 mM and the sensitivity was 12.2 $\mu A/cm^2 \cdot mM$. The Michaelis-Menten constant was calculated to be 6.8 mM indicating good affinity of the biosensor towards glucose and high enzymatic activity.

Chapter 6

Silicon nanowire growth via the vapour-liquid-solid method

This chapter will give an overview of the one-dimensional silicon nanostructures that have revolutionised many fields of science and technology since their discovery.

Basic properties of silicon nanowires, such as optical and electronic will be specified. A comprehensive review of various growth methods for one-dimensional nanostructures of silicon will then be discussed.

This chapter then focuses on providing scientific experimental data conducted in this work regarding the low temperature growth of silicon nanowires from gallium catalyst layers and the effect of various growth parameters on the nanowires structures.

6.1. Silicon nanowires

Silicon as an element was first identified in 1823 [205], but only had a few uses until the discovery of its possible application as a transistor via impurity doping in 1947. This discovery shaped the fields of electronics, mechatronics and modern computer science. It created the "Information age" by revolutionising aspects such as information storage and access, imaging, sensing and actuation. It was during the late 20^{th} century that it was realised that the behaviour of the materials strongly depends on their scale and this phenomenon is mostly obvious at nanoscale [7].

Silicon nanowires (SiNW) are one of the most important 1D semiconductor materials due to their structural, mechanical, electronic, optical and thermoelectric properties. In addition, they are of great interest due to their possible application in already established industrial processes and Si-based microelectronics [1]. Silicon NWs have been used in nanoscale logic, computational circuits, nanodiodes and random access memory [206]. These nanowires are promising building blocks for field-effect transistors, solar cells, lithium batteries, tissue and cell engineering [3], and chemical sensors [5].

For the application of SiNWs in various devices, including gas and biosensors, effective control over nanowire diameter, position, length, orientation, structure, and surface properties is required. Some of these parameters are possible to control by using a catalyst and a vapour-liquid-solid growth process [207].

6.1.1. Basic properties of silicon nanowires

Due to the large surface to volume ratio of nanowires, surface characteristics, such as bonding, composition and surface defects, are dominant in determining the physical properties of the nanowires, including thermal, electrical and optical properties [208].

Thermal transport in nanowires mainly occurs via phonons. Strong phonon scattering at small diameters reduces heat transport through nanowires, thus increasing the thermoelectric efficiency. This effect makes nanowires good candidates for thermoelectric cooling and electrical current generation applications [209].

Silicon nanowires fabricated by top-down and bottom-up approaches have different electrical properties. Top-down fabrication approach gives nanowires that inherit the properties of the bulk Si wafer used, thus do not require further doping for conductivity alterations. Nanowires grown by the bottom-up approach are mainly intrinsic or insulating, and therefore require doping process to gain conductivity [1]. This is done either (i) during the fabrication process by the introduction of dopant precursors, such as phosphine and diborane for n- and p- type doping correspondingly or (ii) post- growth doping, such as ion implantation. Ion implantation is a difficult process, thus the first method is commonly used.

Much focus in SiNW fabrication has been given to the improvement of carrier mobility as this determines the device performance. As mentioned above, due to high surface to volume ratio, their electrical characteristics are expected to be highly dependent on their surface properties. It was reported that thermal annealing and passivation of surface defects via chemical modification can highly enhance carrier mobility [210].

An interesting and important factor in the optical properties of semiconductors is its bandgap. Even though bulk silicon has an indirect bandgap of approximately 1.17 eV [211], many groups have reported growth of SiNWs with direct bandgap [212-214].

Experimental measurements of optical bandgap of SiNWs are complicated to perform, compared to theoretical calculations, due to the optical influence of the substrate. Jung *et al.* [215] have managed to extract the optical bandgaps of the SiNWs and determine the correlation of the bandgap with the diameter of the nanowires. They have observed increase in the bandgap (blueshift in the bandgap energies) from ~1.24 eV to ~1.4 eV when decreasing the NW diameter from 112 nm to 68 nm.

Silicon nanowires have gained much attention for their application in biosensors due to their fast response, good reversibility, and often due to their oxide coated surface which keeps it hydrogen free and makes functionalisation easier [216].

6.1.2. Silicon nanowire fabrication

Various fabrication methods have been suggested for SiNW growth including bottom-up and top-down approaches. Some commonly accepted fabrication methods include vapour-liquid-solid (VLS) growth, solid-liquid-solid (SLS) growth [217], oxide–assisted growth (OAG), laser ablation, solution-phase synthesis, lithography, chemical etching and molecular beam epitaxy (MBE) [5]. These methods are explained in more details below:

- Vapour-liquid-solid growth

The VLS mechanism for SiNW growth has been the most widely adopted technique and the growth of silicon whiskers (wires) via this mechanism has first been reported in detail by Wagner and Ellis [218]. In this method usually a metal catalyst is involved, thus also being referred to as metal-catalysed VLS (MC-VLS). The principle of this method is the transformation of metal catalyst into a liquid alloy of catalyst and semiconductor compound. It has been suggested in various reports that a liquid particle is a more favourable site for Si deposition due to the higher (unity) sticking coefficient of liquids compared to solids [218-220]. This explanation has recently been referred to as "misunderstanding" by K. W. Kolasinski [221] with the following statement: "For growth of SiNWs from silanes, which have a much higher dissociative sticking coefficient on the particle than on the substrate or sidewalls, the reason for greater rate dissociation is because of the catalytic action of the metal in the particle not the fact that it is liquid. There is no general evidence for the assertion that the sticking coefficient must be larger on the liquid than a metal". K. W. Kolasinski has also mentioned that the sticking coefficient alone cannot be responsible for the formation of nanowires and other factors should be taken into account. One of the suggested factors is the possible lowering of the existing barrier by the catalytic particle. This will help to incorporate new material at the growth interface compared to the nucleation of an island on the substrate or the sidewall.

In the VLS method the catalytic particle/metal should be able to form low-temperature eutectic phase/alloy with silicon. A Si containing gas (precursor gas) is introduced into the system. When the temperature of the metal catalyst reaches the metal/Si eutectic temperature gaseous silicon penetrates into the droplet forming a metal/Si alloy. As long as the substrate temperature is kept at temperatures above the eutectic point, the alloy droplet stays in a liquid form and can be saturated with silicon. During this penetration a quasi-equilibrium concentration is established and under the influence of the concentration gradient, silicon migrates to the liquid-solid interface. When the concentration of Si in the droplet reaches

supersaturation, it starts to precipitate in the form of wires. The nanowire growth continues as long as precursor gas is continuously provided in the system [5, 222].

❖ Vapour-solid-solid growth

This growth method is similar to the VLS growth process. The difference of these is in the phase that the catalyst particle is during the nanowire growth. In the VSS growth, the growth takes place below the metal-silicon eutectic temperature and therefore this alloy is in a solid form (metal silicide). This method of nanowire growth is usually a slower process as the diffusion of the silicon atom into the solid particle would take longer in comparison to the diffusion into the liquid alloy [223-224].

❖ Solid-liquid-solid growth

In the SLS growth of SiNWs no precursor gas is used unlike in the case for VLS process. Here the nanowire material is coming directly from the substrate. Yu *et al.* have reported SLS growth of SiNWs using Ni catalyst [225]. They have shown that the deposited Ni film reacts with the Si substrate at temperatures higher than Ni/Si eutectic temperatures and forms Si_2Ni alloy droplets (liquid form). When the droplet gets supersaturated with Si atoms a second liquid-solid interface forms, resulting in the growth of SiNWs.

❖ Oxide-assisted growth

It has been shown that it is possible to grow SiNWs without metal catalyst. This is done by evaporation of the source materials and its vapour transport. In this case silicon monoxide or a mixture of silicon and silicon dioxide is the silicon source. The temperature gradient along the furnace tube is a crucial parameter for this growth method (1350 – 900 ºC). It was noticed that SiO_2- based target increases the deposition rate compared to pure Si, therefore the process is known as oxide-assisted growth [226-227].

❖ Laser ablation

This is yet another way for synthesis of SiNWs. In this method the target materials which can be either metal + Si, or SiO_2 + Si, is heated in the furnace to a certain temperature and ablated by the laser beam. This can create nanoclusters of catalyst. The size of the formed catalyst will determine the size of the nucleation and hence the diameter of the nanowire. There is an inert gas (He, Ar, Ar +H_2 and N_2) used in order to transport the ablated material to the part of the chamber where cooling takes place and the material is deposited as nanowires. This method is known to yield nanowires with very high growth rate and uniformly curving features, yet the necessity of using high-energy, low-wavelength focused pulsed laser prevents it from being used for wide applications [5, 224].

❖ Solution-based synthesis method

In this growth method the pressurised supercritical organic fluids enriched with liquid silicon precursor and metal catalyst particles are used. At temperatures above the catalyst-silicon eutectic temperature the silicon precursor decomposes and silicon forms an alloy with the catalyst. By the same way as was the case for the VLS growth, this alloy gets supersaturated with silicon and silicon nanowire starts to precipitate from it. This can also take place from a solid catalyst particle. Another method for solution-based growth uses organic solvent at atmospheric pressure (instead of the supercritical liquid) with good nanowire outcome [227].

- Molecular beam epitaxy

In this method a high purity silicon source is heated until its evaporation temperature. The vapour of the silicon is directed towards the substrate where they get absorbed and crystallised. In this method an ultra high vacuum is required to keep the purity of the wires intact. The disadvantage of this method is that the diameter of the wires cannot be reduced under 40 nm [227].

- Lithography

The two top-down methods for silicon nanowire fabrication are lithography (often using electron-beam lithography (EBL)) and chemical etching. Usually these two are used together in sequence. Using these methods it is possible to get horizontal, as well as vertical nanowires [227].

In lithography, in general, a pattern is getting transferred from a mask to wafer. Due to its higher resolution EBL can pattern features in the nanometer scale [228].

- Chemical etching

Chemical etching can be divided into two categories: dry and wet etching. In dry etching the etchant is supplied from a vapour whereas in wet etching, as the name suggests, the process takes place in a solution. In this nanostructure synthesis method a mask is used to stop local etching, therefore etching conditions and the mask define the topography of the obtainable structures. It is also possible to perform a crystal orientation dependent wet etching. A commonly used etching technique is metal assisted chemical etching which is taking place via a wet route and fabricates anisotropic high aspect ratio micro and nanostructured semiconductors without lateral damage [229-230].

It is possible to grow SiNWs with diameters ranging from approximately 5 nm to several hundred and lengths from 100 nm to tens of micrometers by a bottom-up approach. Top-down approach suffers from the difficulty of production of nanowires with less than 10 nm in diameter [1].

In general, during catalytic growth of the nanowires (VLS, VSS and SLS) three periods take place: (I) initiation, (II) steady state and (III) termination [221].

During the initiation period (in case of evaporated catalyst particles) the surface of the catalyst layer has to be cleaned of impurities, including any oxide layer. For the direct physical evaporation of the catalytic particle onto the substrate, the catalyst might form islands in the case when the metal does not wet the substrate (Volmer-Weber growth). Alternatively, when heated, Ostwald ripening will be responsible for island size distribution of the catalyst material. The initial stage also includes the formation of eutectic state with the metal and the growth material (often referred to as incubation period). It is noteworthy that the incorporation of the growth material into the catalytic particle will increase the volume and the diameter of the particle from its original size [221, 223, 231].

The second growth period (steady state) is described by a uniform radius growth of the nanowire where the growth material is transported into the particle/nanowire interface. The uniformity of the nanowire diameter is explained by the fact that the particle has reached a steady state and their diameter is not changing in this regime [221].

The termination stage might cause tapering of the nanowires and/or interruption of the growth. This will occur if no more growth material is supplied, temperature is reduced below the critical value, or the particle has been consumed [221, 232].

The nanowire growth can take place via several routes (Figure 6-1).

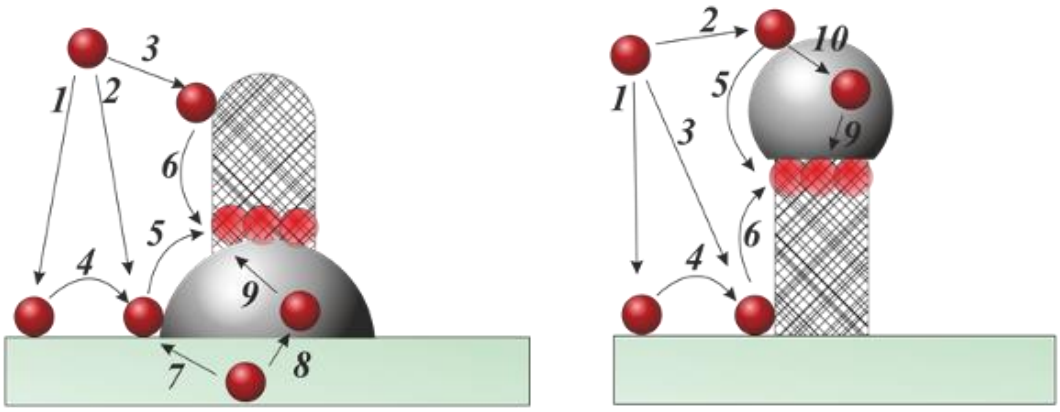

Figure 6-1. Various routes of catalytic growth of nanowires [221].

The following section will discuss the dynamic processes affecting the VLS growth of the nanowire illustrated in Figure 6-1. In the VLS growth mechanism adsorption of the vapour (either molecular or dissociative) may occur on the substrate (1), catalyst particle (2) or nanowire (3). In order for the catalyst particle to play the role of directing material to the growth interface, the sticking coefficient on the catalyst should be higher than anywhere else.

After adsorption these atoms can diffuse along the substrate (4), catalyst particle (5) or nanowire sidewall (6). In order for the growth to take place only in one direction and only on the nanowire/particle interface, the diffusion along the substrate and the sidewall should be suppressed. Otherwise the diameter of the nanowire can grow independently from the axial growth. Other possibilities include diffusion of the growth material into (10) and through the catalyst particle (9), in some cases direct diffusion of mobile substrate atoms into the particle (8) or surface diffusion along the substrate (7) followed by diffusion into particle/nanowire interface.

The four main growth types investigated so far in literature are illustrated in Figure 6-2. It is noticeable that the catalyst particle can stay at the root of the nanowire (catalyst on the bottom (COB) growth) [217, 233] as represented in Figure 6-2(a,c) or sit on the tip (catalyst on the tip (COT) mechanism) [223, 234] as can be seen in Figure 6-2(b,d). In addition, it is possible for one catalyst particle to generate one (singlewire growth in Figure 6-2(a,b)) or more (multiwire growth in Figure 6-2(c,d)) nanowires [217, 223, 233-234].

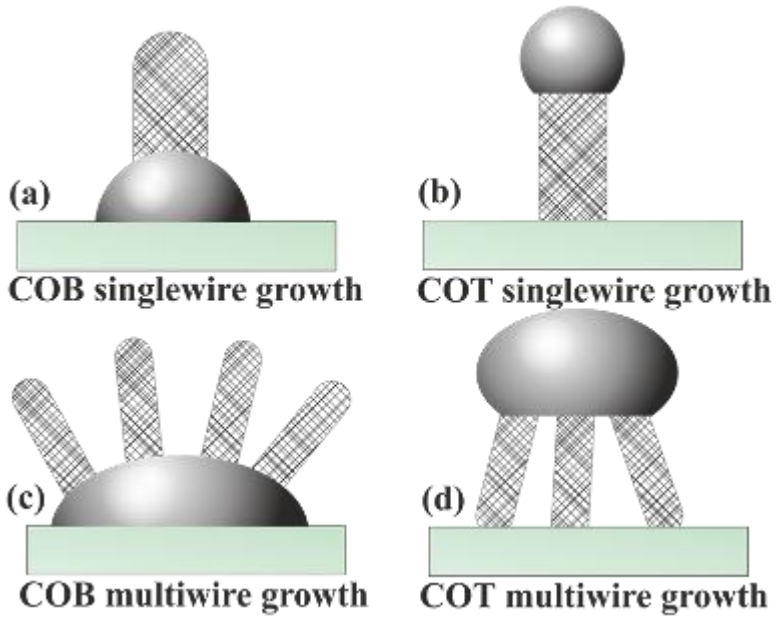

Figure 6-2. Possible catalytic growth mechanisms of nanowires: (a) and (b) correspond to singlewire growth in a COB and COT mechanisms respectively, (c) and (d) correspond to the multiwire growth via COB and COT mechanisms correspondingly.

Both, base [217] and tip growth [207, 235] have been reported for bottom-up nanowire growth. The base or tip growth is determined by the wetting conditions of the substrate and the catalyst. In case of good wetting the interaction between the catalyst and substrate will be strong, thus keeping the particle at the substrate surface facilitating base growth. If the

interaction is not strong (bad wetting) then tip growth is expected [206]. During the SLS growth COB processes have been investigated by H.F. Yan *et al.* [217]. Whereas one of the characteristics of the VLS growth process is the catalyst particle positioning on the tip of the wire [207, 236-237].

Out of various growth methods discussed above, the most popular growth approach is the MC-VLS growth.

6.1.3. Plasma-enhanced CVD growth of SiNWs from various catalysts

Plasma-assisted or plasma-enhanced chemical vapour deposition technique of nanowire growth is a type of an MC-VLS fabrication method. The PECVD technique is quite a popular technique for thin film deposition, but it was not widely used for nanowire growth. First demonstration of SiNW growth via the PECVD method was done by Hofmann *et al.* in 2003 [238] using gold as catalyst.

In general, in a CVD process there should be a precursor gas carrying silicon. Silane (SiH_4), disilane (Si_2H_6), silicon dichloride ($SiH_2{\cdot}Cl_2$) and silicon tetrachloride ($SiCl_4$) have been used as gaseous silicon carriers [224]. Many elements have been used as catalysts for growing SiNWs such as Au [238-240], Pt [241], Ag [242], Pd [243], Cu [244], Ni [206], Al [232], Fe [245], Ga [246], Pb [242], In [247], Zn [248], Co [249], Ti [250], Bi [251] and Sn [252], as well as metal alloys, such as Ga-Au [253] and Pd-Au [254]. In particular, gold has been the most successful and most investigated catalyst for the growth of SiNWs. The reason is its ability to dehydrogenate/dissociate silane. However, Au is an undesired component for Si-based technology as its incorporation into silicon leads to the creation of electronic states that are almost in the middle of the bandgap. This can result in degradation of the carrier mobility and a reduction of minority carrier lifetime [207, 246-247]. Therefore, alternative catalysts or even catalyst-free growth of the nanowires have been investigated. When choosing the metallic catalyst for silicon, the desirable characteristics are the ability to form a low temperature eutectic phase with silicon (eutectic temperatures of various metals with Si are given in Table 6-1), low solubility in Si, high threshold concentration before device performance degradation, or for which the ionisation energies are close to the band edges, which will increase the possible induction of doping of the wires, low vapour pressure, ability to solve silicon at a wide temperature range [255].

Table 6-1. Eutectic temperatures of Si with various metal catalysts.

Alloy	Eutectic temperature (°C)
Au/Si	370 [222]
In/Si	Around 157 [250]
Al/Si	577.8 [1]
Ga/Si	29.8 [207]
Ni/Si	993 [217]
Cu/Si	802 [256]
Sn/Si	232 [252]
Ag/Si	845 [257]

Some of these metals are not able to catalyse silane decomposition like is the case for gold, but when plasma is introduced into the CVD process the dissociation of silane is not required to be done by the metal particles anymore as plasma pre-dissociates silane and thereafter transports those particles to the catalyst/substrate. Plasma is used to lower the growth temperature even below the eutectic temperature (thus increasing the possibility of various cheap substrates to be used, including glass and plastic) and/or widen the possibility of using more catalyst types. It also increases the growth rate of the nanostructures at lower substrate temperatures [223, 227, 258-259]. When plasma is introduced into the CVD method, the silane dissociation which was the rate determining step in the CVD process of nanowire growth is no longer rate determining and therefore the other factors, dissolution of silicon into metal and precipitation of the SiNW, start playing a role, whereas these were considerably fast in comparison to silane dissociation in case for the CVD growth. In addition, plasma can locally heat the metal-Si catalytic particle keeping it in a liquid form even below the eutectic temperature [258]. The disadvantage of using plasma enhanced CVD process is the introduction of uncatalysed Si/amorphous Si (a-Si) (referred to as parasitic deposition [260]) deposition on the substrate, catalyst particles and nanowire sidewalls, therefore a prompt activation of the catalyst particle is necessary before it gets buried under the a-Si layer [223]. Hence, it would be beneficial to use catalyst particles that have low Si solubility and therefore the incubation (initiation) time will be less and will not compete with the a-Si deposition.

6.1.4. Gallium as a catalyst for silicon nanowire growth

Recently gallium has been used as an alternative catalyst for SiNW growth due to its chemically stable characteristics: it has a low eutectic temperature with Si at 29.774 ºC at under 0.01 atom % Si (ensuring quick metal particle supersaturation), solves silicon in a wide temperature range, is not reactive to Si to form silicide and has low vapour pressure [224, 233, 237]. In addition, it acts as a p-dopant in silicon. Thus, its incorporation should increase the carrier density in the nanowire, without highly suppressing mobility or minority carrier lifetime [246].

Due to its low solubility of Si, metal particles would quickly become saturated [247] and the critical nucleus diameter of Si grown from Ga is estimated to be 6 nm at a temperature of 400 ºC (for Si concentrations of 1 atom %), whereas these from noble metals and transition metals (with Si dilution of 20 -30 atom %) are larger than equilibrium sizes of the droplets which are 0.2 μm. The supersaturation of Ga with Si decides the diameter of nanostructures and depends on process variables such as substrate temperature, gas-phase composition and plasma kinetics. Therefore, when using Ga as catalyst, there is no need in creating quantum-sized droplets [233].

Gewalt *et al.* [260] mentioned that unlike Au and Al, Ga does not act as a catalyst in the SiNW growth but as a solvent (Si reservoir). This is due to the fact that it does not chemically assist the dissociation of SiH_4. Therefore, the decomposition must be enhanced via the plasma treatment. It is suggested that when precursor gas is mixed with high concentration of hydrogen gas, atomic hydrogen can mediate the silane or silyl decomposition and silicon dissolution by providing hydrogenated Ga sites on the catalyst for silyl substitution [231] (see Equation 6-1).

$$\mathrm{SiH_x(g)} + \mathrm{xH(g)} \xrightarrow{Ga} Ga - Si(l) + xH_2 \qquad \textbf{Equation 6-1}$$

where (g) and (l) stand for gas and liquid phases correspondingly.

In addition to playing the mediator role for silane decomposition and silicon dissolution in Ga, hydrogen plasma also gets rid of Ga oxide layer from the catalyst surface activating Ga function, cleans the surface and assists in forming islands and promotes etching of Si. Continuous hydrogen flow throughout silicon nanowire growth ensures that the catalyst surface does not reoxidise and continues to grow nanowires [207, 223, 247].

Even though it is mentioned that plasma is required to decompose silane as Ga does not act as catalyst, SiNWs have been grown via a CVD method with no plasma between 400 –

420 ºC [261]. This was done in high hydrogen pressure and was suggested that hydrogen reduced gallium oxide activating the function of Ga. No nanowires were grown under 400 ºC suggesting that Ga required to be at certain temperature to ensure the dissociation of SiH_4.

This chapter is devoted to the low temperature VLS growth of SiNWs via a PECVD technique using Ga as catalyst material.

6.2. Experimental procedure

For the growth and optimisation experiments of SiNWs from Ga catalyst, glass substrates and p-Si substrates with 1 µm oxide layer were used.

The Si/SiO_2 substrates were used without surface pre-treatment or cleaning, whereas glass substrates were cleaned according to the procedure explained in Appendix A.

6.2.1. Evaporation

Various thicknesses of gallium layers were deposited on the substrates (glass and p-Si/SiO_2) via physical evaporation. The thicknesses of gallium layers used were 2 nm, 3 nm, 7.5 nm, 10 nm, 20 nm, 25 nm, 40 nm, 50 nm, 100 nm, 250 nm, and 400 nm.

Firstly, the samples were loaded into the evaporation chamber. The vacuum pressure at which the deposition took place was at $2x10^{-6}$ Pa or lower. The layer thickness was measured by an Edwards FTM7 film thickness monitor. After the Ga deposition the samples were left in the chamber for approximately 30 minutes to cool down before removal and placement in the PECVD chamber.

6.2.2. PECVD growth

Nanowire growth was performed in the PECVD reactor. The samples were placed into the chamber for at least 12 hours prior to the deposition in order to assure high vacuum. The vacuum level at which the deposition was carried out was 3 Pa (23 mTorr).

Firstly, 100 sccm (standard cubic cm per minute) hydrogen was introduced into the chamber at the pressure defined for the certain experiment. When the pressure in the chamber attained the set value, the sample temperature was increased up to the deposition temperature. As soon as the temperature of the substrate reached the deposition temperature, hydrogen plasma was struck for 5 minutes followed by introduction of silane (SiH_4) into the chamber without plasma interruption. After the deposition the process was interrupted by firstly

terminating the plasma. The samples were allowed to cool down to below 80 ºC and then removed from the chamber for characterisation and testing. The deposition temperature, pressure, RF power level and the silane flow rate were the process variables.

6.2.3. Experimental conditions

The growth conditions of 200 mTorr chamber pressure, 25 Watts of RF power, 20 sccm silane flow rate and the temperature of 400 ºC will be referred to as "Standard" condition throughout the chapter. For the investigation of low temperature growth of SiNWs using Ga as a catalyst the process variables were altered from their "Standard" values as presented below:

1) Catalyst material investigation; approximately 30 nm thick Ga, Al, Cu and Au catalyst layers were inserted into the PECVD chamber simultaneously. The growth of the SiNWs was attempted on these samples at "Standard" conditions in order to see the catalyst choice effect on the nanostructure growth.
2) Catalyst (Ga only) layer thickness variation; Ga layers between 2 nm and 400 nm were investigated. All the samples with different Ga thicknesses were loaded together into the PECVD chamber for all the experiments. This arrangement allowed the investigation of the effect of the seeding layer thickness on the nanowire growth when changing the other VLS growth parameters.
3) Growth temperature variation; VLS growth temperature was varied between 100 °C and 400 °C in the increments of 50 ºC. Pressure and power comparison experiments were performed both at 150 ºC and 400 ºC.
4) Plasma RF power variation; the RF power influence on the nanowire growth was investigated at 400 ºC using RF powers of 10 W, 25 W, 50 W and 100 W. In addition, RF power variation was investigated at 150 ºC using power values of 10 W, 25 W and 40 W.
5) Gas pressure variation; the pressure of the PECVD chamber was varied for experiments at 400 ºC between three values; 100 mTorr, 200 mTorr, and 350 mTorr. For the experiments carried out at 150 ºC, the pressure was varied between 100 mTorr, 200 mTorr and 300 mTorr.
6) Silane flow rate variation; this parameter was only investigated for samples grown at 400 ºC, the flow rate values used were 10 sccm, 20 sccm and 40 sccm.

7) Substrate material variation; p-Si/SiO_2 and p-Si/Si_3N_4 were used in order to understand the possible effect of the oxygen in the SiO_2 layer on the nanowire growth.

All the results for these parameter variations are presented and discussed in the following section.

6.3. Results and discussions

Prior to the division of this chapter into sections of various growth parameter investigations, an important observation was made: at the beginning of the SiNW growth experiments only silane gas was used for the nanowire fabrication process and no hydrogen pre-treatment and/or mixture with silane was employed. For those experiments there was either no nanowire growth observed or very sparse growth was achieved. In addition, the repetitions of these experiments with exact same conditions did not show consistency. In the attempt to understand this phenomenon, various types of substrates, including brass, aluminium, ITO, oxide covered silicon and bare silicon substrates coated with various thicknesses of Ga layers were used to attempt the nanostructure growth. Moreover, various growth parameters were tested with no change in the outcome. The results of these experiments are demonstrated via several SEM images in Appendix B.

With the introduction of the hydrogen gas into the process the nanowire growth outcome changed drastically and the results became consistent with subsequent repetitions. This section shows the results of various growth parameter variation experiments and discusses the effect of various parameters on the nanowire growth.

6.3.1. Catalyst material investigation

For the comparison of possible applications of different materials as catalysts for SiNW growth 30 nm thick layers of Al, Au, Cu and Ga were evaporated and nanowire growth attempted at “Standard” conditions (Figure 6-3). The deposition was carried out for 10 minutes and the results can be seen in Figure 6-3.

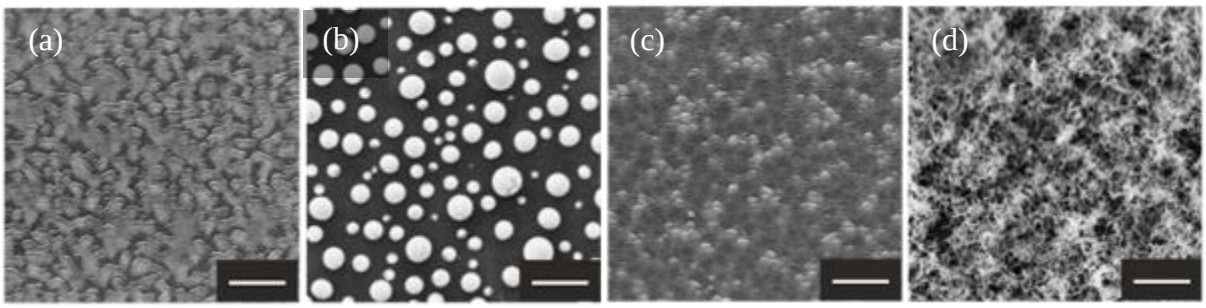

Figure 6-3. SEM images of SiNW growth attempt from 30 nm (a) Al, (b) Au, (c) Cu and (d) Ga catalyst layers. Scale bars are all 2 µm.

It can be seen from Figure 6-3 that no wire growth was achieved for Au, Al and Cu catalysts at 400 °C. This could be explained by the growth temperature used which is very low compared to the eutectic temperatures of these metals with Si (see Table 6-1). It can be seen that Al/Si and Cu/Si eutectic temperatures are above the deposition temperature used in this work, therefore limiting the possibility of the VLS growth and Au/Si eutectic temperature is just below the growth temperature, whereas this for Ga/Si system is very low compared to the temperatures used in this work. Silicon NW growth at temperatures ≤ 400 ºC with Au as catalyst has been reported previously [226, 238, 240, 262-263] but most of these use very thin layers of Au (between 0.2 -5 nm). Silicon NW growth from 100 nm Au, Ag, and Cu catalyst layers has been reported by D. Parlevliet and J. C. L. Cornish in a pulsed PECVD chamber [257] and from 16 nm and 40 nm sized Au colloids by an inductively coupled plasma CVD [259]. But obviously using the growth conditions that initiated nanowire growth from the Ga layer in this work were not optimal for the nanowire growth from the Au, Cu and Ag layers.

6.3.2. Gallium layer thickness/temperature variation

As it was mentioned earlier, a number of samples with various thicknesses of Ga layers were simultaneously loaded in the PECVD reactor for all experiments. Therefore, the dependence of each catalyst layer on various deposition parameters was observed. It was discovered that the influence of each growth parameter on the nanowire fabrication depended on the thickness of the catalyst layer.

Catalyst layers between 2 nm and 400 nm were used for SiNW growth temperature investigation experiments. Influence of the layer thickness on the growth structure was investigated at the temperatures ranging from 100 °C to 400 ºC in 50 ºC intervals. The results revealed that the required temperature for the nanowire growth was considerably lower for thin Ga layers compared to thick layers. In addition, it was discovered that the thinner layers

yielded individual nanowires whereas the thicker layers resulted in branched nanostructures with thicker cores as will be demonstrated below.

The growth parameters used were those of "Standard" condition with 10 minute growth duration. The nanowires resulting from 400 nm Ga layer can be seen in Figure 6-4.

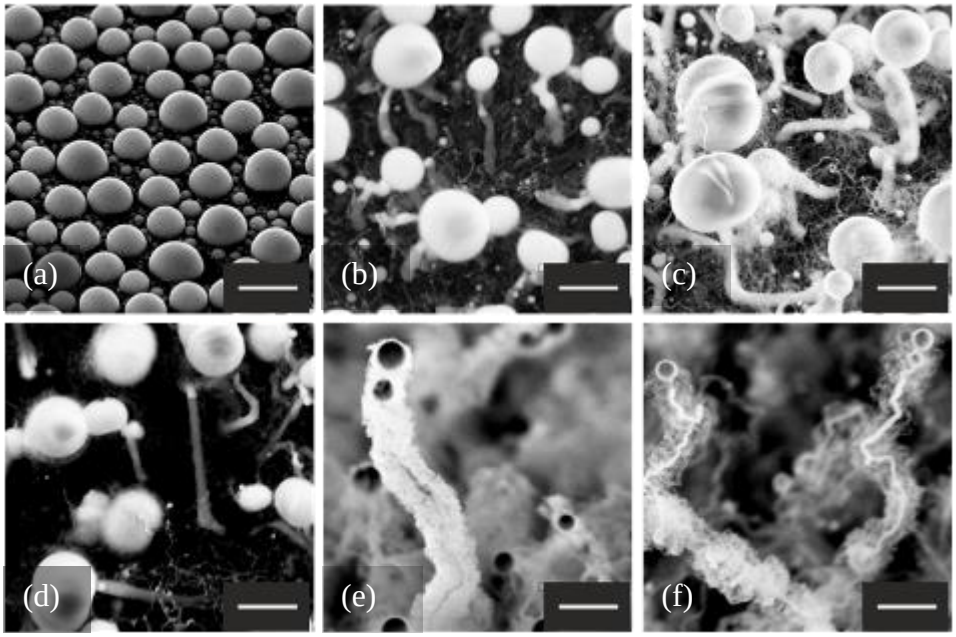

Figure 6-4. SEM images of SiNWs grown for 10 mins from 400 nm Ga catalyst at (a) 150 ºC, (b) 200 ºC, (c) 250 ºC, (d) 300 ºC, (e) 350 ºC and (f) 400 ºC (scale bars are all 2 µm).

It can be seen from the images that SiNW growth critical temperature for 400 nm Ga seed layer is above 150 ºC for this set of experiments with the other parameters set to the values discussed earlier. It is also noticeable that at lower temperatures there is no branched wire growth. In addition, it can be confidently stated that the growth type is catalyst on the top growth as the gallium droplets are easily seen on the top of the wires indicating a VLS growth. Moreover, on the wires grown at 350 °C (Figure 6-4(e)) two or more droplets can be seen on each wire. This is due to Ga being in a molten form and parts of the catalyst particles being left behind and/or wetting the surface of the nanowire. These in their turn act as nanowire growth initiation points (catalysts) resulting in branched nanowire growth that can be seen in Figure 6-4 (e,f). The suggestion of the Ga droplet wetting the surface of the nanowire could be verified by doing a very long deposition. In this case if the wetting theory is correct, the droplet would slowly get smaller and eventually vanish from the tip of the main nanostructure.

The temperature variation investigations for 40 nm Ga layer can be seen in Figure 6-5. As these samples were simultaneously deposited with 400 nm Ga samples, the rest of the growth

parameters were the same as in the case shown for 400 nm Ga layers. The same applies to the samples with 7.5 nm and 2 nm Ga layers.

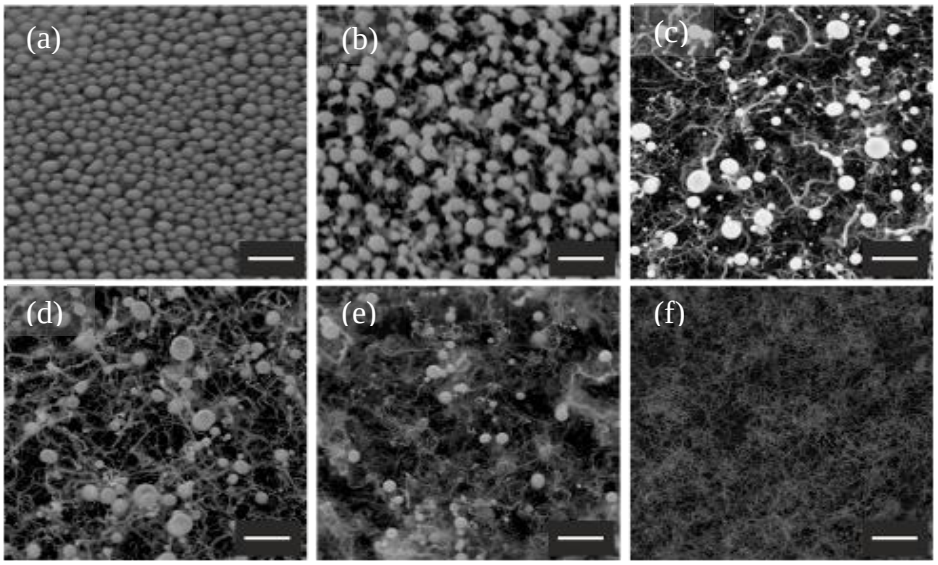

Figure 6-5. SEM images of SiNWs grown for 10 mins from 40 nm Ga catalyst at (a) 100 ºC, (b) 150 ºC, (c) 200 ºC, (d) 300 ºC, (e) 350 ºC and (f) 400 ºC (scale bars are all 2 µm).

It can be seen from Figure 6-5 (b) that for 40 nm Ga layer the SiNW growth process starts at 150 °C (or below) compared to 200 °C in case of 400 nm Ga. In addition, it is obvious that less branched nanostructures get formed from 40 nm layer. Moreover, the nanowire growth at 400 ºC shows no noticeable catalyst particle remaining at the top of the nanowires. We suggest that the reason behind the particle disappearance is the consumption of the particles at high temperatures. This is also noticeable in Figure 6-5 where the average size of the particles is reduced when increasing the temperature from 300 ºC (d) to 350 ºC (e).

A more vivid example of the low temperature growth of SiNWs is seen for Ga layers of 7.5 nm (Figure 6-6) thickness.

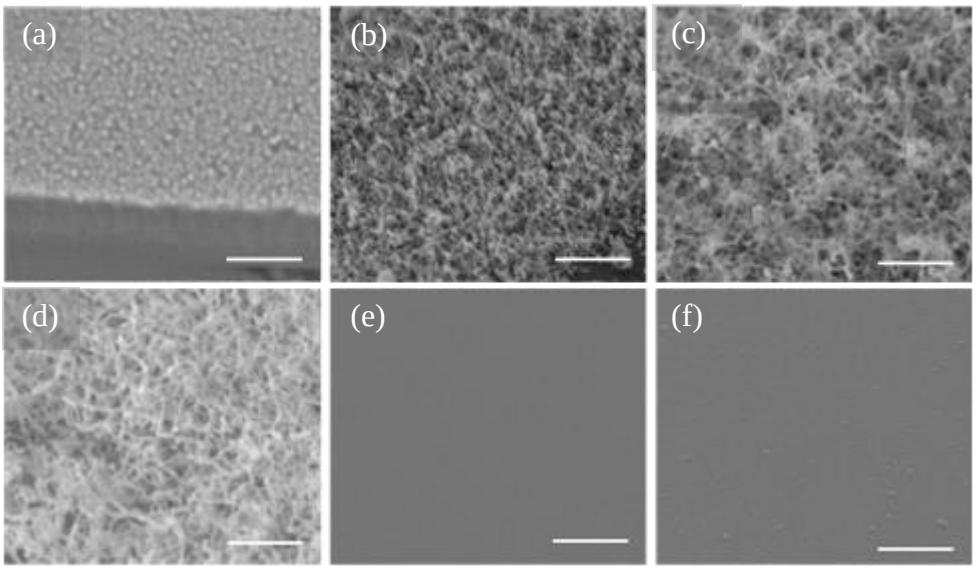

Figure 6-6. SEM images of SiNWs grown for 10 mins from 7.5 nm Ga catalyst at (a) 100 ºC, (b) 150 ºC, (c) 200 ºC , (d) 250 ºC, (e) 350 ºC, and (f) 400 ºC. Scale bars are all 1 µm.

It was observed that nanowire growth from 7.5 nm Ga catalyst layer is initiated at temperatures above 100 ºC and below 350 ºC. It can also be seen that the nanowires grown at higher temperatures (200 ºC and 250 ºC) are longer in comparison to the nanowires grown at 150 ºC. This result could be due to the acceleration of the silicon adsorption on the catalyst particle and therefore faster precipitation. In addition, it can be seen that the nanowires grown at 150 ºC (Figure 6-6 (b)) have smaller diameters than those grown at higher temperatures (Figure 6-6(c,d)). This observation is in agreement with the reports published by Ozaki *et al.* [264] and Gentile *et al.* [265].

For these samples (7.5 nm) no nanowire growth was observed for temperatures of 350 ºC and above. The reason for the lack of nanowires above 250 ºC could be (i) due to Ga etching from the surface at higher temperatures or (ii) due to increased rate of uncatalysed a-Si deposition on the catalyst surface [238] before the incubation period is finished thus preventing the catalyst assisted growth of the nanowires. In order to find out the real issue, the EDS analyses of the as-deposited samples and the samples with attempted nanowire growth at 400 ºC from Ga layers of 7.5 nm were performed (Figure 6-7).

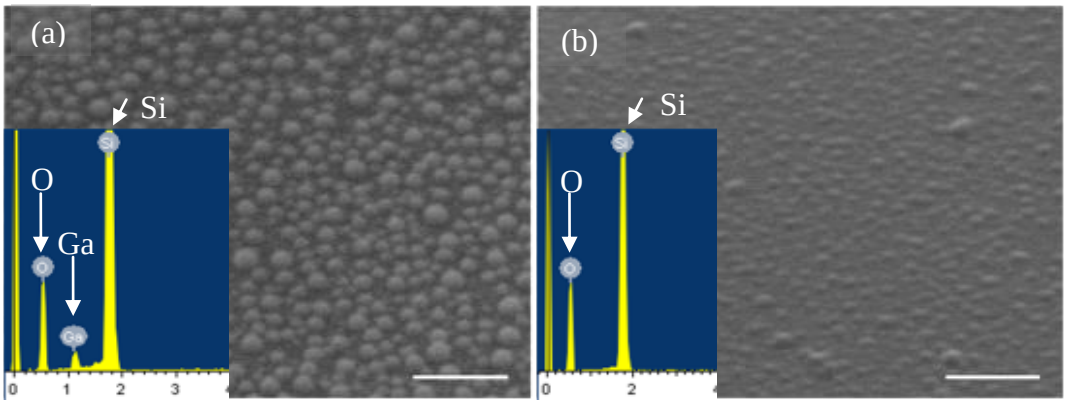

Figure 6-7. SEM images of the as-deposited 7.5 nm Ga layer (a) and an attempt of SiNW growth from 7.5 nm Ga layer at 400 ºC (b). The insets are EDS results for the element composition of the samples. Scale bars are 300 nm.

It can be seen that the Ga peak for the sample with the attempted nanowire growth is not visible (Figure 6-7(b)) suggesting that Ga has indeed been etched from the surface. But, on the other hand, the roughness of the substrate suggests that there might be Ga particles buried under the a-Si layer [238], unnoticed by the EDS due to either (i) the extremely low percentage of Ga in comparison to a-Si coverage or (ii) deep burial (above 3.5 µm) of Ga particles where the EDS electrons do not penetrate to at beam acceleration voltage of 20 kV [266].

The SiNW growth attempts from 2 nm thick Ga layers are illustrated in Figure 6-8.

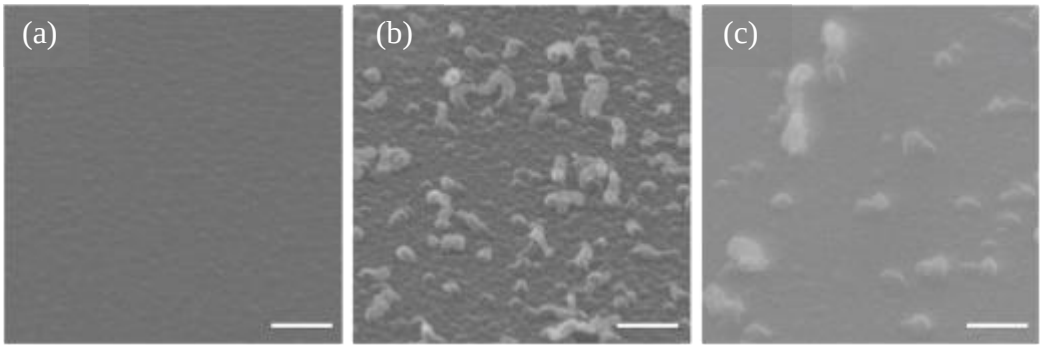

Figure 6-8. SEM images of SiNWs grown from 2 nm Ga catalyst layer at (a) 100 ºC, (b) 150 ºC and (d) 200 ºC. Scale bars are all 200 nm.

Even though the growth rate and density is very low for 2 nm Ga layer, short nanostructures are still undoubtedly observable on the sample used for 150 ºC deposition.

These experiments show that, as would be expected, there is a threshold temperature required for the initiation of the SiNW growth from Ga catalyst. This temperature is above 100 ºC for the catalyst layers and other growth parameters used in this work. It is feasible to further reduce the growth temperature by further reducing the Ga layer thickness and

changing the other growth parameters such as chamber pressure and RF power, in addition attempting the nanowire growth at temperatures between 100 ºC and 150 ºC as these temperatures were not investigated in the framework of this thesis.

It is noticeable from most of the SEM images of SiNWs grown from different thicknesses of Ga (Figure 6-3 - Figure 6-6) that the catalyst particles are sitting on the tips of the nanowires. This indicates COT growth and thus supporting the VLS growth mechanism [227]. To make sure that the particle sitting on the nanowire tips is the catalyst particle, the backscattered electron image (Figure 6-9(b)) was taken. The vivid brightness difference proves that the particle of interest is made of Ga (or a mixture of Ga/Si).

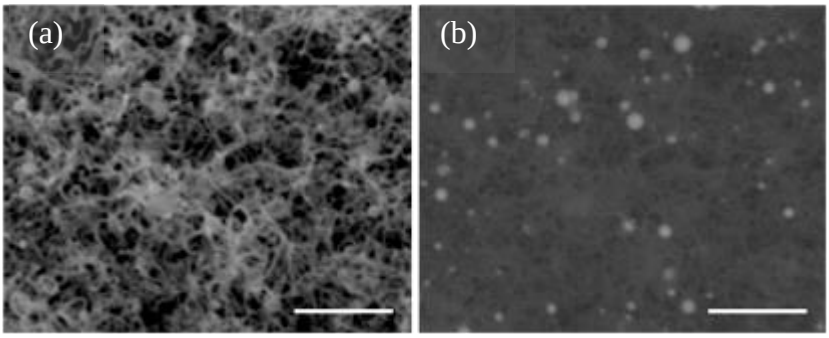

Figure 6-9 Secondary electron (a) and backscattered electron (b) images of SiNWs grown from 7.5 nm Ga catalyst layer at 200 ºC. Scale bars are 1 µm.

Higher magnification images of various Ga layers used for SiNW deposition at 150 ºC are shown in Figure 6-10.

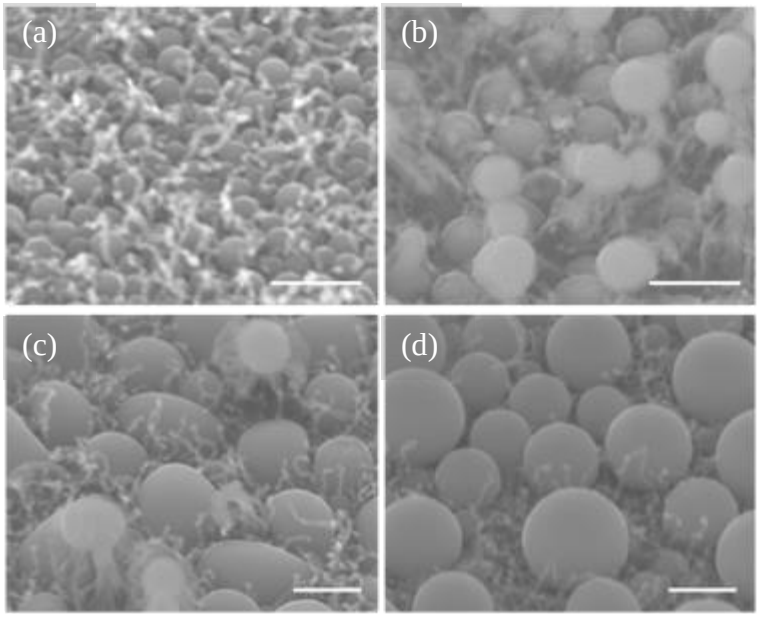

Figure 6-10. SEM images of SiNWs grown at 150 ºC from 28 nm (a), 40 nm (b), 100 nm (c) and 250 nm (d) thick Ga layers. Scale bars are 500 nm.

The high magnification SEM images in Figure 6-10 show that the SiNW growth takes place also from thick Ga layers at 150 ºC, but only from the small Ga droplets that are situated in between the large ones.

These images confirm that low temperature (150 ºC) SiNWs grown with Ga as catalyst require small catalyst particles/droplets in order to initiate the growth. This is possibly due to slow droplet saturation (increased incubation period) with atomic silicon at low temperatures [267]. In this case big Ga droplets will take a longer time to saturate (compared to small particles) and in the meanwhile might get completely covered with the a-Si terminating the possible nanowire growth from these droplets. The other possibility is the slow incubation and growth rate of the thicker nanowires from big catalyst particles taking longer than the 10 minute deposition time.

In the meanwhile, the lack of SiNW growth from thin catalyst layers at higher temperatures is suggested to be due to small gallium droplets being etched away or getting covered by a-Si resulting in no catalyst particle left for the initiation of the nanowire growth.

6.3.3. Plasma RF power variation

The RF power comparison experiments were also conducted for various Ga layers simultaneously. In these experiments the deposition conditions were those of "Standard" conditions with the growth duration of 10 minutes except for the chamber pressure which was set to 350 mTorr. The results for 25 nm thick Ga layers are shown in Figure 6-11.

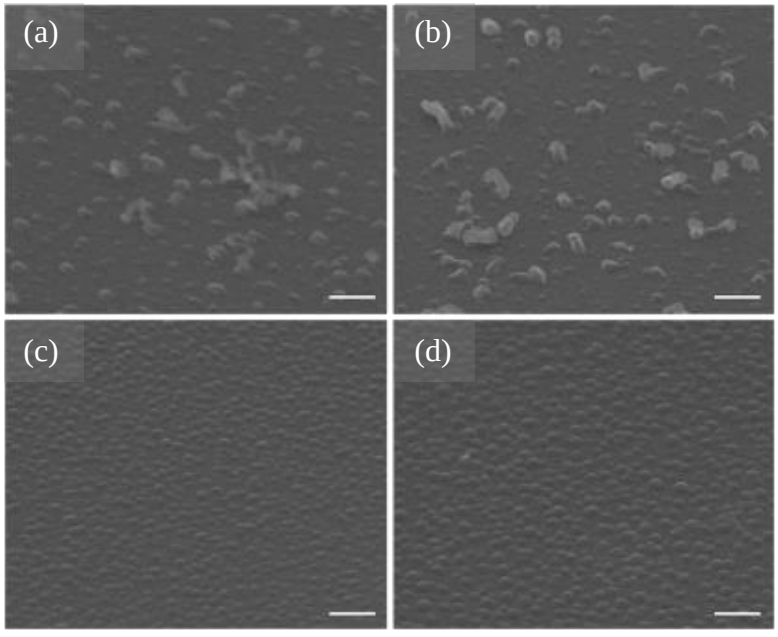

Figure 6-11. SEM images of SiNW growth from 25 nm Ga layer with RF power of (a) 10 W, (b) 25 W, (c) 50 W and (d) 100 W. The scale bars are all 400 nm.

It can be seen from Figure 6-11 that at 350 mTorr pressure used for power comparison experiments no nanostructure growth is observed for RF powers of 50 W and 100 W whereas some structures are observable at 10 W and 25 W powers. If the growth duration was prolonged, the structures grown at lower power would most probably develop into nanowires. The reason for this observation could once again be due to an increased rate of the a-Si deposition with higher RF powers (due to higher rate of silane decomposition) [238]. It can also be seen from the surface features in Figure 6-11 that the grainy structure of the substrates is more uniform for the samples deposited at higher RF powers. This suggests that when using high RF power the a-Si deposition rate increases and thus a-Si covers the sample surface before the nanowire growth initiation hence fixing the catalyst particles in their initial positions, whereas the grains and nanostructures on the lower RF-power samples are more sparsely distributed implying that some of the catalyst particles have got etched away or combined into bigger droplets. The other possibility of the RF power influence may be the etching of the gallium layers at high RF powers resulting in no material left for the initiation of the nanowire growth. A similar observation was made for the SiNWs grown from 50 nm thick Ga layer (Figure 6-12).

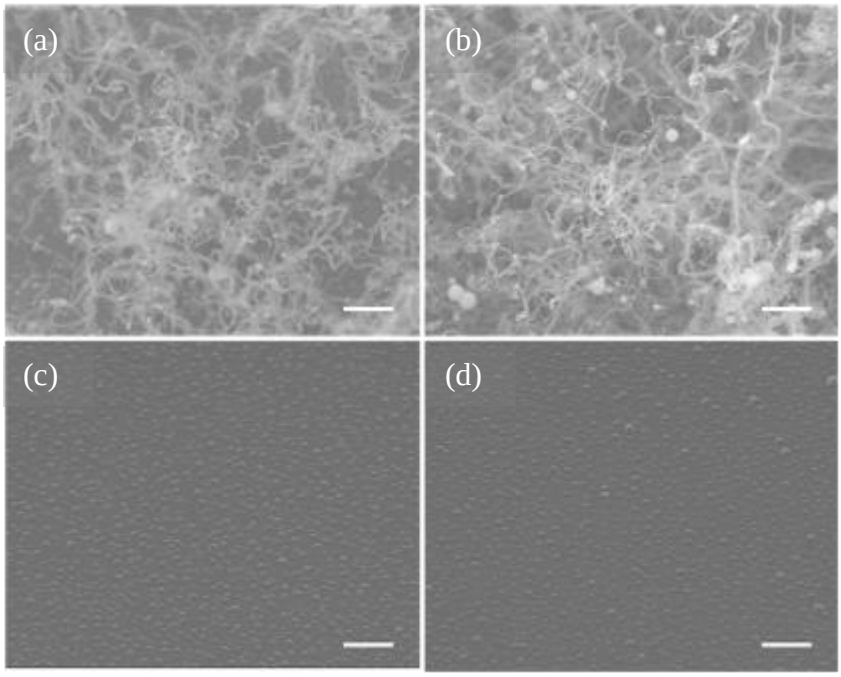

Figure 6-12. SEM images of SiNW deposition from 50 nm Ga layer with RF power of (a) 10 W, (b) 25 W, (c) 50 W and (d) 100 W. The scale bars are all 1 µm.

It is clear from Figure 6-12 that high RF powers result in no nanowire growth from 50 nm Ga layers, whereas proper growth is observed for the samples grown at 10 W and 25 W RF powers.

The high RF power experiments using 100 nm Ga layers showed different growth characteristics from the initial SEM observations (Figure 6-13).

Due to the very curvy nature of the nanowires grown from 100 nm Ga layer at various RF power levels (Figure 6-13) it is difficult to analyse the differences in the nanowire growth. When investigating the images, the nanowires grown at lower powers seem to be more branched in comparison to nanowires grown with 50 W and 100 W powers. This could be due to one of the reasons suggested as for thin Ga layers: high energy gas particles (with high RF powers) may hit the small catalyst particles that are left behind on the nanowire surface (wetting due to liquid Ga droplet remaining on the top of the nanowire) and etch those off.

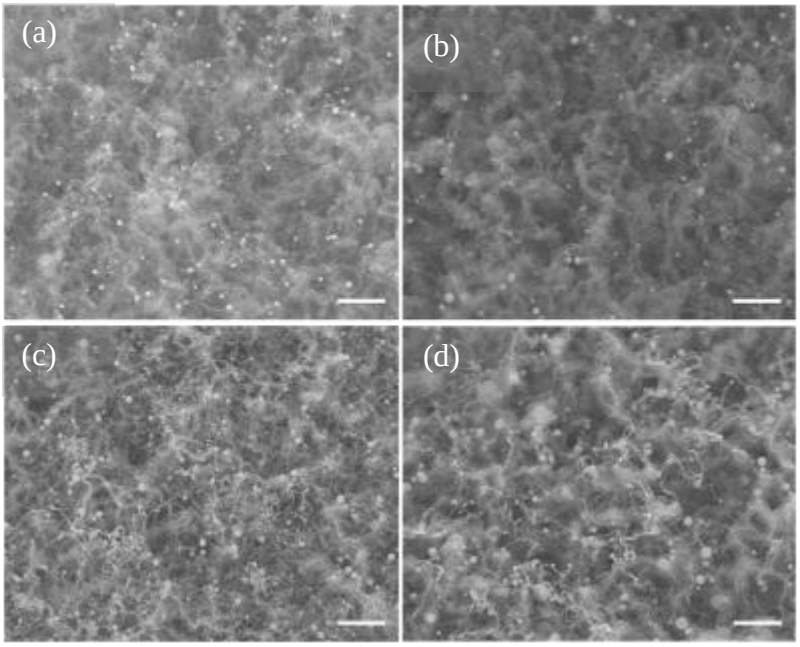

Figure 6-13. SEM images of SiNW deposition from 100 nm Ga layer with RF power of (a) 10 W, (b) 25 W, (c) 50 W and (d) 100 W. The scale bars are all 4 µm.

The RF power variation experiments show that SiNW growth from Ga catalyst is highly dependent on the power level, especially for thin Ga layers. The results indicate that high RF power levels hinder the nanowire growth. The two possible explanations to the phenomenon are suggested to be (i) higher rate of a-Si deposition or (ii) high energy gas particles that etch the formed material off the substrate at higher RF powers stopping the initiation and growth of the nanowires.

6.3.4. Gas pressure variation

Three experiments were performed to understand the influence of the chamber pressure on the nanowire growth. The deposition was carried out with "Standard" conditions for 20 minutes.

The growth results for 20 nm Ga samples are shown in Figure 6-14. As it was already shown in Figure 6-11, there is no nanowire growth from thin Ga layers at pressures of 200 mTorr and above (Figure 6-14). In addition, the catalyst particle sizes seem smaller compared to 100 mTorr growth condition (Figure 6-14(a)).

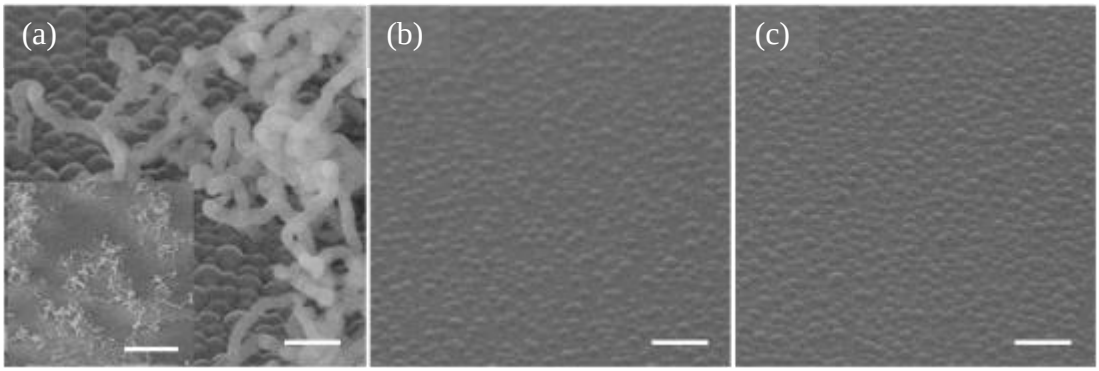

Figure 6-14. SEM images of SiNWs grown from 20 nm Ga layer at 400 ºC with chamber pressures of (a) 100 mTorr, (b) 200 mTorr, and (c) 350 mTorr. Scale bars are all 400 nm. The inset in (a) shows a lower magnification image of the sample with a scale bar of 10 µm.

This outcome could be due to (i) absorption of Si atoms by catalyst particles in low pressure case and thus enlargement of the particles/alloy or (ii) deposition of a-Si layer at high pressures resulting in less noticeable granule shapes. But an interesting observation is that the low gas pressure (100 mTorr) creates favourable conditions for the nanowire growth. A possible explanation may be the increase in the energy of the particle (due to increase in the mean free path of the gas particles) when reducing the pressure, resulting in better insertion of this particle into the liquid catalyst droplet. On the same note, high gas pressure means more precursor particles and less energy resulting in the uncatalysed Si deposition on the surface of the substrate and catalyst preventing the incubation process and thus the nanowire growth.

The SEM images of pressure variation experiments for 100 nm thick Ga layers are shown in Figure 6-15.

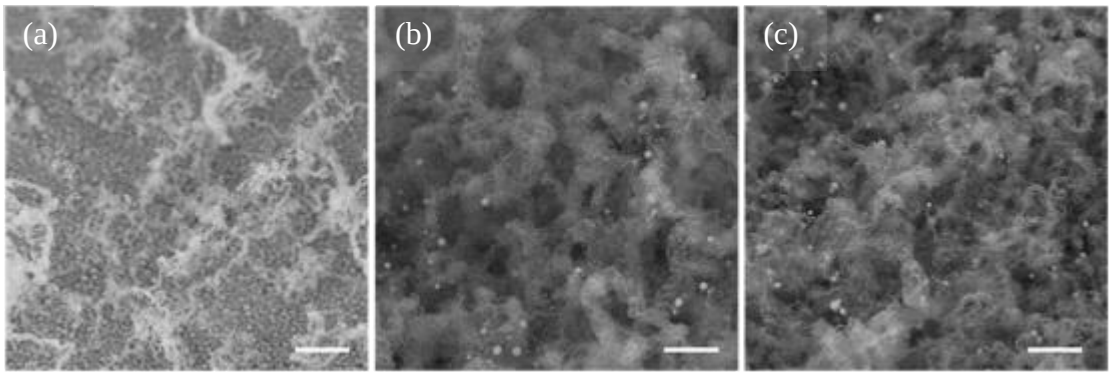

Figure 6-15. SEM image of SiNWs grown from 100 nm Ga layer at 400 ºC with chamber pressures of (a) 100 mTorr, (b) 200 mTorr, and (c) 350 mTorr. Scale bars are 4 µm.

The results of the pressure comparison experiments for 100 nm Ga layer show that branched nanowire structure is not noticeably affected by the growth pressure of 200 mTorr and above whereas low pressures cause more sparse distribution of the nanowires. These results are in contradiction with the pressure comparison results obtained for the nanowires grown from 20 nm Ga layer. At the same time, these are in agreement with the observations made by Hofmann *et al.* [238]. But once again, from the two images in Figure 6-15 (b and c) it is not possible to form a conclusive opinion about the differences in the nanowire structures when grown at 200 mTorr and 350 mTorr pressure values.

The effect of the gas pressure on the SiNW growth is still not finalised and further experimentation is required to design where the process will be monitored in more details and the influence of the gas pressure on the nanowire growth explained.

6.3.5. Silane flow rate variation

Westwater *et al.* [240] have reported that low silane partial pressures result in kink-free nanowire growth with Au catalyst layers. In order to find out whether the silane flow rate influences the nanowire structures and distribution grown in this work the SiH_4 flow rate comparison experiments were carried out where the rest of the parameters were fixed to the "Standard" condition values, with exception of 350 mTorr pressure and 10 minute growth duration. Three samples of various thicknesses of Ga layers were investigated with two values of SiH_4 flow rate (Figure 6-16).

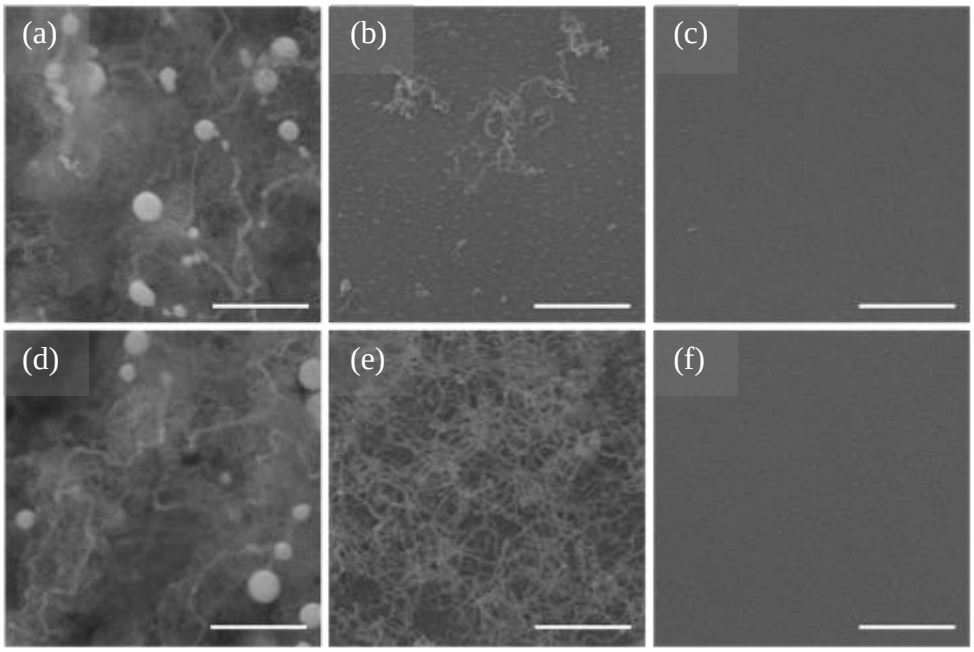

Figure 6-16. SEM images of SiNW deposition at 400 ºC from 100 nm (a,d), 40 nm (b, e) and 20 nm (c, f) Ga layers. Top row (images a, b, c) represents samples deposited at 10 sccm SiH_4, bottom row (d,e,f) shows the samples deposited at 20 sccm SiH_4 flow rate. The scale bars are all 2 µm.

From Figure 6-16 (b and e) it can be concluded that SiH_4 flow rate plays a major role in the nanowire growth process, especially for certain catalyst layer thicknesses. But no kink-free nanowires were observed for lower silane flow rates. Once again, it is difficult to draw some precise conclusion about the SiH_4 flow rate effect on the SiNW growth behaviour from thicker catalyst layers (Figure 6-16(a,d)) due to the shape of the nanowires but the image for 40 nm Ga layer is a vivid evidence of the influence of the flow rate. It can be seen, as observed by other research groups [209, 238], that high concentration of silicon radicals in the chamber results in increased deposition rate of SiNWs. The lower silane flow rate may cause slow enough initiation process during which the catalyst layer gets etched away from the substrate resulting in sparse catalysed growth of the SiNWs.

6.3.6. Investigation of growth parameter influence on SiNWs grown at 150 ºC

As shown in Section 6.3.2 it was possible to grow SiNWs at 150 ºC. This is the lowest temperature PECVD growth of SiNWs ever reported in published literature [268]. This section will investigate the influence of the gas pressure and power on the SiNW growth at 150 ºC.

6.3.6.1. Power variation

The experiments for the RF power comparison were performed with 20 sccm SiH_4 flow rate and with pressure set to 200 mTorr. The deposition duration was 10 minutes.

The SEM images for the power comparison results obtained with 3 nm Ga layers are shown in Figure 6-17.

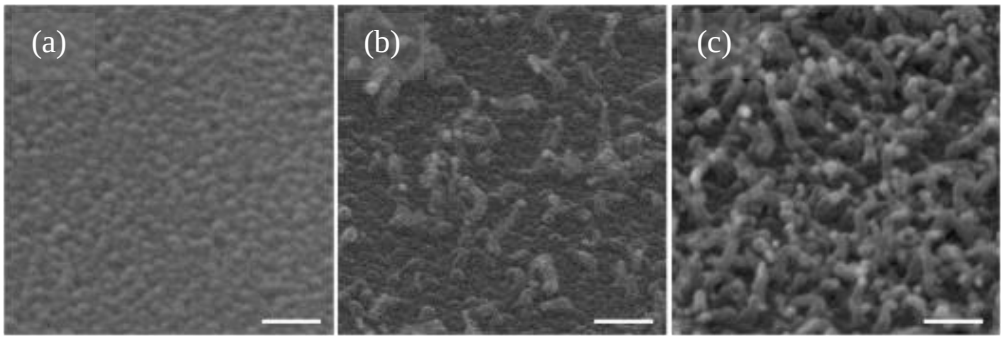

Figure 6-17. SEM images of SiNWs grown at 150 ºC from 3 nm Ga catalyst with (a) 10 W, (b) 25 W and (c) 40 W RF power. Scale bars are 200 nm.

It can easily be seen from Figure 6-17 that nanowire growth from 3 nm Ga layers at 150 ºC is assisted by high RF powers. This outcome is in agreement with the results published by Qin *et al.* [259] where they have observed denser, longer and thicker nanowire growth from Au colloids at higher RF powers. The same results are obtained for the thicker Ga layers of 10 nm and 20 nm (Figure 6-18).

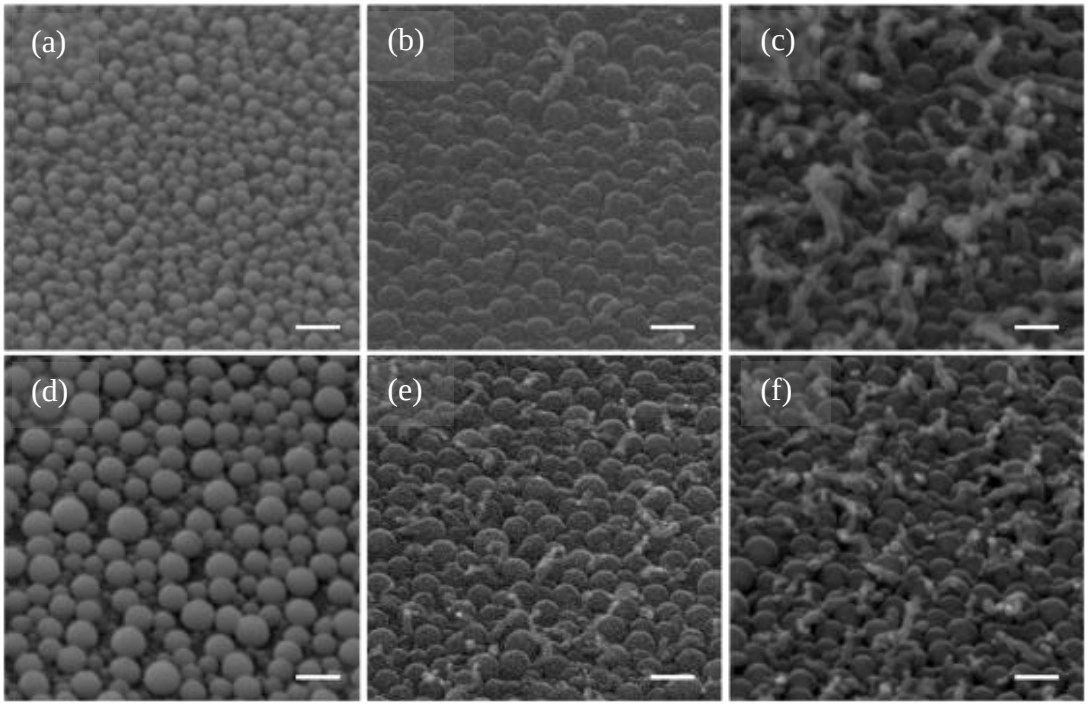

Figure 6-18. SEM images of SiNWs grown at 150 ºC from 10 nm (top row) and 20 nm (bottom row) Ga catalyst with (a, d) 10 W, (b, e) 25 W and (c, f) 40 W RF power. Scale bars are 200 nm.

These results suggest that at low temperatures the energy of the system is not sufficient for the initiation of the nanowire growth reactions at low RF powers. However, when the energy of the gas particles is altered via the RF power, the reaction gets higher energy transferred by the particles and the nanowire growth takes place. The SEM images shown in Figure 6-19 are of thicker Ga layers used for SiNW growth at 150 ºC.

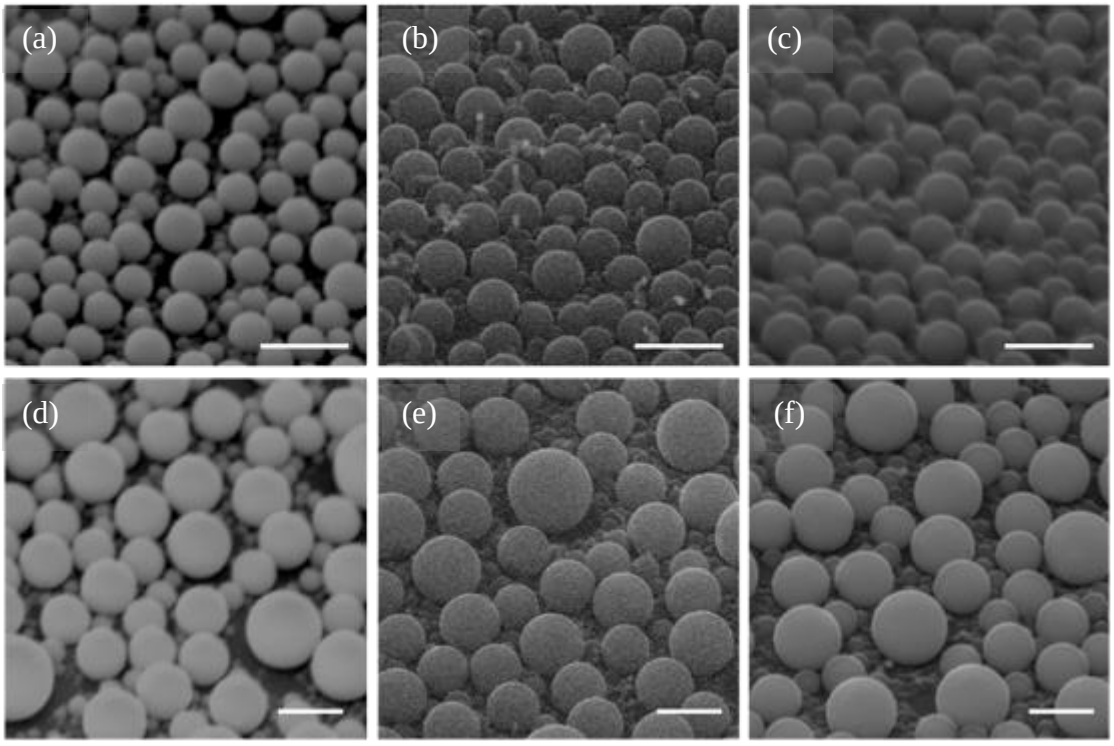

Figure 6-19. SEM images of SiNWs grown at 150 ºC from 40 nm (top row) and 100 nm (bottom row) Ga catalyst with (a, d) 10 W, (b, e) 25 W and (c, f) 40 W RF power. Scale bars are 400 nm.

It can be seen from Figure 6-19 that large catalyst particles do not result in nanowire growth at low temperatures. This could be due to the requirement of a high silicon atom concentration for supersaturation of the droplets into nanowires, the rate of which is slower at lower temperatures. A few small nanowires are observed for the 40 nm Ga layer with 25 W RF power (Figure 6-19(b)). These are grown from small catalyst particles that are visible on the tips of the wires, but no nanowire growth is observed from the large droplets. There is also a possibility to have some nanostructure formation beneath the large droplets considering that the growth is taking place via a COT method. But in the case of big droplets we will not be able to see the nanowire growth under the droplet due to high weight of the catalyst particle.

Considering the general tendency of the catalyst particles of forming larger droplets with thicker Ga layers, it would be commonsensical to expect similar results to that of 100 nm Ga

assisted nanowire growth from 250 nm Ga layer. However, a completely different outcome was observed for the samples using 250 nm Ga layers (Figure 6-20).

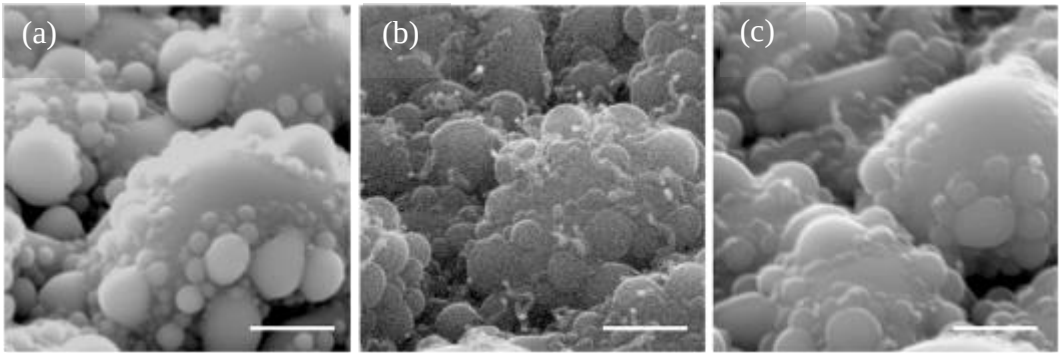

Figure 6-20. SEM images of SiNWs grown at 150 ºC from 250 nm Ga catalyst with (a) 10 W, (b) 25 W and (c) 40 W RF power. Scale bars are 400 nm.

From Figure 6-20 it can be seen that the droplets of Ga have a very different shape to those of 100 nm seed layers of Ga. Individual spheres are no longer observed for thinner catalyst layers. In addition, there are small circular formations on top of the main layer. It can also be seen that 250 nm Ga layer with its novel shape is a more favourable catalyst for the SiNW growth. It was suggested by Yu *et al.* [269] that at low temperatures the catalyst at the bottom growth is more dominant as the Si diffusion inside the catalyst is less effective and therefore local supersaturation occurs, resulting in the COB growth. From Figure 6-20 it is noticeable that the growth of the SiNWs indeed took place via local supersaturation from the catalyst layer. In order to find out whether the shape of the Ga layer is forming during the deposition or whether the pre-deposited samples have the new shape, the SEM analyses of the pre-deposited catalyst layers were performed (Figure 6-21).

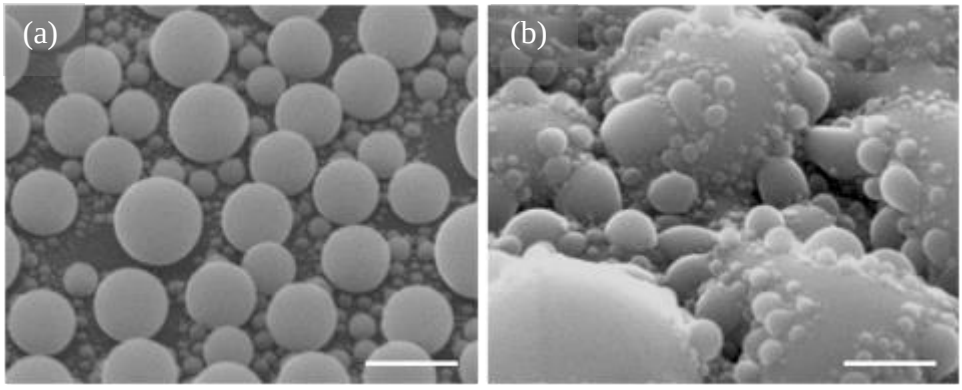

Figure 6-21. SEM images of (a) 100 nm and (b) 250 nm Ga catalyst layers. Scale bars are 400 nm.

Figure 6-21 shows that Ga catalyst layers already have the morphology observed in Figure 6-19 and Figure 6-20 prior to deposition. The images suggest that when the catalyst particles get to a certain critical size they merge into each other forming continuous layer

with small particles sitting on the top of the layers. After the smoother surface is formed, smaller particles forming on the surface are favourable sites for SiNW growth initiation as observed in Figure 6-20.

6.3.6.2. Pressure variation

The experiments for pressure comparison were performed with 20 sccm SiH_4 flow rate and 25 W RF power. The deposition duration was 10 minutes. The SEM images of the SiNW growth from the samples with 3 nm Ga layers are shown in Figure 6-22.

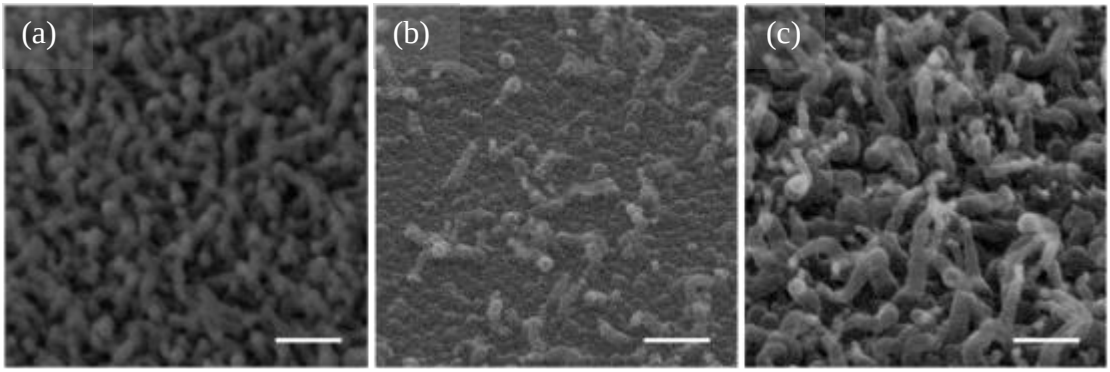

Figure 6-22. SEM images of SiNWs grown at 150 ºC from 3 nm Ga catalyst with (a) 100 mTorr, (b) 200 mTorr and (c) 300 mTorr pressure. Scale bars are 200 nm.

It can be seen from Figure 6-22 that nanowire growth is observed at all the experimental pressures, but for denser and smaller (both in diameter and length) nanowire fabrication low pressure is more favourable, with larger diameter nanowire growth was observed at higher pressure (300 mTorr) which is in agreement with observations of Hetzel *et al.* [261], Yoshida *et al.* [270] and Zhang *et al.* [271]. It was interesting to note that the nanowire yield at 200 mTorr pressure was not as high. The following explanation could be given for the results: when the pressure is low, the mean free path of the gas molecules is larger and the energy is higher. In these conditions gas molecules create smaller catalyst particles. As the catalyst particle gets small but dense, the supersaturation at each particle will be attained faster and due to the small size of particle the nanowires will grow fast, dense and thin [259, 265]. When the pressure gets higher, the energy of the gas particles gets dissipated before the particle gets to the samples surface, therefore does not get the energy to create many small particles resulting in larger catalyst droplets. These droplets will get supersaturated slower as the size is bigger, but due to high number of silicon molecules at high chamber pressure the supersaturation will take place even in a shorter period of time and therefore result in longer nanowires. However, as the droplets are larger, the resulting nanowires will also be larger. It

is also interesting to note that the nanowires have tapered structures. This can be explained via two possibilities: (i) consumption of the catalyst particle sitting on the tip of the nanowires [221] or (ii) parasitic a-Si deposition along the nanowire sidewalls [260]. To find out which of these theories is predominant a long deposition can be performed. If it is the etching that is responsible for the tapering of the nanostructures, the growth will eventually terminate, whereas if it is the amorphous deposition that causes the tapering, then at some point the nanowires will get thick enough to coagulate.

Similar results are obtained for the SiNW growth from 10 nm and 20 nm Ga catalyst layers (Figure 6-23).

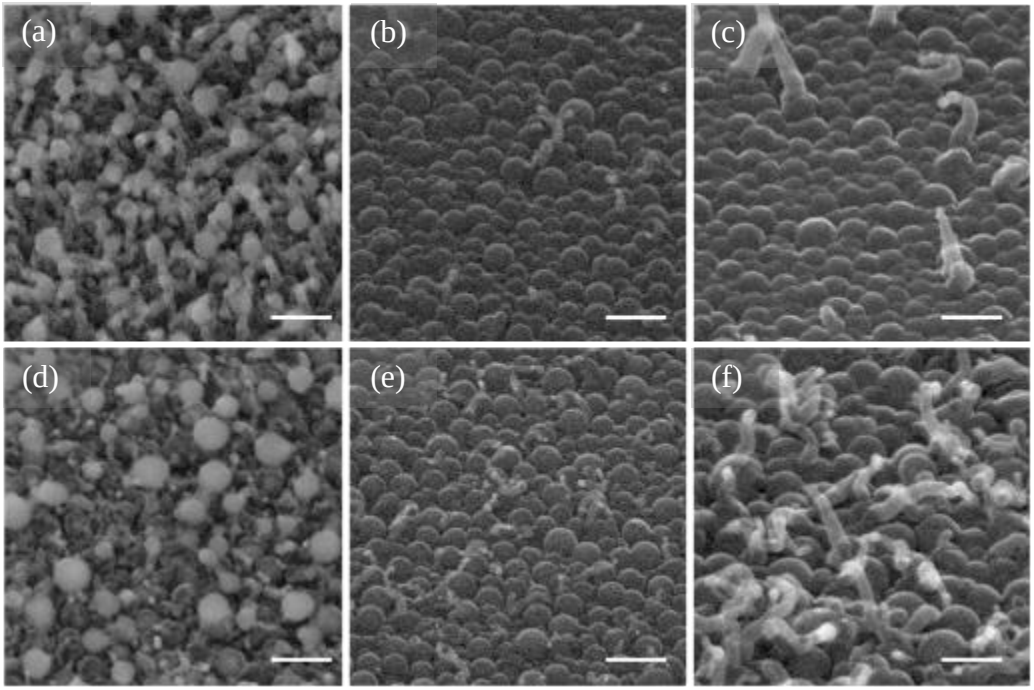

Figure 6-23. SEM images of SiNWs grown at 150 ºC from 10 nm (top row) and 20 nm (bottom row) Ga catalyst with (a, d) 100 mTorr, (b, e) 200 mTorr and (c, f) 300 mTorr pressure. Scale bars are 200 nm.

In case of pressure comparison experiments for 10 nm and 20 nm Ga catalyst layers, the most favourable nanowire growth pressure is 100 mTorr (Figure 6-23(a,d)). With higher thicknesses of the catalyst layer, the catalyst particles are also getting larger resulting in a longer incubation time for the supersaturated Ga/Si alloy formation. In the meanwhile the a-Si deposition covers the surface of the catalyst particles terminating the nanowire growth. As the pressure gets higher the catalyst droplet sizes are getting bigger (as was explained for the thinner layers) and hence the initiation process is getting even longer, therefore resulting in only few nanowires. Therefore, the 150 ºC SiNW growth at 200 mTorr and 300 mTorr pressures is only favoured by small Ga particles. Similar results are obtained also for 40 nm and 100 nm Ga layers as can be seen in Figure 6-24.

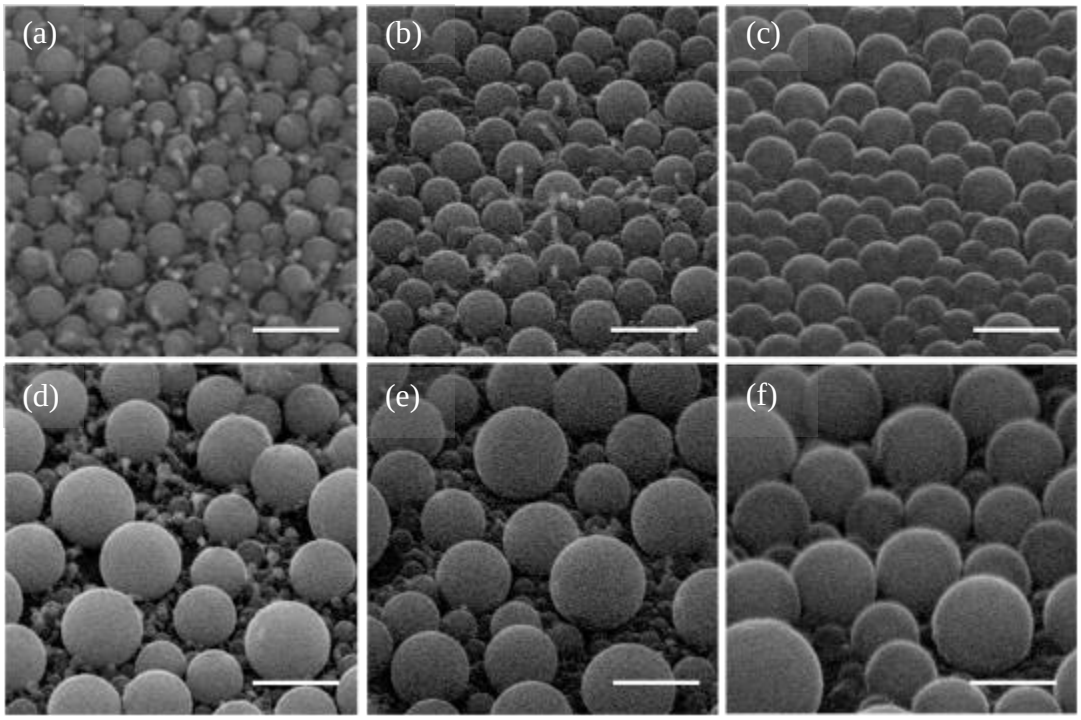

Figure 6-24. SEM images of SiNWs grown at 150 ºC from 40 nm (top row) and 100 nm (bottom row) Ga catalyst with (a, d) 100 mTorr, (b, e) 200 mTorr and (c, f) 300 mTorr pressure. Scale bars are 400 nm.

Only small Ga particles give rise to nanowire growth and only for lower pressures.

As the case was for experiments for power comparison (Figure 6-20), similar results were obtained for 250 nm Ga layer in pressure comparison experiments (Figure 6-25).

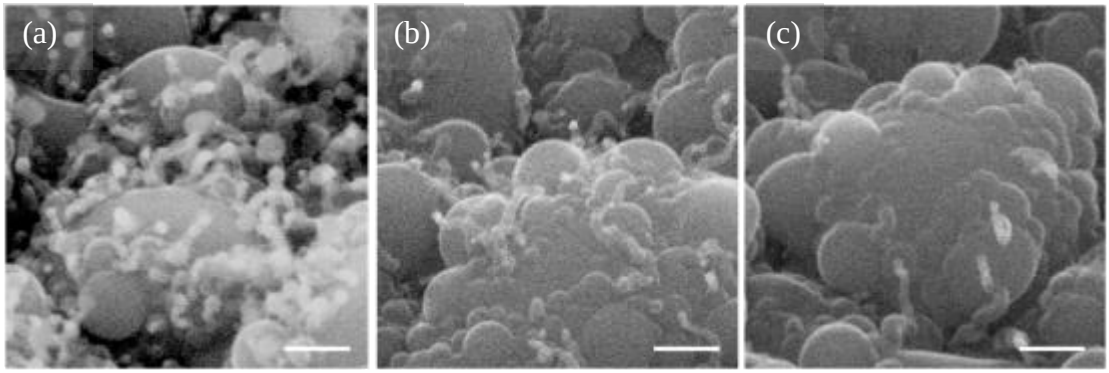

Figure 6-25. SEM images of SiNWs grown at 150 ºC from 250 nm Ga catalyst with (a) 100 mTorr, (b) 200 mTorr and (c) 300 mTorr pressure. Scale bars are 200 nm.

Small nanowire growth is observed from 250 nm Ga layers at 100 mTorr and 200 mTorr pressures (Figure 6-25(a,b)) whereas only few nanowires are observed on the samples grown in a higher pressure conditions (Figure 6-25(c)).

To conclude, SiNW growth at 150 ºC highly depends on the chamber pressure and RF power values. The general observed trend was that nanowire growth was more favourable at

high power or low pressure values. Both trends (high power and low pressure) result in change in energy of the gas particles [272]. Therefore, it suggests that there is a threshold value of the energy of the system that is required for the growth of SiNWs at temperatures as low as 150 ºC.

The tapering of the nanowires is noticeable for the samples grown at 150 ºC. This is suggested to be due to (i) uncatalysed Si deposition along the nanowire sidewalls which is an unavoidable process when using a PECVD fabrication method, or (ii) consumption of the catalyst particle with time. The suggestion is given on the possible investigation method to be employed in order to find out the cause of the nanowire tapering.

6.3.7. Substrate material investigation

It has been suggested by Ozaki *et al.* [264] that oxygen on the substrate surface can result in kinks in SiNWs.

To find out whether the kinks in the nanowires grown in this work were caused by the oxygen present as a barrier between Ga and Si, SI_3N_4 covered Si substrate was investigated. The resulting nanowires from Si/Si_3N_4 substrate showed no difference compared to Si/SiO_2 substrates (see Figure 6-26).

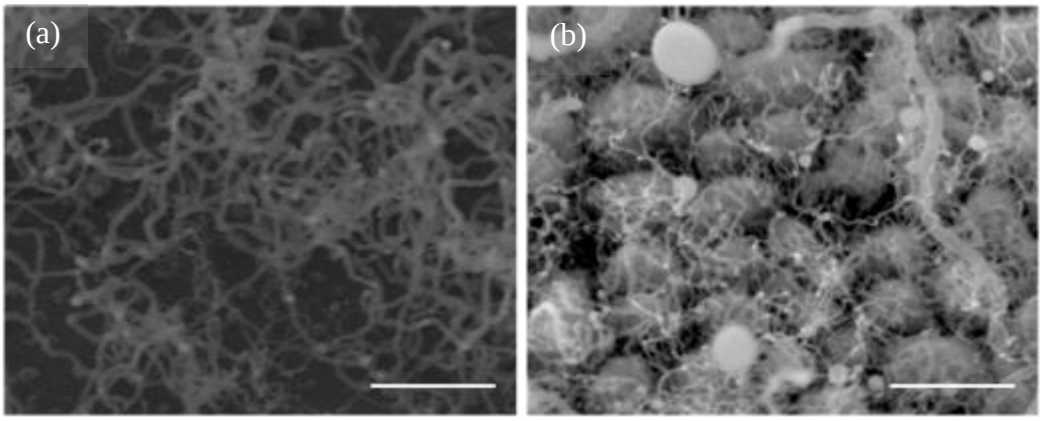

Figure 6-26. SEM images of SiNWs grown at 400 °C (a) and 200 °C (b) from 50 nm Ga deposited onto Si_3N_4/Si substrate. Scale bars are 1 µm.

These results suggest that the oxygen existence in the substrate is not the cause of the kinks in the nanowires fabricated in this work.

The kinks and twisting of the nanowires can be explained via various possibilities, including instabilities in temperature, pressure and gases [209], low growth temperature [273] or wormlike amorphous nanowire growth due to higher rate of Si diffusive transport into the catalyst particle in comparison to the crystallisation rate for the given diameter [238]. In order

to find out whether the reason behind the kinky nature is the amorphous nanowire formation, Raman analyses were conducted on the SiNWs.

6.3.8. Crystallinity analyses of the SiNWs

In order to find out the crystallinity of the SiNWs fabricated in this work, Raman analyses of samples with SiNWs were performed on a glass substrate.

The spectra and the corresponding SEM image represented in Figure 6-27 correspond to two Raman spectra of two samples grown in the same PECVD conditions simultaneously; the black spectrum represents the PECVD deposition at 400 °C from a sample with 100 nm Ga layer and the red spectrum represents that for the sample with no catalyst layer.

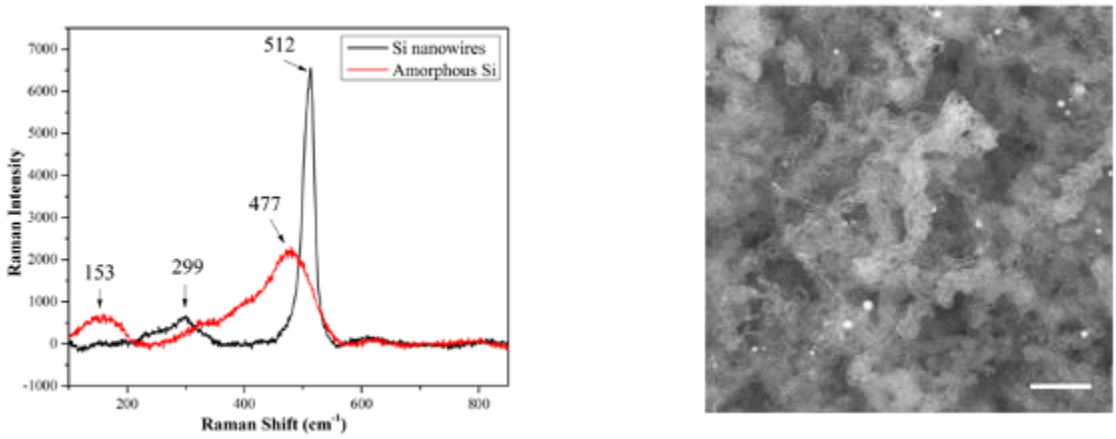

Figure 6-27. Typical room temperature Raman spectrum and the corresponding SEM image of the SiNWs grown from 100 nm Ga catalyst layer, with "Standard" conditions (black line) and amorphous Si (red line). Scale bar is 2 µm.

A sharp peak at 512 cm^{-1} that corresponds to first-order Raman scattering of crystalline Si is evident for the sample with catalyst layer (resulting from SiNW growth as shown in the SEM image), whereas the sample with no catalyst layer has a broad amorphous band at about 480 cm^{-1}. In addition, the peaks at about 150 cm^{-1} and 300 cm^{-1} (second-order Raman scattering) are also assigned to amorphous Si (a-Si) and crystalline Si (c-Si) respectively [274-276]. These spectra point at two important facts; (i) crystalline nature of the SiNWs and (ii) the necessity of catalyst layer for crystalline SiNW growth.

Raman spectra and the corresponding SEM images for SiNWs grown from samples with two different catalyst layer thicknesses (100 nm and 7.5 nm) at 200 ºC are shown in Figure 6-28.

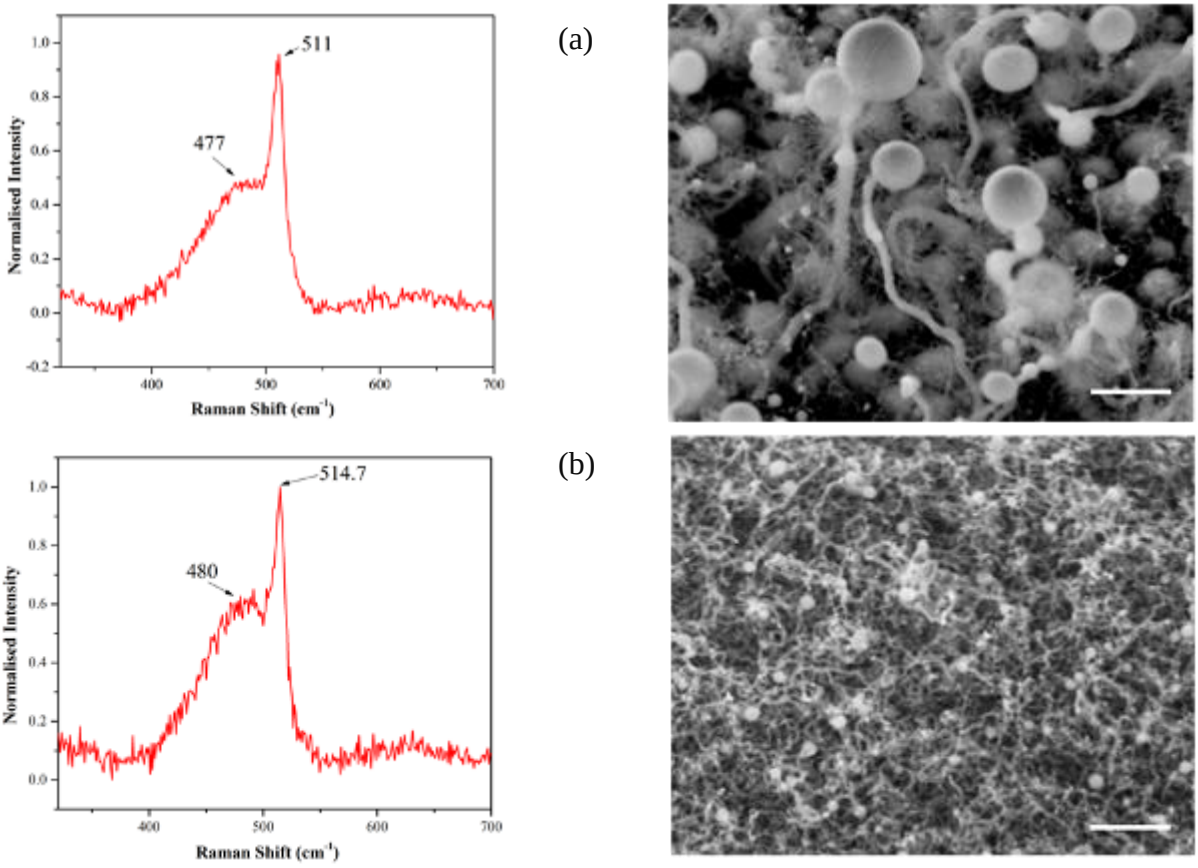

Figure 6-28. Typical room temperature Raman spectra and the corresponding SEM images of SiNWs grown from 100 nm (a) and 7.5 nm (b) Ga catalyst layers, at 200 ºC, for 10 mins at 200 mTorr chamber pressure and 25 W RF power. Scale bars are 1 µm.

It can be seen from Figure 6-28 that SiNW samples exhibit sharp crystalline peaks convoluted with broad a-Si band. The a-Si deposition is an unavoidable simultaneous process taking place when the nanowire growth is performed in a PECVD reactor. The peak characteristic to a-Si in Figure 6-28 can be due to coverage of (i) SiNWs with a-Si shell, (ii) the substrate with a-Si layer or (iii) both SiNWs and the substrate surface.

The separation of the a-Si and c-Si peaks was performed using multiple peak fitting function and the results of the deconvolution can be seen in Figure 6-29.

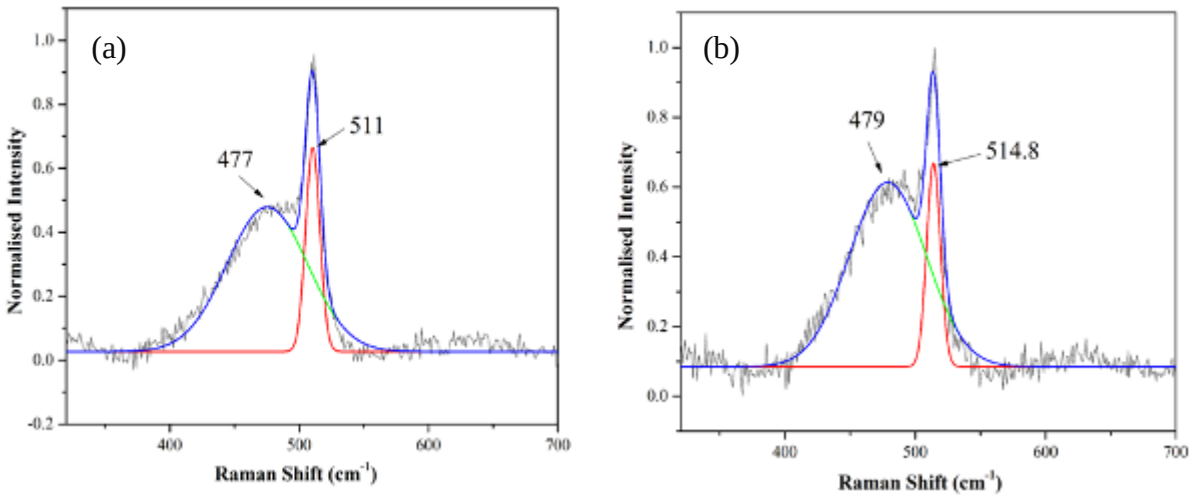

Figure 6-29. The deconvoluted Raman spectra of SiNWs grown from (a) 100 nm and (b) 7.5 nm Ga catalyst layers.

Raman spectrum of thick growth of SiNWs from 60 nm Ga layer at 350 mTorr and 10 W growth conditions for 10 minutes can be seen in Figure 6-30.

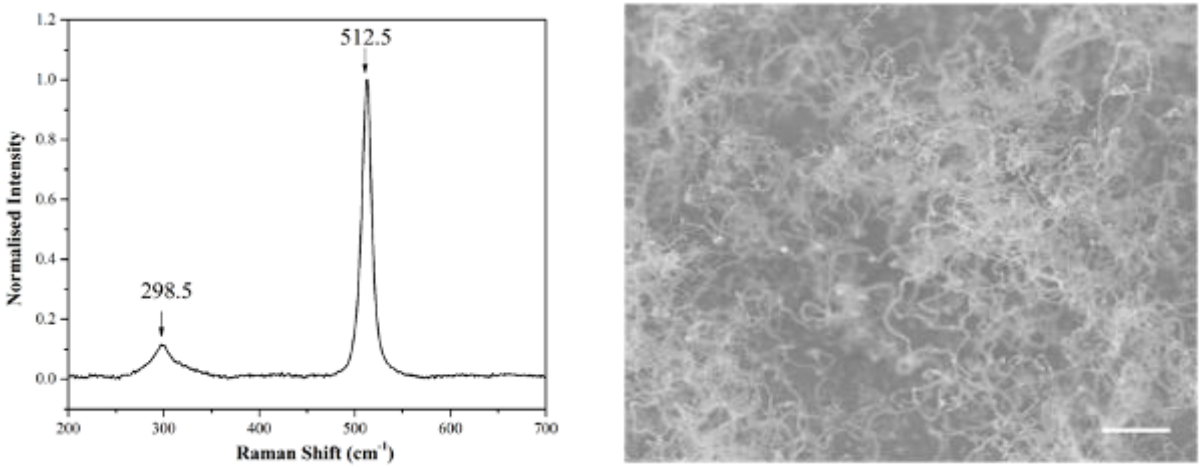

Figure 6-30. Typical room temperature Raman spectrum and the corresponding SEM image of SiNWs grown from 60 nm Ga catalyst layer, at 400 ºC, for 20 mins at 350 mTorr chamber pressure and 10 W RF power. Scale bar is 2 µm.

It is interesting to note from Figure 6-30 that low RF levels result in crystalline nanowires with no a-Si. This is in agreement with the suggestion of Hoffmann *et al.* that high RF powers result in higher level of a-Si deposition (and vice versa) due to high rate of silane decomposition [238].

As it could be easily observed from all the Raman spectra (Figure 6-27- Figure 6-30) obtained for SiNWs grown in this work, all the c-Si peaks were red-shifted. It is known that the increase of the frequency shift and broadening and asymmetry of the Raman peak can be due to reduction of the nanocrystalline grain size [277]. Thus various important parameters,

such as the frequency shift, the broadening coefficient and the asymmetry coefficient of the spectra were measured and compared to the c-Si values measured by Sharma *et al.* [278]. The broadening coefficient (C_b) was calculated from $FWHM_{SiNW}/FWHM_{c\text{-}Si}$ (FWHM standing for full width at half maximum) and the asymmetry coefficient (C_a) was calculated from LWHM/RWHM, where LWHM (and RWHM) stand for left (and right) width at half maximum. The FWHM, C_b and C_a are not measured for the SiNWs grown at 200 ºC as the measurement would have to be done from the fitted curve and would not be accurate. The results of the measurements can be seen in Table 6-2.

Table 6-2. The Raman frequency, the frequency shift, FWHM, the coefficient of broadening and the asymmetric coefficient of SiNWs grown in this work in comparison to those of c-Si reported by Sharma *et al.* [278].

Sample	Raman frequency (cm^{-1})	Frequency shift (cm^{-1})	FWHM	C_b	C_a
c-Si	521.08	0	4.0831	1	1
SiNWs from Figure 6-27	512	9.08	22.25	5.45	1.76
SiNWs from Figure 6-28 (a)	511	10.08	-	-	-
SiNWs from Figure 6-28 (b)	514.7	6.38	-	-	-
SiNWs from Figure 6-30	512.5	8.38	12.09	2.96	1.08

It can be seen from the results of Raman peak analysis (Table 6-2) that the peaks of SiNWs have undergone downshift as well as asymmetric broadening which is possible to indicate phonon quantum confinement effect. Other possibilities for red-shifting include stress caused by the external amorphous SiO_x layer on the nanowires [275] which is an inevitable process when PECVD deposition is carried out [260].

But it is important to note that the Raman power used in this work was 5 mW. It has been shown previously that Raman spectra of SiNWs is a function of the excitation power [279]. It was shown that with an increase of the power the spectrum was red-shifted and this can be attributed to the local heating and damage of the sample. Red-shifting of Raman peak due to both sample heating and confinement effect were reported by various groups [280-282].

In order to further confirm the crystallinity of the nanostructures transmission electron microscopy (TEM) was utilised for one sample. Selected area electron diffraction (SAED) aperture was used for the demonstration of the diffraction pattern of the wire (see Figure 6-31).

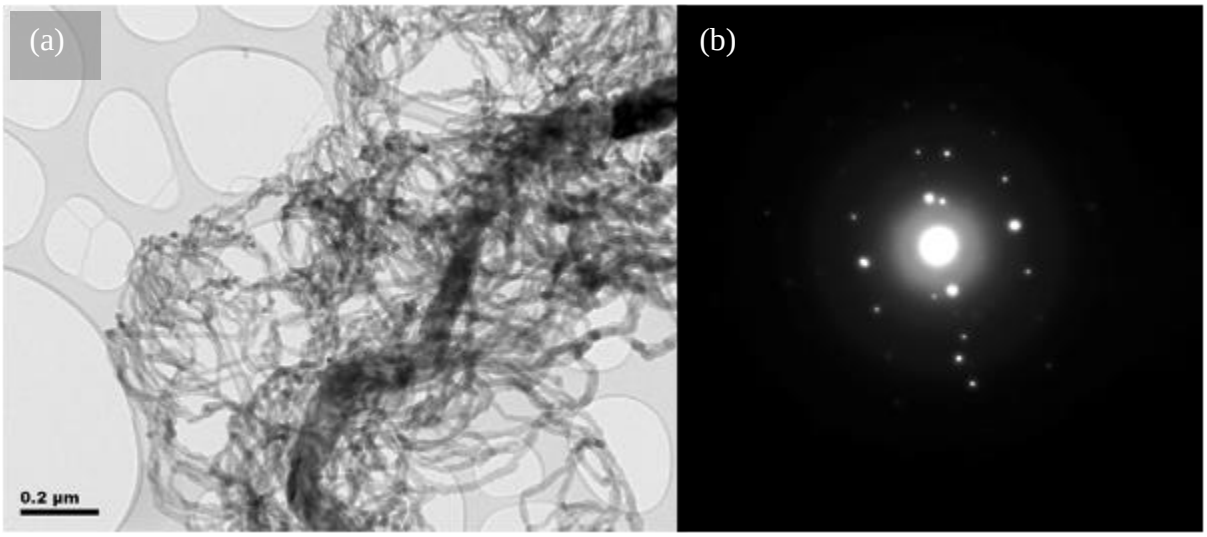

Figure 6-31. (a) The TEM image and (b) the corresponding SAED pattern of the SiNW grown from 100 nm Ga catalyst layer for 20 mins using "Standard" conditions.

It can be seen from Figure 6-31 that the nanowires investigated via TEM have the branched structure that was observed for NW growth with thick catalyst layers at high temperature. Due to the wormlike structure of the nanowire the diffraction pattern is influenced by various crystal orientations present at the site. The spots in Figure 6-31(b) confirm the crystalline structure [7, 27] of the SiNWs agreeing with the data obtained by Raman spectrometry. Unfortunately, it was discovered (after the patterns were obtained) that the TEM was not calibrated and therefore the d-spacing of the lattice planes was not possible to calculate. However, the pattern was a proof of the crystalline structure of the nanowires which was the primary target of the TEM investigation.

6.4. Conclusions

This chapter reports the lowest temperature for the SiNW growth via PECVD method published in the literature. The influence of various growth parameters including temperature, chamber pressure, RF power and silane flow rate on the nanowire growth were investigated. The parameter variation was performed at two temperatures: 400 ºC and 150 ºC (the lowest observed growth temperature).

All the nanowires obtained at all the investigated temperatures were curved and showed COT growth characteristics corresponding to the VLS growth. In addition, nanowires grown at high temperatures resulted in branched nanostructures. This growth is suggested to be due to a molten Ga droplet sitting on the top of the nanowire and wetting the surface of the

nanowire as the latter grows. The Ga-wetted nanowire surface itself becomes an initiation point for smaller diameter nanowire growth.

It was discovered that high growth temperatures require thicker catalyst layers otherwise the seed layer gets etched away (or covered by a-Si layer) and low growth temperatures require thin catalyst layers. The suggestion is that at low temperatures the supersaturation of the catalyst particle takes a longer time and in the meanwhile the larger particles get covered by an a-Si layer which terminates the further absorption of Si radicals and growth of the nanowire. Another possibility is the slow growth rate (due to higher silicon atom requirement both for supersaturation and for larger nanowire diameter) of the nanowires from large catalyst particles, therefore the growth does not take place during the ten minutes investigated in this work.

The results obtained for the 150 ºC experiments showed that a certain combination of power and pressure is required for the initiation of SiNW growth; these conditions being either low gas pressure or high RF power. The suggestion for this observation is that in order for the nanowire growth reaction to take place, a certain energy level is required for the system which can be obtained via increasing the energy of gas particles (ions) by reducing the pressure (thus increasing the mean free path) or increasing the RF power [77].

The Raman and TEM investigations of the SiNWs grown in this work confirmed the crystalline structure of the nanowires with amorphous contamination which is suggested to have resulted from the uncatalysed Si deposition covering the substrate including the nanowire sidewalls.

Chapter 7

Metalorganic compounds as catalysts for silicon nanostructure growth

"Any knowledge that doesn't lead to new questions quickly dies out: it fails to maintain the temperature required for sustaining life."

...Wislawa Szymborska

In this chapter a new group of materials, metalorganic compounds, are used for the attempt of growing Si nanostructures using these compounds as catalysts.

In the first part of the chapter these compounds are discussed along with their thermal decomposition information. The second part of the chapter looks into incorporation of these materials as catalysts for the growth of Si nanostructures. The results of the growth attempts and the structure of the nanostructures are investigated, with theories of the growth mechanisms proposed.

7.1. Metalorganic compounds

As the name suggests, metalorganic (MO) (as well as metal-organic and metallo-organic) compounds contain metal and an organic ligand. The difference between metalorganic and organometallic compounds is the chemical element by which the organic component is connected to the metal. In organometallic compounds the bond is between metal and carbon, whereas metalorganic compounds (MOC) are a group such that they exclude direct metal-carbon bond [283]. According to this definition, the compounds used in this work (nickel(II) formate (NFM), nickel(II) formate dihydrate (NFD), nickel(II) acetate tetrahydrate ($NiAc{\cdot}4H_2O$), gallium(III) acetylacetonate ($Ga(acac)_3$) and palladium(II) acetate (PdAc) should be classified as metalorganic. Despite the aforementioned definition, most of the compounds formed between a metal and a ligand are referred to as organometallic in literature [284-285]. In this work all the compounds that do not include a direct metal-carbon bond will be referred to as metalorganic.

7.1.1. The thermal decomposition of MOCs

The chemical structures of MOCs used in this work can be seen in Figure 7-1.

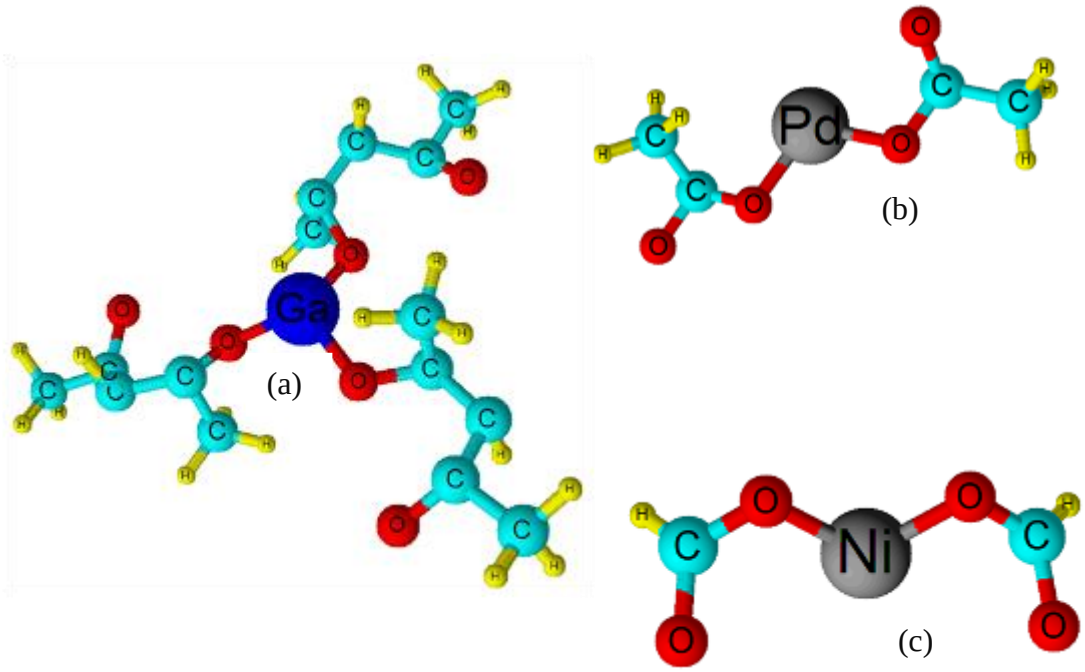

Figure 7-1. Chemical structures of MOCs used in this work; (a) $Ga(acac)_3$, (b) PdAc and (c) NFM.

The chemical structures of $NiAc{\cdot}4H_2O$ and NFD are the same as that of PdAc (Figure 7-1(b)) and NFM (Figure 7-1(c)) with four and two water molecules around the structures respectively.

These MOCs are used as stable sources of metal in this work. It is possible to manufacture fine metal powders using MOCs via various methods including chemical reduction methods, evaporation, gas-phase reduction of metal salts, atomization, electrolysis and spray pyrolysis [286-287].

Each of these methods has its advantages, but one of the simplest one-step methods for metal powder fabrication is through temperature treatment method; upon heating, MOCs easily decompose to metal with simultaneous liberation of their ligands in a gaseous form.

The decomposition reactions for the compounds used in this work are given below.

Nickel formate dihydrate decomposition takes place in two steps [288]. During the first step it loses the water (7-1), after which the decomposition of the anhydrous salt into metallic Ni powder can take place via three possible reactions ((7-2), (7-3) or (7-4)). In high vacuum thermal decomposition conditions the metal oxide formation route (7-4) will be less apparent, thus resulting in two dominating decomposition possibilities ((7-2) and (7-3)).

$$Ni(HCOO)_2 \cdot 2H_2O \rightarrow Ni(HCOO)_2 + 2H_2O \quad \textbf{(7-1) Dehydration}$$

$$Ni(HCOO)_2 \rightarrow Ni + H_2 + 2CO_2 \quad \textbf{(7-2) Decomposition}$$

$$Ni(HCOO)_2 \rightarrow Ni + HCOOH + CO_2 \quad \textbf{(7-3) Decomposition}$$

$$Ni(HCOO)_2 \rightarrow NiO + HCOH + CO_2 \quad \textbf{(7-4) Decomposition}$$

Nickel(II) formate decomposition should in theory follow only the second step of those for NFD decomposition, but it will be shown later via thermogravimetric analysis and Fourier Transform Infrared Spectroscopy that when kept in normal atmospheric conditions, with time NFM absorbs water from air, therefore transforming into NFD.

Nickel acetate tetrahydrate decomposition also takes place in two steps via water loss (7-5) and further decomposition into metallic Ni (7-6) and/or NiO (7-7) [289-291].

$$Ni(CH_3COO)_2 \cdot 4H_2O \rightarrow Ni(CH_3COO)_2 + 4H_2O \quad \textbf{(7-5) Dehydration}$$

$$Ni(CH_3COO)_2 \rightarrow Ni + CO_2 + C + CO + CH_4 \quad \textbf{(7-6) Decomposition}$$

$$Ni(CH_3COO)_2 \rightarrow NiCO_3 + CH_3COCH_{3(g)} \rightarrow NiO + CO_2 \quad \textbf{(7-7) Decomposition}$$

Due to PdAc having the same ligand as $NiAc \cdot 4H_2O$ its decomposition should in theory take place by the same route as that of $NiAc \cdot 4H_2O$ without the first dehydration step. Gallium acetylacetonate thermal decomposition reactions are also expected to take place in one step as there is no water decomposition step involved in the reaction [292]. Unfortunately, no representation of the reactions taking place for $Ga(acac)_3$ decomposition is readily available, but it should follow a similar route to the rest of the MOCs and eventually result in Ga and/or GaO_x oxide forms (most likely being Ga_2O [293]).

7.2. Growth of silicon nanostructures from metalorganic compounds

The growth of silicon nanostructures can be performed using various synthesis techniques (see Chapter 6), with chemical vapour deposition (CVD) being the most prominent of these techniques. In the CVD process the nanowire fabrication is achieved using oxygen-free Si precursors, such as silane, disilane, dichlorosilane and tetrachlorosilane [224]. It is clear that in these circumstances (when Si is not supplied by direct elemental Si) a catalyst particle is required to initiate the Si nanowire growth. Numerous catalyst materials have been investigated for the CVD growth of SiNWs such as gold, silver, platinum, copper, gallium, indium, aluminium, palladium and nickel, and the nanowire growth mechanisms from these

are already studied and established [227]. In general, these metal catalysts are directly deposited via thermal evaporation [206], e-beam evaporation [263], ion-implantation [222] deposition from a solution [250, 265] or sputtering [254] on a desired substrate and then used for subsequent silicon nanostructures growth. A question arises whether it is possible to obtain the metal catalyst particles by other indirect and simple means. It is well known that when heated to their decomposition temperatures, MOCs dissociate to their metallic elements (or mixture of metal/metal oxide) with the simultaneous evolution of volatile products, the distribution of which depends on the chamber environment (nitrogen, oxygen, air, vacuum or other) [78, 291]. The abovementioned characteristics of the MO compounds reveal the prospect of this group of materials to form clusters/nanoparticles upon heating at appropriate conditions. In this chapter MO compounds are investigated as seed materials for initiation of the Si nanostructures growth. Considering that some of these MO materials decompose at temperatures ≤ 300 ºC, it will make the growth of Si nanostructures via low-temperature CVD technique possible. For example, Ni and Pd have been demonstrated as catalyst materials for the VLS growth of Si nanowires but the growth temperatures for both were above 700 ºC [206, 225, 294-296] classifying them as high temperature CVD growth techniques [224]. A VSS growth of silicon nanowires from Pd nanoparticles has also been demonstrated at 490 ºC by Wittemann *et al.* [243]. The high temperature is often required for the formation of islands from the catalyst layer, whereas, as mentioned above, taking into account the decomposition characteristics of the MO compounds, it is possible to form catalyst islands at lower temperatures, thus also reducing the Si nanostructure growth temperature using the MOC corresponding to its metal. To the best of our knowledge, such investigations have not been published except for a patent from our research group [297]. As such there are many open questions to this research including:

- Whether the growth from the MOCs is even possible.
- Whether the growth temperature for Si nanostructures can be reduced.
- Whether the growth of the nanostructures from the pre-annealed samples is possible or the growth (if any) takes place in situ, simultaneously with the decomposition of the MOC.

There are many more questions in regard to the use of MOCs as potential catalyst materials for the growth of Si nanostructures. To answer some of the aforementioned questions, a systematic study was undertaken to establish the role of MOCs for the growth of silicon nanostructures by the PECVD technique. In addition to being an unexplored field of research, these materials may offer extra valuable advantages over the conventional metal

catalyst utilisation. Some of the benefits include; long lifetime for storage of the samples coated with MOCs prior to the nanostructure growth, unlike pure metal catalysts which are prone to oxidation when kept in natural environment; very simple preparation of the compound solution (mixing of the compound with the appropriate solvent), uncomplicated deposition methods (one can use simple drop casting or paintbrush methods).

Prior to investigating the possibility of using MOCs as catalyst materials for Si nanostructure growth, it is important to understand their decomposition characteristics, such as the decomposition temperature and residual material left after decomposition. For this reason, the experimental section is divided into two sections: (i) decomposition study of metalorganic compounds and (ii) attempt to grow nanostructures from the MOCs.

7.3. Experimental procedure

Experimental procedure for this chapter consists of two sections: (i) investigation of the decomposition of MOCs and (ii) attempt of nanostructure growth from MO catalysts via PECVD technique. Considering that one of the MO compounds was Ni-based, nanostructure growth was also attempted directly from pure Ni and NiO layers in order to compare the similarities (if any) between Ni, NiO and Ni- based MOC catalysed nanostructures.

The samples were prepared on Si and glass substrates. For the analysis of the resultant nanostructured materials composition via Energy-dispersive X-ray spectroscopy (EDS) copper substrates were initially used in order to stop the Si substrate influencing the EDS results. However, it was discovered that nanostructure growth was also taking place from the Cu substrate itself (see Appendix B), therefore instead the samples were scratched from Si or glass substrates directly onto conductive carbon tape for EDS analysis.

The concentrations of the solutions containing MOCs used were approximately 0.3 M throughout all the experiments.

The deposition of the MOCs was carried out via various techniques such as evaporation (for $Ga(acac)_3$), dip-coating and spin-coating (for NFM), drop-casting and paint brushing (for all the MOCs) on substrates placed on a hot plate (90 ºC for methanol- and chloroform- based solutions and 150 ºC for D.I. water-based solutions).

The solvents used for dilution of each MOC, the prepared solution concentration and the solution deposition methods used are represented in Table 7-1.

Table 7-1. Information on MOC solution concentration and deposition techniques.

MO compound	Solvent	Concentration	Solution deposition method
$Ga(acac)_3$	Methanol	120mg/mL	Brush at 90 ºC Drop-cast at 90 ºC
NFM	D.I. water	30mg/mL	Dip coating Drop-cast at 150 ºC
	Methanol	50mg/mL	Brush at 90 ºC Drop-cast at 90 ºC
NFD	Methanol	50mg/mL	Brush at 90 ºC Drop-cast at 90 ºC
$NiAc{\cdot}4H_2O$	Methanol	80 mg/mL	Brush at 90 ºC
PdAc	Chloroform	75 mg/mL	Brush at 90 ºC Drop-cast at 90 ºC

The painting with a brush allowed an attainment of a more uniform layer compared to drop-casting. The optical microscope images for the deposition of $Ga(acac)_3$ via these two methods can be found in Appendix B. The hot-plate helped with the immediate evaporation of the solution assisting with better uniformity and prohibiting coagulation of the MOCs in one position (around the edges of the dried circles).

After initial investigation of various deposition methods, drop-casting and paint brushing were chosen as the main deposition techniques for investigation of Si nanostructure growth from MOCs; drop-casting was chosen for NFM and NFD (this was the only reliable deposition method for NFM and NFD MOCs for repetitive growth of nanostructures) and paint brushing for PdAc and $NiAc{\cdot}4H_2O$ (for its ease of preparation and higher uniformity compared to drop casting).

The first part of the experiments in this chapter is devoted to the investigation of the MOC decomposition. The thermal decomposition experiments were performed using TGA and DSC in the environment of continuous nitrogen flow. Due to the environment not being completely isolated, metal oxide formation is expected during decomposition, whereas when the decomposition is performed in high vacuum conditions (in the PECVD chamber) it is

expected that the oxide formation will be reduced or eliminated. In order to find out whether there is a difference in the decomposition mechanisms of the MOCs when annealed in various environments, FTIR analyses were performed on as-annealed samples. In addition, the AFM analyses of the decomposition of a thin (100 nm) spin-coated PdAc layer were performed. The sample was heated to its decomposition temperature (200 ºC) in situ in the AFM chamber. The reason for not expanding the AFM analyses on the rest of the MOCs was the limitation of the temperature that was possible to achieve via the AFM. The imaging was done via non-contact mode.

The second section of the experiments looks into the attempt to fabricate Si nanostructures from the as-deposited MO layers. The growth was performed in a PECVD reactor with silane (SiH_4) as the precursor gas and hydrogen as the carrier gas. The growth conditions given in Table 7-2 are the most commonly used conditions and will be referred to as "Standard" conditions. Only those growth parameters that are different from the "Standard" conditions for certain experiments will be stated. If the growth conditions are not mentioned, it is assumed that "Standard" conditions are used.

Table 7-2. "Standard" PECVD conditions used in this work.

Temperature (ºC)	**Pressure (mTorr)**	**Power (Watts)**	**SiH_4 flow rate (sccm)**	**H_2 flow rate (sccm)**
400	200	25	20	100

The PECVD deposition duration was varied between 10-30 minutes.

The results of the Si nanostructure growth attempts were characterised via SEM, EDS, TEM and Raman spectroscopy.

7.4. Results and Discussions

7.4.1. Metalorganic compound decomposition results and discussion

7.4.1.1. Thermal analyses of MO compound decomposition

As mentioned earlier, the decomposition of the MOCs, including NFM, NFD, $NiAc{\cdot}4H_2O$, PdAc and $Ga(acac)_3$ were analysed using TGA, DSC, and FTIR techniques.

Information about decomposition temperature and the leftover material for each MOC can be obtained via TG analyses. The TGA data for NFM and NFD obtained in continuously

flowing nitrogen environment with heating rates of 5 ºC/min and 25 ºC/min is shown in Figure 7-2. The decomposition of the MOCs at 25 ºC/min heating rate is investigated as this is the rate used for the heating of the samples for the PECVD deposition experiments.

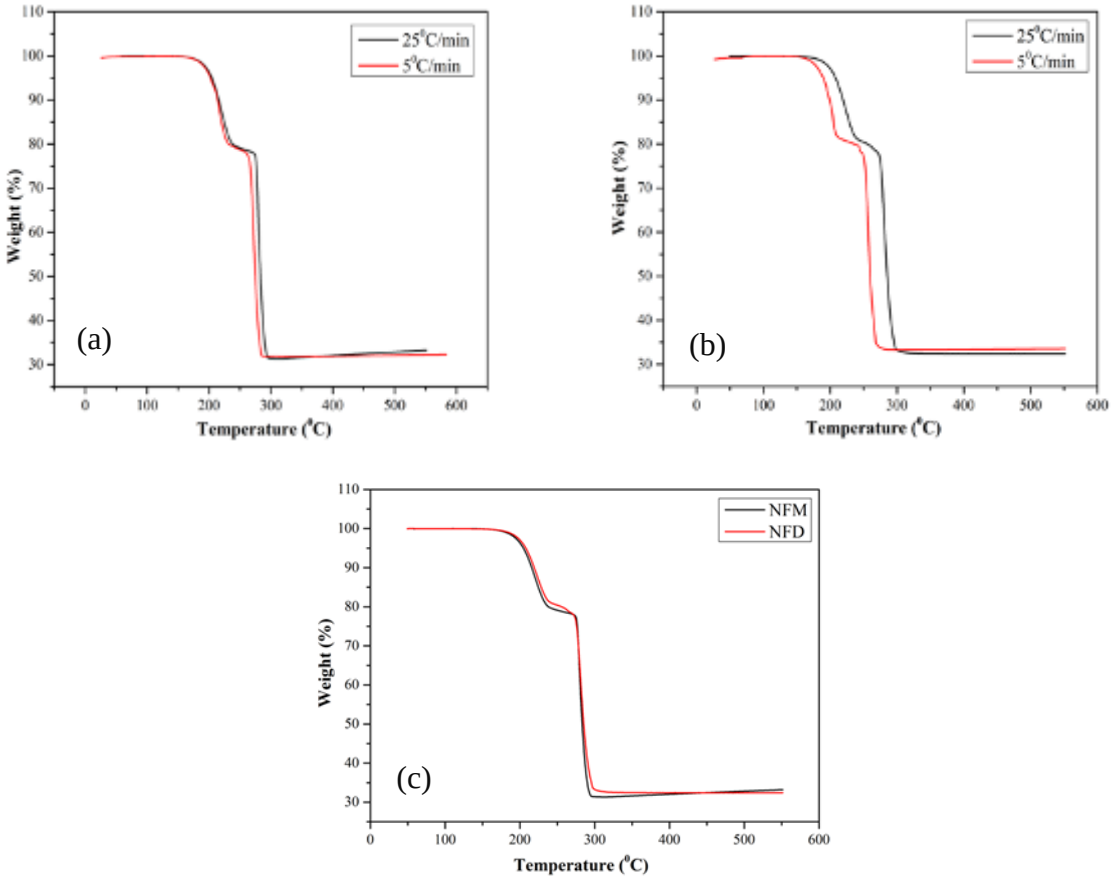

Figure 7-2. Normalised TGA data of (a) NFD, (b) NFM at sample heating rates of 5 ºC/min and 25 ºC/min, and (c) comparison of NFD and NFM TGA data at 25 ºC/min heating rate.

Considering the difference in water content of NFM and NFD MOCs it was expected to see a one step decomposition of NFM in comparison to the two step decomposition of NFD discussed earlier. But it can be seen from Figure 7-2 that NFM and NFD decomposition curves are very similar and both materials lose the same amount of water at the first step. The explanation to this phenomenon is that NFM has undergone humidification when kept under standard atmospheric conditions (not vacuum sealed) in the laboratory. The graphs of NFM and NFD at 5 ºC/min heating function show a noticeable weight loss at around 180 °C explained by water loss, the second weight loss at 240 °C corresponds to the decomposition of the anhydrous NFM into metallic Ni. These values agree with the published data [298].

The TGA data for $Ga(acac)_3$, PdAc and $NiAc{\cdot}4H_2O$ MOCs is shown in Figure 7-3.

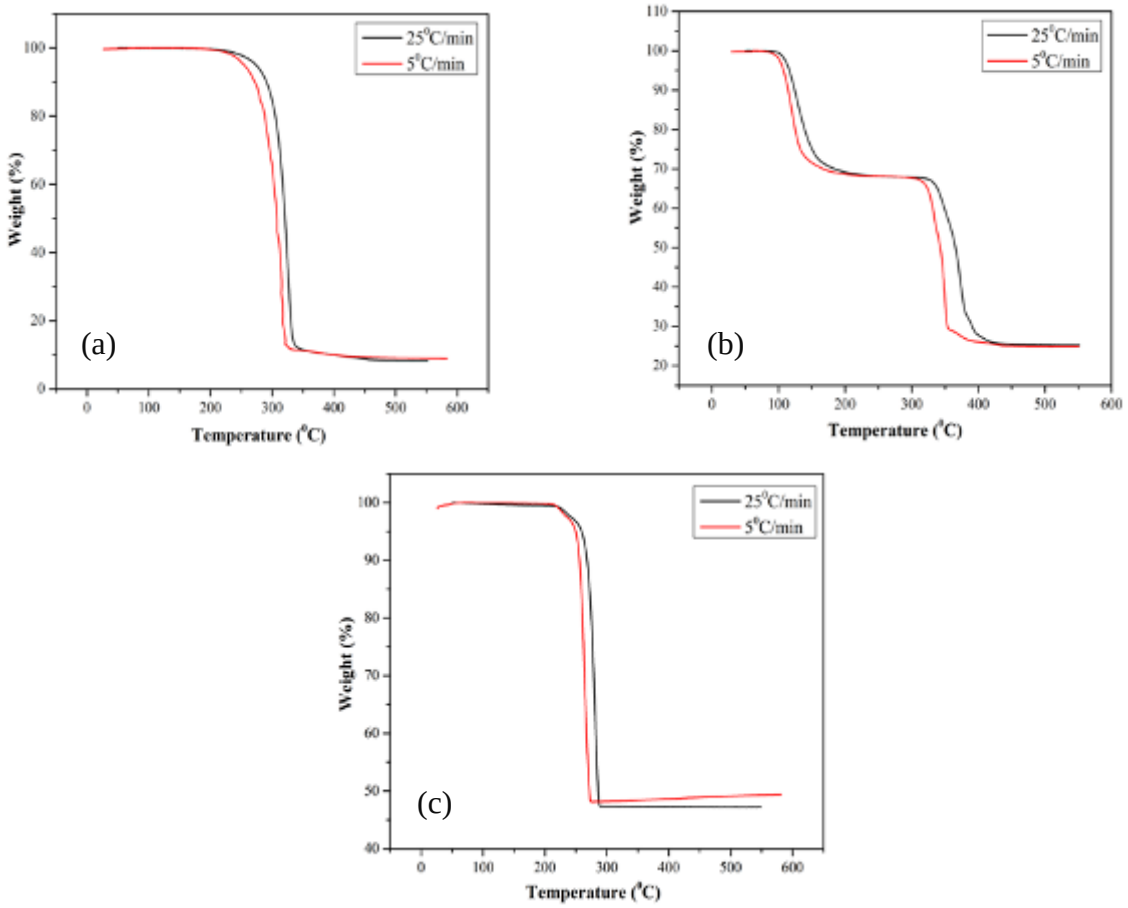

Figure 7-3. Normalised TGA data of (a) $Ga(acac)_3$, (b) $NiAc{\cdot}4H_2O$ and (c) PdAc compounds at 5 ºC/min and 25 ºC/min heating rates .

The expected two-step decomposition of $NiAc{\cdot}H_2O$ is also present in Figure 7-3(b). Water loss takes place at around 120 °C (measured at half fall of 5 ºC/min curve) and the further decomposition into Ni metal (and small amount of NiO as will be seen further on) takes place at around 330 °C. This data also corresponds to the previously reported values [289-290].

Gallium(III) acetylacetonate and palladium(II) acetate undergo only a one-step decomposition as expected starting from 230 °C and 200 °C correspondingly measured on the data of 5 ºC/min curve.

It is important to note that TGA analyses were not performed in vacuum, but in nitrogen environment, therefore increasing the possibility of metal oxide formation in the final product.

In order to find out the concentration distribution of metal/metal oxide formed after decomposition, the weight losses for each MOC were measured (for 5 ºC/min heating rate data) and compared with theoretically calculated molecular weight of the materials. These

calculations were done in percentages. At first, the amount of the materials remaining after decomposition were measured, secondly, the theoretical values were calculated for the molecular weights of the (i) metal and (ii) metal oxide amounts in the corresponding amount of MOCs, and thirdly, these three values were compared. In addition, the experimental and theoretical results for the water contents were also compared. The measurements for NFM and NFD were found to be the same and therefore only NFD calculation results will be discussed.

The results of these measurements and calculations are presented in Table 7-3 and Figure 7-4.

Table 7-3. Results of decomposition of MO compounds.

	NFD	**$NiAc{\cdot}4H_2O$**	**$Ga(acac)_3$**	**PdAc**
Molecular Weight (g/mol)	184.76	248.84	367.05	224.50
Theoretical metal content (%)	31.77	23.58	18.99	47.4
Theoretical metal oxide content (%)	40.43	30.02	23.35	54.53
Experimental remaining material (%)	32.40	25	15.04	48.85
Theoretical H_2O content (%)	19.50	28.96	-	-
Experimental H_2O content (%)	20	31.96	-	-

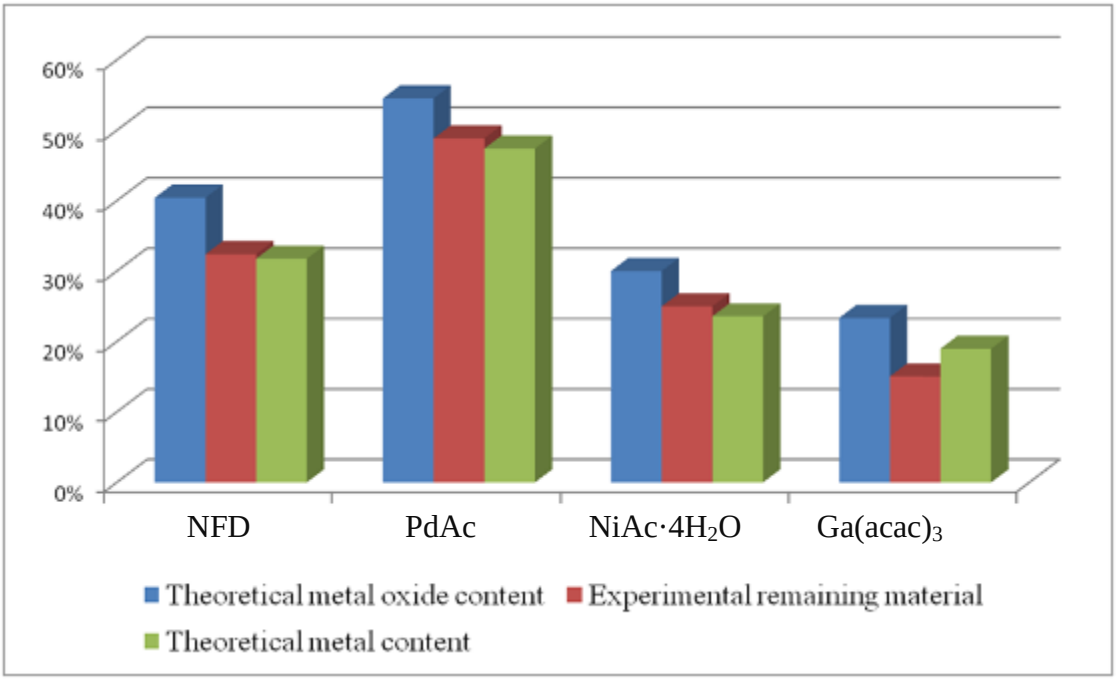

Figure 7-4. Comparison of the theoretical and experimental data on the MOC decomposition.

It can be seen from Table 7-3 and Figure 7-4 that the final product weight after decomposition for all of the compounds is below the theoretical value of their equivalent metal oxides. However, most of them (except for $Ga(acac)_3$) have higher values than if the remaining powder was pure metal. This is most likely an indication of a small amount of metal oxide formation but in order to cover all the possibilities, increased product weight from its pure metal content could also mean partial decomposition of the MOC, or simultaneous oxide formation with partial decomposition.

In the case of $Ga(acac)_3$ compound the graph indicates loss of some of the metal as well as the ligand. The TGA for $Ga(acac)_3$ was repeated 3 times with the same outcome each time. This was an unexpected result and we suggest the following explanation for the observation; gallium, remaining after the decomposition of the MOC, is in a liquid form at the decomposition temperatures. In these circumstances, there could be a possibility that Ga is being forced out of the sample boat by the pressure of the decomposing vapours or losing some metal from its vapour state. The second option is less likely considering the low vapour pressure of Ga [224]. Due to the aforementioned phenomenon it is difficult to conclude whether the remaining material of $Ga(acac)_3$ decomposition is pure metal or metal oxide.

When looking at the water loss of the NFD and $NiAc{\cdot}4H_2O$ compounds, it is obvious that the materials have absorbed some water while being stored in atmospheric conditions. This observation also serves as an evidence for the suggestion of NFM humidification.

The DSC curves (Figure 7-5) show the difference in the heat flow between the sample of interest and the reference sample which was an empty boat in this case.

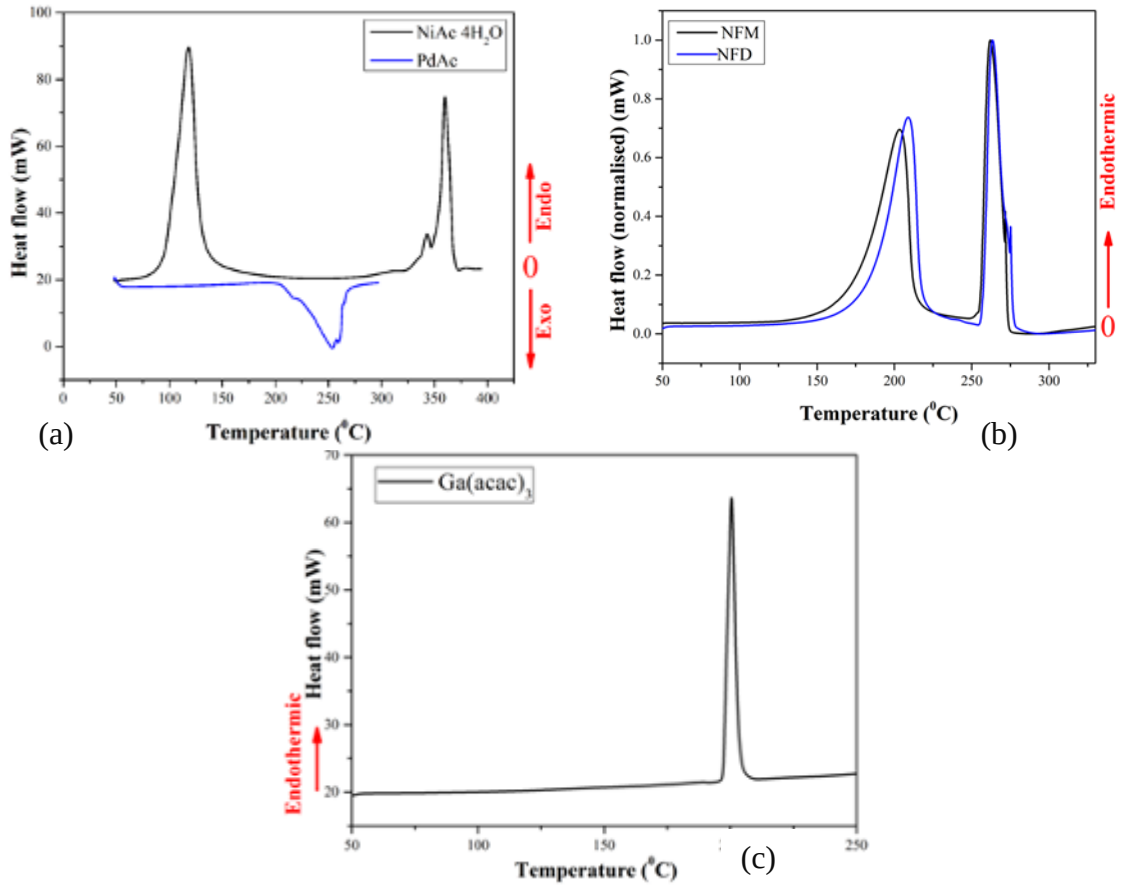

Figure 7-5. DSC curves for (a) NiAc·4H_2O and PdAc, (b) NFM and NFD, and (c) Ga(acac)$_3$.

It can be seen from the DSC data (Figure 7-5) that all the MOCs except for PdAc compound undergo an endothermic decomposition, whereas the nature of the PdAc decomposition is exothermic. The exothermic process has been observed by Gallagher and Gross [292] in the presence of oxygen. Even though the thermal decomposition is taking place in the constant flow of nitrogen gas, still some oxygen will be present in the system, whereas the likelihood of oxygen presence is reduced when the samples are heated in vacuum in the PECVD chamber.

7.4.1.2. Optical analysis of the MOC decomposition

In order to investigate the possible effect of the environment (whether vacuum as in the PECVD chamber or nitrogen as in the TGA chamber) on the product formation during the MOC decomposition, optical analyses were performed on the MO layers decomposed in different conditions. The optical analyses of the as-prepared MO layers and their decomposed states in various conditions were performed via FTIR spectroscopy. Moreover, FTIR spectroscopy was an additional method for the verification of NFM transformation into NFD.

The substrates used for the FTIR analyses were p-type Si (not HF (hydrogen fluoride)-treated).

As it was mentioned earlier NFM and NFD showed similar decomposition characteristic via TGA and DSC; losing the same amount of water during the first step of decomposition. The same conclusion was drawn when analysing these materials in their powder forms via the FTIR analyses (Figure 7-6).

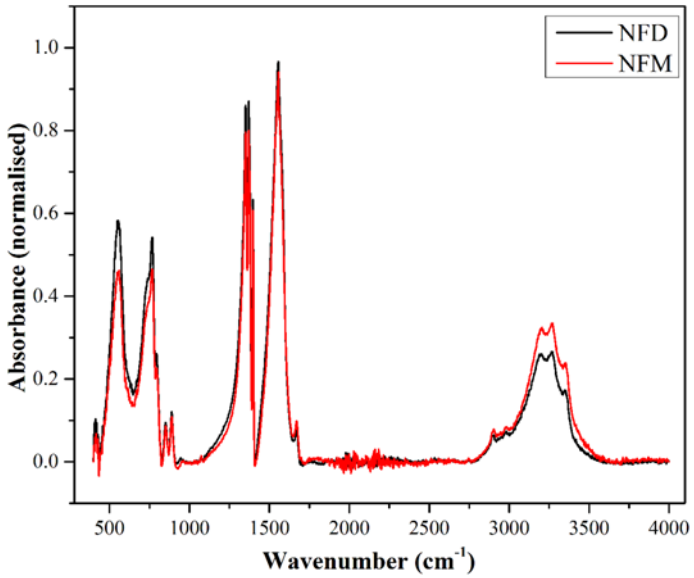

Figure 7-6. FTIR spectra of NFM and NFD powders showing similar water content.

The bands between 3168 – 3647 cm^{-1} in Figure 7-6 are due to $\nu_{as}(OH)$ and $\nu_{sym}(OH)$ coordinated water modes [299]. It can be seen from Figure 7-6 that NFD has approximately the same water content as NFM, therefore proving that the NFM has transformed into NFD via absorption of humidity in the air.

The FTIR analyses were performed on four different samples including the as-deposited (drop-cast or paint brushed) and annealed for 30 minutes at various conditions metalorganic compound films. The conditions of annealing were (i) 400 ºC in furnace in constant nitrogen flow, (ii) 400 ºC and (iii) 300 ºC in vacuum at 3 Pa (23 mTorr) base pressure. These experiments were performed to understand the decomposition mechanism of the MOCs at different environmental conditions and particularly to find out whether it enhances the possibility of the metal oxide formation as an MO decomposition product when the compounds are annealed in nitrogen as is the case during the TGA analyses compared to vacuum annealing as for the attempt of nanostructure growth in the PECVD chamber.

Figure 7-7 represents the FTIR spectra of $Ga(acac)_3$ films as-deposited and decomposed in various environments.

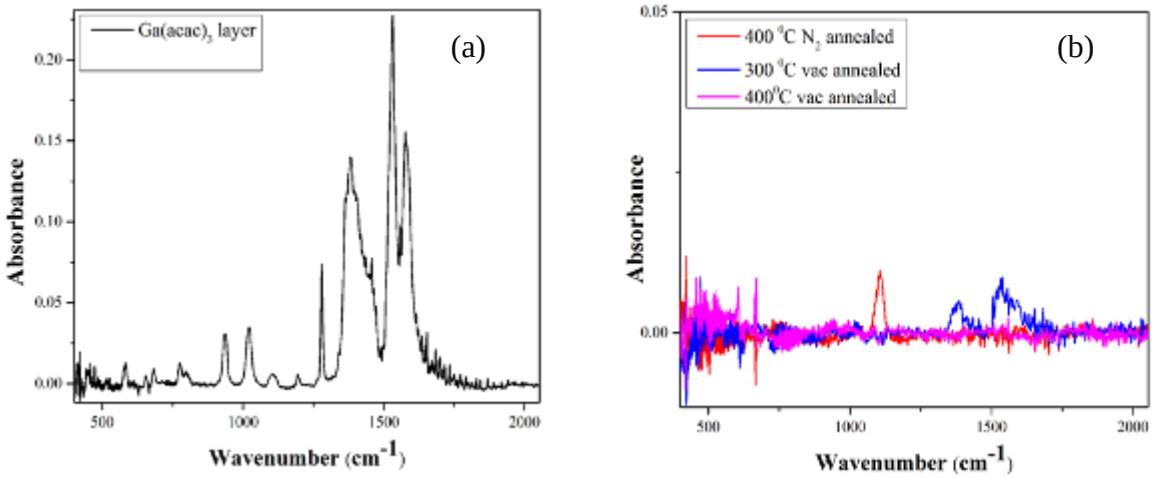

Figure 7-7. FTIR analyses of $Ga(acac)_3$ (a) as-deposited and (b) decomposition at 300 ºC (blue) and 400 ºC (purple) in vacuum and 400 ºC (red) in nitrogen ambient.

The peak at 1106 cm^{-1} in Figure 7-7 represents native oxide layer on the silicon substrate [300-301]. Considering that all the samples used p-Si substrates, this peak will be observed in several FTIR spectra when the native oxide layer of the reference substrate (bare p-Si) was different in thickness compared to that of the MOC deposited samples. It can be seen from Figure 7-7 that some of the $Ga(acac)_3$ peaks are still present for the layer annealed at 300 ºC. This indicates that not all $Ga(acac)_3$ decomposes to metallic Ga at these temperatures. This could be due to (i) the length of time that samples were kept in the reactor that was not enough for the decomposition to fully accomplish or (ii) the effective substrate temperature was under 300 ºC. The assignments of FTIR peaks for $Ga(acac)_3$ are given in Table 7-4.

The FTIR spectra of $NiAc{\cdot}4H_2O$ decomposition at different conditions in comparison to as-deposited layer can be seen in Figure 7-8.

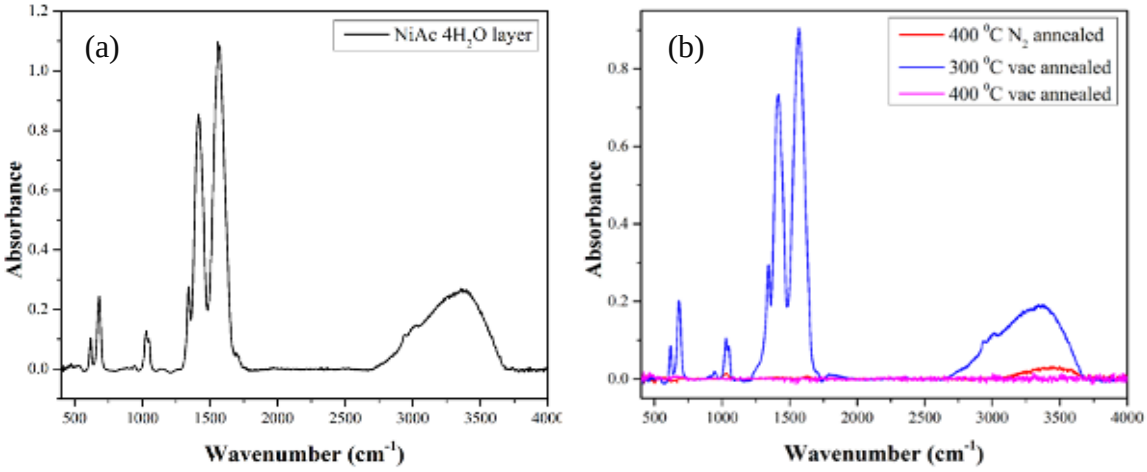

Figure 7-8. FTIR analyses of $NiAc{\cdot}4H_2O$ (a) as-deposited and (b) decomposition at 300 ºC (blue) and 400 ºC (purple) in vacuum and 400 ºC (red) in nitrogen ambient.

As expected from the TGA and DSC analyses, it can be seen from Figure 7-8(b) that most of the compound is still intact after annealing at 300 ºC, but shows decomposition when annealed at 400 ºC leaving metallic Ni behind. The assignments of the FTIR peaks for $NiAc{\cdot}4H_2O$ are given in Table 7-4.

The FTIR spectra of NFM decomposition at various conditions can be seen in Figure 7-9.

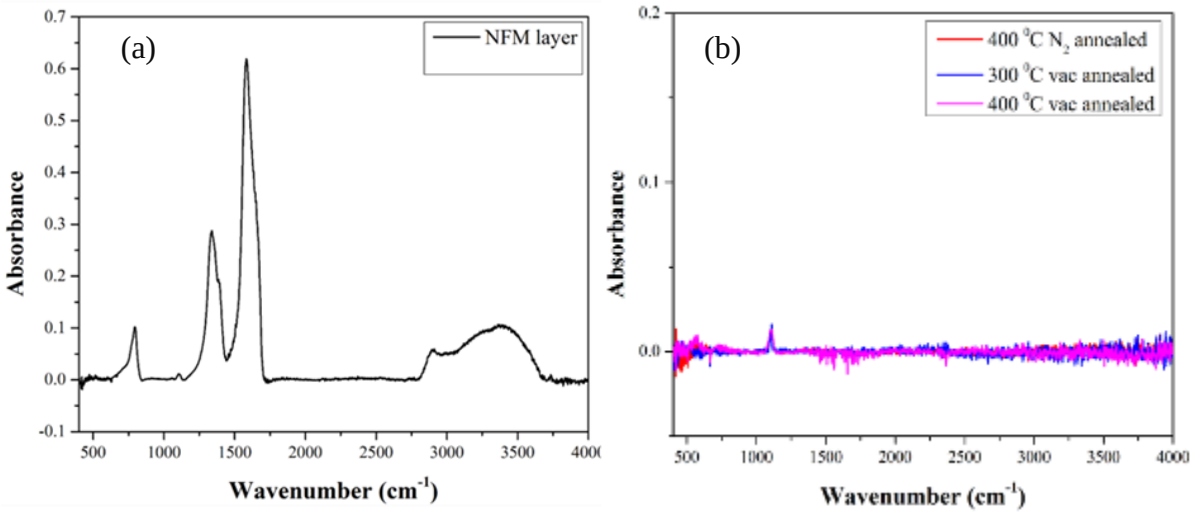

Figure 7-9. FTIR analyses of NFM (a) as-deposited and (b) decomposition at 300 ºC (blue) and 400 ºC (purple) in vacuum and 400 ºC (red) in nitrogen ambient.

It is obvious from Figure 7-9(b) that NFM decomposes to metallic Ni starting from 300 ºC without leaving metal oxide after decomposition. The assignments of the FTIR peaks for NFM are presented in Table 7-4.

Figure 7-10 represents the FTIR spectra for PdAc decomposition in various conditions.

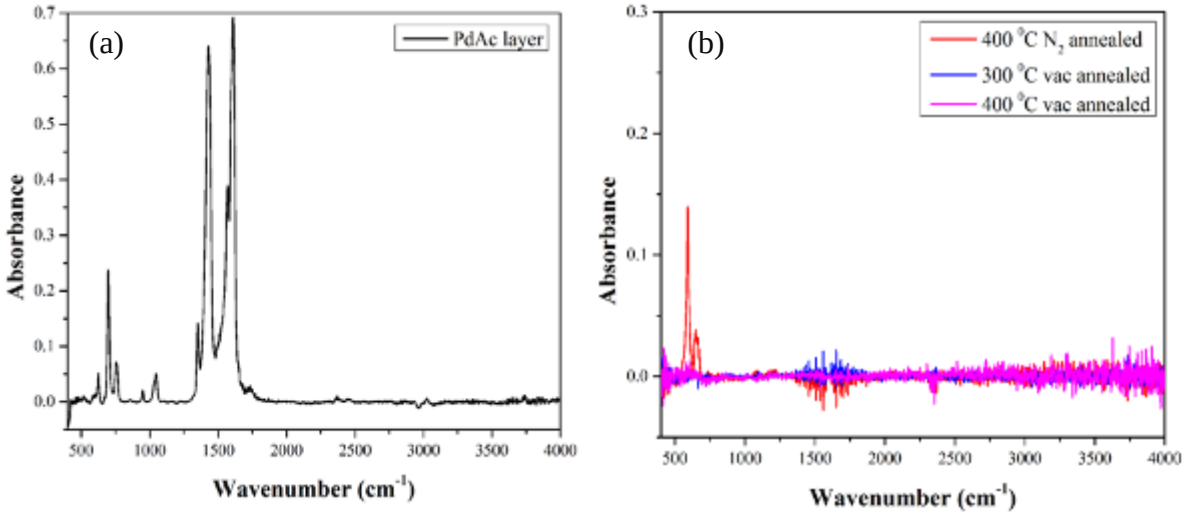

Figure 7-10. FTIR analyses of PdAc (a) as-deposited and (b) decomposition at 300 ºC (blue) and 400 ºC (purple) in vacuum and 400 ºC (red) in nitrogen ambient.

It can be seen from Figure 7-10(b) that two new bands appear at 590 cm^{-1} and 650 cm^{-1} for the sample annealed in furnace. These correspond to PdO and PdO_2 formations [302-303]. Whereas no oxidation of Pd metal takes place when the samples are annealed in vacuum. The FTIR peak assignments for PdAc can be seen in Table 7-4.

Table 7-4. The FTIR frequencies of MOCs and their assignments (ν-stretching, δ-in plane bending, π-out-of-plane bending, ρ-rocking) [78, 290-291, 304-313] ("sh" stands for shoulder).

$Ga(acac)_3$	PdAc	$NiAc{\cdot}4H_2O$	NFM	Assignments
581				ν(GaO),Ring defect
	625	619		ρ(COO),
682				ν(Ga-O), ν(C-CH3), Ring defect
	697	682		δ_s(COO)
775	757	-	796	π(CH)
937				ν(C-O)
	949	945		ν_s(C-CH3)
1021	1031sh, 1046	1030, 1049sh		ρ(CH_3)
1194				
1279				ν(C=C) ν(C-CH3)
1383			1339 1389sh	δ_s(CH_3) $\nu_s CO_2$)
	1359sh	1342sh		δ_s(CH_3)
	1430	1417		ν_s(CO_2)
1531, 1577sh				ν(C=C), ν (C=O), δ(C=CH)
	1568sh, 1577	1566	1584	ν_{as}(CO_2)
			2901	
2914 2992	2914 2992	2914 2992		ν_s(C-CH_3) ν_{as}(C-CH_3)
		2608-3700	2608-3700	ν(O-H), H_2O mode

In general, no metal oxide formation was observed via FTIR analyses (except for PdAc compound) during the Ni- and Ga- based MO decompositions in vacuum or in nitrogen environment. The latter contradicts the results from the TGA data. The reason of this contradiction might be the nitrogen partial pressure difference in the TGA system and in the furnace used for FTIR analyses. If the nitrogen partial pressure is high in the system/chamber then the oxide formation will be reduced.

The results from this section, including the low temperature for the MOC decomposition and the oxide free material formation in vacuum conditions serve a good basis for the attempt of utilisation of these materials as catalyst layers for Si nanostructure growth.

7.4.1.3. Palladium acetate decomposition imaging via the AFM

A thin layer of spin-coated PdAc MOC was investigated before and after its decomposition in air via AFM (Figure 7-11). The average thickness of the PdAc layer before and after decomposition was approximately 100 nm and 13 nm respectively (measured via AFM). The large surface feature on both AFM images in Figure 7-11 is a dirt particle (used for imaging the same section of the sample). It can be seen from Figure 7-11(b) that the thick smooth layer of PdAc disappears leaving grains behind. These are most likely PdO_x as the decomposition is taking place in air. This investigation shows that it is possible to achieve metal clusters as catalysts for nanostructure growth rather than smooth layer.

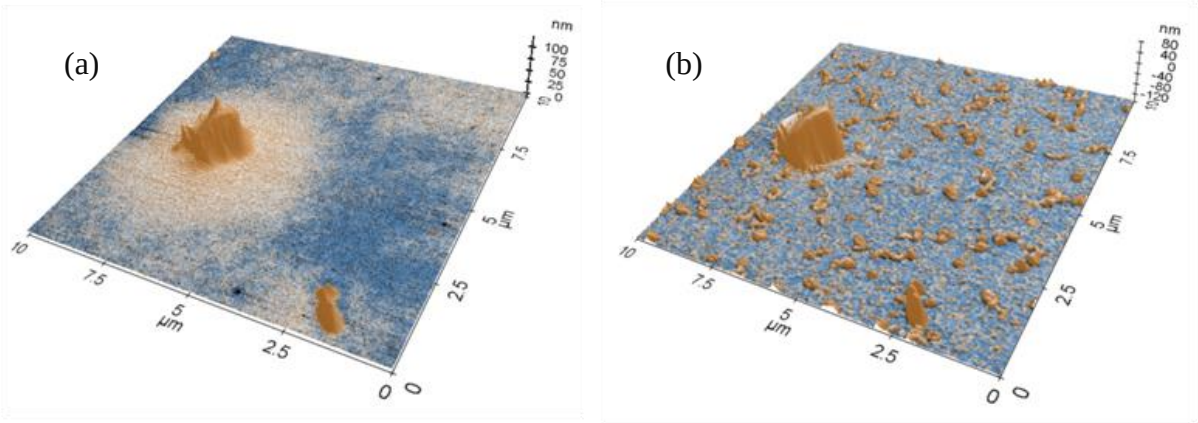

Figure 7-11. AFM images of PdAc decomposition on the Si substrate; (a) before and (b) after decomposition.

7.4.2. Silicon nanostructure growth attempt and discussion

This section represents the attempt to grow various types of nanostructures using the MOC layers as catalysts. The deposition process was carried out using the PECVD technique. A variety of metalorganic compounds can be tested for this purpose, but this work focuses on the nanostructure fabrication attempt from four types of MOCs discussed above; namely NFM, $Ga(acac)_3$, $NiAc{\cdot}4H_2O$ and PdAc. The results of the nanostructure growth attempt can be seen in Figure 7-12 where the 1D silicon nanostructure growth is clearly identifiable during the 10 minute PECVD deposition. The growth was performed at 400 ºC with "Standard" conditions defined in Table 7-2.

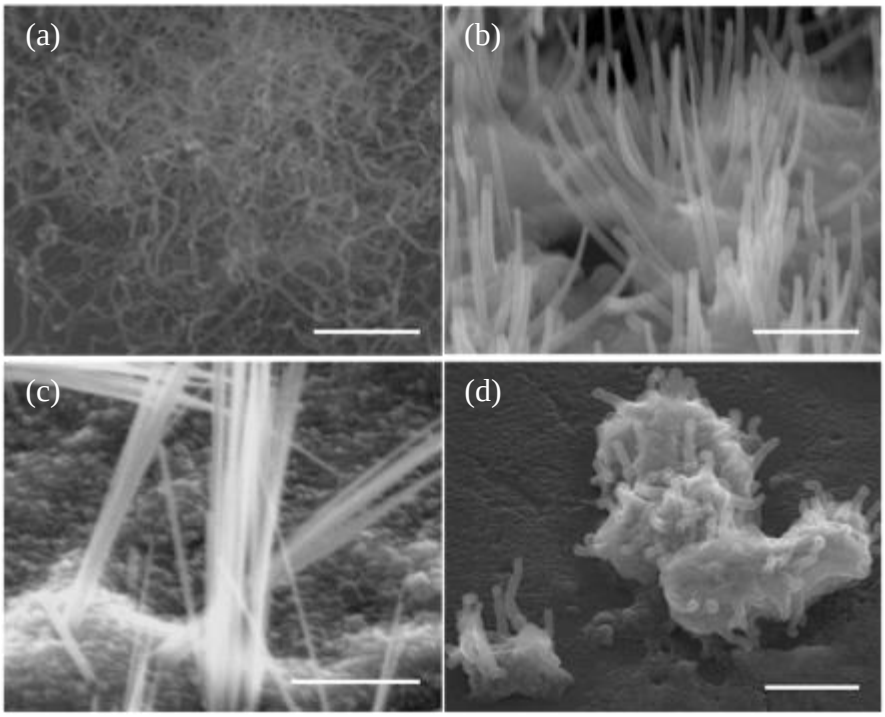

Figure 7-12. SEM images of 10 min growth of Si nanostructures from various MOCs as catalysts; (a) $Ga(acac)_3$, (b) NFM, (c) $NiAc{\cdot}4H_2O$, and (d) PdAc. The scale bars are all 1 µm.

It is evident from Figure 7-12 that the nanostructures grown from different catalysts show large differences in appearance. The nanowires grown from the $Ga(acac)_3$ layer are very long and curly (Figure 7-12 (a)), slightly curved/straight growth from NFM catalyst (Figure 7-12(b)), straight cluster growth from $NiAc{\cdot}4H_2O$ (Figure 7-12(c)), and shorter, thick and twisty nanostructures grown from PdAc (Figure 7-12(d)).

It is also noticeable that the nanostructures grow at different rates for each of the MOC layers. The curved nanostructure growth rate from NFM catalyst is roughly 300 nm per minute, that from $NiAc{\cdot}4H_2O$ is approximately 500 nm per minute, whereas around 50 nm

per minute growth rate was observed from PdAc catalyst layer. Due to the very curly structure of nanostructures grown from $Ga(acac)_3$ it is hard to give a conclusive estimate for the growth rate, even though it is obvious that the growth rate is very high in comparison to these from PdAc, NFM and $NiAc{\cdot}4H_2O$. The nanostructure diameters were also investigated and found to be larger at the bottom compared to the tops as can be seen in Figure 7-13.

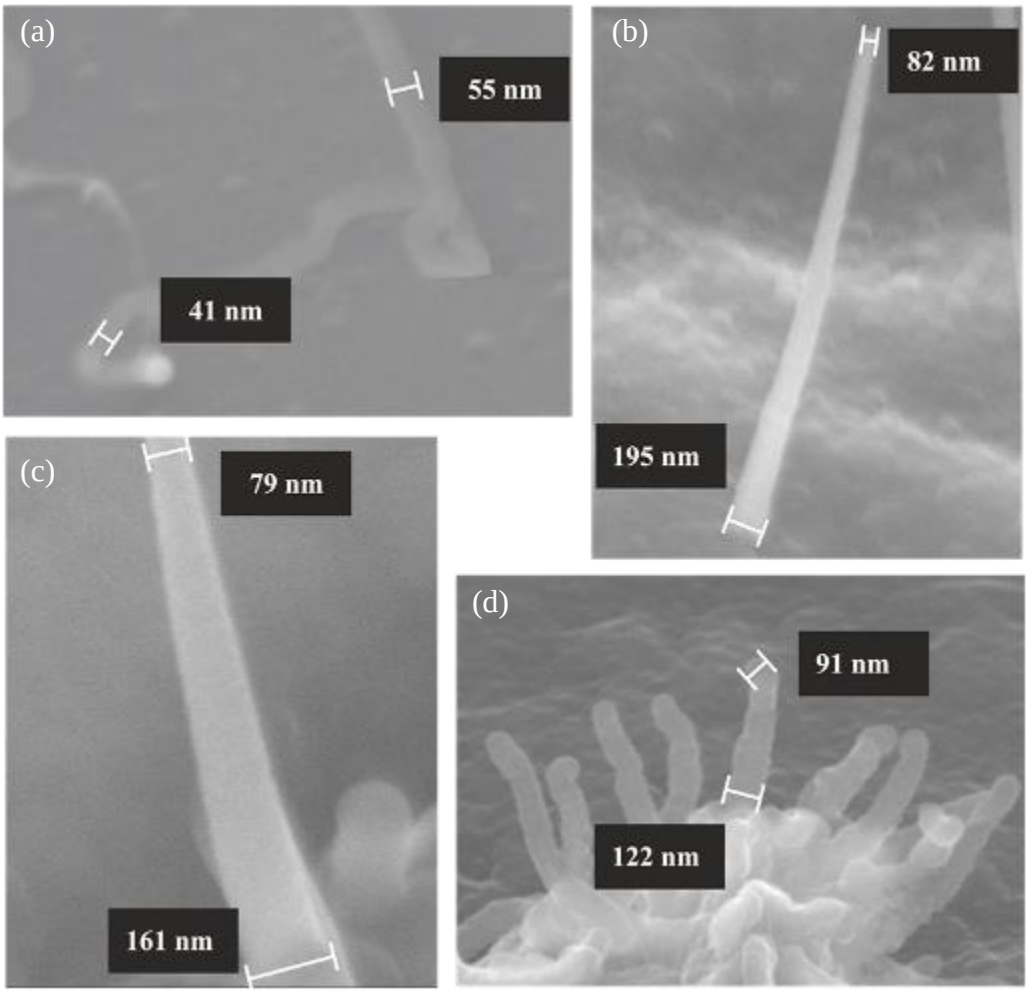

Figure 7-13. SEM images with diameters at the bottom and top of Si nanostructures for (a) $Ga(acac)_3$, (b) $NiAc{\cdot}4H_2O$, (c) NFM and (d) PdAc

Differences in the diameter across the 1D nanostructures can be attributed to two possibilities; continuous uncatalysed amorphous Si deposition on the sidewalls of nanostructures during the growth which is an unavoidable process during the PECVD deposition and causes tapering of the nanowires [232, 258, 273]. The other possibility of the nanostructure tapering, which would occur if the VLS growth mechanism took place, would be the consumption of the catalyst particle [221], hence the size reduction of the catalyst particle sitting on the tip of the nanostructure. It is generally accepted that in VLS growth the size of the catalyst particle determines the diameter of the nanostructure, hence the decrease

in the catalyst particle with time would cause the tapering of the nanostructures [237]. But as the growth of the nanostructures undertaken in this section takes place under the Si/appropriate metal eutectic temperature, the growth should not be following the VLS route (except for the Ga-based MOC) and therefore the abovementioned possibility is highly unlikely. In addition, no catalyst particle is observed on the tip of the nanostructures in the SEM images in Figure 7-13. In order to find out whether the tapering is caused due to the uncatalysed Si-deposition on the sidewalls of the nanostructures the high resolution TEM analysis would be the best choice of equipment. This investigation can be done in the future.

In order to understand the mechanisms that govern the growth of the nanostructures in this fabrication method, it is important to understand the role that catalyst layer is playing in the initiation and fabrication of the nanostructures.

With the purpose of finding out whether the in situ decomposition of the MOCs has a direct influence on the nanostructure growth, the pre-annealed samples of the MOCs used for the FTIR decomposition studies (samples from Figure 7-7 - Figure 7-10) were used for the attempt of the nanostructure fabrication. As a result, the Ni-based MOCs did not promote any detectable nanostructure growth (the SEM images can be found in Appendix B), whereas Ga-based compounds gave rise to nanowires (see Figure 7-14).

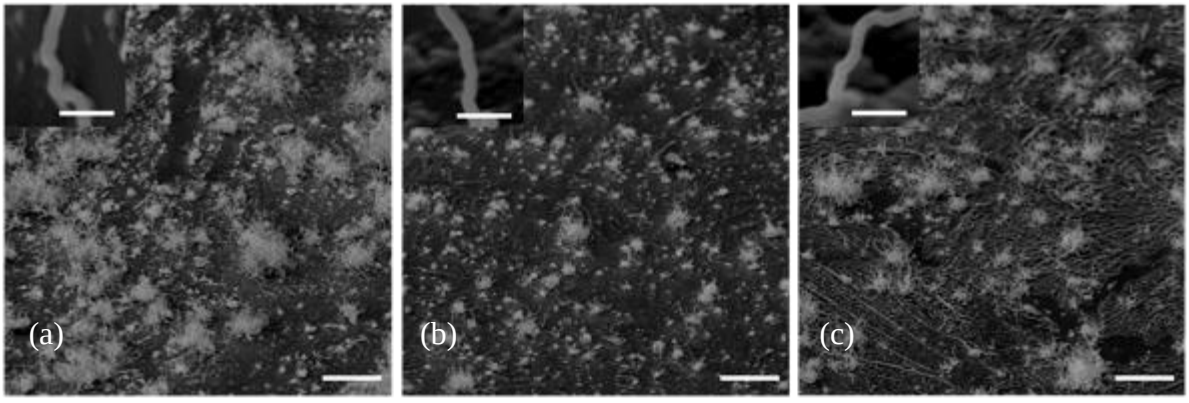

Figure 7-14. Si nanostructure growth attempted from pre-annealed $Ga(acac)_3$; annealed at (a) 300 ºC in vacuum, (b) 400 ºC in vacuum, and (c) 400 ºC in furnace in N_2 ambient, scale is 10 µm. Insets are higher magnification images of nanowires (scales of insets are all 500 nm).

It can be seen from Figure 7-14 that $Ga(acac)_3$ nanowires are growing from all the diversely annealed layers discussed above, but there is a noticeable difference in the density and size of the catalyst/nanowire cluster formations; these being larger and nanowires longer for samples annealed at 300 ºC. Despite the cluster size difference, the diameters of most of the nanowires of all the samples were in the same range (between 120 and 130 nm).

Palladium-based MOCs, when annealed prior to the growth of Si nanostructure process, result in some structures (Figure 7-15), however, these are substantially different structures to those which were observed for the MO catalyst in situ decomposition studies presented in Figure 7-13(d).

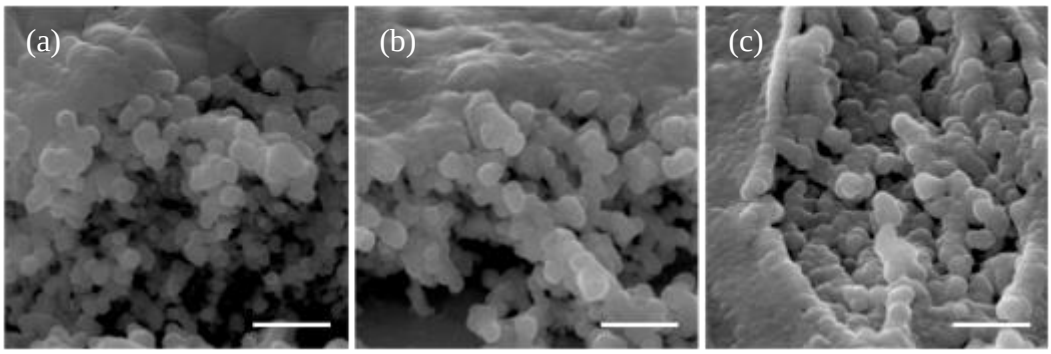

Figure 7-15. Si nanostructure growth attempted from pre-annealed PdAc; annealed at (a) 300 ºC in vacuum, (b) 400 ºC in vacuum, and (c) 400 ºC in furnace in N_2 ambient, scale is 1 µm.

In order to find out whether this drastic change in the 1D nanostructure growth performance from the Ni- and Pd- based MOCs was caused by the oxidation of the metallic catalyst layers in the air while the samples were undergoing FTIR analyses, a slightly different experiment was designed. In this experiment the heat treatment was still performed on the catalyst layers to assure the full decomposition of the MOCs for 30 minutes prior to the nanostructure fabrication. However, the samples were not removed from the vacuum chamber before the nanostructure growth, so were never exposed to temperature cycling, or atmospheric conditions. No hydrogen gas was used during this heat treatment process of the MOCs. After the initial decomposition step hydrogen was introduced into the chamber, followed by the hydrogen plasma for 5 minutes and then "Standard" growth conditions were used to attempt the growth of the nanostructures. The results of this experiment are shown in Figure 7-16.

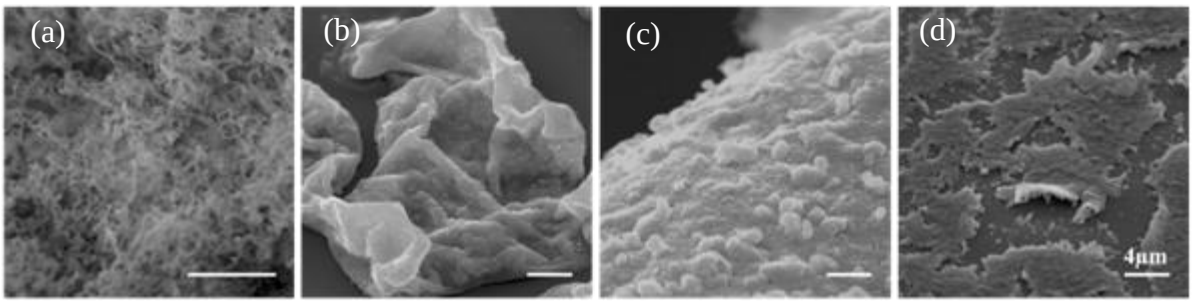

Figure 7-16. Si nanowire growth attempt from 30 min vacuum decomposed MOCs followed by the "Standard" Si nanostructure growth conditions; the compounds used were (a) $Ga(acac)_3$, (b) $NiAc{\cdot}4H_2O$, (c) NFM, and (d) PdAc. Scale bars are all 2 µm, except for the PdAc image.

It is obvious when looking at Figure 7-16 that the only SiNW growth has taken place from $Ga(acac)_3$ catalyst layer, whereas the rest of the MOCs did not initiate nanostructure growth when pre-annealed prior to the nanostructure growth step. The reason for the nanostructure growth results from Ga-based catalyst layer in contradiction to no growth from Ni- and Pd- based MOCs can be (i) low eutectic point for Ga-Si system, (ii) low Si solubility in Ga and (iii) low melting point of Ga. One of the experimental differences in this experimental setup was the lack of hydrogen gas environment when the samples were being heated and decomposed. Therefore, it could be possible that the main reason for the absence of the nanostructures was the lack of hydrogen pre-treatment of the sample.

In order to eliminate or confirm the possibility of the hydrogen pre-treatment of the catalyst being the cause for the lack of the nanostructure growth, an additional experiment was designed and conducted where the samples were heated till 400 ºC with no hydrogen in the chamber (as was the case for the previous experiment) and as soon as the growth temperature was achieved, hydrogen plasma was struck for 5 minutes followed by the "Standard" condition growth of the nanostructures. Therefore, the only difference between this and the previous experiment was the duration of the MO decomposition at 400 ºC. The images of the nanostructures grown at these conditions can be seen in Figure 7-17.

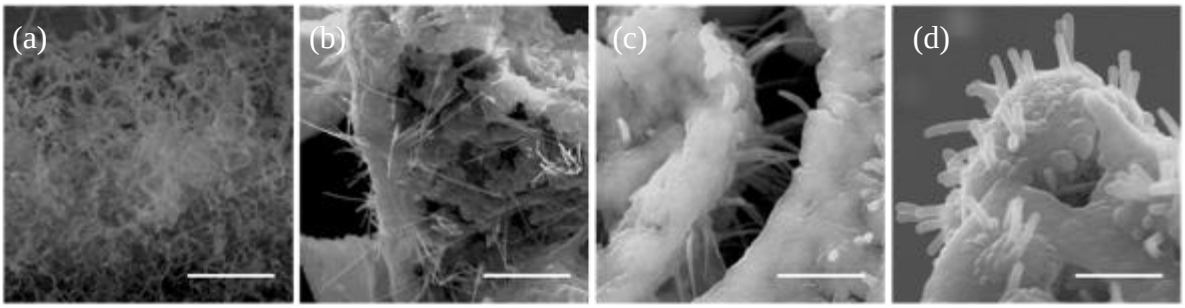

Figure 7-17. SiNWs grown from MOCs heated till the growth temperature in vacuum with no hydrogen present in the deposition chamber; MOCs used were (a) $Ga(acac)_3$, (b) $NiAc{\cdot}4H_2O$, (c) NFM, and (d) PdAc. Scale bars are all 2 µm.

It can be seen from Figure 7-17 that nanostructure growth was also achieved in a deposition condition where no hydrogen was present during the sample heating procedure. This confirms that the lack of hydrogen pre-treatment of the catalyst layers for the samples grown after 30 min pre-annealing of MO layer (Figure 7-16), was not the cause of the nanostructure growth suppression from Ni- and Pd- based catalysts.

As mentioned in the experimental section, the MOCs were deposited on substrates via few methods: dip-coating (for NFM and NFD as this process requires the catalyst to be

water-soluble), spin-coating (used for NFM and $Ga(acac)_3$), evaporation (for $Ga(acac)_3$ and NFM), thin-layer paint-brushing and drop-casting.

An interesting and important investigation was the discovery that MOC catalysed Si nanostructure growth required certain MOC deposition method to initiate the Si nanostructure growth. It was noticed that NFM required drop-casting to result in the nanowire growth, whereas no wires were observed from NFM layers deposited via the evaporation, spin-coating, paintbrushing or dip-coating methods (see Figure 7-18).

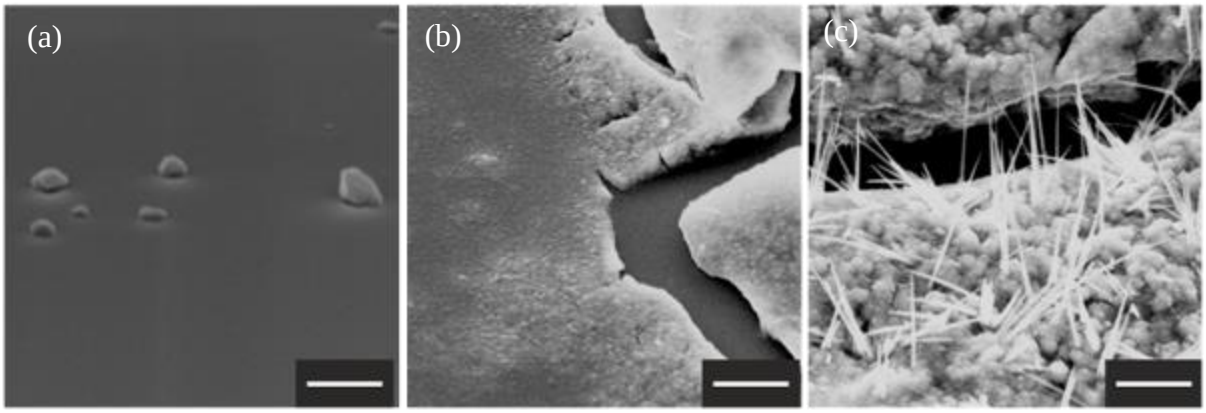

Figure 7-18. Attempt of SiNW growth from NFM layer using various deposition methods; (a) evaporation, (b) dip-coating, (c) drop-casting. Scale bars are all 4 µm.

It can be seen from Figure 7-18 that the only nanowire growth is observed from the drop-cast NFM layers, even though some of the dip-coated samples had several nanostructures grown at the rough and thick edges of the cracked layer (The SEM images of those are presented in Appendix B).

The preference for the nanowire growth from the PdAc catalyst was towards the paintbrush, whereas $Ga(acac)_3$ resulted in nanowire growth from all of its deposition methods including evaporated and spin-coated $Ga(acac)_3$ samples (the SEM images can be found in Appendix B). For its simplicity compared to the evaporation and spin-coating, and better uniformity compared to drop-casting method, paint-brushing was chosen as the general deposition technique for $Ga(acac)_3$ samples.

An interesting observation was also made with the NFM layer, where layers peeling off the substrate showed growth of the nanowires from the bottom side of the film (Figure 7-19).

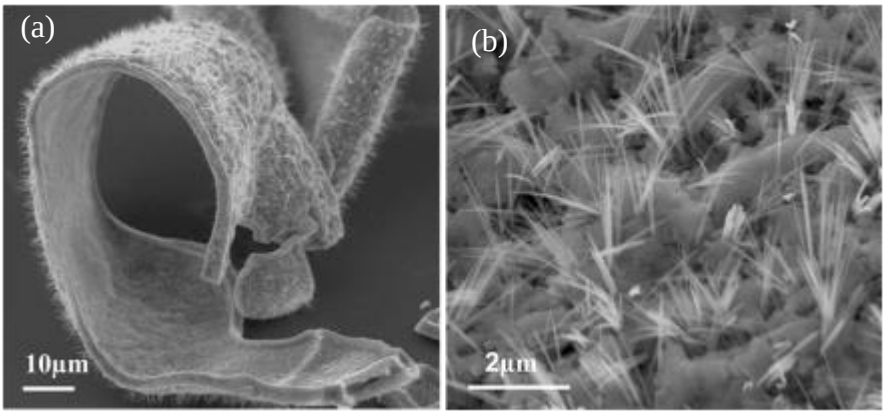

Figure 7-19. Low (a) and high (b) magnification images of SiNWs grown from drop-cast layers of NFM at "Standard" conditions for 10 mins.

As mentioned above, the drop-cast layers of NFM peeled off of the substrate and curved when heating the samples, with the nanowire growth taking place both from the bottom and from the top side of the film. However, a denser growth was observed from the bottom side of the seed layers compared to the top side (More images are available in Appendix B). In addition, it is observable from Figure 7-19(b) that the nanowire growth takes place from the rough holes in the film rather than the smooth surfaces. At this point it is difficult to conclude which process occurs first; whether the peeling off takes place due to the substrate heating and the MO layer property prior and independent to the nanowire growth or whether it is the influence of the nanowires growing downward and forcing the layer off the substrate. A growth mechanism will be suggested for this phenomenon later in this chapter. Considering that the decomposition temperatures for $Ga(acac)_3$, NFM and PdAc are below 300 ºC, Si nanostructure growth was attempted at 300 ºC.

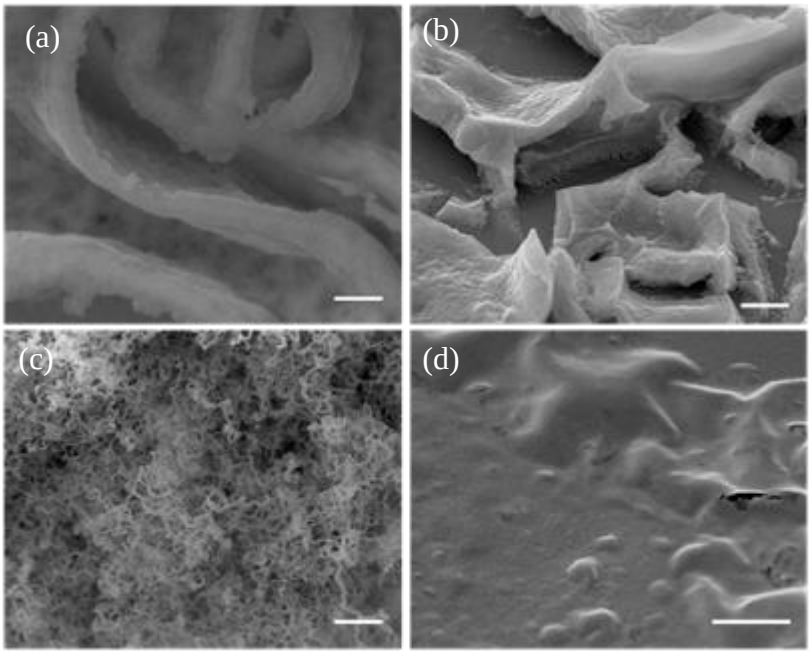

Figure 7-20. SEM images of SiNW growth attempts at 300 ºC from (a) NFM, (b) NiAc·4H_2O, (c) Ga(acac)$_3$, and (d) PdAc. The scale bars are 2 µm for (a-c) and 10 µm for (d).

Once again the nanostructure growth is only observed for Ga(acac)$_3$ sample (Figure 7-20 (c)). This experiment shows that the decomposition of the MOCs is not a sufficient condition for the initiation of the Si nanostructure growth and that a threshold energy (temperature) is required for the nanostructure fabrication. The threshold temperature for Ga(acac)$_3$ catalysed nanostructure growth is lower. This could be due to (i) its low melting point or (ii) low Si/Ga eutectic temperature compared to Pd and Ni metals leading to a VLS growth mechanism. But it is worth noting that the growth of the Si nanostructures from the Ga(acac)$_3$ compound does not take place via the exact same route as for the Ga-catalysed SiNWs as discussed in Chapter 6 where it follows catalyst at the top growth mechanism and the structures at 400 ºC are formations of branched nanostructures, whereas these grown from Ga-based MOC do not form branched nanostructures and show mainly catalyst at the bottom characteristics with some Ga cluster contamination/formation along the wire length and the tip as will be seen in the following section.

7.4.2.1. Backscattered images and EDS analysis

For the investigation of Ga(acac)$_3$ catalysed Si nanostructure composition and nature EDS spot analyses were performed for these samples (Figure 7-21).

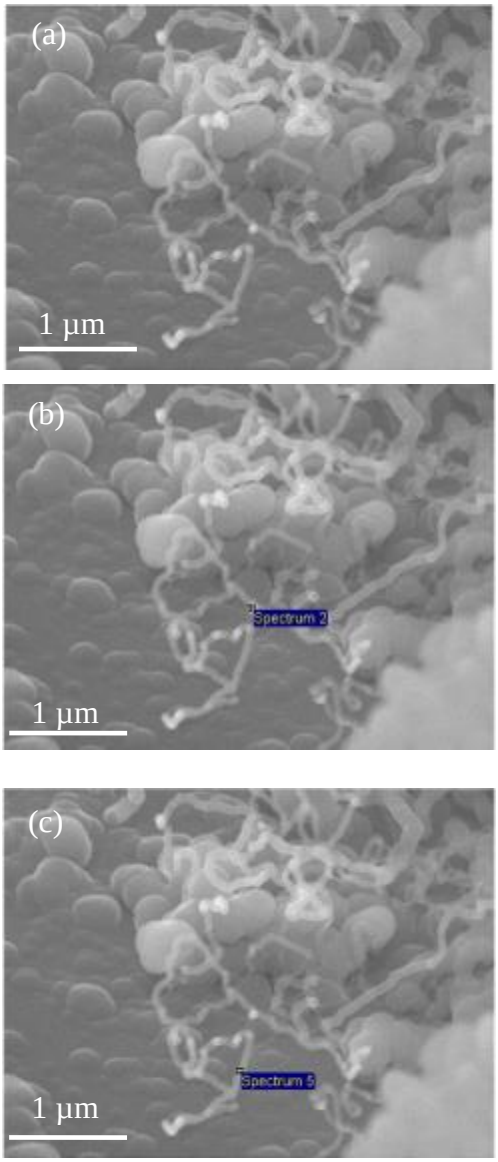

Element	Weight %	Atomic %
Si	67.42	52.70
Ga	0.14	0.04
O	26.39	36.20
C	6.05	11.06
Total	100	

Element	Weight %	Atomic %
Si	69.21	54.56
Ga	0.37	0.12
O	23.39	32.37
C	7.03	12.95
Total	100	

Element	Weight %	Atomic %
Si	68.88	53.64
Ga	0	0
O	22.69	31.01
C	8.43	15.35
Total	100	

Figure 7-21. EDS element analysis of Si nanostructures grown from $Ga(acac)_3$ catalyst material. The substrate is also Si.

It can be seen from Figure 7-21 that Ga clusters appear along the nanostructure length in the form of particles (or clusters), but these are not continuously distributed along the nanostructure length as is the case for the NFM catalysed nanostructures discussed below.

An interesting observation was made from the comparison of the secondary electron (SE) and backscattered electron (BE) images of silicon nanostructures grown from NFM as is shown in Figure 7-22. It can be seen that a brighter line is going across the nanostructure core. The brighter line in the BE image represents (i) a heavier element, which in case of using NFM MOC could be Ni instead of Si or (ii) a denser crystal formation of the same

element.

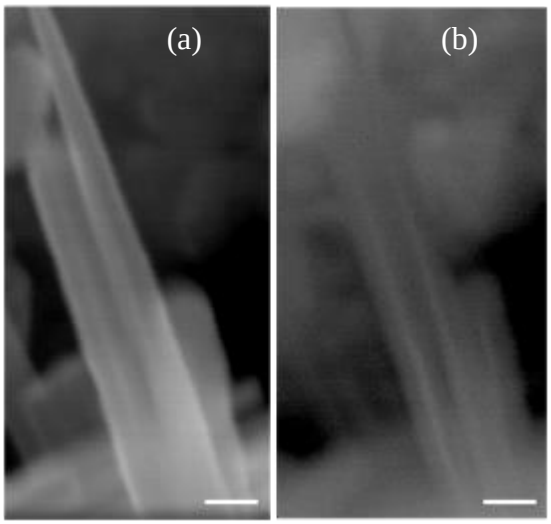

Figure 7-22. Secondary electron (a) and backscattered electron (b) images of Si nanostructures grown from NFM MO catalyst. Scale bar is 100 nm for both images.

In order to find out the material and nature of the bright lines, the EDS analyses were performed on the nanowires that were scratched from the sample directly onto the conductive carbon tape. The EDS results in a form of the element maps can be seen in Figure 7-23.

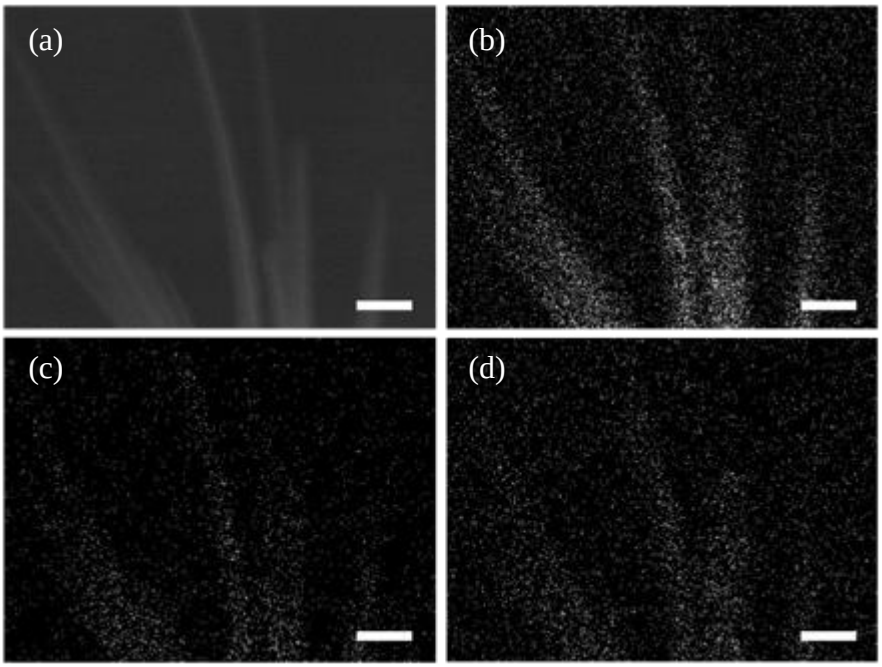

Figure 7-23. EDS images of the nanostructures grown from NFM catalyst layer; (a) backscattered electron image, (b) silicon map, (c) nickel map and (d) oxygen map. Scale is 200 nm for all the images.

It is now definitely clear that there is Ni and O in the nanostructures (Figure 7-23 (c, d)). These results suggest that the nanostructure could be Ni silicide or Ni disilicide rather than being pure Si nanostructure [314-316] or be contaminated with Ni, the latter being inside or

on the surface of the nanostructure (resulting in the consumption of the catalyst as mentioned earlier). It is known that nickel can diffuse into silicon at temperatures higher than 300 °C forming silicide [247]. In order to form final conclusion on the composition of the nanostructures, it is important to do further analysis on the nanostructures.

It is also observable that the concentration of Ni is less and more concentrated in the centre of the wires compared to Si (Figure 7-23 (b)). Therefore, it is possible that Ni is (i) forming the nanowire core by itself (if this was the case the growth of Ni nanowires would also take place without silane gas. This experiment was performed without any type of growth observed), (ii) forming Ni silicide nanowire or (iii) just a contaminant appearing in the Si nanowire. All of these nanowires however seem to have a thicker outer layer made of Si shell most likely being a-Si. The oxygen concentration most probably is native oxide formed on the Si nanostructure surface. Spot analyses on the nanostructures were performed via the EDS (Figure 7-24), but unfortunately, the spot size of the EDS beam is one μm therefore the attempt to investigate the material dispersion within a nanostructure that is under 100 nm in diameter would not be precise.

After performing EDS analyses, from the tables in Figure 7-24 it is proven that Ni concentration is definitely less compared to Si concentration in the nanowire. But again, it is important to keep in mind that the spot size of the EDS beam is one μm and the nanostructure diameter is around and below 100 nm, therefore introducing errors in the estimation of the element dispersion. In addition, if the nanowire is covered with an a-Si shell then the amount of Si from the shell will also contribute to the Si percentage in the EDS results.

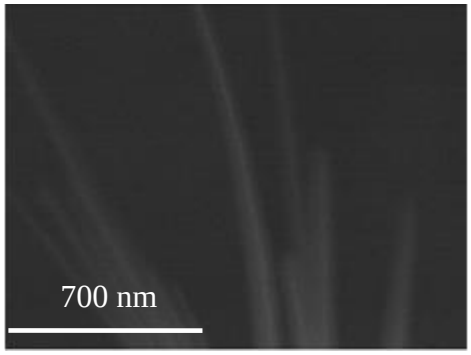

Element	Weight %	Atomic %
Si	1.53	0.69
Ni	1.35	0.29
O	9.17	7.23
C	87.02	91.36
Na	0.44	0.24
S	0.48	0.19
Total	100	

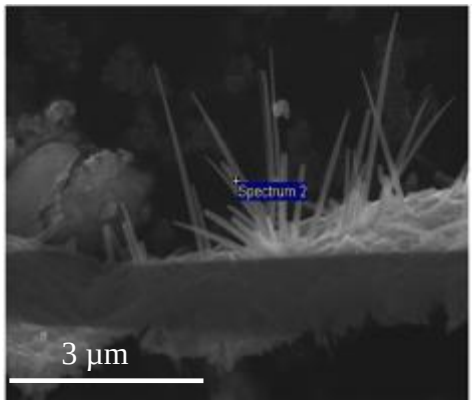

Element	Weight %	Atomic %
Si	2.67	1.23
Ni	3.18	0.70
O	11.27	9.12
C	82.1	88.56
Na	0.41	0.23
S	0.38	0.15
Total	100	

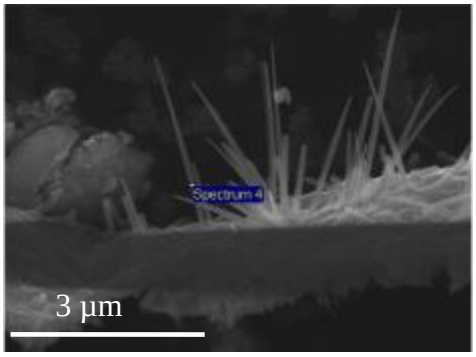

Element	Weight %	Atomic %
Si	2.30	1.06
Ni	2.69	0.59
O	11.52	9.28
C	82.75	88.73
Na	0.36	0.2
S	0.37	0.15
Total	100	

Figure 7-24. EDS element analysis of Si nanostructures grown from NFM catalyst material.

Considering that both NFM and $NiAc{\cdot}4H_2O$ are Ni- based materials, the EDS analyses for $NiAc{\cdot}4H_2O$ catalysed nanostructures were also performed to compare with those from NFM (Figure 7-25).

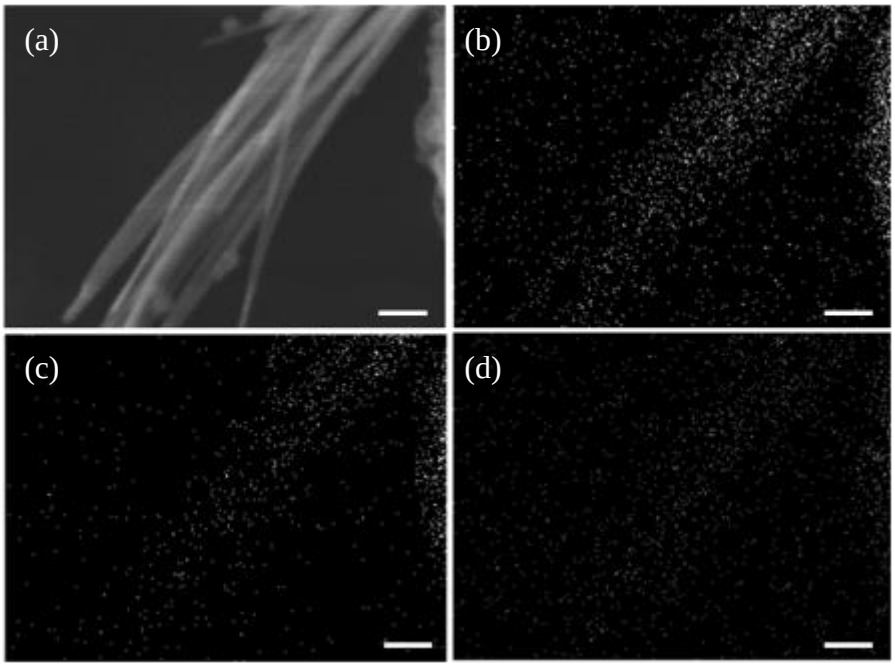

Figure 7-25 EDS images of nanostructures grown from NiAc·4H_2O catalyst layer; (a) backscattered electron image, (b) silicon concentration, (c) nickel concentration, and (d) oxygen concentration. The scale bar is 200 nm for all the images.

It can be seen from Figure 7-25 that nanowires grown from NiAc·4H_2O also have similar nature to those from NFM. They also have Ni element embedded in their structure, therefore suggesting that the growth mechanism for both Ni- based MOC catalysed nanowire growth is the same.

The EDS analyses for the PdAc- catalysed nanostructure growth were performed on the Si substrate and therefore the results were not clear and precise, and will not be presented in the current work.

Growth of the nanostructures at the same PECVD conditions was simultaneously attempted from the evaporated layers of Ni and NiO which held no nanowires. The images of these samples can be seen in Appendix B. This also suggests that the MOC in situ decomposition does indeed play a major role in the formation and initiation of the 1D nanostructure growth from the corresponding metallic elements at 400 ºC.

7.4.2.2. Crystallinity investigation

The samples of $Ga(acac)_3$ and NFM were subjected to Raman spectroscopic analysis to investigate the crystallinity of the nanostructures. It is reported in literature that crystalline silicon (c-Si) has a sharp first-order optical mode (1TO) Raman peak at 520 cm^{-1} (due to scattering of first-order optical phonon of c-Si [278]) whereas there is a broad peak

representing amorphous Si (a-Si) that is at around 480 cm^{-1} [276, 317-318]. The Raman spectra of the nanostructures grown in this work from $Ga(acac)_3$ is presented in Figure 7-26.

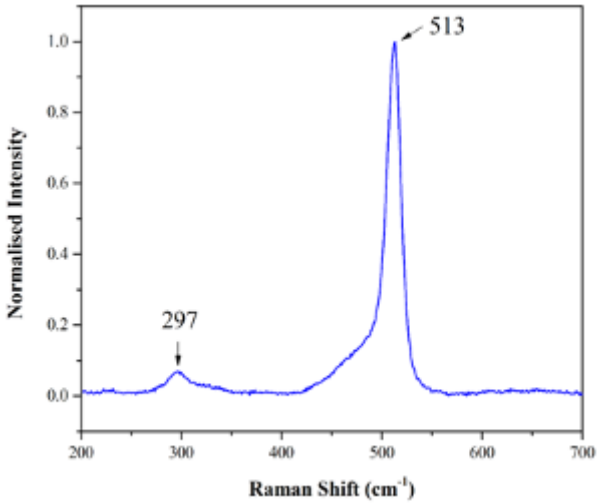

Figure 7-26. The Raman spectra of Si nanostructures grown from $Ga(acac)_3$ catalyst layer.

It is noticeable from Figure 7-26 that there is a sharp c-Si peak at 513 cm^{-1} with a small shoulder on the left representing a-Si. The absorption peak at about 300 cm^{-1} observable in Figure 7-26 is also assigned to c-Si [275].

The separate a-Si and c-Si peaks can be obtained by deconvoluting the spectra via curve fitting procedure (see Figure 7-27).

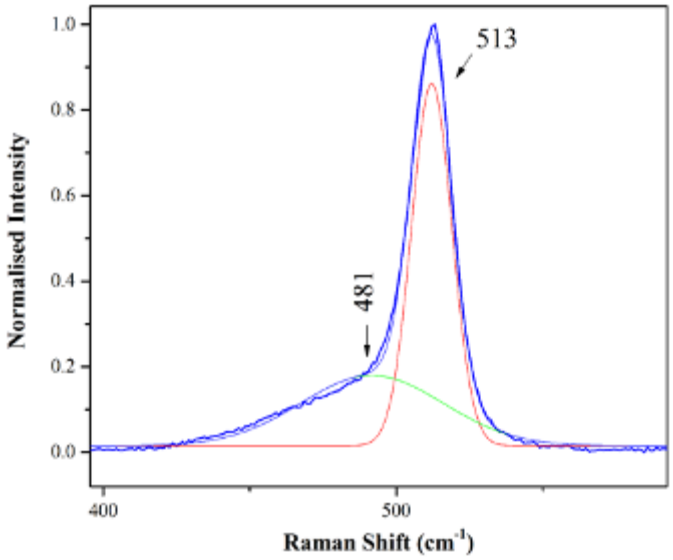

Figure 7-27. The deconvoluted spectra of Si nanowires grown from $Ga(acac)_3$ catalyst layer.

The sharp peak at 513 cm^{-1} proves that the nanostructures are crystalline. A characteristic amorphous peak at around 481 cm^{-1} is also showing that in addition to crystalline

nanostructure growth there is simultaneous a-Si deposition during the PECVD growth (parasitic a-Si deposition).

It is known that for nanocrystalline silicon with decrease of the grain size the frequency shift increases and the Raman peak becomes larger and more asymmetric [277]. Therefore, the frequency shift, full width at half maximum (FWHM) and the symmetry of the 1TO peak of the nanowires grown in this work were measured from the Raman spectra. The results are shown in Table 7-5. The broadening coefficient (C_b) was calculated from $FWHM_{SiNW}/FWHM_{c\text{-}Si}$, whereas the asymmetry coefficient was calculated from LWHM/RWHM where LWHM (and RWHM) are Left (and Right) width at half maximum.

Table 7-5. The Raman frequency, the frequency shift, FWHM, the coefficient of broadening and the asymmetric coefficient of SiNWs grown from $Ga(acac)_3$ catalyst layer in comparison to those of c-Si reported by Sharma *et al.* [278].

Sample	Raman frequency (cm^{-1})	Frequency shift (cm^{-1})	FWHM	C_b	C_a
c-Si	521.08	0	4.0831	1	1
SiNW from $Ga(acac)_3$	513.26	7.82	16.5	4.04	1.56

It can be seen from the results of 1TO Raman peak analysis (Table 7-5) that the peak has undergone downshift as well as asymmetric broadening indicating phonon quantum confinement effect. Unfortunately, the red-shifting of the 1TO peak from 520 cm^{-1} and the asymmetric broadening can also be attributed to the usage of high laser power during the analysis, in particular 5 Watts, which causes local heating of the nanostructures, possibly damage and red-shift [279-281, 319]. For this reason, it is difficult to confidently conclude that the shift and asymmetric broadening are due to quantum confinement effect.

To conclude, Raman analysis of the sample of Si nanowires grown from $Ga(acac)_3$ shows that SiNWs are crystalline in nature with mixture of a-Si layer possibly covering the nanowires and the sample surface.

The Raman spectra of the nanowires grown from NFM layer can be seen in Figure 7-28.

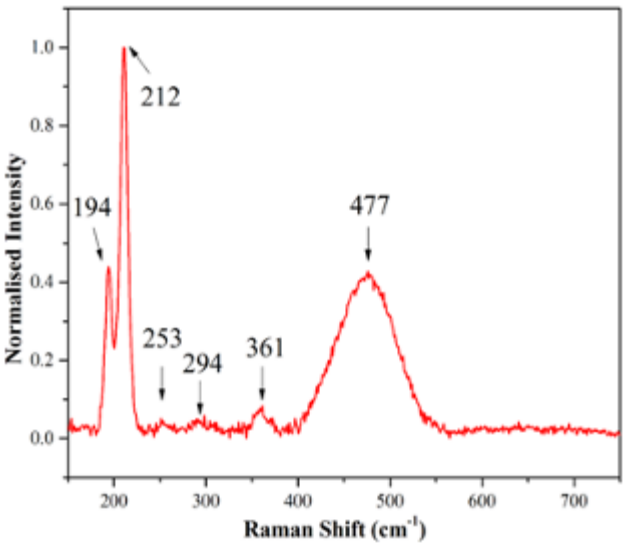

Figure 7-28. The Raman spectra of Si nanostructures grown from NFM catalyst layer.

There is an obvious peak at 477 cm^{-1} that corresponds to the amorphous silicon. There also are strong peaks observed at 194 cm^{-1} and 212 cm^{-1} with lower intensity peaks at 253, 294 and 361 cm^{-1} which correspond to Ni silicide (NiSi) film and/or powder formation [320-323]. Ni_2Si peaks are at around 100 cm^{-1} and 140 cm^{-1} [324], therefore it is not possible to find out whether these structures are formed or not. From the Raman spectra several scenarios are possible; (i) Ni silicide nanowire growth, (ii) amorphous nanowire growth from a Ni silicide catalyst layer (hence Raman showing the peaks of the layer), and (iii) small amount of crystalline SiNW growth (thus not noticed via Raman spectroscopy) in comparison to high percentage of Ni silicide catalyst material and a-Si parasitic deposition. It is also possible that the laser beam is not actually analysing the nanowire but the film surrounding it in which case it would be Ni silicide covered by a-Si deposition.

To investigate the crystallinity of the nanostructures grown from NFM catalyst layer, the sample used for Raman analysis (SiNWs grown from NFM) was subjected to TEM analysis (see Figure 7-29).

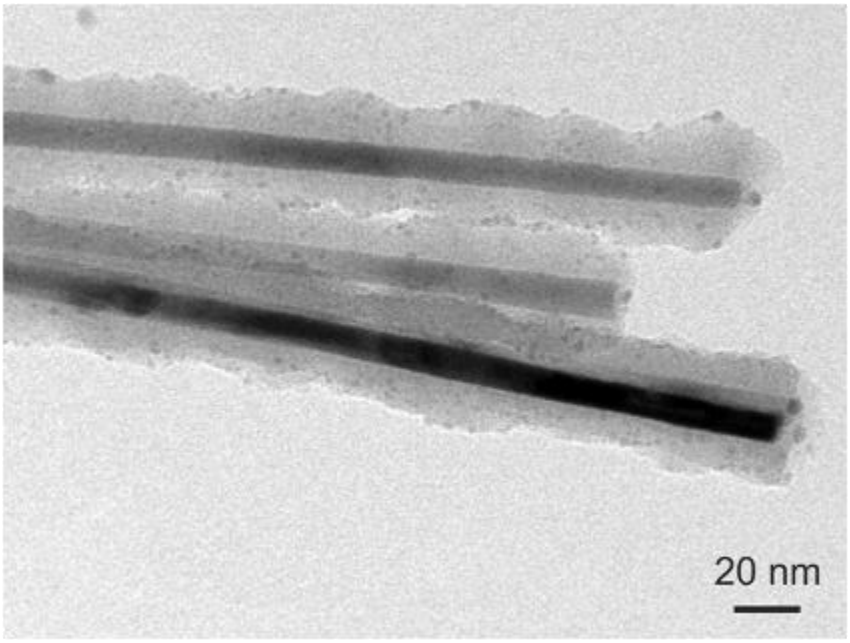

Figure 7-29. TEM image of Si nanostructures grown from NFM catalyst layer.

The core/shell structure observed in Figure 7-22 is immediately visible in Figure 7-29 thus confirming the SEM results. In order to investigate the crystallinity of the nanostructures, selected area electron diffraction (SAED) analysis was performed on the nanostructure. The diffraction pattern obtained can be seen in Figure 7-30.

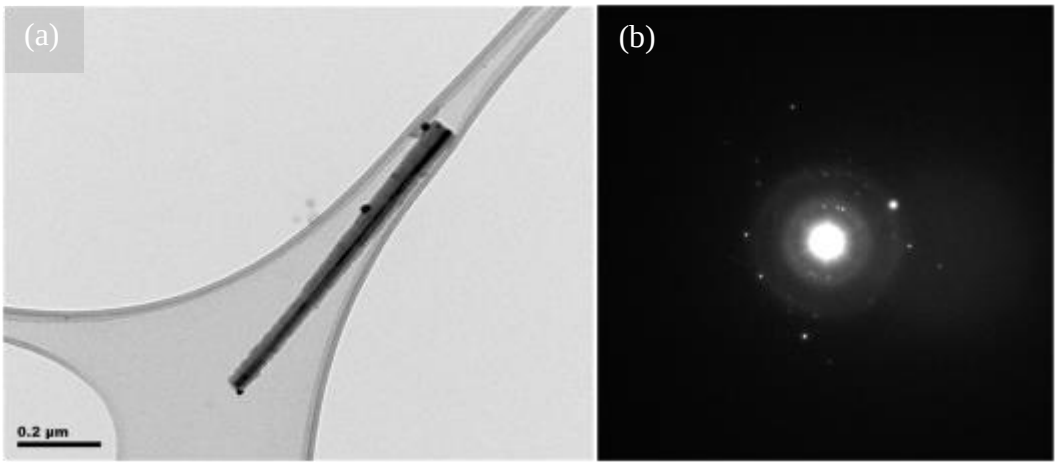

Figure 7-30. (a) TEM image and (b) corresponding SAED pattern of Si nanostructure grown from NFM catalyst layer.

It can be seen from Figure 7-30(b) that the diffraction pattern represents rings and bright spots representing crystalline structure for the nanostructure [7, 27]. Unfortunately, it was not possible to calculate the d-spacing of the lattice planes from the diffraction pattern due to the TEM not being calibrated. The calculation of the d-spacing would give an understanding

whether the Ni-silicide is formed or Si nanowire with Ni impurities. However, the SAED results indicate that the nanostructure has definitely got a crystalline structure.

When comparing the EDS, Raman and TEM results for the Si nanostructure growth from Ni- based MOCs, two possible cases are left for consideration; either (i) Ni silicide nanowire core growth with a-Si deposition on the sample, or (ii) c-Si nanowire growth with Ni contamination from a Ni silicide catalyst and a-Si deposition across the sample.

7.4.3. Suggestions for the nanostructure growth mechanisms from the MO compounds

From the results obtained in this chapter it is obvious that there are still many open questions to be investigated in order to have a final understanding about the MOC catalysed nanostructure growth mechanism and nanostructure nature. It was shown that in situ decomposition of MOCs during nanostructure growth in the PECVD reactor is of critical importance as to whether the nanostructures will grow or not. The full understanding of this phenomenon requires further research but several assumptions can be made. First of all, it is clear from the temperatures used that no material in liquid form is present for the nanostructure growth from Ni- and Pd- based catalysts, whereas Ga is in its liquid form at the growth temperatures used in this chapter. Therefore, the suggestions for the growth mechanisms can be divided into two groups; one for the $Ga(acac)_3$ catalysed growth and the second group for Ni- and Pd- based catalyst materials.

For $Ga(acac)_3$ based samples the nanowire growth is most probably governed by the VLS method as after the MOC decomposition the remaining Ga is in its liquid form at the fabrication temperatures. In addition, the wormlike structure of the wires remind of those grown from evaporated Ga layers. The difference in the nanowire growth from the MOC is the lack of Ga particle on the top of most of the wires, instead it exists along the nanowire length, suggesting that it was consumed during the growth. In addition, Ga was left at the bottom of the nanowires implying that the growth of the nanowires took place via local supersaturation from the Ga clusters that were left after the MOC decomposition.

For the Ni- and Pd- based MOCs the VLS and SLS growth possibilities are excluded due to the used fabrication temperature. The most likely possibility of the growth mechanism involves the VSS growth. But the VSS mechanism alone cannot be responsible for the growth otherwise the nanostructure growth would also be observed from the evaporated layers of Ni and/or NiO.

Two processes that are possibilities to influence the growth of the nanostructures from these MOCs are described below.

1) During the MOC decomposition there are active sites on the compound that have just lost their bonds with the organic compound and are in favourable condition for reacting with Si ions in the environment creating a solid alloy (Ni silicide). Whereas, if the process of the precursor gas introduction into the chamber takes time, these sites get deactivated by interacting with neighbouring Ni clusters forming a smooth layer thus hindering the nanowire initiation and growth.
2) Another possibility is the certain sized cluster formation of metals during the MOC decomposition which are favourable for absorption of silicon vapour (undergoing local supersaturation) for the VSS growth initiation. However, with time the size of these clusters enlarges causing longer incubation time which is not sufficient for the nanostructure growth prior to the a-Si coverage. The fact that no nanostructure growth was observed from the evaporated Ni layer and the smooth side of the NFM layer after its decomposition additionally supports this mechanism. Evaporated Ni, being a continuous smooth layer, is harder to get locally supersaturated, therefore just gets covered with a-Si layer instead.

The observation of high density nanowire growth from the bottom side of the peeled layers of NFM could be due to; (i) the fact that due to the bottom side of the layer being in contact with the substrate, Si from the substrate starts its diffusion into Ni forming silicide compound before the introduction of silane. Therefore, the incubation time for this side of the layer is less in comparison with the top side of the layer. Due to this effect the top layer can get covered with a-Si before the incubation period is finished (due to slow diffusion of the gas particles into the solid catalyst layer) thus causing termination of the nanowire growth process. The observation of the more uniform top surface layer might be associated with the a-Si coverage. (ii) Another explanation may be due to the bottom side of the layer getting to the decomposition temperature before the top side of the layer. In this case the growth will start from the bottom side of the layer whereas the top side of the layer will get covered with a-Si inhibiting the growth. (iii) Alternatively, the top side of the MOC layer could undergo decomposition accompanied by formation of smooth surface which is not favourable for nanowire growth initiation. This effect (no nanowire formation) can also be seen when attempting to grow Si nanowires from uniform layers of NFM, such as dip-coated or spin-coated. But the difference in the growth performance from dip-coated and drop-cast samples

can also be conditioned with the thickness of the layer, availability of Ni particles involved in case of Ni silicide nanostructure growth.

Another question that was opened by this chapter is the understanding of the Ni- based MOC catalysed Si nanostructure nature, whether they are Ni silicide nanostructures or Ni-contaminated Si nanostructures grown on Ni silicide substrate. It might be possible to find this out in the future by calculating the d-spacing from the SAED images as this value is specific to the crystal structure of each material/compound.

Having novel materials and fabrication steps involved, there are many open questions and suggestions for the possible growth mechanisms taking place during the nanostructure initiation and formation. This is an interesting and promising branch in nanomaterial fabrication techniques that opens up new horizons and doors for further investigation within many researchers and groups working in the field.

7.5. Conclusions

A new type of catalyst materials were used for the growth of Si nanostructures via the PECVD technique. It was discovered that different MOCs result in diverse nanostructure shapes depending on the catalyst material choice, therefore this method has the potential to raise the opportunity for the controlled growth of nanostructures of different shapes.

It was observed in this chapter that Ga- based MOCs result in crystalline curved nanowires (grown via the VLS mechanism) with higher growth rate compared to that of Ni- and Pd- based nanostructures (grown via the VSS mechanism). In addition, it was discovered that in order for the Ni- and Pd- based nanostructures to yield Si nanostructures an important factor is their in situ decomposition during the growth. In addition, the nanostructures catalysed by Ni- based MOCs have core/shell structures. Based on the EDS, Raman and TEM analyses two possibilities are suggested (i) c-Si nanowire growth from Ni silicide catalyst layer with Ni contamination along the nanowire or (ii) Ni silicide nanowire growth. In both cases it is suggested that the core is surrounded by an a-Si shell.

Due to the novelty of this work there are still many unanswered questions being raised by this chapter. Some obvious questions, such as the nanostructure composition and crystallinity, as well as the role of the in situ decomposition of MOC during the nanostructure growth were discussed. Two growth mechanisms are suggested. The first one suggests the availability of newly created active bonds in Ni- based MOC from ligand evolution for forming Ni- silicide compound. The second mechanism suggests the size of the Ni cluster formation (with the

MOC decomposition) to play the main role. These clusters are suggested to get supersaturated with Si resulting in nanostructures, and with increased time these clusters get larger requiring longer time for supersaturation thus resulting in no nanowire growth. However, systematic theoretical and experimental analyses are required for the in depth understanding of the MOC/Si nanostructure systems.

Chapter 8

Silicon nanowires application in gas sensing

"Everything should be made as simple as possible, but not simpler."

... Albert Einstein

The first part of this chapter gives an overview of the research done in the field of SiNW-based gas sensors with the focus being on the sensors operating as resistors. Various sensor structures are presented that have been reported in the literature and the suggested sensing mechanism discussed.

The second part of the chapter demonstrates the gas sensor fabrication during this PhD project. The gas sensors were fabricated for isopropyl alcohol (IPA) vapour detection using SiNWs grown using Ga and $Ga(acac)_3$ as catalyst layers and compared to amorphous Si layer based devices.

This chapter does not aim to provide thorough analysis of the gas sensors fabricated in this work, such as detection of various gases, improved sensitivity or selectivity compared to reported sensors, but an initial attempt to show the potential of the SiNWs grown in this work for gas sensor application.

8.1. Introduction

The research into silicon nanowire-based chemical sensors is quite new. The first report of silicon nanowire application in chemical sensing was published by Cui *et al.* [325] in 2001. Apart from being compatible with current silicon based devices, SiNWs have good biocompatibility and affinity to environment, fast response, good reversibility, and oxide-coated or H-terminated surface, allowing easy attachment to various functional groups [208, 216]. High surface to volume ratio of SiNWs makes their surface characteristics dominant in determining their physical properties including electrical, optical and thermal. From these characteristics electrical conductivity of SiNWs is a unique property of interest in comparison to bulk Si. It is possible to change the surface characteristics of the nanowires via chemisorption due to electron exchange between surface absorbents and the nanowire [208]. Due to these characteristics SiNWs have been used as nanostructured electrodes to promote direct electron transfer between biomolecules and electrodes [216].

It is possible to tune electronic properties and sensitivity of SiNWs by changing the dopant concentration and nanostructure size correspondingly. The challenge with SiNWs is the spontaneous oxide layer formation which limits the stability of the material in ambient conditions [68].

Various types and structures of gas sensors have been reported by various researchers and research groups using SiNWs. These structures will be demonstrated further in this chapter. In general, several types of interactions of the analyte gases with the semiconductor surfaces may occur. One type of interaction is the reduction (oxidation) of the semiconductor by the analyte. This interaction occurs for non-stoichiometric materials, thus applying to materials made of more than one element. Ion exchange is another type of interaction which may occur for oxide semiconductors. The third type of interaction takes place via adsorption [48]. Out of the listed methods, the most quoted detection method (which also should be valid for SiNWs) is based on adsorption, the direct binding of gas species onto the Si surface [48]. The gases with species that withdraw electrons from the p-Si are oxidising gases, these include NO_2 and N_2O. This group of gases gets adsorbed on the semiconductor surface and withdraw electrons, causing hole accumulation or electron depletion thus causing increase in conductance. The reducing gases such as NH_3 and H_2 act in the opposite manner by donating electrons to the Si causing hole depletion and electron accumulation, therefore decrease in conductance of p-Si [326-327]. If n-Si is used, then the same gases will have the opposite effect on the conductance. Due to this electron exchange between the gas molecules and Si, it is possible to detect these gases by measuring the conductance response of the SiNWs.

There are several reports in the use of SiNW gas sensors exploiting various transduction mechanisms in the literature. Guo *et al.* [328] used polymer-coated micro-diaphragm incorporated with piezoresistive SiNWs for the sensor. In the aforementioned report the polymer became swollen by absorbing the chloroform vapours and resulted in bending the SiNWs. The output response was the voltage change exploiting the piezoelectric behaviour of the SiNWs. Song and Zhu reported SiNW based gas sensors based on small defect in silicon waveguide [329]. These small defects can produce a strong resonance with the incident light. The sensor works by measuring the resonant peaks which are sensitive to the air composition. Transistors based on SiNW channels have also been demonstrated as gas sensors [330]. The most popular and easy to fabricate gas sensor incorporating SiNWs is the two terminal resistor made of SiNWs. In this structure the nanowire(s) is grown between two electrodes across which a constant DC voltage is applied and the current (resistance) measured. The sensing occurs via absorption of the analyte onto SiNWs altering the value of the device

resistance. The different resistor gas sensor structures based on SiNWs reported in the literature are discussed in more details in the following subsection.

8.1.1. Silicon nanowire based resistors as gas sensors

Not many device structures for resistor gas sensors based on SiNWs have been reported to date, but a very high sensitivity has been achieved using these sensors. The main difference between the variety of SiNW-based gas sensors is the different growth methods applied for SiNW fabrication rather than the device structure itself. The reported devices are based on SiNWs fabricated via both bottom-up [331] and top-down [326] techniques.

When a resistor gas sensor is used the relative sensitivity of the device is defined as percent change in the current (resistance) per the addition of a certain amount of analyte (gas) [327, 332-333] and is measured via Equation 8-1.

$$S = \frac{I_g - I_0}{I_0} = \frac{R_g - R_0}{R_0} \qquad \textbf{Equation 8-1}$$

where I_g (R_g) and I_0 (R_0) are the current (resistance) with the gas to be detected and without the gas (background) respectively.

In 2003 Zhou *et al.* [331] reported gas sensors based on bottom-up grown SiNWs fabricated via the oxide-assisted growth method. When exploring the properties of SiNWs for gas sensing it was observed that even at room temperature the electrical resistance of the HF-etched SiNWs (unlike the non-etched SiNWs) sensor device dramatically decreased upon exposure to 1000 ppm ammonia gas and water vapour. A very simple device structure was achieved by using a bundle of nanowires pressed on the insulating glass substrate and making silver glue electrodes at the two ends of the bundle with the distance of 5 mm between electrodes. The gas sensor structure fabricated in this thesis was motivated by the simplicity of the aforementioned fabrication principle.

The detection experiments were performed in vacuum and the ammonia was diluted in N_2, the sensitivity of the device towards the gas was measured in respect to the resistance of the nanowires. It was discovered that the HF-etched SiNW sensitivity was reversible after the gas and/or vapour was removed from the chamber. They also discovered that non-HF-etched SiNW resistance was affected only very slightly in the same procedure.

It is suggested by Zhou *et al.* [331] that the gas molecules affect the resistance of the SiNWs via two routes; (i) contact resistance across two nanowires and (ii) surface resistance

along the individual nanowire. When there is oxide layer covering the SiNW surface, the resistance of the oxide sheath is affected negligibly thus blocking any change in the resistance when the gases or water vapour is introduced into the chamber.

In the same year Elibol *et al.* [334] reported a single crystal SiNW-based gas sensor fabricated via top-down approach (see Figure 8-1) utilising multiple fabrication steps for oxygen and nitrogen detection.

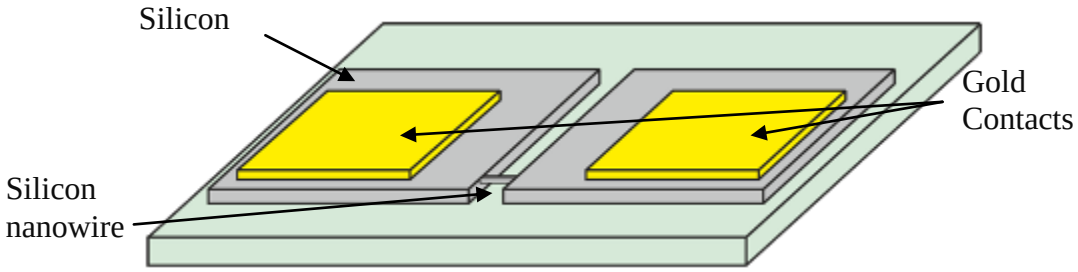

Figure 8-1. The gas sensor structure fabricated by Elibol *et al.* [334].

The nanowires were immersed in a buffered HF solution for complete removal of the oxide layer. The experiments were performed in a closed chamber with controlled gas composition and pressure. The device showed quasireversible adsorption which was eliminated via heating of the sample up to 80 ºC and leaving to cool down. The tests were performed with 20% oxygen in argon as the analyte gas and nitrogen purge for the device recovery.

Tibuzzi *et al.* [335] reported an MOS structure based device with Pd-SiO_2-p-doped Si wire junction structure that was used as H_2 sensor. The amount of hydrogen was 100 ppm and the recovery gas used was synthetic air. The measurements were carried out at room temperature and at atmospheric pressure. In this sensor the important detection role was played by Pd which is known to catalyse the H_2 molecules dissociation into H^+ ions. No change in resistance was observed when the device was exposed to H_2 prior to Pd deposition.

An important advance in the SiNW-based gas sensor research was reported by McAlpine *et al.* [336] where a flexible vapour sensor was developed on plastic and taken further towards "nano-electronic nose" design. The p-SiNW-based sensor was fabricated via multiple steps that involved SiNW fabrication on Si/SiO_2 substrate via reactive ion etching (RIE) process and their subsequent transfer onto plastic substrate. The SiNWs were connected to Ti electrodes and NO_2 diluted in N_2 was tested as analyte. The analyses were performed in a vacuum chamber and the sensor was reversed to its base value after the analyte gas was removed from the chamber. Concentrations of NO_2 as low as 20 ppb (parts per billion) were detected by the sensor. In addition, a 'nano-electronic nose' was fabricated

based on this device, where the sensing elements were chemically modified for detecting two gases including hexane and acetone vapours.

Another top-down mechanism was applied by Peng *et al.* [55] for obtainment of dense and vertically aligned porous SiNWs for gas sensing applications. The single crystalline porous (rough surface) SiNWs were achieved by metal-assisted chemical etching method and used for NO_x detection in dry air at room temperature. Gold electrodes were used for electrical contacts. NO concentrations as low as 500 ppb were detected via decrease in the SiNW electrical resistance. It is suggested that via NO adsorption on the SiNW surface the gas molecules donate electrons to SiNWs increasing its carrier density, thus the conductance of the nanowires. In addition, they tested the sensor with exposure to interfering gases such as NH_3, benzene, methanol, ethanol and other organic vapours with little resistance alteration.

Between 2009 and 2012 two research groups from China and France had a high input in exploring various gas sensor structures fabricated with SiNWs. These structures are discussed below.

The research group in China was lead by Xin-Ping Qu and they developed gas sensors based on boron doped SiNWs fabricated via various top-down combinational approaches [326-327, 337]. The final structure of these gas sensors can be seen in their first two works [326-327] where they used RIE for the nanowire fabrication and the third work [337] where they used angle deposition, all combined with nanoimprint lithography. After the nanowire growth the gas sensors were fabricated using Al pads with heat treatment for obtainment of ohmic contacts.

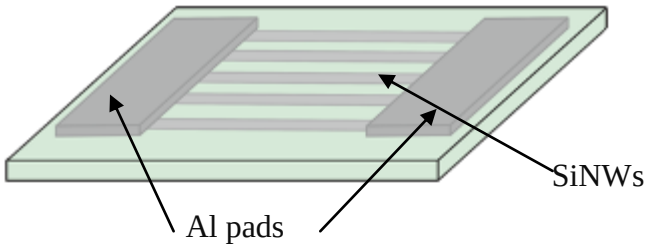

Figure 8-2. The gas sensor structure reported by Wan *et al.* [327].

The detectors were resistor sensors for NO_2 and NH_3 detection, whereas N_2 was used for steady current and dilution of the analyte gases. The concentrations of NO_2 and NH_3 tested were 250 ppm diluted in N_2. The tests were undertaken with constant DC voltage in room temperature with no vacuum system. They noticed that the sensitivity of the nanowires increased with increase in their surface to volume ratio. In addition, it was observed that the RIE process resulted in nanowires with higher sensitivity due to increased surface roughness

(increasing the surface to volume ratio), surface defects and charges on the p-Si nanowires. The diameters of all the nanowires tested by Gao *et al.* in all the published papers combined were between 22 nm (on top) and 130 nm [337]. The highest sensitivity towards 250 ppm of NO_2 was achieved with 60 nm diameter nanowire fabricated via angle deposition combinational method and was 155%.

The researchers of the university of Rennes, France demonstrated SiNW-based resistor sensors for detection of air humidity and smoke in 2010 [338] and ammonia and smoke in 2012 [333, 339-340]. They reported fabrication of SiNWs by two different approaches; (i) bottom-up approach via VLS growth from Au catalyst, SiNWs bridging between highly doped polysilicon islands, using a low pressure chemical vapour deposition (LPCVD) technique (Figure 8-3(a,b)) and (ii) top-down approach via sidewall spacer method using an LPCVD technique to deposit a-Si followed with its subsequent crystallisation and reactive ion etching which leads to nanosized sidewall spacer formation (Figure 8-3(c)). Prior to gas sensing experiments the SiNWs were subjected to HF treatment to remove the native oxide layer and promote the adsorption of chemical species on the surface. The electrodes for the second approach were thermally evaporated aluminium instead of highly doped polysilicon.

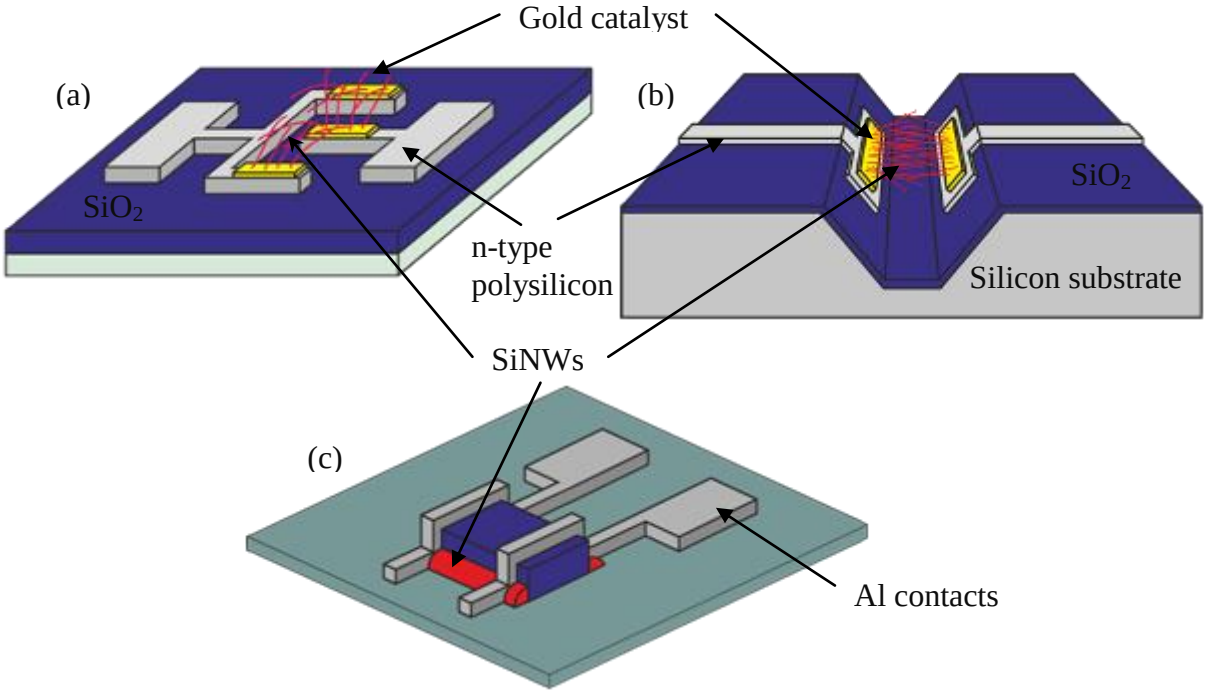

Figure 8-3. The gas sensor structures fabricated by the researchers in the university of Rennes [333, 340]; (a) comb-shaped, (b) V-groove shaped and (c) grounded sidewall spacer.

The electrical sensitivity measurements of the resistors were performed in an isolated chamber at room temperature and the resistance of the device was shown to drop upon

exposure to humidity, smoke and ammonia. The nanowires grown via top-down technique showed quasi-reversible behaviour upon exposure to smoke.

In addition, in the second sensor fabrication approach (sidewall spacer formation demonstrated in Figure 8-3(c)) Jacques *et al.* [340] compared the sensitivities of grounded to the substrate and suspended in the air SiNWs finding the suspended nanowires to have higher sensitivity due to higher surface area being exposed to the analyte.

The sensitivities of the comb-shaped, V-groove shaped, grounded and suspended sidewall spacer resistors to 350 ppm NH_3 were 4042%, 2217%, 200% and 600% respectively [333, 340].

A bottom-up approach was also utilised by Hsueh *et al.* [341] to grow SiNWs for humidity sensors. The nanowires were grown via PECVD from Au catalyst layer and copper contact electrodes. The sensor current was shown to decrease with increase of the humidity. In addition, it was found that the response of the sensor was improved for thinner catalyst layers which caused growth of longer and thinner nanowires. Therefore once again it was shown that higher surface ratio plays a dominating role in the improvement of the sensor sensitivity.

In addition to all the ohmic contact based resistor sensors discussed above, boron doped SiNW/palladium contacts have also been used as gas sensors based on Schottky barrier formation when detecting hydrogen down to concentrations as low as 5 ppm [332]. The native SiO_2 oxide layer is formed at the Si-Pd interface preventing the Pd silicide formation. Under ambient conditions Pd and Si form an ohmic contact, but when H_2 is introduced into the chamber, Schottky barrier is formed preventing the holes from crossing over from Pd to the SiNW. In this device it is shown that the sensing principle is based on SiNW/Pd Schottky barrier modulation and not on nanowire surface interaction with oxidising or reducing agents in the gas.

From the description of SiNW-based gas sensor structures reported in literature it was noticed that most of the device fabrication is quite complicated using multi-step procedures. As the primary interest of this work was the testing of the SiNWs for gas sensing and not the achievement of high sensitivity, a simple resistor device fabrication method was employed to detect the IPA vapours with the structure motivated from the work of Zhou *et al.*[331].

8.2. Experimental procedure

The SiNW-based sensory devices fabricated in this work from Ga and $Ga(acac)_3$ catalyst layers were exposed to IPA vapours.

The fabrication steps for these gas sensors included:

(i) Deposition of the catalyst layer via thermal evaporator for Ga and painting for $Ga(acac)_3$ on a 3x3 cm glass substrate.

(ii) PECVD growth of SiNWs for 40 minutes using "Standard" conditions defined in Chapter 7 with the addition of 10 sccm Phosphine gas which was introduced into the chamber 5 minutes after hydrogen plasma was struck and 5 minutes before SiH_4 was introduced.

(iii) Deposition of 200 nm thick Al top electrodes with 100 μm gap between them.

The structure of the gas sensors can be seen in Figure 8-4.

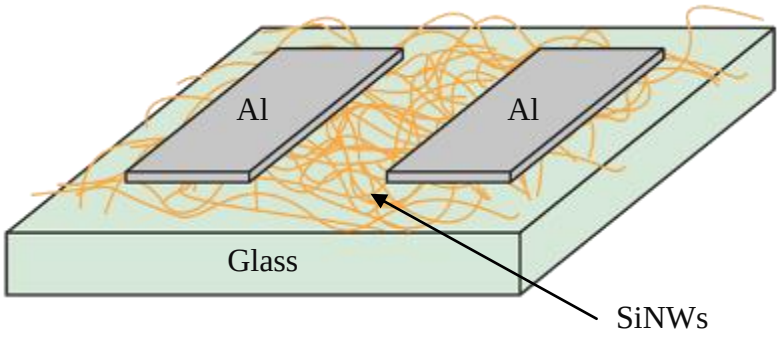

Figure 8-4. The structure of the gas sensor fabricated in this work.

After the device fabrication, a DC voltage was applied across the SiNWs between the two Al contacts . The value of the bias was chosen based on the I-V measurements to be as low as possible but which would give current above 20 pA. For the device discussed in this work the value of the bias was 5 V.

The electrical conductivity of the devices were measured using a HP 4140B picoammeter in the absence and presence of IPA. The "chamber" for gas testing was prepared using a simple plastic container with 2 holes cut in two of its opposite sides: a larger square hole (3x3 cm) for the probes to connect to the electrodes and a small one (1x1 cm) for the introduction of the IPA solution into a bowl next to the sample in the "chamber" via a pipette. The schematics of the experimental setup can be seen in Figure 8-5.

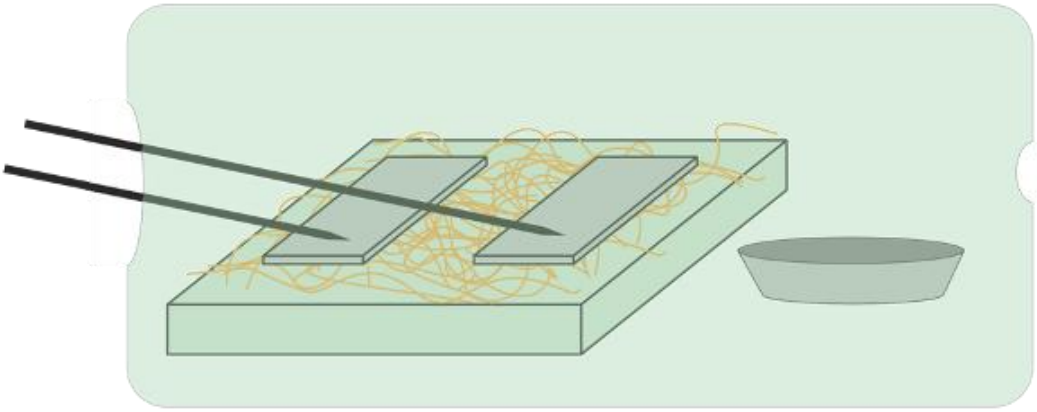

Figure 8-5. The experimental setup used for gas sensing.

The experiments were performed at room temperature. The amount of IPA introduced into the container was 150 (± 10) µL whereas the container size was approximately 1 L. The understanding and calculations in respect to ppm is vague in this context due to two reasons: (i) the container was not airtight (sealed) so the evaporated IPA could easily escape the chamber and (ii) the whole amount of IPA did not immediately evaporate when introduced into the chamber, instead the evaporation time for the whole liquid was extended up to 15-20 minutes.

It is also important to note that due to the photoconductivity of SiNWs grown in this thesis [268] the experiments were carried out in the dark.

8.3. Results and discussions

Prior to exposing the SiNW-based device to the IPA vapours, the current-voltage (I-V) characteristics of the samples were measured. The results of the I-V measurements for the $Ga(acac)_3$ - and Ga - based SiNW samples as well as a-Si based sample can be seen in Figure 8-6.

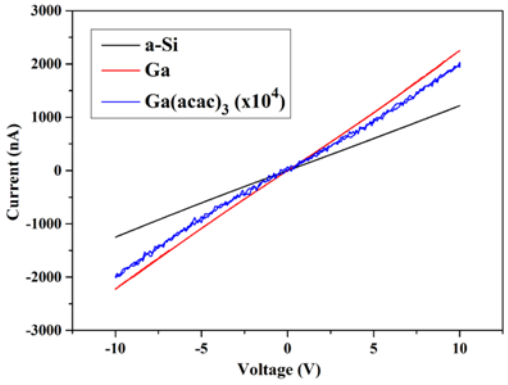

Figure 8-6. The I-V characteristics of the a-Si , Ga and $Ga(acac)_3$ (multiplied 10,000 times) based SiNW devices.

It can be seen from Figure 8-6 that the samples of SiNWs, grown in the PH_3 environment (for n-doping), with Al electrodes deposited on the top show linear I-V relationship. In addition, it can be seen that the sensors with the nanowires grown from $Ga(acac)_3$ compound as catalyst are significantly more resistive (four orders of magnitude higher resistance) in comparison to the Ga-catalysed (Figure 8-6) SiNW samples. In order to understand the reason behind the differences in the resistance of these samples, it is important to point out that the gas sensor fabricated in this work represents a network of interconnecting nanowires. In such a system many factors can determine its resistance, including the properties of the interconnecting nanowires and the number of uninterrupted nanowire bridges/channels between the two electrodes. In case of the silicon nanowires grown from Ga evaporated layer and $Ga(acac)_3$ layer , even if the crystallinity and doping of the nanowires from both catalysts are considered the same (an assumption , but not a fact, made based on the Raman analyses and the fact that the samples were fabricated at the same time in the PECVD chamber), the difference in the resistance may be due to few factors. The first possibility is the coverage of the SiNW surface (grown from Ga catalyst layer) with either thin Ga layer or small droplets (coming from the molten droplet sitting on the tip of the SiNWs during its growth, as was shown in Chapter 6). This will cause low resistivity surface on the nanowires which would be the preferential route for the current to pass between the electrodes. The second possible reason for the difference in the resistance could be the effective length and the cross sectional area of the interconnecting SiNW channels between the electrodes ($R = \rho L/A$, where R is the resistance, L is the length and A is the cross sectional area of the channel, and ρ is the resistivity of the SiNWs, which may also vary for nanowires grown from different catalyst layers). The third probable reason is suggested to be the variation in the amount of a-Si deposition on the sample surfaces, which would influence the resistivity of the individual channels. The fourth suggestion for the difference in the resistances is the possibility of an oxide layer formation surrounding the SiNWs grown from $Ga(acac)_3$ layer (thus increasing the resistance) compared to Ga-based Si nanowires. Further analyses are required in order to conclude which of the abovementioned factors are causing the difference in the resistances of various samples.

In order to find out the bridging of the nanowires between the electrodes, SEM images of the nanowire-based samples were taken. The Figure 8-7 shows the SiNWs grown from Ga catalyst layer with Al electrodes deposited on the top.

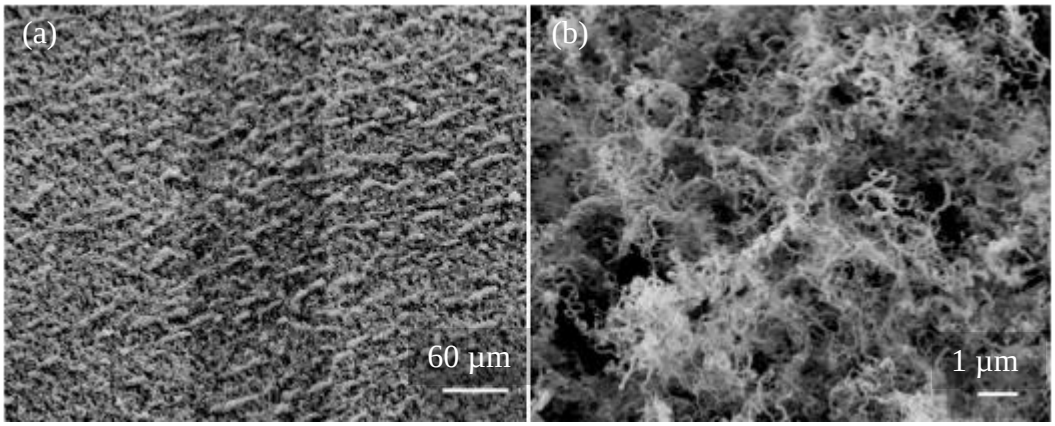

Figure 8-7. SEM images of the gas sensor device with SiNWs grown from 100 nm Ga catalyst layer; (a) low magnification image with the vertical dark line across the image being the gap between Al contacts, (b) higher magnification image of the SiNWs in the gap between electrodes.

It can be seen from Figure 8-7 that there is still dense nanowire growth from Ga catalyst based sensor even with slight growth parameter alteration which involved PH_3 introduction in the growth process. Due to the dense growth of the nanowires, it is assumed that the contact between the nanowires is sufficient for bridging between the Al electrodes.

It has been reported in the literature that PH_3 incorporation into the nanowire growth chamber does not massively reduce the nanowire growth rate [224] but in this report it was discovered that the $Ga(acac)_3$ based SiNW growth rate was influenced by PH_3 incorporation. The comparison of the nanowire growth rate with and without PH_3 with the same "Standard" conditions for 30 minutes can be seen in Figure 8-8.

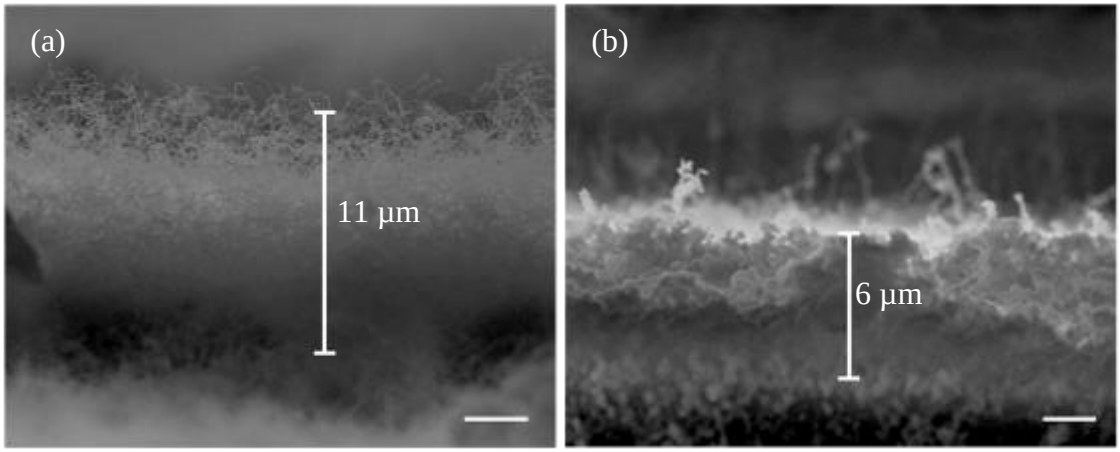

Figure 8-8. SEM images of SiNWs grown from $Ga(acac)_3$ without (a) and with (b) PH_3. Scale bars are both 2 µm.

The optimisation of the SiNW growth conditions with PH_3 doping was not the scope of this study and therefore it is not investigated in depth in the framework of this thesis.

Even though the SiNW growth rate with PH_3 was not as high as without the dopant gas, still it can be seen in Figure 8-9 that the SiNWs created a high density nanowire network providing a contact between the two Al electrodes.

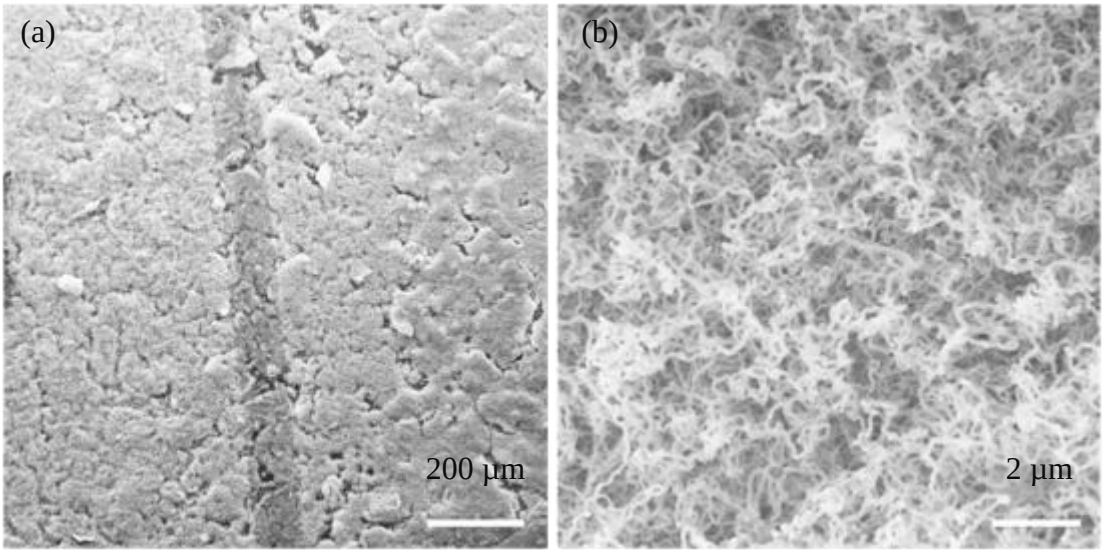

Figure 8-9. SEM images of the gas sensor device with SiNWs grown from $Ga(acac)_3$ catalyst layer; (a) low magnification image with the vertical dark line across the image being the gap between Al contacts, (b) higher magnification image of the SiNWs in the gap between electrodes.

When the voltage was applied across the device, the current of the 100 nm Ga-based SiNW samples did not change when the IPA was injected into the "chamber". The same characteristics were observed for the a-Si based sample. In addition, the same structures of devices were prepared with intrinsic SiNWs (with possibility of p-doping due to Ga catalyst) grown from both Ga- and $Ga(acac)_3$ catalyst layers but no current was measured across these nanowires even when the voltage was scanned to the values of ±100 V.

The lack of response of the devices with the exposure to the IPA vapours in the case of Ga-based SiNWs is suggested to be either (i) the a-Si layer formation on the nanowire surface (in this case the gas molecules will get absorbed onto the surface of the a-Si layer not reaching the crystalline core, where the exchange of the electrons take place) or (ii) Ga layer coverage on the surface of the nanowire emerging during the SiNW growth process from the molten Ga droplet sitting on the tip of the nanowire (in this case this layer will not allow the exchange of electrons between the gas and the SiNW).

A very different outcome was observed for $Ga(acac)_3$ – based samples when tested for gas sensing. The exposure of this sample to the IPA vapours showed increase in the device conductivity (see Figure 8-10) pointing at sensing capabilities of the SiNWs.

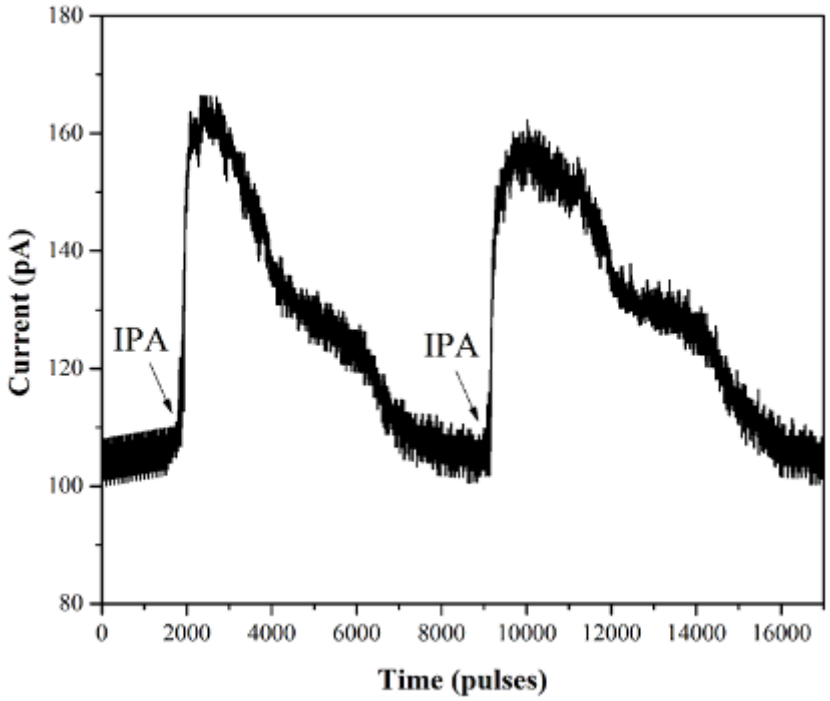

Figure 8-10. The current response of $Ga(acac)_3$ based SiNWs to IPA vapours with 5 V applied voltage.

In Figure 8-10 the time between the pulses is approximately half a second. The extended duration of the increased current does not indicate that the sensor is slow to recover to its steady state but due to the time it takes for the vapour to completely disappear from the container. The sensing (sharp increase) of the vapour took place within one second of the IPA introduction into the chamber (drop into the bowl directly beside the sample). The sensitivity of the device was calculated from Equation 8-1 to be 53% for 150 µL of IPA vapour in 1 L of air.

The suggestion for the sensing mechanism of the described gas sensor is the adsorption of the gas molecules on the SiNWs surface and the electrical charge transfer between the analyte and the SiNWs. This may affect the surface resistance of the individual nanowire or the contact resistance between neighbouring nanowires. As the current of the device is increasing upon the vapour exposure, it is suggested that the IPA gas molecules are acting as electron donors, thus injecting electrons into the Si crystal increasing the carrier transport along the nanowires and decreasing the resistance of the nanowires. Alternatively, they can help the transport of electrons between the wires. In addition, as the carrier mobility depends on the nanowire structural defects, the contact resistance between nanowires can be positively affected upon exposure to the IPA vapours via passivating these defects, such as dangling bonds which have been shown to exist in Si structures [342].

It can also be seen from Figure 8-10 that the electrical response of the SiNWs is reversible, i.e. the sensor returns to its primary conductivity state after the vapour leaves the chamber and is responsive to the second exposure to IPA. The smaller change in conductivity of the nanowires with the second addition of IPA is evident from the graph. The possibility of the amount of IPA being less during the second exposure (compared to the initial exposure) is not a valid reason for smaller conductivity change. This exclusion is based on the experiment condition that uses a large enough amount of IPA that does not fully evaporate upon the entry into the "chamber". This knowledge suggests that the reason for the decrease in conductivity lies within the sensor itself. It is possible that some of the molecules of IPA have not desorbed from the nanowires after the first exposure inactivating the sites and reducing the active sites on the nanowires.

An interesting step-like recovery of the sensor after the IPA exposure can also be seen from Figure 8-10. These phases of recovery are numbered in Figure 8-11.

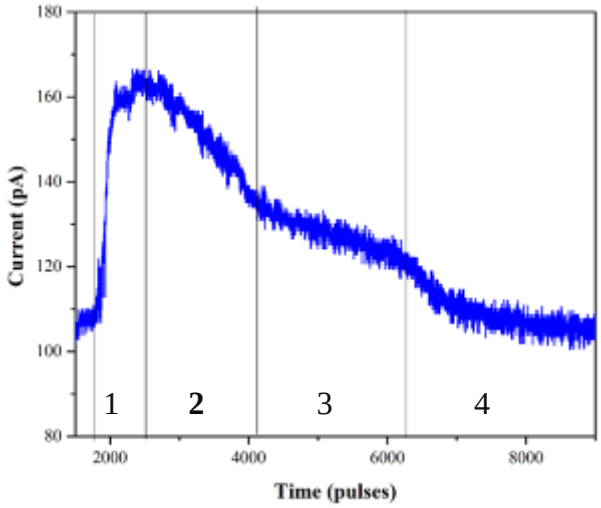

Figure 8-11. The four stages of SiNW based sensor recovery after exposure to IPA vapours.

As it can easily be distinguished from Figure 8-11 the sensor operation consists of the following segments upon exposure to the IPA vapour; (1) sharp increase in conductivity when IPA is introduced, (2) sharp decrease to half the sensing conductivity, (3) slower decrease of the sensor current towards the steady state and (4) second sharp decrease to the steady state. In order to understand these phases of recovery, it was important to find out at which stage the liquid IPA was completely transformed into vapour. When the amount of the liquid IPA was investigated (with a naked eye) it was observed that the transformation of the liquid IPA into vapour was finalised only towards the end of the 2nd segment. In addition, at the transition between the 3rd and 4th segments the amount of the IPA vapour was low enough not to be detectable via its odour.

Suggestions for each of the four stages of the sensor operation are the following:

At the first stage when the liquid IPA is injected inside the chamber from a higher level beside the sample, the vapours of the latter are directed towards the sample surface thus causing an initial high concentration exposure resulting in a high conductivity change.

After the initial stage of high IPA vapour concentration at the samples surface the vapours start to disperse inside the whole chamber and also leave the chamber through the holes due to the concentration gradient in the chamber. Due to the vapour molecules dispersing in the whole chamber, the concentration of those reduces at the sample surface causing decrease in the sensor conductivity.

With the consumption of the liquid IPA as no more new gas molecules are being produced the concentration gradient thus the speed of the gas molecules leaving the chamber reduces.

When the majority of the IPA gas molecules are removed from the chamber, the recovery of the sensor accelerates due to increased desorption of the gas molecules from the sample surface and due to lack of new molecules taking the place of those.

The sensor deterioration with time was also investigated with the sample being kept in air ambient. The same device with the same voltage applied between the Al contacts was tested with the exposure to IPA twice with one month interval (see Figure 8-12).

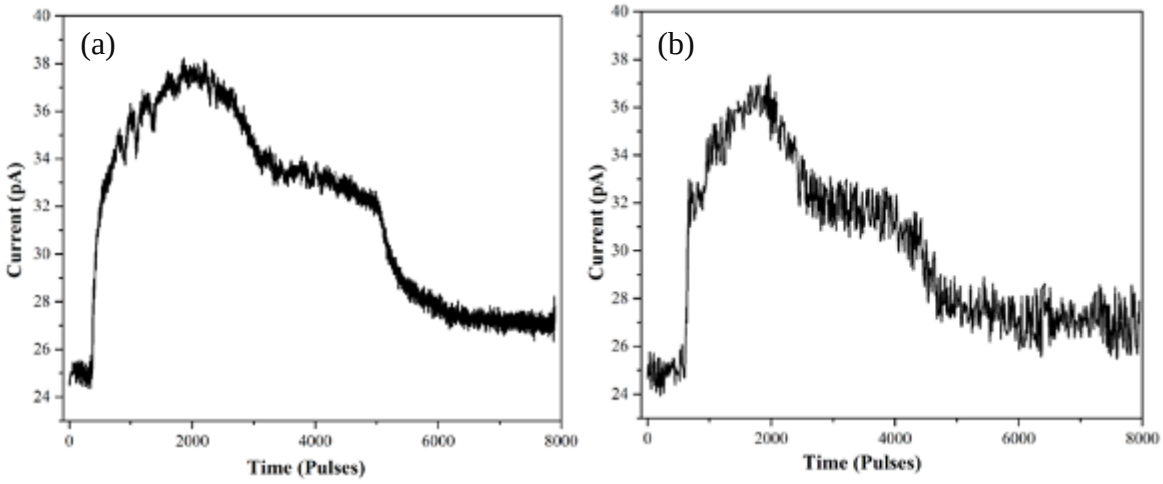

Figure 8-12. The I-t response of SiNWs to IPA vapours before (a) and after (b) one month keeping in air.

It can be seen from Figure 8-12 that the sensor still works after keeping 1 month in air. The reduction in response was calculated to be 9%. The sensitivity decrease may be due to (i) the number of sensing cycles the sensor has gone through or (ii) the environment it was kept in. Therefore, when kept in more isolated conditions, there is a chance of enhancing the

lifespan of the sensor, therefore making the sensor fabricated in a simple mechanism in this work a valuable device for a long term utilisation.

8.4. Conclusions

In this chapter SiNW based gas sensors were fabricated for IPA vapour detection. The sensing mechanism was based on resistance change of the SiNW devices with exposure to the IPA vapour. The device based on Ga catalysed SiNWs did not work as a sensor, the suggested reason being the growth of a thick SiO_2 shell around the nanowire core prohibiting the interaction of the n-Si core with the IPA vapour.

The device based on SiNWs grown from $Ga(acac)_3$ catalyst layer resulted in change of resistance when exposed to the IPA vapours with 57% sensitivity to 150 µL of IPA vapour in 1 L of air. The device was still usable after keeping the sample in air for a month with 9% decrease in sensitivity.

The work presented in this chapter was not an attempt to provide thorough analysis of gas sensors using SiNWs but mainly suggesting that the nanowires grown in this work have the potential to be used in gas sensors. This objective was achieved for the $Ga(acac)_3$ catalysed SiNWs.

Chapter 9

Conclusions and Future Work

This chapter is the conclusion of the research presented in the current thesis and it also suggests future work based on the observations made in the framework of this project.

9.1. Conclusions

This thesis was dedicated to the fabrication of various nanostructures for their potential application in chemical sensors. Due to the expanding interest in these materials and commercialisation requirements, novel nanostructures and growth methods utilising low temperature fabrication techniques are in demand. Various types of one-dimensional nanostructures were fabricated in this work, including zinc oxide nanowires and silicon nanostructures for gas and biosensor incorporation.

Zinc oxide nanowires were fabricated via a two-step hydrothermal growth method for incorporation into a glucose biosensor. The hydrothermal growth technique of ZnO nanowires is a well established method and was used as an initial step in this research. Various growth parameters including the solution temperature and nucleation layer thickness were optimised in order to grow uniformly sized and consistently distributed nanowires across the sample. The structural and optical characteristics of these nanowires were characterised via SEM, UV-Vis and XRD spectrometry. Zinc oxide nanowires were of single crystalline structure with (002) growth direction. The optimum conditions for the growth of uniformly sized and consistently distributed nanowires along the surface were 75 nm nucleation layer combined with solution temperature in the range of 70 ºC and 80 ºC.

After the nanowire optimisation, their potential in chemical sensing was tested via their incorporation into an electrochemical glucose biosensor. The analyses were performed via cyclic voltammetry and chronoamperometry. The sensitivity of the biosensor was 12.2 $\mu A/cm^2 \cdot mM$ and Michaelis-Menten constant was 6.8 mM showing good affinity of the biosensor towards glucose and high catalytic activity of the GOD enzyme.

For the Si nanowires grown from Ga catalyst layers via the PECVD technique the lowest growth temperature in the published literature (150 ºC) is demonstrated. The variation of various growth parameters, such as the catalyst layer thickness, growth temperature, chamber pressure and plasma power was investigated for the optimisation of the SiNW growth. An interesting correlation between the catalyst layer thickness and growth temperature was

observed. It was discovered that the high growth temperatures (above 300 ºC) result in branched Si nanostructures (singular nanowire with thin horizontal nanowires growing from the main body) growth whereas low temperatures result in a singular nanowire formation. In addition, it was found that for low temperature growth of SiNWs thin catalyst layers are required whereas for higher growth temperatures (still below 400 ºC) thicker catalyst layers are needed. Raman and TEM analysis demonstrated the crystalline nature of the nanostructures.

Metalorganic compounds (NFM, NFD, $NiAc{\cdot}4H_2O$, PdAc and $Ga(acac)_3$) were demonstrated as catalysts for Si nanostructure growth via a PECVD technique. This is the first time in published literature that these types of catalyst have been used, thus opening a completely new branch of research in the area of nanostructure fabrication. Very diverse growth patterns of Si nanostructure were observed when using these catalysts. The growth mechanisms are proposed for these systems which should be investigated in the future work for further confirmation. These involve VSS growth for Pd- and Ni- based MOCs and VLS growth for the Ga- based MOC. The nanostructures grown from $Ga(acac)_3$ showed crystalline Si structure when analysed by Raman spectroscopy, whereas the Si nanostructure grown from NFM was demonstrated (via EDS analyses) to have nickel incorporated in the core of the wire. The Raman analysis performed on the sample revealed Ni silicide peaks. When investigated via the TEM these nanowires showed a core/shell crystalline structure . Two possibilities are suggested based on the EDS, Raman and TEM analyses; (i) the nanowires are composed of a Ni silicide core incorporated in an a-Si shell or (ii) c-Si nanowires with Ni contamination incorporated in an a-Si shell and grown from Ni silicide layer.

Gas sensors with a simple structure were successfully fabricated using SiNWs grown from $Ga(acac)_3$ catalyst layers for the detection of the IPA vapours. The conductivity of the SiNWs changed upon exposure to the vapours of IPA indicating the potential of using these nanowires in chemical sensing devices.

9.2. Suggestions for Future Work

The aim of this work was to fabricate various 1D nanostructures and to show their potential for future application in chemical sensors.

- Zinc oxide nanowire growth via hydrothermal method is a highly reported technique which has been investigated by many research groups. However, being a solution based technique, there are many growth parameters that can influence the final structure of

the sample thus the research into this growth method is still underway. In the framework of this research, an interesting phenomenon was observed in the form of circle formations of the substrate made of larger and small nanowires. This phenomenon is an interesting observation that to our knowledge has not been reported in the past. Further research in understanding the mechanism of formation of these structures would give an opportunity to control this phenomenon and obtain various sample designs.

- In this thesis 150 ºC was the lowest temperature demonstrated for the growth of SiNWs using Ga catalyst layers via a PECVD technique. However, the temperature range between 100 ºC and 150 ºC was not studied and optimised in respect to growth parameters. It would be an interesting and important discovery to find out the more accurate lowest temperature for the growth of these nanowires. In addition, the variation of growth parameters could be addressed towards fabrication of straight SiNWs instead of wormlike structures observed in the current work.

- One of the most important outcomes of this work was the demonstration of Si nanostructure growth from metalorganic compounds. This investigation opens up new opportunities to expand on the field of nanostructure fabrication research. Even though the growth of nanostructures was demonstrated, and a growth theory proposed, there are many open questions regarding the growth mechanism. It would be valuable research to suggest a growth mechanism theory supported by experimental data and theoretical calculations. In addition, only three metal-based MOCs were used in this work which gives an opportunity to expand on the choice of the metalorganic compounds based on various metals.

- In this thesis the potential application of ZnONWs and SiNWs (fabricated in the framework of this PhD project) was demonstrated, however these were just initial experimentations, a proof of concept showing the applicability of these nanostructures in sensors. Future in depth work is required in order to fabricate high sensitivity gas and biosensors. Moreover, no gas sensing was achieved with SiNWs grown from Ga catalyst layer. This is suggested to be due to a thick SiO_2 shell encompassing the crystalline Si core, thus affecting the sensitivity of the nanowires. Further analysis of these nanowires and their growth optimisation could be directed towards fabrication of gas sensors.

Appendices

Appendix A – Substrate cleaning

The whole process for cleaning glass substrates took place in a clean room, mainly (except for the cutting process) in a laminar flow bench to ensure dust free environment and to prevent chemical contamination of the room. The solution immersion processes were all performed in the ultrasonic bath.

Glass cleaning

(1) 30 minute ultrasonication in 5 % Decon-90 in 18 MΩ De-ionised (D.I.) water solution.
(2) 2 minute ultrasonication (rinse) in 18 MΩ D.I. water (repeat 5 times).
(3) 15 minute ultrasonication in acetone (Fisher Electronics grade).
(4) 15 minute ultrasonication in propan-2-ol (Fisher Electronics grade).
(5) 2 minute ultrasonication (rinse) in 18 MΩ D.I. water (repeat 5 times).
(6) Blow drying with nitrogen.
(7) 1 hour baking on hot plate in air at 150 ºC.

Silicon wafer cleaning

(1) 10 minutes "bomb" clean with 50% sulphuric acid and 50% hydrogen peroxide (H_2O_2) (the mixture is obtained by slowly adding the H_2O_2 onto the acid).
(2) 2 minute ultrasonication (rinse) in 18 MΩ D.I. water (repeat 5 times).
(3) 30 second dip into buffered hydrofluoric acid (HF) (Fisher electronic grade), H2O:HF = 10:1 mixture.
(4) 2 minute ultrasonication (rinse) in 18 MΩ D.I. water (repeat 5 times).
(5) Spin drying (3000 rpm) under nitrogen for 30 seconds.
(6) 15 minute baking in air at 100 ºC.

Appendix B –Supplementary Results

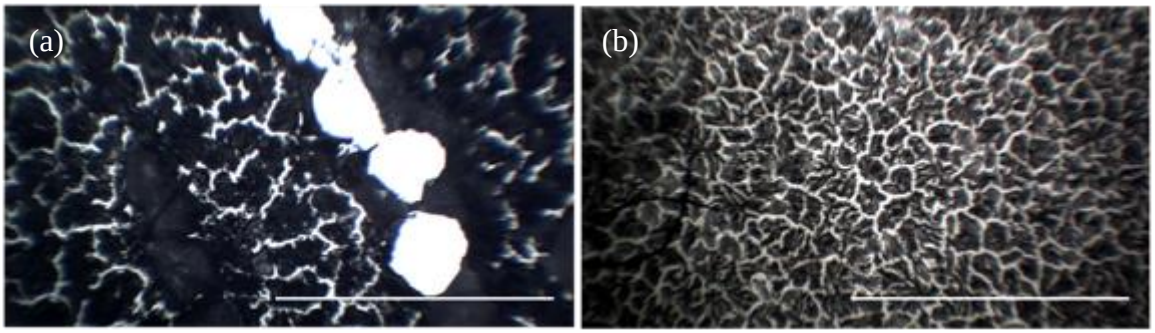

Figure 10-1. Optical microscope images of $Ga(acac)_3$ catalyst layers deposited via (a) drop-casting and (b) paint-brushing. The scale bars are both 1mm.

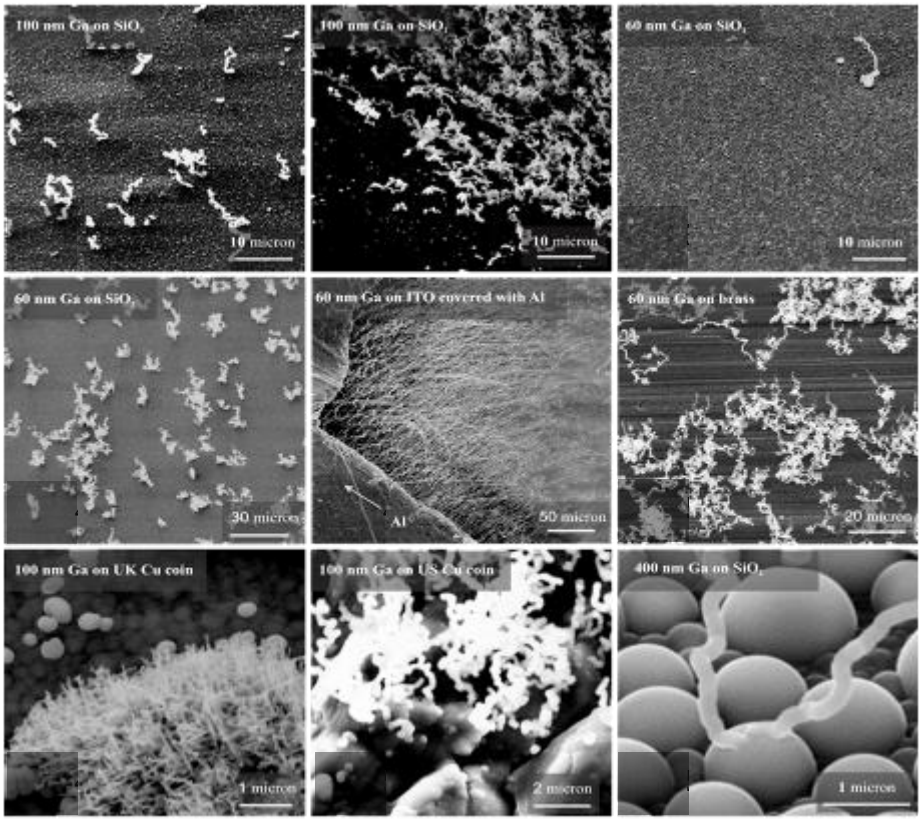

Figure 10-2. SEM images of initial attempts of SiNW growth without H2 gas dilution of SiH4. These samples represent five different runs with ““Standard”” growth conditions and 30 min growth duration. The numbers in the left bottom corner correspond to the number of the run.

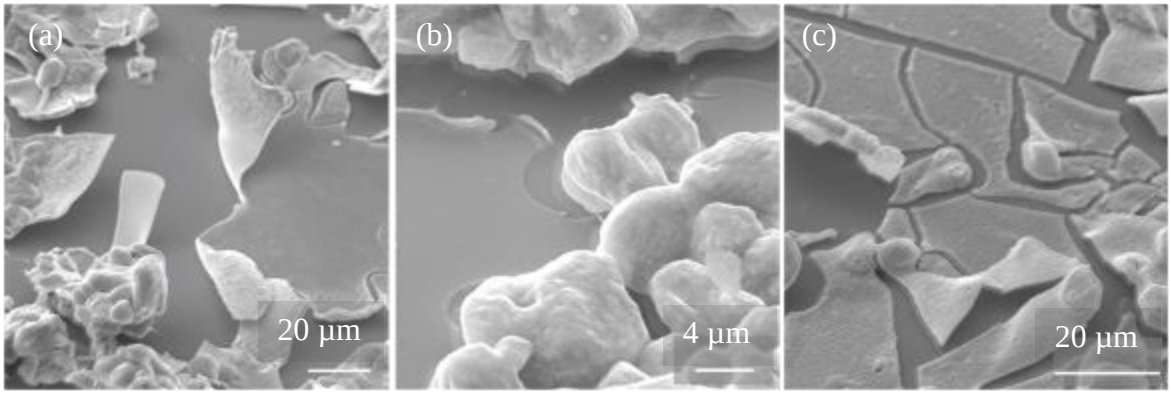

Figure 10-3. SEM images of Si nanostructure growth attempt from NFM catalyst layers initially annealed at (a) 300 ºC in vacuum, (b) 400 ºC in vacuum and (c) 400 ºC in air.

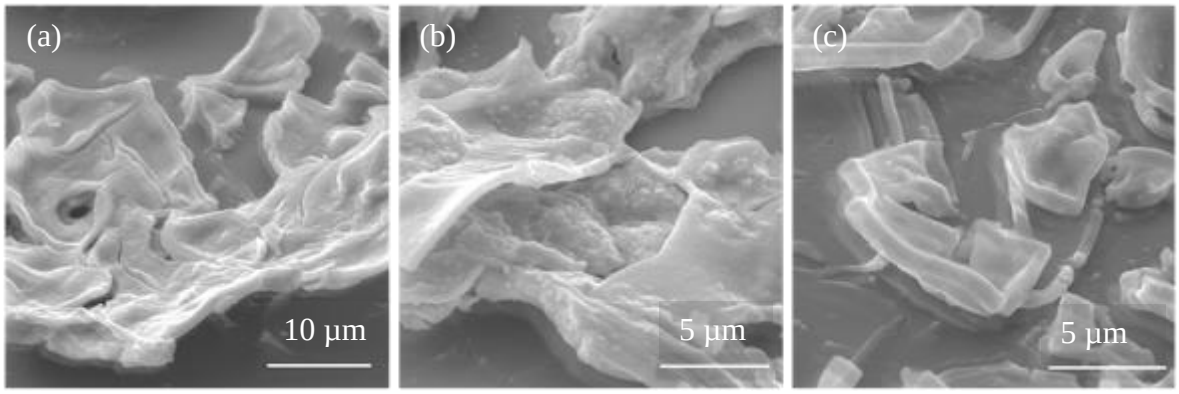

Figure 10-4. SEM images of Si nanostructure growth attempt from NiAc·4H_2O catalyst layers initially annealed at (a) 300 ºC in vacuum, (b) 400 ºC in vacuum and (c) 400 ºC in air.

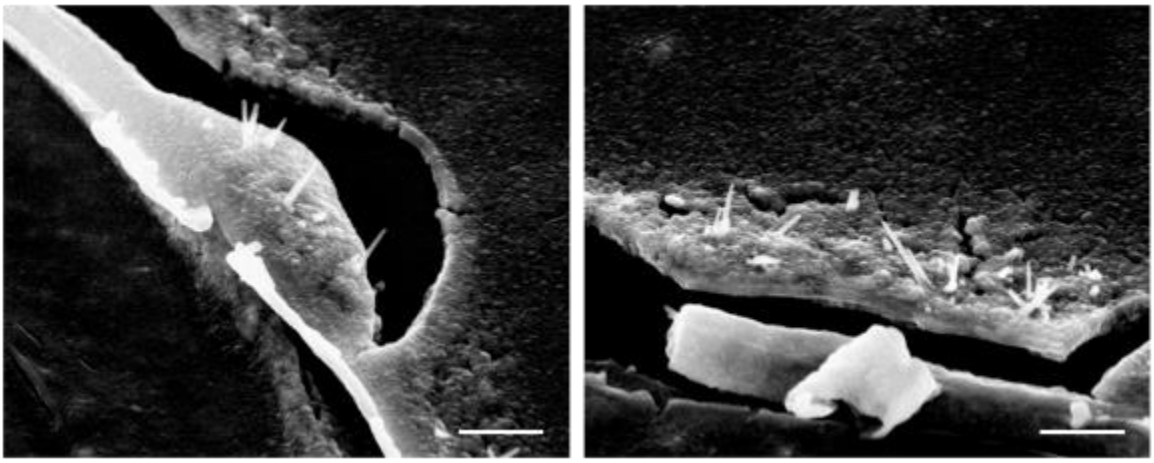

Figure 10-5. SEM images of Si nanostructure growth from the edges of dip-coated NFM catalyst layer. The growth was performed with "Standard" conditions for 20 mins (scale bars are 5 µm).

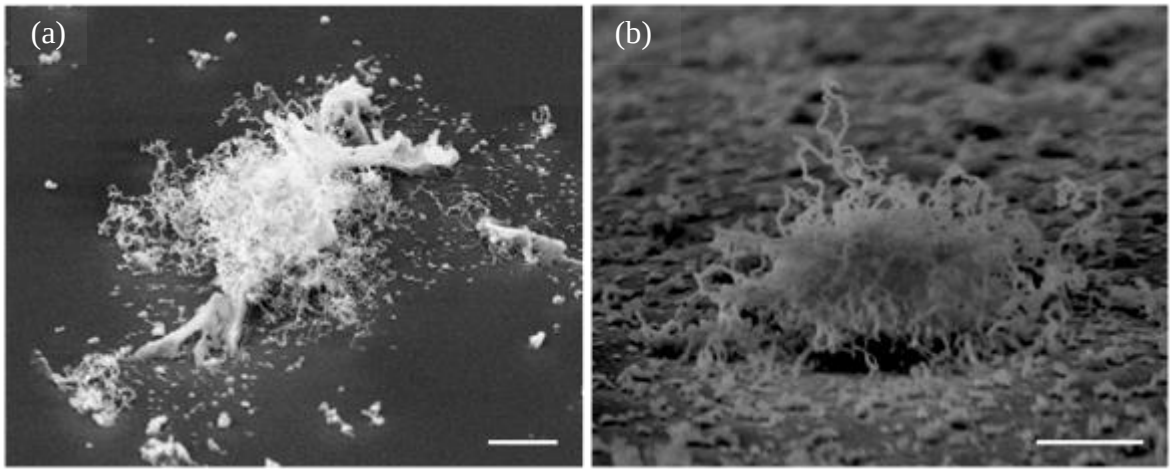

Figure 10-6. SEM images of SiNWs grown from $Ga(acac)_3$ (a) evaporated and (b) spin-coated layers.

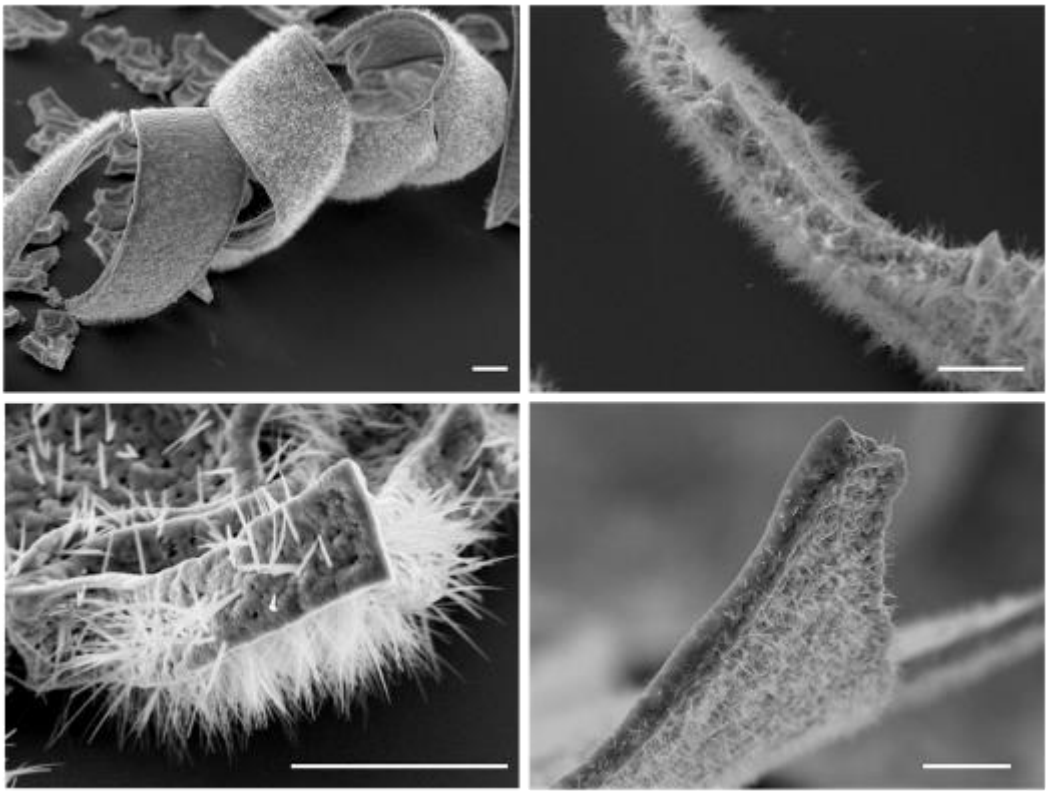

Figure 10-7. SEM images demonstrating the growth of Si nanostructures from the bottom of theNF catalyst layer ("Standard" conditions were applied with 20 min growth duration). The scale bars are all 10 µm.

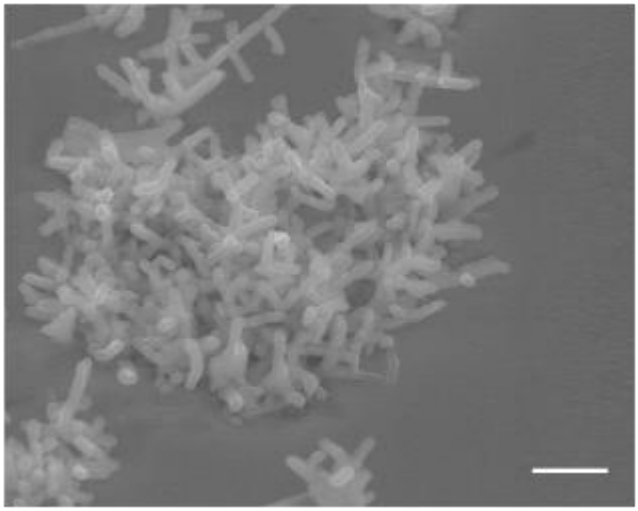

Figure 10-8. Silicon nanostructure growth from Cu substrate with no catalyst layer deposition. The scale is 2 μm.

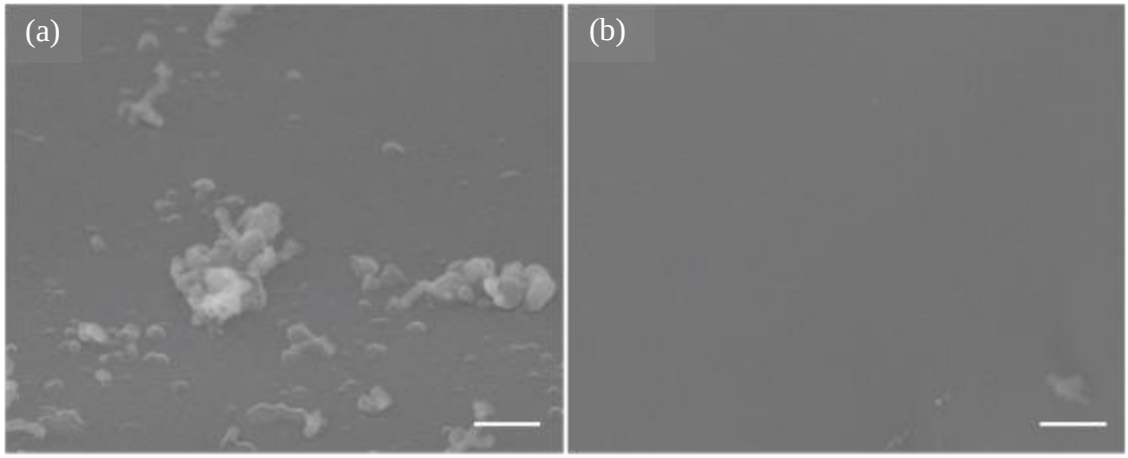

Figure 10-9. SEM images of SiNW growth attempt from 40 nm (a) Ni and (b) NiO catalyst layers.

Appendix C - Physical Constants

Values sourced from CODATA recommended values of the fundamental physical constants [343].

h…… Planck Constant…..……..……...…. 4.135 667 516 x 10^{-15} eV s

c…… Speed of light in vacuum……..... 299 792 458 m s^{-1}

R…….. Universal gas constant…….…. 8.314 4621 J mol-1 K-1

F…… Faraday constant…….…. 96 485.3365 C mol^{-1}

References

1. K.-Q. Peng and S.-T. Lee, *Silicon Nanowires for Photovoltaic Solar Energy Conversion.* Advanced Materials, 2011. **23**(2): 198-215.

2. J.G. Lu, P. Chang, and Z. Fan, *Quasi-one-dimensional metal oxide materials-Synthesis, properties and applications.* Materials Science and Engineering R: Reports, 2006. **52**(1-3): 49-91.

3. C. Yi, C.-W. Li, H. Fu, M. Zhang, S. Qi, N.-B. Wong, S.-T. Lee, and M. Yang, *Patterned growth of vertically aligned silicon nanowire arrays for label-free DNA detection using surface-enhanced Raman spectroscopy.* Analytical and Bioanalytical Chemistry, 2010. **397**(7): 3143-3150.

4. Z. Fan and J.G. Lu, *Zinc oxide nanostructures: Synthesis and properties.* Journal of Nanoscience and Nanotechnology, 2005. **5**(10): 1561-1573.

5. M. Shao, D.D.D. Ma, and S.-T. Lee, *Silicon Nanowires - Synthesis, Properties, and Applications.* European Journal of Inorganic Chemistry, 2010(27): 4264-4278.

6. Ü. Özgür, Y.I. Alivov, C. Liu, A. Teke, M.A. Reshchikov, S. Doğan, V. Avrutin, S.J. Cho, and H. Morkọ, *A comprehensive review of ZnO materials and devices.* Journal of Applied Physics, 2005. **98**(4): 1-103.

7. M. F. Ashby, P.J. Ferreira, and D.L. Schodek, *Nanomaterials, Nanotechnologies and Design*. 2009: Elsevier Ltd.

8. K. Arivalagan, S. Ravichandran, K. Rangasamy, and E. Karthikeyan, *Nanomaterials and its potential applications.* International Journal of ChemTech Research, 2011. **3**(2): 534-538.

9. R.P. Feynman, *There's Plenty of Room at the Bottom.* Engineering and Science, 1960. **23**(5): 22-36.

10. K. Kalantar-Zadeh and B. Fry, *Nonatechnology Enabled Sensors*. 2007: Springer.

11. *National Nanotechnology Initiative*, available from: http://www.nano.gov/nanotech-101/nanotechnology-facts; [accessed on 24/11/2011].

12. R. Comparelli, M.L. Curri, P.D. Cozzoli, and M. Striccoli, *Nanomaterials for Biosensors*. 3rd ed. Nanotechnologies for the Life Sciences, ed. C.S.S.R. Kumar. Vol. 8. 2010: Wiley-VCH Verlag GmbH & Co.

13. M. Kumar Teli, S. Mutalik, and G.K. Rajanikant, *Nanotechnology and Nanomedicine: Going Small Means Aiming Big.* Current Pharmaceutical Design, 2010. **16**(16): 1882-1892.

14. Y. Xia, P. Yang, Y. Sun, Y. Wu, B. Mayers, B. Gates, Y. Yin, F. Kim, and H. Yan, *One-dimensional nanostructures: Synthesis, characterization, and applications.* Advanced Materials, 2003. **15**(5): 353-389.

15. J.N. Tiwari, R.N. Tiwari, and K.S. Kim, *Zero-dimensional, one-dimensional, two-dimensional and three-dimensional nanostructured materials for advanced electrochemical energy devices.* Progress in Materials Science, 2012. **57**(4): 724-803.

16. A. Kolmakov and M. Moskovits, *Chemical sensing and catalysis by one-dimensional metal-oxide nanostructures.* Annual Review of Materials Research, 2004. **34**: 151-180.

17. C. Pan and J. Zhu, *The syntheses, properties and applications of Si, ZnO, metal, and heterojunction nanowires.* Journal of Materials Chemistry, 2009. **19**(7): 869-884.

18. X. Ye and L. Qi, *Two-dimensionally patterned nanostructures based on monolayer colloidal crystals: Controllable fabrication, assembly, and applications.* Nano Today, 2011. **6**(6): 608-631.

19. R. Mishra, *Impact tolerance of 3D woven nanocomposites: A simulation approach.* Journal of the Textile Institute, 2012. **104**(5): 562-570.

20. S. Guo and D. Therriault, *Direct-write microfabrication of biodegradable polymer nanocomposites 3D scaffolds*, in *AMERICAN SOCIETY FOR COMPOSITES*. 2011. p. 1649-1659

21. K. Xue, Y. Xu, and W. Song, *One-step synthesis of 3D dendritic gold@polypyrrole nanocomposites via a simple self-assembly method and their electrocatalysis for H 2O 2.* Electrochimica Acta, 2012. **60**: 71-77.

22. X. Chen, K. Sun, E. Zhang, and N. Zhang, *3D porous micro/nanostructured interconnected metal/metal oxide electrodes for high-rate lithium storage.* RSC Advances, 2013. **3**(2): 432-437.

23. D. Pan, M. Ombaba, Z.Y. Zhou, Y. Liu, S. Chen, and J. Lu, *Direct growth of carbon nanofibers to generate a 3D porous platform on a metal contact to enable an oxygen reduction reaction.* ACS Nano, 2012. **6**(12): 10720-10726.

24. S. Jing, S. Xing, Y. Wang, H. Hu, B. Zhao, and C. Zhao, *Synthesis of 3D well-packed octahedral PbS nanocrystal arrays.* Materials Letters, 2008. **62**(6-7): 977-979.

25. A. Viudez, M. Blázquez, R. Madueño, J. Morales, T. Pineda, and L. Sánchez, *3D gold nanocrystal arrays: A framework for reversible lithium storage.* Journal of Physical Chemistry C, 2010. **114**(5): 2360-2364.

26. S.H. Oh, J.G. Kim, C.S. Kim, D.S. Choi, S. Chang, and M.Y. Jeong, *The fabrication of 3-D nanostructures by a low-voltage EBL.* Applied Surface Science, 2011. **257**(9): 3817-3823.

27. T. Pradeep, *Nano The essentials Understanding Nanoscience and Nanotechnology*. 2008: The McGraw-Hill Companies, Inc.

28. L. Benea, P.L. Bonora, A. Borello, S. Martelli, F. Wenger, P. Ponthiaux, and J. Galland, *Composite Electrodeposition to Obtain Nanostructured Coatings.* Journal of the Electrochemical Society, 2001. **148**(7): C461-C465.

29. W. Dobbs, J.M. Suisse, L. Douce, and R. Welter, *Electrodeposition of silver particles and gold nanoparticles from ionic liquid-crystal precursors.* Angewandte Chemie - International Edition, 2006. **45**(25): 4179-4182.

30. I. Gurrappa and L. Binder, *Electrodeposition of nanostructured coatings and their characterization - A review.* Science and Technology of Advanced Materials, 2008. **9**(4): 043001.

31. K.L. Choy, *Chemical vapour deposition of coatings.* Progress in Materials Science, 2003. **48**(2): 57-170.

32. T. Iino and K. Nakamura, *Acoustic and acousto-optic characteristics of silicon nanofoam.* Japanese Journal of Applied Physics, 2009. **48**(7 PART 2).

33. N. Mingo, D. Hauser, N.P. Kobayashi, M. Plissonnier, and A. Shakouri, *Nanoparticle-in-alloy approach to efficient thermoelectrics: Silicides in SiGe.* Nano Letters, 2009. **9**(2): 711-715.

34. N. Yamazoe, *Toward innovations of gas sensor technology.* Sensors and Actuators, B: Chemical, 2005. **108**(1-2 SPEC. ISS.): 2-14.

35. R.W. Cattrall, *Chemical Sensors*. 1997, Oxford Scientific Publications: New York.

36. A.F. Collings and F. Caruso, *Biosensors: Recent advances.* Reports on Progress in Physics, 1997. **60**(11): 1397-1445.

37. J.D. Newman and S.J. Setford, *Enzymatic biosensors.* Molecular Biotechnology, 2006. **32**(3): 249-268.

38. A.P.F. Turner, *Biosensors*. Vol. I. 2001.

39. A.P.F. Turner, Karube, I. and Wilson, G.S., *Biosensors:Fundamentals and Applications.* 1987.

40. A.P.F. Turner, *Biosensors: Past, Present and Future*, available from: http://www.cranfield.ac.uk/health/researchareas/biosensorsdiagnostics/page18795.html; [accessed on 24/11/2011].

41. L.C. Clark Jr and C. Lyons, *Electrode systems for continuous monitoring in cardiovascular surgery.* Annals of the New York Academy of Sciences, 1962. **102**: 29-45.

42. C.G.J. Koopal, *Third Generation Amperometric Biosensors* 1992: Katholieke Universiteit.

43. J. Wang, *Electrochemical glucose biosensors.* Chemical Reviews, 2008. **108**(2): 814-825.

44. J.M. Cooper and A.E.G. Cass, *Biosensors*. Second ed. 2004: Oxford University Press.

45. B. Ding, M. Wang, J. Yu, and G. Sun, *Gas sensors based on electrospun nanofibers.* Sensors, 2009. **9**(3): 1609-1624.

46. J. Janata, *Principles of Chemical Sensors*, ed. D. Hercules. 1989, New York: Plenum Press.

47. J. Mizsei, *How can sensitive and selective semiconductor gas sensors be made?* Sensors and Actuators: B. Chemical, 1995. **23**(2-3): 173-176.

48. S.R. Morrison, *Semiconductor gas sensors.* Sensors and Actuators, 1981. **2**(C): 329-341.

49. C.H. Xu, S.Q. Shi, and C. Surya, *Gas Sensors Based on One-Dimensional Nanostructures*. Handbook of Nanoceramics and Their Based Nanodevices, ed. T. Tseng and H.S. Nalwa. 2006: Amer Scientific Pub.

50. G. Jiménez-Cadena, J. Riu, and F.X. Rius, *Gas sensors based on nanostructured materials.* Analyst, 2007. **132**(11): 1083-1099.

51. J.S. Wilson, *Sensor Technology Handbook*. 2005: Elsevier Inc.

52. R. Bogue, *Nanosensors: A review of recent progress.* Sensor Review, 2008. **28**(1): 12-17.

53. H. Ju, *Sensitive biosensing strategy based on functional nanomaterials.* Science China Chemistry, 2011. **54**(8): 1202-1217.

54. N.M. Shaalan, T. Yamazaki, and T. Kikuta, *Synthesis of metal and metal oxide nanostructures and their application for gas sensing.* Materials Chemistry and Physics, 2011. **127**(1-2): 143-150.

55. K.Q. Peng, X. Wang, and S.T. Lee, *Gas sensing properties of single crystalline porous silicon nanowires.* Applied Physics Letters, 2009. **95**(24): 243112.

56. I. Raible, M. Burghard, U. Schlecht, A. Yasuda, and T. Vossmeyer, *V2O5 nanofibres: Novel gas sensors with extremely high sensitivity and selectivity to amines.* Sensors and Actuators, B: Chemical, 2005. **106**(2): 730-735.

57. M. Andersson, R. Pearce, and A. Lloyd Spetz, *New generation SiC based field effect transistor gas sensors.* Sensors and Actuators, B: Chemical, 2013. **179**: 95-106.

58. P. Rai, S. Raj, K.J. Ko, K.K. Park, and Y.T. Yu, *Synthesis of flower-like ZnO microstructures for gas sensor applications.* Sensors and Actuators, B: Chemical, 2013. **178**: 107-112.

59. K. Fan, H. Qin, L. Wang, L. Ju, and J. Hu, *CO2 gas sensors based on La1-xSrxFeO 3 nanocrystalline powders.* Sensors and Actuators, B: Chemical, 2013. **177**: 265-269.

60. L. Haichen, *Research and Development of Nanometer Al2O3 Material Made for Rapid Detection of Gas Concentration Sensor*. 2013. p. 42-44.

61. Q. Zhou, W. Chen, S. Peng, and X. Su, *Nano-tin oxide gas sensor detection characteristic for hydrocarbon gases dissolved in transformer oil*, in *High Voltage Engineering and Application*. 2012. p. 384-387.

62. W.M. Kwok, Y.C. Bow, W.Y. Chan, M.C. Poon, P.G. Han, and H. Wong. *Study of porous silicon gas sensor*. 1999: IEEE.

63. N.A. Bakar, A. Rahmi, A.A. Umar, M.M. Salleh, and M. Yahaya. 2011. p. 276-279.

64. N.V. Hullavarad and S.S. Hullavarad, *Direct-vapor-phase grown IrO2 micronanostructures for ethanol, acetone, and propanol gas sensor.* IEEE Transactions on Nanotechnology, 2010. **9**(5): 625-629.

65. P.G. Datskos and T. Thundat, *Nanocantilever Signal Transduction by Electron Transfer.* Journal of Nanoscience and Nanotechnology, 2002. **2**(3-4): 369-373.

66. O.A. Sadik, A.O. Aluoch, and A. Zhou, *Status of biomolecular recognition using electrochemical techniques.* Biosensors and Bioelectronics, 2009. **24**(9): 2749-2765.

67. Y. Umasankar and S.M. Chen, *A review on the electrochemical sensors and biosensors composed of nanowires as sensing material.* Sensors, 2008. **8**(1): 290-313.

68. I.M. Feigel, H. Vedala, and A. Star, *Biosensors based on one-dimensional nanostructures.* Journal of Materials Chemistry, 2011. **21**(25): 8940-8954.

69. R.V. Stuart, *Vacuum Technology, Thin Films and Sputtering, An Introduction*. 1983, London: Academic Press Inc. 151.

70. S.A. Campbell, *Fabrication Engineering at the Micro- and Nanoscale*. Third ed. 2008, New York: Oxford University Press.

71. N. Harris, *Modern Vacuum Practice*. 3rd ed. 2007, Glasgow: Bell and Bain Ltd.

72. Edwards, *EH Series Mechanical Booster Pumps and Combination Units*. Issue B. 1990: Edwards High Vacuum International.

73. I. Brodie and J.J. Muray, *The Physics of Microfabrication*. 1982, New York and London: Plenum Press.

74. R. Waser, *Nanoelectronics and Information Technology*. 2nd ed. Advanced Electronic Materials and Novel Devices. 2005: Wiley-VCH.

75. I. AJA International, *What is sputtering*, available from: http://www.ajaint.com/whatis.htm; [accessed on 07/12/2011].

76. D.K. Ngwashi, (2010). *An Investigation of the Performance and Stability of Zinc Oxide Thin-film Transistors and the Role of High-k Dielectrics.*Ph.D. Thesis. De Montfort University, Leicester

77. S. Paul, (2000). *Growth, characterisation and electronic applications of amorphous hydrogenated carbon.*Ph.D. Thesis. De Montfort University, Leicester

78. T.A. Mih, (2011). *A Novel Low-Temperature Growth Method of Silicon Structures and Application in Flash Memory.*Ph.D. Thesis. De Montfort University, Leicester, UK

79. P.E.J. Flewitt and R.K. Wild, *Physical Methods for Materials Characterisation*. Graduate Student Series in Materials Science and Engineering, ed. B. Cantor. 1994: IOP Publishing Ltd.

80. E.N. Kaufmann, *Characterization of Materials*. Vol. 2. 2003: John Wiley & Sons.

81. J.F. Shackelford, *Introduction to Materials Science for Engineers*. 6th ed. 2005: Pearson Education Inc.

82. D.K. Schroder, *Semiconductor Material and Device Characterization*. 3rd ed. 2006: John Wiley & Sons, Inc.

83. D.C. Prime, (2010). *Switching mechanisms, electrical characterisation and fabrication of nanoparticle based non-volatile polymer memory devices.*Ph.D. Thesis. De Montfort University, Leicester, UK

84. E.N. Kaufmann, *Characterization of Materials*. Vol. 1. 2003: John Wiley & Sons.

85. J. Tauc, R. Grigorovici, and A. Vancu, *Optical Properties and Electronic Structure of Amorphous Germanium.* Physica Status Solidi (B) Basic Research, 1966. **15**(2): 627-637.

86. Microspectra.com, *Science of Micro Raman Spectroscopy*, available from: http://www.microspectra.com/support/technical-support/raman-science/35-technical-support/126-science-of-micro-raman-spectroscopy; [accessed on 13.09.12].

87. Y. Hatakeyama and F.X. Quinn, *Thermal Analysis Fundamentals and Applications to Polymerb Science*. Second ed. 2000: John Wiley & Sons.

88. L.R.F. A. J. Bard, *Electrochemical Methods, Fundamental and Applications*. 2nd ed. 2001: John Wiley & Sons.

89. A.H. C. H. Hamann, W. Vielstich, *Electrochemistry*. 1998: Wiley-VCH.

90. S.P. Kounaves, *Handbook of Instrumental Techniques for Analytical Chemistry*. 1st ed, ed. F. Settle. 1997: Prentice Hall Professional Technical References.

91. M. Dominiczak, *Flesh and Bones of Metabolism*. 2006: Mosby.

92. G.A. Mabbott, *An introduction to cyclic voltammetry.* Journal of Chemical Education, 1983. **60**(9): 697-702.

93. J. Jiang, *Electrochemical Studies of Nano-structured Materials for Biosensors*. 2009: LAP LAMBERT Academic Publishinf AG & Co. KG.

94. D. Andrienko, *Cyclic Voltammetry*, available from: http://www.mpip-mainz.mpg.de/~andrienk/journal_club/cyclic_voltammetry.pdf; [accessed on 17/09/12].

95. P.T. Kissinger and W.R. Heineman, *CYCLIC VOLTAMMETRY*. Journal of Chemical Education, 1983. **60**(9): 702-706.

96. D.H. Evans, K.M. O'Connell, R.A. Petersen, and M.J. Kelly, *Cyclic voltammetry.* Journal of Chemical Education, 1983. **60**(4): 290-293.

97. R.S. Nicholson and I. Shain, *Theory of Stationary Electrode Polarography.* Analytical Chemistry, 1964. **36**(4): 706-723.

98. B. Eggins, *Biosensors, An Introduction*. 1996: John Wiley & Sons Ltd.

99. S. Barth, F. Hernandez-Ramirez, J.D. Holmes, and A. Romano-Rodriguez, *Synthesis and applications of one-dimensional semiconductors.* Progress in Materials Science, 2010. **55**(6): 563-627.

100. B.D. Yao, Y.F. Chan, and N. Wang, *Formation of ZnO nanostructures by a simple way of thermal evaporation.* Applied Physics Letters, 2002. **81**(4): 757.

101. X.Y. Kong and Z.L. Wang, *Spontaneous Polarization-Induced Nanohelixes, Nanosprings, and Nanorings of Piezoelectric Nanobelts.* Nano Letters, 2003. **3**(12): 1625-1631.

102. J.Y. Lao, J.G. Wen, and Z.F. Ren, *Hierarchical ZnO Nanostructures.* Nano Letters, 2002. **2**(11): 1287-1291.

103. Y.S. Jung, O. Kononenko, J.S. Kim, and W.K. Choi, *Two-dimensional growth of ZnO epitaxial films on c-Al2O 3 (0 0 0 1) substrates with optimized growth temperature and low-temperature buffer layer by plasma-assisted molecular beam epitaxy.* Journal of Crystal Growth, 2005. **274**(3-4): 418-424.

104. Z. Lockman, K.A. Razak, T.K. Huat, T.W. Kian, L.C. Li, G. Kawamura, and A. Matsuda, *Formation of 1-dimensional (1D) and 3-dimensional (3D) ZnO nanostructures by oxidation and chemical methods.* Materialwissenschaft und Werkstofftechnik, 2012. **43**(5): 457-460.

105. Y. Inoue, M. Okamoto, T. Kawahara, Y. Okamoto, and J. Morimoto, *Thermoelectric properties of amorphous zinc oxide thin films fabricated by pulsed laser deposition.* Materials Transactions, 2005. **46**(7): 1470-1475.

106. T.G. Pedersen, *Quantum size effects in ZnO nanowires.* Physica Status Solidi C: Conferences, 2005. **2**(12): 4026-4030.

107. R.K. Kumar, M. Husain, and Z.H. Khan, *Optical studies on amorphous ZnO film.* Digest Journal of Nanomaterials and Biostructures, 2011. **6**(3): 1317-1323.

108. S. Baruah and J. Dutta, *Hydrothermal growth of ZnO nanostructures.* Science and Technology of Advanced Materials, 2009. **10**(1).

109. J.H. Yang, J.H. Zheng, H.J. Zhai, L.L. Yang, Y.J. Zhang, J.H. Lang, and M. Gao, *Growth mechanism and optical properties of ZnO nanotube by the hydrothermal method on Si substrates.* Journal of Alloys and Compounds, 2009. **475**(1-2): 741-744.

110. A. Sugunan, H.C. Warad, M. Boman, and J. Dutta, *Zinc oxide nanowires in chemical bath on seeded substrates: Role of hexamine.* Journal of Sol-Gel Science and Technology, 2006. **39**(1): 49-56.

111. E. Topoglidis, A.E.G. Cass, B. O'Regan, and J.R. Durrant, *Immobilisation and bioelectrochemistry of proteins on nanoporous TiO2 and ZnO films.* Journal of Electroanalytical Chemistry, 2001. **517**(1-2): 20-27.

112. F. Zhang, X. Wang, S. Ai, Z. Sun, Q. Wan, Z. Zhu, Y. Xian, L. Jin, and K. Yamamoto, *Immobilization of uricase on ZnO nanorods for a reagentless uric acid biosensor.* Analytica Chimica Acta, 2004. **519**(2): 155-160.

113. A. Wei, X.W. Sun, J.X. Wang, Y. Lei, X.P. Cai, C.M. Li, Z.L. Dong, and W. Huang, *Enzymatic glucose biosensor based on ZnO nanorod array grown by hydrothermal decomposition.* Applied Physics Letters, 2006. **89**(12).

114. J.J. Wu and S.C. Liu, *Low-temperature growth of well-aligned ZnO nanorods by chemical vapor deposition.* Advanced Materials, 2002. **14**(3): 215-218.

115. D. Zhang, S.K. Lee, S. Chava, C.A. Berven, and V. Katkanant, *Investigation of electrical and optoelectronic properties of zinc oxide nanowires.* Physica B-Condensed Matter, 2011. **406**(20): 3768-3772.

116. B.P. Zhang, N.T. Binh, K. Wakatsuki, Y. Segawa, Y. Yamada, N. Usami, M. Kawasaki, and H. Koinuma, *Formation of highly aligned ZnO tubes on sapphire (0001) substrates.* Applied Physics Letters, 2004. **84**(20): 4098-4100.

117. X.Y. Xing, K.B. Zheng, H.H. Xu, F. Fang, H.T. Shen, J. Zhang, J. Zhu, C.N. Ye, G.Y. Cao, D.L. Sun, and G.R. Chen, *Synthesis and electrical properties of ZnO nanowires.* Micron, 2006. **37**(4): 370-373.

118. R.B.M. Cross, M.M. De Souza, and E.M. Sankara Narayanan, *A low temperature combination method for the production of ZnO nanowires.* Nanotechnology, 2005. **16**(10): 2188-2192.

119. N. Gabrielyan, S. Paul, and R.B.M. Cross. *Optimising the low temperature growth of uniform ZnO nanowires*. in *Proc. MRS*. 2010.

120. H.E. Unalan, P. Hiralal, N. Rupesinghe, S. Dalal, W.I. Milne, and G.A.J. Amaratunga, *Rapid synthesis of aligned zinc oxide nanowires.* Nanotechnology, 2008. **19**(25): 255608.

121. B. Liu and H.C. Zeng, *Hydrothermal synthesis of ZnO nanorods in the diameter regime of 50 nm.* Journal of the American Chemical Society, 2003. **125**(15): 4430-4431.

122. G. Sun, M. Cao, Y. Wang, C. Hu, Y. Liu, L. Ren, and Z. Pu, *Anionic surfactant-assisted hydrothermal synthesis of high-aspect-ratio ZnO nanowires and their photoluminescence property.* Materials Letters, 2006. **60**(21-22): 2777-2782.

123. J.B. Cui and U.J. Gibson, *Enhanced nucleation, growth rate, and dopant incorporation in ZnO nanowires.* Journal of Physical Chemistry B, 2005. **109**(46): 22074-22077.

124. R. Liu, A.A. Vertegel, E.W. Bohannan, T.A. Sorenson, and J.A. Switzer, *Epitaxial electrodeposition of zinc oxide nanopillars on single-crystal gold.* Chemistry of Materials, 2001. **13**(2): 508-512.

125. C.K. Xu, G.D. Xu, Y.K. Liu, and G.H. Wang, *A simple and novel route for the preparation of ZnO nanorods.* Solid State Communications, 2002. **122**(3-4): 175-179.

126. X.H. Kong, X.M. Sun, X.L. Li, and Y.D. Li, *Catalytic growth of ZnO nanotubes.* Materials Chemistry and Physics, 2003. **82**(3): 997-1001.

127. Y.W. Wang, L.D. Zhang, G.Z. Wang, X.S. Peng, Z.Q. Chu, and C.H. Liang, *Catalytic growth of semiconducting zinc oxide nanowires and their photoluminescence properties.* Journal of Crystal Growth, 2002. **234**(1): 171-175.

128. H. Ham, G.Z. Shen, J.H. Cho, T.J. Lee, S.H. Seo, and C.J. Lee, *Vertically aligned ZnO nanowires produced by a catalyst-free thermal evaporation method and their field emission properties.* Chemical Physics Letters, 2005. **404**(1-3): 69-73.

129. A. Umar, E.K. Suh, and Y.B. Hahn, *Non-catalytic growth of high aspect-ratio ZnO nanowires by thermal evaporation.* Solid State Communications, 2006. **139**(9): 447-451.

130. L.S. Wang, X.Z. Zhang, S.Q. Zhao, G.Y. Zhou, Y.L. Zhou, and J.J. Qi, *Synthesis of well-aligned ZnO nanowires by simple physical vapor deposition on c-oriented ZnO thin films without catalysts or additives.* Applied Physics Letters, 2005. **86**(2): 024108.

131. Y. Sun, G.M. Fuge, and M.N.R. Ashfold, *Growth of aligned ZnO nanorod arrays by catalyst-free pulsed laser deposition methods.* Chemical Physics Letters, 2004. **396**(1-3): 21-26.

132. T. Okada, B.H. Agung, and Y. Nakata, *ZnO nano-rods synthesized by nano-particle-assisted pulsed-laser deposition.* Applied Physics A: Materials Science and Processing, 2004. **79**(4-6): 1417-1419.

133. J.Q. Hu, Q. Li, N.B. Wong, C.S. Lee, and S.T. Lee, *Synthesis of uniform hexagonal prismatic ZnO whiskers.* Chemistry of Materials, 2002. **14**(3): 1216-1219.

134. G.H. Lee, *Synthesis of pencil-shaped ZnO nanowires using sunlight.* Materials Letters, 2012. **73**: 53-55.

135. S. Ji and C. Ye, *Synthesis, growth mechanism, and applications of zinc oxide nanomaterials.* Journal of Materials Science and Technology, 2008. **24**(4): 457-472.

136. Y.-B. Hahn, *Zinc oxide nanostructures and their applications.* Korean Journal of Chemical Engineering, 2011. **28**(9): 1797-1813.

137. S. Kodambaka, J. Tersoff, M.C. Reuter, and F.M. Ross, *Germanium nanowire growth below the eutectic temperature.* Science, 2007. **316**(5825): 729-732.

138. Q. Ahsanulhaq, A. Umar, and Y.B. Hahn, *Growth of aligned ZnO nanorods and nanopencils on ZnO/Si in aqueous solution: Growth mechanism and structural and optical properties.* Nanotechnology, 2007. **18**(11).

139. L. Schmidt-Mende and J.L. MacManus-Driscoll, *ZnO - nanostructures, defects, and devices.* Materials Today, 2007. **10**(5): 40-48.

140. E.J.H. Lee, C. Ribeiro, E. Longo, and E.R. Leite, *Oriented attachment: An effective mechanism in the formation of anisotropic nanocrystals.* Journal of Physical Chemistry B, 2005. **109**(44): 20842-20846.

141. Y.T. Yin, W.X. Que, and C.H. Kam, *ZnO nanorods on ZnO seed layer derived by sol-gel process.* Journal of Sol-Gel Science and Technology, 2010. **53**(3): 605-612.

142. L.-W. Ji, S.-M. Peng, J.-S. Wu, W.-S. Shih, C.-Z. Wu, and I.T. Tang, *Effect of seed layer on the growth of well-aligned ZnO nanowires.* Journal of Physics and Chemistry of Solids, 2009. **70**(10): 1359-1362.

143. B. Nikoobakht, C.A. Michaels, S.J. Stranick, and M.D. Vaudin, *Horizontal growth and in situ assembly of oriented zinc oxide nanowires.* Applied Physics Letters, 2004. **85**(15): 3244-3246.

144. P. Colson, A. Schrijnemakers, B. Vertruyen, C. Henrist, and R. Cloots, *Nanosphere lithography and hydrothermal growth: How to increase the surface area and control reversible wetting properties of ZnO nanowire arrays?* Journal of Materials Chemistry, 2012. **22**(33): 17086-17093.

145. X. Zhang, L. Zhang, M. Gao, W. Zhou, and S. Xie, *High-resolution nanosphere lithography (NSL) to fabricate highly-ordered ZnO nanorod arrays.* Journal of Nanoscience and Nanotechnology, 2010. **10**(11): 7432-7435.

146. H.J. Fan, B. Fuhrmann, R. Scholz, F. Syrowatka, A. Dadgar, A. Krost, and M. Zacharias, *Well-ordered ZnO nanowire arrays on GaN substrate fabricated via nanosphere lithography.* Journal of Crystal Growth, 2006. **287**(1): 34-38.

147. S.H. Lee, H.J. Lee, K. Ino, H. Shiku, T. Yao, and T. Matsue, *Microfluid-assisted dielectrophoretic alignment and device characterization of single ZnO wires.* Journal of Physical Chemistry C, 2009. **113**(45): 19376-19381.

148. Z. Yang, Y.Y. Shi, X.L. Sun, H.T. Cao, H.M. Lu, and X.D. Liu, *The competition growth of ZnO microrods and nanorods in chemical bath deposition process.* Materials Research Bulletin, 2010. **45**(4): 474-480.

149. J. Song and S. Lim, *Effect of seed layer on the growth of ZnO nanorods.* Journal of Physical Chemistry C, 2007. **111**(2): 596-600.

150. W.Y. Wu, T.L. Chen, and J.M. Ting, *Effects of seed layer precursor type on the synthesis of ZnO nanowires using chemical bath deposition.* Journal of the Electrochemical Society, 2010. **157**(8): K177-K181.

151. L.E. Greene, M. Law, D.H. Tan, M. Montano, J. Goldberger, G. Somorjai, and P. Yang, *General route to vertical ZnO nanowire arrays using textured ZnO seeds.* Nano Letters, 2005. **5**(7): 1231-1236.

152. E. Makarona, T. Speliotis, G. Niarchos, D. Niarchos, and C. Tsamis, *ZnO nanorod growth based on a low-temperature silicon-compatible combinatorial method.* Physica Status Solidi (C) Current Topics in Solid State Physics, 2008. **5**(12): 3809-3812.

153. S.F. Wang, T.Y. Tseng, Y.R. Wang, C.Y. Wang, H.C. Lu, and W.L. Shih, *Effects of preparation conditions on the growth of ZnO nanorod arrays using aqueous solution method.* International Journal of Applied Ceramic Technology, 2008. **5**(5): 419-429.

154. L. Vayssieres, *Growth of arrayed nanorods and nanowires of ZnO from aqueous solutions.* Advanced Materials, 2003. **15**(5): 464-466.

155. K. Govender, D.S. Boyle, P.B. Kenway, and P. O'Brien, *Understanding the factors that govern the deposition and morphology of thin films of ZnO from aqueous solution.* Journal of Materials Chemistry, 2004. **14**(16): 2575-2591.

156. M.N.R. Ashfold, R.P. Doherty, N.G. Ndifor-Angwafor, D.J. Riley, and Y. Sun, *The kinetics of the hydrothermal growth of ZnO nanostructures.* Thin Solid Films, 2007. **515**(24 SPEC. ISS.): 8679-8683.

157. Y. Sun, D.J. Riley, and M.N.R. Ashfold, *Mechanism of ZnO nanotube growth by hydrothermal methods on ZnO film-coated Si substrates.* Journal of Physical Chemistry B, 2006. **110**(31): 15186-15192.

158. P. Singh, A. Kumar, A. Kaushal, D. Kaur, A. Pandey, and R.N. Goyal, *In situ high temperature XRD studies of ZnO nanopowder prepared via cost effective ultrasonic mist chemical vapour deposition.* Bulletin of Materials Science, 2008. **31**(3): 573-577.

159. S. Hullavarad, N. Hullavarad, D. Look, and B. Claflin, *Persistent photoconductivity studies in nanostructured ZnO UV sensors.* Nanoscale Research Letters, 2009. **4**(12): 1421-1427.

160. V. Ghafouri, M. Shariati, and A. Ebrahimzad, *Photoluminescence investigation of crystalline undoped ZnO nanostructures constructed by RF sputtering.* Scientia Iranica, 2012. **19**(3): 934-942.

161. E. Elizabeth, R. Yogamalar, S. Ramasamy, and A.C. Bose, *Influence of iron dopant on structure, surface morphology and optical properties of ZnO nanoparticles.* Advanced Materials Research, 2009. **67**: 245-250.

162. C.C. Yang and S. Li, *Size, dimensionality, and constituent stoichiometry dependence of bandgap energies in semiconductor quantum dots and wires.* Journal of Physical Chemistry C, 2008. **112**(8): 2851-2856.

163. K.F. Lin, H.M. Cheng, H.C. Hsu, L.J. Lin, and W.F. Hsieh, *Band gap variation of size-controlled ZnO quantum dots synthesized by sol-gel method.* Chemical Physics Letters, 2005. **409**(4-6): 208-211.

164. D. Pamu, P. Dharama Raju, and A.K. Bhatnagar, *Structural and optical properties of Ba (Zn1 / 3 Ta2 / 3) O3 thin films deposited by pulsed laser deposition.* Solid State Communications, 2009. **149**(43-44): 1932-1935.

165. X.Q. Meng, W. Zhen, J.P. Guo, and X.J. Fan, *Structural, optical and electrical properties of ZnO and ZnO-Al2O3 films prepared by dc magnetron sputtering.* Applied Physics A: Materials Science and Processing, 2000. **70**(4): 421-424.

166. C. Aydn, M.S. Abd El-Sadek, K. Zheng, I.S. Yahia, and F. Yakuphanoglu, *Synthesis, diffused reflectance and electrical properties of nanocrystalline Fe-doped ZnO via sol-gel calcination technique.* Optics and Laser Technology, 2013. **48**: 447-452.

167. N.J. Ronkainen, H.B. Halsall, and W.R. Heineman, *Electrochemical biosensors.* Chemical Society Reviews, 2010. **39**(5): 1747-1763.

168. A. Shokuhi Rad, M. Jahanshahi, M. Ardjmand, and A.A. Safekordi, *Hydrogen peroxide biosensor based on enzymatic modification of electrode using deposited silver nano layer.* International Journal of Electrochemical Science, 2012. **7**(3): 2623-2632.

169. A. Gupta, B.C. Kim, D. Li, E. Edwards, C. Brantley, and P. Ruffin, *Zinc oxide nanowires for biosensing applications*, in *11th IEEE Conference on Nanotechnology*. 2011. p. 1615-1618.

170. M. Tominaga, S. Nomura, and I. Taniguchi, *Bioelectrocatalytic current based on direct heterogeneous electron transfer reaction of glucose oxidase adsorbed onto multi-walled carbon nanotubes synthesized on platinum electrode surfaces.* Electrochemistry Communications, 2008. **10**(6): 888-890.

171. W. Wang, L. Zhang, S. Tong, X. Li, and W. Song, *Three-dimensional network films of electrospun copper oxide nanofibers for glucose determination.* Biosensors and Bioelectronics, 2009. **25**(4): 708-714.

172. M. Viticoli, A. Curulli, A. Cusma, S. Kaciulis, S. Nunziante, L. Pandolfi, F. Valentini, and G. Padeletti, *Third-generation biosensors based on TiO2 nanostructured films.* Materials Science and Engineering C, 2006. **26**(5-7): 947-951.

173. E. Reitz, W. Jia, M. Gentile, Y. Wang, and Y. Lei, *CuO nanospheres based nonenzymatic glucose sensor.* Electroanalysis, 2008. **20**(22): 2482-2486.

174. A.A. Ansari, P.R. Solanki, and B.D. Malhotra, *Sol-gel derived nanostructured cerium oxide film for glucose sensor.* Applied Physics Letters, 2008. **92**(26): 263901.

175. F. Kormos, L. Sziráki, and I. Tarsiche, *Potentiometric biosensor for urinary glucose level monitoring.* Laboratory Robotics and Automation, 2000. **12**(6): 291-295.

176. J. Zang, M.L. Chang, X. Cui, J. Wang, X. Sun, H. Dong, and C.Q. Sun, *Tailoring zinc oxide nanowires for high performance amperometric glucose sensor.* Electroanalysis, 2007. **19**(9): 1008-1014.

177. X. Liu, Q. Hu, Q. Wu, W. Zhang, Z. Fang, and Q. Xie, *Aligned ZnO nanorods: A useful film to fabricate amperometric glucose biosensor.* Colloids and Surfaces B: Biointerfaces, 2009. **74**(1): 154-158.

178. K. Yang, G.W. She, H. Wang, X.M. Ou, X.H. Zhang, C.S. Lee, and S.T. Lee, *ZnO nanotube arrays as biosensors for glucose.* Journal of Physical Chemistry C, 2009. **113**(47): 20169-20172.

179. T. Kong, Y. Chen, Y. Ye, K. Zhang, Z. Wang, and X. Wang, *An amperometric glucose biosensor based on the immobilization of glucose oxidase on the ZnO nanotubes.* Sensors and Actuators, B: Chemical, 2009. **138**(1): 344-350.

180. J.X. Wang, X.W. Sun, A. Wei, Y. Lei, X.P. Cai, C.M. Li, and Z.L. Dong, *Zinc oxide nanocomb biosensor for glucose detection.* Applied Physics Letters, 2006. **88**(23): 233106.

181. C. Shan, H. Yang, D. Han, Q. Zhang, A. Ivaska, and L. Niu, *Graphene/AuNPs/chitosan nanocomposites film for glucose biosensing.* Biosensors and Bioelectronics. **25**(5): 1070-1074.

182. Y. Wei, Y. Li, X. Liu, Y. Xian, G. Shi, and L. Jin, *ZnO nanorods/Au hybrid nanocomposites for glucose biosensor.* Biosensors and Bioelectronics, 2010. **26**(1): 275-278.

183. X.R. Li, Y.H. Bai, J.J. Xu, and H.Y. Chen, *Glucose biosensors based on nano-composites of multi-walled carbon nanotubes and zinc oxide nanorods.* Chinese Journal of Inorganic Chemistry, 2010. **26**(11): 2047-2056.

184. G.Q. Mo, J.S. Ye, and W.D. Zhang, *Unusual electrochemical response of ZnO nanowires-decorated multiwalled carbon nanotubes.* Electrochimica Acta, 2009. **55**(2): 511-515.

185. Z.W. Zhao, X.J. Chen, B.K. Tay, J.S. Chen, Z.J. Han, and K.A. Khor, *A novel amperometric biosensor based on ZnO:Co nanoclusters for biosensing glucose.* Biosensors and Bioelectronics, 2007. **23**(1): 135-139.

186. A. Fulati, S.M.U. Ali, M.H. Asif, N.U.H. Alvi, M. Willander, C. Brännmark, P. Strlfors, S.I. Börjesson, F. Elinder, and B. Danielsson, *An intracellular glucose biosensor based on nanoflake ZnO.* Sensors and Actuators, B: Chemical, 2010. **150**(2): 673-680.

187. Y. Lei, X. Yan, J. Zhao, X. Liu, Y. Song, N. Luo, and Y. Zhang, *Improved glucose electrochemical biosensor by appropriate immobilization of nano-ZnO.* Colloids and Surfaces B: Biointerfaces, 2011. **82**(1): 168-172.

188. Y. Yang, H. Yang, M. Yang, Y. Liu, G. Shen, and R. Yu, *Amperometric glucose biosensor based on a surface treated nanoporous ZrO 2/Chitosan composite film as immobilization matrix.* Analytica Chimica Acta, 2004. **525**(2): 213-220.

189. B. Fang, C. Zhang, G. Wang, M. Wang, and Y. Ji, *A glucose oxidase immobilization platform for glucose biosensor using ZnO hollow nanospheres.* Sensors and Actuators, B: Chemical, 2011. **155**(1): 304-310.

190. S.V. Dzyadevych, V.N. Arkhypova, A.P. Soldatkin, A.V. El'skaya, C. Martelet, and N. Jaffrezic-Renault, *Amperometric enzyme biosensors: Past, present and future.* ITBM-RBM, 2008. **29**(2-3): 171-180.

191. A. El-Ansary and L.M. Faddah, *Nanoparticles as biochemical sensors*. 2010, Dovepress- Nanotechnology, Science and Applications. p. 65-76.

192. S.M.U. Ali, M. Kashif, Z.H. Ibupoto, M. Fakhar-E-Alam, U. Hashim, and M. Willander, *Functionalised zinc oxide nanotube arrays as electrochemical sensors for the selective determination of glucose.* Micro and Nano Letters, 2011. **6**(8): 609-613.

193. Z. Dai, G. Shao, J. Hong, J. Bao, and J. Shen, *Immobilization and direct electrochemistry of glucose oxidase on a tetragonal pyramid-shaped porous ZnO nanostructure for a glucose biosensor.* Biosensors and Bioelectronics, 2009. **24**(5): 1286-1291.

194. A. Kumar, J. Weber, and S. Jeedigunta, *Fabrication and characterization of ZnO nanowire arrays with an investigation into electrochemical sensing capabilities.* Journal of Nanomaterials, 2008. **2008**(1): 638523.

195. A. Umar, M.M. Rahman, S.H. Kim, and Y.B. Hahn, *ZnO nanonails: Synthesis and their application as glucose biosensor.* Journal of Nanoscience and Nanotechnology, 2008. **8**(6): 3216-3221.

196. X. You, J. Park, Y. Jang, S.W. Kim, J.J. Pak, and N.K. Min, *Enzymatic glucose biosensor based on porous ZnO/Au electrodes*, in *4th International Conference on Nano/Molecular Medicine and Engineering*. 2010. p. 56-59.

197. X.W. Sun, J.X. Wang, and A. Wei, *Zinc oxide nanostructured biosensor for glucose detection.* Journal of Materials Science and Technology, 2008. **24**(4): 649-656.

198. E. Darque-Ceretti, D. Hélary, and M. Aucouturier, *An investigation of gold/ceramic and gold/glass interfaces.* Gold Bulletin, 2002. **35**(4): 118-129.

199. H. Aouani, J. Wenger, D. Gérard, H. Rigneault, E. Devaux, T.W. Ebbesen, F. Mahdavi, T. Xu, and S. Blair, *Crucial role of the adhesion layer on the plasmonic fluorescence enhancement.* ACS Nano, 2009. **3**(7): 2043-2048.

200. G. Shuyi, H. Yilin, X. Xiangdong, L. Yin, Z. Hongjun, H. Tonglin, and F. Shaojun, *Influence of binding layer on the reflective performance of a Au film in vacuum ultraviolet wavelength region.* Applied Optics, 2007. **46**(36): 8641-8644.

201. *Platypus Technologies*, available from: http://www.platypustech.com/goldsubstrates.html; [accessed on 24/09/12].

202. X. Chen and S. Dong, *Sol-gel-derived titanium oxide/copolymer composite based glucose biosensor.* Biosensors and Bioelectronics, 2003. **18**(8): 999-1004.

203. S. Zhang, N. Wang, H. Yu, Y. Niu, and C. Sun, *Covalent attachment of glucose oxidase to an Au electrode modified with gold nanoparticles for use as glucose biosensor.* Bioelectrochemistry, 2005. **67**(1): 15-22.

204. J. Jing, *Electrochemical Studies of Nano-structured Materials for Biosensors*. 2009: LAP LAMBERT Academic Publishing.

205. Y. Bentor, *Chemical Elements.com-Silicon*, available from: http://www.chemicalelements.com/elements/si.html; [accessed on 03/04/13].

206. X.H. Chen, Y.J. Xing, J. Xu, J. Xiang, and D.P. Yu, *Rational growth of highly oriented amorphous silicon nanowire films.* Chemical Physics Letters, 2003. **374**(5-6): 626-630.

207. I. Zardo, L. Yu, S. Conesa-Boj, S. Estrade, P.J. Alet, J. Roessler, M. Frimmer, P. Roca i Cabarrocas, F. Peiro, J. Arbiol, J.R. Morante, and A. Fontcuberta i Morral, *Gallium assisted plasma enhanced chemical vapor deposition of silicon nanowires.* Nanotechnology, 2009. **20**(15): 155602.

208. F. Liao, S. Liu, M. Shao, and S.T. Lee, *Surface-dependent chemical properties of silicon nanowires: The acceleration of copper oxidation.* Applied Physics Letters, 2012. **100**(9): 093114

209. S.T. Picraux, S.A. Dayeh, P. Manandhar, D.E. Perea, and S.G. Choi, *Silicon and germanium nanowires: Growth, properties, and integration.* JOM, 2010. **62**(4): 35-43.

210. Y. Cui, Z.H. Zhong, D.L. Wang, W.U. Wang, and C.M. Lieber, *High performance silicon nanowire field effect transistors.* Nano Letters, 2003. **3**(2): 149-152.

211. H. Scheel, S. Reich, and C. Thomsen, *Electronic band structure of high-index silicon nanowires.* Physica Status Solidi (B) Basic Research, 2005. **242**(12): 2474-2479.

212. R. Rurali, *Colloquium: Structural, electronic, and transport properties of silicon nanowires.* Reviews of Modern Physics, 2010. **82**(1): 427-449.

213. C. Harris and E.P. O'Reilly, *Nature of the band gap of silicon and germanium nanowires.* Physica E: Low-Dimensional Systems and Nanostructures, 2006. **32**(1-2 SPEC. ISS.): 341-345.

214. D. Yao, G. Zhang, and B. Li, *A universal expression of band gap for silicon nanowires of different cross-section geometries.* Nano Letters, 2008. **8**(12): 4557-4561.

215. J.Y. Jung, K. Zhou, H.D. Um, Z. Guo, S.W. Jee, K.T. Park, and J.H. Lee, *Effective method to extract optical bandgaps in Si nanowire arrays.* Optics Letters, 2011. **36**(14): 2677-2679.

216. S. Yan, N. He, Y. Song, Z. Zhang, J. Qian, and Z. Xiao, *A novel biosensor based on gold nanoparticles modified silicon nanowire arrays.* Journal of Electroanalytical Chemistry, 2010. **641**(1-2): 136-140.

217. H.F. Yan, Y.J. Xing, Q.L. Hang, D.P. Yu, J. Xu, H.Z. Zhang, Z.H. Xi, and S.Q. Feng, *Controlled growth of amorphous silicon nanowires via a solid-liquid-solid (SLS) mechanism*, in *Nanophase and Nanocomposite Materials Iii*, S.P.J.C.H.H. Komarneni, Editor. 2000. p. 225-229.

218. R.S. Wagner, W.C. Ellis, K.A. Jackson, and S.M. Arnold, *Study of the filamentary growth of silicon crystals from the vapor.* Journal of Applied Physics, 1964. **35**(10): 2993-3000.

219. T.Y. Tan, N. Li, and U. Gösele, *Is there a thermodynamic size limit of nanowires grown by the vapor-liquid-solid process?* Applied Physics Letters, 2003. **83**(6): 1199-1201.

220. E.I. Givargizov, *Fundamental aspects of VLS growth.* Journal of Crystal Growth, 1975. **31**(C): 20-30.

221. K.W. Kolasinski, *Catalytic growth of nanowires: Vapor-liquid-solid, vapor-solid-solid, solution-liquid-solid and solid-liquid-solid growth.* Current Opinion in Solid State and Materials Science, 2006. **10**(3-4): 182-191.

222. S. Christiansen, R. Schneider, R. Scholz, U. Gösele, T. Stelzner, G. Andrä, E. Wendler, and W. Wesch, *Vapor-liquid-solid growth of silicon nanowires by chemical vapor deposition on implanted templates.* Journal of Applied Physics, 2006. **100**(8): 084323.

223. F. Iacopi, P.M. Vereecken, M. Schaekers, M. Caymax, N. Moelans, B. Blanpain, O. Richard, C. Detavernier, and H. Griffiths, *Plasma-enhanced chemical vapour deposition growth of Si nanowires with low melting point metal catalysts: an effective alternative to Au-mediated growth.* Nanotechnology, 2007. **18**(50): 505307.

224. V. Schmidt, J.V. Wittemann, and U. Gösele, *Growth, thermodynamics, and electrical properties of silicon nanowires.* Chemical Reviews, 2010. **110**(1): 361-388.

225. D.P. Yu, Y.J. Xing, Q.L. Hang, H.F. Yan, J. Xu, Z.H. Xi, and S.Q. Feng, *Controlled growth of oriented amorphous silicon nanowires via a solid-liquid-solid (SLS) mechanism.* Physica E, 2001. **9**(2): 305-309.

226. A. Colli, S. Hofmann, A. Fasoli, A.C. Ferrari, C. Ducati, R.E. Dunin-Borkowski, and J. Robertson, *Synthesis and optical properties of silicon nanowires grown by different methods.* Applied Physics A: Materials Science and Processing, 2006. **85**(3): 247-253.

227. V. Schmidt, J.V. Wittemann, S. Senz, and U. Gósele, *Silicon nanowires: A review on aspects of their growth and their electrical properties.* Advanced Materials, 2009. **21**(25-26): 2681-2702.

228. S.F. Abd Rahman, U. Hashim, M.N. Md Nor, and M.E.A. Shohini, *Fabrication of nano and micrometer structures using electron beam and optical mixed lithography process.* International Journal of Nanoelectronics and Materials, 2011. **4**: 49-58.

229. A.S. Alagoz and T. Karabacak, *A systematic study of metal-assisted chemical etching parameters for well-ordered silicon nanowire array fabrication*, in *MRS Proceedings*. 2012. p. 101-105.

230. X. Li, *Metal assisted chemical etching for high aspect ratio nanostructures: A review of characteristics and applications in photovoltaics.* Current Opinion in Solid State and Materials Science, 2012. **16**(2): 71-81.

231. S. Sharma and M.K. Sunkara, *Direct synthesis of single-crystalline silicon nanowires using molten gallium and silane plasma.* Nanotechnology, 2004. **15**(1): 130-134.

232. J. Bae, N.N. Kulkarni, J.P. Zhou, J.G. Ekerdt, and C.K. Shih, *VLS growth of Si nanocones using Ga and Al catalysts.* Journal of Crystal Growth, 2008. **310**(20): 4407-4411.

233. M.K. Sunkara, S. Sharma, R. Miranda, G. Lian, and E.C. Dickey, *Bulk synthesis of silicon nanowires using a low-temperature vapor-liquid-solid method.* Applied Physics Letters, 2001. **79**(10): 1546-1548.

234. J.F. Hsu and B.R. Huang, *The growth of silicon nanowires by electroless plating technique of Ni catalysts on silicon substrate.* Thin Solid Films, 2006. **514**(1-2): 20-24.

235. S. Wan, Y. Yu, and J. Zhang, *The synthesis of aligned silicon nanowires under ambient atmospheric pressure.* Journal of Non-Crystalline Solids, 2009. **355**(8): 518-520.

236. Y. Cui, L.J. Lauhon, M.S. Gudiksen, J. Wang, and C.M. Lieber, *Diameter-controlled synthesis of single-crystal silicon nanowires.* Applied Physics Letters, 2001. **78**(15): 2214-2216.

237. Z.W. Pan, Z.R. Dai, C. Ma, and Z.L. Wang, *Molten gallium as a catalyst for the large-scale growth of highly aligned silica nanowires.* Journal of the American Chemical Society, 2002. **124**(8): 1817-1822.

238. S. Hofmann, C. Ducati, R.J. Neill, S. Piscanec, A.C. Ferrari, J. Geng, R.E. Dunin-Borkowski, and J. Robertson, *Gold catalyzed growth of silicon nanowires by plasma enhanced chemical vapor deposition.* Journal of Applied Physics, 2003. **94**(9): 6005-6012.

239. H. Jagannathan, Y. Nishi, M. Reuter, M. Copel, E. Tutuc, S. Guha, and R.P. Pezzi, *Effect of oxide overlayer formation on the growth of gold catalyzed epitaxial silicon nanowires.* Applied Physics Letters, 2006. **88**(10): 103113.

240. J. Westwater, D.P. Gosain, S. Tomiya, S. Usui, and H. Ruda, *Growth of silicon nanowires via gold/silane vapor-liquid-solid reaction.* Journal of Vacuum Science & Technology B, 1997. **15**(3): 554-557.

241. E.C. Garnett, W. Liang, and P. Yang, *Growth and electrical characteristics of platinum-nanoparticle-catalyzed silicon nanowires.* Advanced Materials, 2007. **19**(19): 2946-2950.

242. F.W. Yuan, H.J. Yang, and H.Y. Tuan, *Seeded silicon nanowire growth catalyzed by commercially available bulk metals: Broad selection of metal catalysts, superior field emission performance, and versatile nanowire/metal architectures.* Journal of Materials Chemistry, 2011. **21**(36): 13793-13800.

243. J.V. Wittemann, A. Kipke, E. Pippel, S. Senz, A.T. Vogel, J. De Boor, D.S. Kim, T. Hyeon, and V. Schmidt, *Citrate-stabilized palladium nanoparticles as catalysts for sub-20 nm epitaxial silicon nanowires.* Applied Physics Letters, 2010. **97**(2): 023105.

244. J. Arbiol, B. Kalache, P.R.I. Cabarrocas, J.R. Morante, and A.F.I. Morral, *Influence of Cu as a catalyst on the properties of silicon nanowires synthesized by the vapour-solid-solid mechanism.* Nanotechnology, 2007. **18**(30): 305606.

245. D.P. Yu, Z.G. Bai, Y. Ding, Q.L. Hang, H.Z. Zhang, J.J. Wang, Y.H. Zou, W. Qian, G.C. Xiong, H.T. Zhou, and S.Q. Feng, *Nanoscale silicon wires synthesized using simple physical evaporation.* Applied Physics Letters, 1998. **72**(26): 3458-3460.

246. S. Conesa-Boj, I. Zardo, S. Estradé, L. Wei, P. Jean Alet, P. Roca i Cabarrocas, J.R. Morante, F. Peiró, A.F.I. Morral, and J. Arbiol, *Defect formation in Ga-catalyzed silicon nanowires.* Crystal Growth and Design, 2010. **10**(4): 1534-1543.

247. H. Griffiths, C. Xu, T. Barrass, M. Cooke, F. Iacopi, P. Vereecken, and S. Esconjauregui, *Plasma assisted growth of nanotubes and nanowires.* Surface and Coatings Technology, 2007. **201**(22-23 SPEC. ISS.): 9215-9220.

248. S.W. Chung, J.Y. Yu, and J.R. Heath, *Silicon nanowire devices.* Applied Physics Letters, 2000. **76**(15): 2068-2070.

249. J.D. Carter, Y. Qu, R. Porter, L. Hoang, D.J. Masiel, and T. Guo, *Silicon-based nanowires from silicon wafers catalyzed by cobalt nanoparticles in a hydrogen environment.* Chemical Communications, 2005(17): 2274-2276.

250. F. Iacopi, P.M. Vereecken, M. Schaekers, M. Caymax, N. Moelans, B. Blanpain, C. Detavernier, J. D'Haen, and H. Griffiths, *Alternative catalysts for si-technology compatible growth of si nanowires*, in *MRS Proceedings*. 2007. p. 8-13.

251. D.D. Fanfair and B.A. Korgel, *Bismuth nanocrystal-seeded III-V semiconductor nanowire synthesis.* Crystal Growth and Design, 2005. **5**(5): 1971-1976.

252. M. Jeon, H. Uchiyama, and K. Kamisako, *Characterization of Tin-catalyzed silicon nanowires synthesized by the hydrogen radical-assisted deposition method.* Materials Letters, 2009. **63**(2): 246-248.

253. A. Lugstein, M. Steinmair, Y.J. Hyun, E. Bertagnolli, and P. Pongratz, *Ga/Au alloy catalyst for single crystal silicon-nanowire epitaxy.* Applied Physics Letters, 2007. **90**(2): 023109.

254. Z.Q. Liu, W.Y. Zhou, L.F. Sun, D.S. Tang, X.P. Zou, Y.B. Li, C.Y. Wang, G. Wang, and S.S. Xie, *Growth of amorphous silicon nanowires.* Chemical Physics Letters, 2001. **341**(5-6): 523-528.

255. Z. Pan, S. Dai, and D.H. Lowndes, *Gallium-catalyzed silicon oxide nanowire growth.* Tsinghua Science and Technology, 2005. **10**(6): 718-728.

256. X. Yan and Y.A. Chang, *Thermodynamic analysis of the Cu-Si system.* Journal of Alloys and Compounds, 2000. **308**(1-2): 221-229.

257. D. Parlevliet and J.C.L. Cornish, *Silicon nanowires: Growth studies using pulsed PECVD*, in *MRS Proceedings*. 2007. p. 537-542.

258. J. Červenka, M. Ledinský, J. Stuchlík, H. Stuchlíková, S. Bakardjieva, K. Hruška, A. Fejfar, and J. Kočka, *The structure and growth mechanism of Si nanoneedles prepared by plasma-enhanced chemical vapor deposition.* Nanotechnology, 2010. **21**(41): 415604.

259. Y. Qin, F. Li, D. Liu, H. Yan, J. Wang, and D. He, *The structure and optical properties of silicon nanowires prepared by inductively coupled plasma chemical vapor deposition.* Materials Letters, 2011. **65**(7): 1117-1119.

260. A. Gewalt, B. Kalkofen, M. Lisker, and E.P. Burte, *Epitaxial growth of Si nanowires by a modified VLS method using molten Ga as growth assistant*, in *MRS Proceedings*. 2009. p. 13-18.

261. M. Hetzel, A. Lugstein, C. Zeiner, T. Wójcik, P. Pongratz, and E. Bertagnolli, *Ultra-fast vapour-liquid-solid synthesis of Si nanowires using ion-beam implanted gallium as catalyst.* Nanotechnology, 2011. **22**(39).

262. J. Kikkawa, Y. Ohno, and S. Takeda, *Growth rate of silicon nanowires.* Applied Physics Letters, 2005. **86**(12): 1-3.

263. S. Akhtar, K. Usami, Y. Tsuchiya, H. Mizuta, and S. Oda, *Vapor-liquid-solid growth of small and uniform-diameter silicon nanowires at low temperature from Si2H6.* Applied Physics Express, 2008. **1**(1): 014003.

264. N. Ozaki, Y. Ohno, and S. Takeda, *Silicon nanowhiskers grown on a hydrogen-terminated silicon 111 surface.* Applied Physics Letters, 1998. **73**(25): 3700-3702.

265. P. Gentile, T. David, F. Dhalluin, D. Buttard, N. Pauc, M. Den Hertog, P. Ferret, and T. Baron, *The growth of small diameter silicon nanowires to nanotrees.* Nanotechnology, 2008. **19**(12): 125608.

266. L. Sharon, Y. Hua, S. Zhao, and Z. Mo, *Studies on electron penetration versus beam acceleration voltage in energy-dispersive X-ray microanalysis*, in *IEEE International Conference on Semiconductor Electronics*. 2006. p. 610-613.

267. B. Kalache, P. Roca i Cabarrocas, and A. Fontcuberta i Morral, *Observation of incubation times in the nucleation of silicon nanowires obtained by the vapor-liquid-solid method.* Japanese Journal of Applied Physics, Part 2: Letters, 2006. **45**(4-7): L190-L193.

268. N. Gabrielyan, K. Saranti, K.N. Manjunatha, and S. Paul, *Growth of low temperature silicon nano-structures for electronic and electrical energy generation applications.* Nanoscale Research Letters, 2013. **8**(1): 83-83.

269. L. Yu, B. O'Donnell, P.J. Alet, S. Conesa-Boj, F. Peiró, J. Arbiol, and P.R.I. Cabarrocas, *Plasma-enhanced low temperature growth of silicon nanowires and hierarchical structures by using tin and indium catalysts.* Nanotechnology, 2009. **20**(22): 225604.

270. T. Yoshida, S. Takeyama, Y. Yamada, and K. Mutoh, *Nanometer-sized silicon crystallites prepared by excimer laser ablation in constant pressure inert gas.* Applied Physics Letters, 1996. **68**(13): 1772-1774.

271. H.Z. Zhang, D.P. Yu, Y. Ding, Z.G. Bai, Q.L. Hang, and S.Q. Feng, (1998). *Dependence of the silicon nanowire diameter on ambient pressure.* 73

272. H.M. Park, C. Garvin, D.S. Grimard, and J.W. Grizzle, *Control of ion energy in a capacitively coupled reactive ion etcher.* Journal of the Electrochemical Society, 1998. **145**(12): 4247-4252.

273. X. Xie, X. Zeng, P. Yang, C. Wang, and Q. Wang, *In situ formation of indium catalysts to synthesize crystalline silicon nanowires on flexible stainless steel substrates by PECVD.* Journal of Crystal Growth, 2012. **347**(1): 7-10.

274. M. Schade, O. Varlamova, J. Reif, H. Blumtritt, W. Erfurth, and H.S. Leipner, *High-resolution investigations of ripple structures formed by femtosecond laser irradiation of silicon.* Analytical and Bioanalytical Chemistry, 2010. **396**(5): 1905-1911.

275. R.P. Wang, G.W. Zhou, Y.L. Liu, S.H. Pan, H.Z. Zhang, D.P. Yu, and Z. Zhang, *Raman spectral study of silicon nanowires: High-order scattering and phonon confinement effects.* Physical Review B - Condensed Matter and Materials Physics, 2000. **61**(24): 16827-16832.

276. A.T. Voutsas, M.K. Hatalis, J. Boyce, and A. Chiang, *Raman spectroscopy of amorphous and microcrystalline silicon films deposited by low-pressure chemical vapor deposition.* Journal of Applied Physics, 1995. **78**(12): 6999-7006.

277. C. Li, G. Fang, S. Sheng, Z. Chen, J. Wang, S. Ma, and X. Zhao, *Raman spectroscopy and field electron emission properties of aligned silicon nanowire arrays.* Physica E: Low-Dimensional Systems and Nanostructures, 2005. **30**(1-2): 169-173.

278. P. Sharma, V. Stolojan, and S.R.P. Silva, *Raman analysis of oxide cladded silicon core nanowires grown with solid silicon feed stock.* Journal of Nanoparticle Research, 2011. **13**(7): 2697-2703.

279. H. Scheel, S. Reich, A.C. Ferrari, M. Cantoro, A. Colli, and C. Thomsen, *Raman scattering on silicon nanowires: The thermal conductivity of the environment determines the optical phonon frequency.* Applied Physics Letters, 2006. **88**(23): 233114.

280. S. Piscanec, M. Cantoro, A.C. Ferrari, J.A. Zapien, Y. Lifshitz, S.T. Lee, S. Hofmann, and J. Robertson, *Raman spectroscopy of silicon nanowires.* Physical Review B - Condensed Matter and Materials Physics, 2003. **68**(24): 2413121-2413124.

281. N. Sakulchaicharoen and D.E. Resasco, *Temperature dependence of the quality of silicon nanowires produced over a titania-supported gold catalyst.* Chemical Physics Letters, 2003. **377**(3-4): 377-383.

282. J. Davenas, E. Beyou, A. Balloffet, D. Cornu, and S. Vignoli, *Silicon nanowire/poly(3-hexylthiophene) hybrids for thin film solar cells.* Journal of Non-Crystalline Solids, 2012.

283. M.N. Rahaman, *Ceramic Processing and Sintering*. Second ed. 2005: Taylor & Francis.

284. *Gallium Acetylacetonate*, available from: http://www.americanelements.com/gaacac.html; [accessed on 10/10/2012].

285. *Toxin and Toxin Target Database*, available from: http://www.t3db.org/toxins; [accessed on 10/09/2012].

286. V. Rosenband and A. Gany, *Preparation of nickel and copper submicrometer particles by pyrolysis of their formates.* Journal of Materials Processing Technology, 2004. **153-154**(1-3): 1058-1061.

287. P. Chokratanasombat and E. Nisaratanaporn, *Preparation of ultrafine copper powders with controllable size via polyol process with sodium hydroxide addition.* Engineering Journal, 2012. **16**(4): 39-46.

288. Y.I. Khimchenko, V.P. Vasilenko, L.S. Radkevich, V.V. Myalkovskii, T.V. Chubar, and V.M. Chegoryan, *Decomposition of iron, cobalt, nickel, and copper formates.* Soviet Powder Metallurgy and Metal Ceramics, 1977. **16**(5): 327-332.

289. J.C. De Jesus, I. González, A. Quevedo, and T. Puerta, *Thermal decomposition of nickel acetate tetrahydrate: An integrated study by TGA, QMS and XPS techniques.* Journal of Molecular Catalysis A: Chemical, 2005. **228**(1-2 SPEC. ISS.): 283-291.

290. G.A.M. Hussein, A.K.H. Nohman, and K.M.A. Attyia, *Characterization of the decomposition course of nickel acetate tetrahydrate in air.* Journal of Thermal Analysis, 1994. **42**(6): 1155-1165.

291. M.A. Mohamed, S.A. Halawy, and M.M. Ebrahim, *Non-isothermal decomposition of nickel acetate tetrahydrate.* Journal of Analytical and Applied Pyrolysis, 1993. **27**(2): 109-110.

292. P.K. Gallagher and M.E. Gross, *The thermal decomposition of palladium acetate.* Journal of Thermal Analysis, 1986. **31**(6): 1231-1241.

293. C.N.R. Rao and A. Govindaraj, *Nanotubes and nanowires.* Proceedings of the Indian Academy of Sciences: Chemical Sciences, 2001. **113**(5-6): 375-392.

294. F.J. Li, S. Zhang, J.H. Kong, J. Guo, X.B. Cao, and B. Li, *Growth of crystalline silicon nanowires on nickel-coated silicon wafer beneath sputtered amorphous carbon.* Thin Solid Films, 2013. **534**: 90-99.

295. S. Hofmann, R. Sharma, C.T. Wirth, F. Cervantes-Sodi, C. Ducati, T. Kasama, R.E. Dunin-Borkowski, J. Drucker, P. Bennett, and J. Robertson, *Ledge-flow-controlled catalyst interface dynamics during Si nanowire growth.* Nature Materials, 2008. **7**(5): 372-375.

296. G.A. Bootsma and H.J. Gassen, *A quantitative study on the growth of silicon whiskers from silane and germanium whiskers from germane.* Journal of Crystal Growth, 1971. **10**(3): 223-234.

297. S. Paul, (20/08/2010). *A low temperature method for the production of polycrystalline silicon, aligned silicon columns and silicon nanowires.* United Kingdom. GB2482915

298. A.H. Qusti, A.A. Samarkandy, S. Al-Thabaiti, and E.-H.M. Diefallah, *The kinetics of thermal decomposition of nickel formate dihydrate in air.* JKAU:Sci, 1997. **9**: 77-81.

299. J. Vicente and A. Arcas, *Aqua palladium complexes: Synthesis, properties and applications.* Coordination Chemistry Reviews, 2005. **249**(11-12): 1135-1154.

300. M.A. Vásquez-A, G. Águila Rodríguez, G. García-Salgado, G. Romero-Paredes, and R. Peña-Sierra, *FTIR and photoluminescence studies of porous silicon layers oxidized in controlled water vapor conditions.* Revista Mexicana de Fisica, 2007. **53**(6): 431-435.

301. Y.J. Oh, S.M. Cho, and C.H. Chung, *An in situ ATR-FTIR study on palladium displacement reaction on hydrogen-terminated silicon surface.* Journal of the Electrochemical Society, 2005. **152**(6): C348-C355.

302. E. Kanezaki, S. Tanaka, K.I. Murai, T. Moriga, J. Motonaka, M. Katoh, and I. Nakabayashi, *Direct detection of a phase change in PdO/CeO2 supported on χ-Al2O3 by means of in situ high-temperature measurements XRD and FTIR.* Analytical Sciences, 2004. **20**(7): 1069-1073.

303. J.M. Tura, P. Regull, L. Victori, and M.D. de Castellar, *XPS AND IR (ATR) ANALYSIS OF Pd OXIDE FILMS OBTAINED BY ELECTROCHEMICAL METHODS.* Surface and Interface Analysis, 1988. **11**(8): 447-449.

304. J.Y. Zhang and I.W. Boyd, *Photo-decomposition of thin palladium acetate films with 126 nm radiation.* Applied Physics A: Materials Science and Processing, 1997. **65**(4-5): 379-382.

305. V. Tsaryuk, J. Legendziewicz, V. Zolin, J. Sokolnicki, R. Szostak, and L. Puntus, *Spectra and details of the structure of europium acetates with derivatives of 1,10-phenanthroline.* Journal of Alloys and Compounds, 2001. **323-324**: 661-666.

306. D.D. Kragten, *Acetoxylation of Ethylene to Vinyl Acetate Over Palladium-based Catalysts*. 1999: Technische Universiteit Eindhoven.

307. L.F. Liao, C.F. Lien, and J.L. Lin, *FTIR study of adsorption and photoreactions of acetic acid on TiO 2.* Physical Chemistry Chemical Physics, 2001. **3**(17): 3831-3837.

308. Z. Nickolov, G. Georgiev, D. Stoilova, and I. Ivanov, *Raman and IR study of cobalt acetate dihydrate.* Journal of Molecular Structure, 1995. **354**(2): 119-125.

309. D. Stoilova and V. Koleva, *Infrared spectroscopic study of mixed copper-cobalt and copper-nickel formate dihydrates (cation distribution in mixed crystals).* Spectrochimica Acta - Part A: Molecular and Biomolecular Spectroscopy, 2001. **57**(13): 2629-2636.

310. S.N. Slabzhennikov, O.B. Ryabchenko, and L.A. Kuarton, *Interpretation of the IR spectra of aluminum, gallium, and indium tris(acetylacetonates).* Russian Journal of Coordination Chemistry/Koordinatsionnaya Khimiya, 2006. **32**(8): 545-551.

311. R.M. Mahfouza, K.M. Al-Khamis, M.R.H. Siddiqui, N.S. Al-Hokbany, I. Warad, and N.M. Al-Andis, *Kinetic studies of isothermal decomposition of unirradiated and γ-*

irradiated gallium acetylacetonate: New route for synthesis of gallium oxide nanoparticles. Progress in Reaction Kinetics and Mechanism, 2012. **37**(3): 249-262.

312. S. Cakic, C. Lacnjevac, G. Nikolic, J. Stamenkovic, M.B. Rajkovic, M. Gligoric, and M. Barac, *Spectroscopic characteristics of highly selective manganese catalysis in acqueous polyurethane systems.* Sensors, 2006. **6**(11): 1708-1720.

313. S.A. Sadeek, *Spectroscopic and thermal studies of the reaction of iodine with cobalt(II) and copper(II) acetylacetonate.* The Journal of the Argentine Chemical Society, 2005. **93**(1/3): 165-176.

314. C.A. Decker, R. Solanki, J.L. Freeouf, J.R. Carruthers, and D.R. Evans, *Directed growth of nickel silicide nanowires.* Applied Physics Letters, 2004. **84**(8): 1389-1391.

315. G.F. Iriarte, *Growth of nickel disilicide nanowires by CVD.* Journal of Non-Crystalline Solids, 2010. **356**(23-24): 1135-1144.

316. G.F. Iriarte, *Growth of nickel silicide (NiSix) nanowires by silane decomposition.* Current Applied Physics, 2011. **11**(1): 82-86.

317. J. Hodkiewicz and M. Wall, *Characterization of microcrystalline and amorphous thin film silicon devices with Raman spectroscopy*, in *Nanotechnology 2010: Bio Sensors, Instruments, Medical, Environment and Energy*. 2010. p. 745-746.

318. S. Bhattacharyya, D. Churochkin, and R.M. Erasmus, *Anomalous Raman features of silicon nanowires under high pressure.* Applied Physics Letters, 2010. **97**(14): 141912.

319. H. Scheel, S. Khachadorian, M. Cantoro, A. Colli, A.C. Ferrari, and C. Thomsen, *Silicon nanowire optical Raman line shapes at cryogenic and elevated temperatures.* Physica Status Solidi (B) Basic Research, 2008. **245**(10): 2090-2093.

320. P.S. Lee, D. Mangelinck, K.L. Pey, Z.X. Shen, J. Ding, T. Osipowicz, and A. See, *Micro-Raman spectroscopy investigation of nickel silicides and nickel (platinum) silicides.* Electrochemical and Solid-State Letters, 2000. **3**(3): 153-155.

321. S.K. Donthu, D.Z. Chi, S. Tripathy, A.S.W. Wong, and S.J. Chua, *Micro-Raman spectroscopic investigation of NiSi films formed on BF 2 +-, B+-and non-implanted (100)Si substrates.* Applied Physics A: Materials Science and Processing, 2004. **79**(3): 637-642.

322. S. Cichoň, B. Barda, and P. Machác, *Ni and Ni silicides ohmic contacts on N-type 6H-SiC with medium and low doping level.* Radioengineering, 2011. **20**(1): 209-213.

323. Q. Wang, Q. Luo, and C.Z. Gu, *Nickel silicide nanowires formed in pre-patterned SiO2 trenches and their electrical transport properties.* Nanotechnology, 2007. **18**(19): 195304.

324. T. Sasaki, S. Nishibe, H. Harima, T. Isshiki, M. Yoshimoto, K. Kisoda, W.S. Yoo, and T. Fukada, *Raman study of low-temperature formation of nickel silicide layers*, in *14th International Conference on Advanced Thermal Processing of Semiconductors*. 2006. p. 217-222.

325. Y. Cui, Q. Wei, H. Park, and C.M. Lieber, *Nanowire nanosensors for highly sensitive and selective detection of biological and chemical species.* Science, 2001. **293**(5533): 1289-1292.

326. C. Gao, S.R. Deng, J. Wan, B.R. Lu, R. Liu, E. Huq, X.P. Qu, and Y. Chen, *22 nm silicon nanowire gas sensor fabricated by trilayer nanoimprint and wet etching.* Microelectronic Engineering, 2010. **87**(5-8): 927-930.

327. J. Wan, S.R. Deng, R. Yang, Z. Shu, B.R. Lu, S.Q. Xie, Y. Chen, E. Huq, R. Liu, and X.P. Qu, *Silicon nanowire sensor for gas detection fabricated by nanoimprint on SU8/SiO2/PMMA trilayer.* Microelectronic Engineering, 2009. **86**(4-6): 1238-1242.

328. H. Guo, L. Lou, X. Chen, and C. Lee, *PDMS-coated piezoresistive NEMS diaphragm for chloroform vapor detection.* IEEE Electron Device Letters, 2012. **33**(7): 1078-1080.

329. J. Song and N. Zhu, *High sensitive gas sensor application based on a small defect in silicon waveguide.* IEEE Photonics Technology Letters, 2009. **21**(2): 82-84.

330. A.A. Talin, L.L. Hunter, F. Ĺonard, and B. Rokad, *Large area, dense silicon nanowire array chemical sensors.* Applied Physics Letters, 2006. **89**(15): 153102.

331. X.T. Zhou, J.Q. Hu, C.P. Li, D.D.D. Ma, C.S. Lee, and S.T. Lee, *Silicon nanowires as chemical sensors.* Chemical Physics Letters, 2003. **369**(1-2): 220-224.

332. K. Skucha, Z. Fan, K. Jeon, A. Javey, and B. Boser, *Palladium/silicon nanowire Schottky barrier-based hydrogen sensors.* Sensors and Actuators, B: Chemical, 2010. **145**(1): 232-238.

333. L. Ni, E. Jacques, R. Rogel, A.C. Salauen, L. Pichon, and G. Wenga, *VLS silicon nanowires based resistors for chemical sensor applications*, in *26th European Conference on Solid-State Transducers, Eurosensor 2012*, R. Walczak and J. Dziuban, Editors. 2012. p. 240-243.

334. O.H. Elibol, D. Morisette, D. Akin, J.P. Denton, and R. Bashir, *Integrated nanoscale silicon sensors using top-down fabrication.* Applied Physics Letters, 2003. **83**(22): 4613-4615.

335. A. Tibuzzi, B. Margesin, M. Decarli, C. Di Natale, M. Zen, A. D'Amico, and G. Soncini, *MOS-Junction-based nanostructures by thermal oxidation of silicon wires for hydrogen detection.* IEEE Transactions on Nanotechnology, 2004. **3**(2): 287-292.

336. M.C. McAlpine, H. Ahmad, D. Wang, and J.R. Heath, *Highly ordered nanowire arrays on plastic substrates for ultrasensitive flexible chemical sensors.* Nature Materials, 2007. **6**(5): 379-384.

337. C. Gao, Z.C. Xu, S.R. Deng, J. Wan, Y. Chen, R. Liu, E. Huq, and X.P. Qu, *Silicon nanowires by combined nanoimprint and angle deposition for gas sensing applications.* Microelectronic Engineering, 2011. **88**(8): 2100-2104.

338. F. Demami, L. Ni, R. Rogel, A.C. Salaun, and L. Pichon, *Silicon nanowires synthesis for chemical sensor applications*, in *Proc. Eurosensors XXIV*. 2010. p. 351-354.

339. F. Demami, L. Ni, R. Rogel, A.C. Salaun, and L. Pichon, *Silicon nanowires based resistors as gas sensors.* Sensors and Actuators, B: Chemical, 2012. **170**: 158-162.

340. E. Jacques, L. Ni, A.C. Salaün, R. Rogel, and L. Pichon. *Polysilicon nanowires for chemical sensing applications*. in *MRS Proceedings*. 2012.

341. H.T. Hsueh, T.J. Hsueh, S.J. Chang, F.Y. Hung, W.Y. Weng, C.L. Hsu, and B.T. Dai, *Si nanowire-based humidity sensors prepared on glass substrate.* IEEE Sensors Journal, 2011. **11**(11): 3036-3041.

342. J.T. Yates Jr, *Surface chemistry of silicon - The behaviour of dangling bonds.* Journal of Physics: Condensed Matter, 1991. **3**(S): S143-S156.

343. N.N.I.o.S.a. Technology), *CODATA Internationally recommended values of the Fundamental Physical Constants*, available from: http://www.nist.gov/pml/index.cfm; [accessed on 26/05/2013].

“Education is what remains after one has forgotten everything he learned in school.”

... Albert Einstein